Microscale and Ultrafast High Cycle Fatigue Testing of Titanium



Arutyun Arutyunyan

Lincoln College

University of Oxford

Supervisors: Prof Angus Wilkinson and Dr Jicheng Gong

A thesis submitted for the degree of

Doctor of Philosophy

Trinity 2019

Acknowledgements

I would first and foremost like to thank my supervisors, Angus Wilkinson and Jicheng Gong. Their support, advice and guidance throughout this process has been invaluable. I'm also grateful to Dave Rugg for thought-provoking discussions and the industrial support for the project. A very big thank you to Phani Karamched for his help with the crack tip lift-outs.

Thank you to the members of the Department who have helped me with training and support; Gareth Hughes, Jennifer Holter and Graham Wyatt for help with electron microscopy, Pete Flaxman and Tony Wheeler for help in the workshop and making specimen holders key to my project, and Rebecca Bradford for ensuring that my time at the Department went as smoothly as possible.

Thank you to Beth who provided tremendous support when I was juggling work with writing. I would also like to thank my grandparents Vladimir Arutyunyan, Natasha Arutyunyan, Sergei Minasian and Julia Minasian; their love and encouragement throughout my life have gotten me to where I am today. To mum, Vladimir, Anna and Marina, I am thankful for the continuous motivation you have given me during my academic pursuits.

Abstract

The fatigue properties and crack growth behaviour in Grade 2 commercially pure titanium (CP Ti) was investigated using a miniature ultrafast testing method. Using finite element modelling (FEM) a dogbone type mesoscale cantilever specimen was designed, that facilitated the shift of stress concentrations from sharp corners in a simple initial cantilever design to the centre of a beam. This ensured that failure was more dependent on microstructure than sample geometry.

Monotonic single crystal microscale cantilever tests were performed that isolated <a> prism, <a> basal and <c+a> first order pyramidal planes. The bulk critically resolved shear stress (CRSS) for these slip systems were 130 MPa, 298 MPa and 795 MPa respectively. These experiments showed that slip is most likely to occur on <a> prism planes. In addition, using von Mises criterion to determine the yield stress from the CRSS of <a> prism (225 MPa) was comparable to the mean bulk 0.2% yield stress measured by monotonic tensile tests (243 MPa). The monotonic bulk tensile tests on typical dogbone samples also demonstrated that the elastic modulus along the length axis of a microcantilever as measured from the microscale tests of <a> prism had good agreement with bulk data (~105 GPa). It has also been shown that in ultrafast mesoscale tests there is good agreement with both microscale and macroscale tests as it has been shown that failure is extremely unlikely to occur below ~240 MPa.

By comparing both single-step and multi-step testing approaches to ultrasonic fatigue testing it has been shown that there is little/no coaxing effect in Grade 2 CP Ti. By fitting a Basquin power law fit to the fatigue data generated, a fatigue coefficient (S) of 675 MPa and fatigue exponent (b) of -0.048 was achieved. In-situ ultrasonic mesoscale testing has also shown the ability to

track crack growth and demonstrate the importance of fatigue crack initiation resistance when designing for high cycle fatigue resistance. In addition, the testing method has been able to distinguish between sample surface conditions and calculate the fatigue performance deficit as a result. Fractography data has also informed that fatigue cracks in these specimens initiate primarily from the surface and the edges of the beam. Furthermore, fractography has allowed for the observation of the steady-state nature of crack growth as the crack extends into the centre of the beam.

A significant correlation was established between increased local GND density as revealed by HR-EBSD, and local surface slip features imaged in SEM, with grain boundaries at which the slip systems available in the two grains were misaligned. Increased plastic work and poor stress transfer between the misaligned shear planes lead to slowing of the fatigue crack and/or a change in crack path generally increasing resistance to short fatigue crack growth at these features.

List of Abbreviations

CP	Commercially pure
CRSS	Critically resolved shear stress
DIC	Digital image correlation
ECCI	Electron channelling contrast imaging
EBSD	Electron backscatter diffraction
FCI	Fatigue crack initiation
FEM	Finite element modelling
FIB	Focussed ion beam
FIP	Fatigue initiation parameters
HCF	High cycle fatigue
HCP	Hexagonal close packed
IPF	Inverse pole figure
LCF	Low cycle fatigue
SCG	Short crack growth
SEM	Scanning Electron Microscopy
TKD	Transmission Kikuchi Diffraction
UTS	Ultimate Tensile Strength
VHCF	Very high cycle fatigue

Contents

Introduction **1**

1 Literature Review **4**
1.1 Titanium in the Aerospace Industry 4
1.2 Fatigue of Titanium and its Alloys 7
1.2.1 Lifing of Components 7
1.2.2 Crack Initiation and Propagation 8
1.2.3 Fractography 12
1.3 Ultrasonic High Cycle Fatigue Testing 14
1.4 Microcantilever Testing 25
1.5 Electron Backscatter Diffraction 30
1.6 Transmission Kikuchi Diffraction 34
1.7 Aims of this Work 35

2 Materials and Experimental Methods **37**
2.1 Materials 37
2.1.1 Commercially Pure Titanium 37
2.2 Sample Preparation 38
2.2.1 Laser cutting 38
2.2.2 Water-jet cutting 38
2.2.3 Focussed Ion Beam Milling 39
2.2.4 Electropolishing 43
2.3 Testing 46
2.3.1 Tensile Testing 46
2.3.2 Ultrasonic Fatigue Testing 47
2.3.3 Nanoindentation 52
2.4 Characterisation and Specimen Analysis Techniques 55
2.4.1 Scanning Electron Microscopy 56
2.4.1.1 Electron Backscatter Diffraction 57
2.4.1.2 Transmission Kikuchi Diffraction 57

3 Cantilever Specimen Design **60**
3.1 The Model 64
3.1.1 Mesocantilevers 64
3.1.2 Microcantilevers 73

3.2 Summary . . . 78

4 Static Loading Material Behaviour **79**
4.1 Tensile Tests . . . 79
4.1.1 Strain Rate Sensitivity . . . 82
4.2 Microcantilever Tests . . . 84
4.2.1 Determining the Elastic Modulus and Critical Resolved Shear Stress . . . 88
4.3 Summary . . . 95

5 Fatigue Properties **96**
5.1 Stress-Life Data (S-N curves) . . . 96
5.1.1 Calibration of Cantilever Deflection . . . 97
5.1.2 Ultrafast High Cycle Fatigue Results . . . 100
5.2 Crack Growth Rate . . . 112
5.3 Fracture Surface Analysis . . . 117
5.4 Variation in Crack Growth Rate . . . 122
5.5 Summary . . . 123

6 Effect of microstruture on crack initiation and short crack growth **126**
6.1 Initiation . . . 128
6.2 Crack Path Analysis . . . 135
6.3 Summary . . . 155

7 Conclusions **156**

8 Future Work **159**

Bibliography **164**

List of Figures

1.1 Density normalised maximum stress (R = 0) vs. cycles to failure for TMCs and two unreinforced metallic alloys. . . . 7
1.2 Typical process for establishing the Approved Life of rotating parts. . . . 8
1.3 Schematic of a Goodman diagram. . . . 9
1.4 Dependence of HCF strength (R = −1) of lamellar microstructures on cooling rate from the β phase field, Ti–6Al–4V. . . . 12
1.5 An example of striations formed by cyclic fatigue in Ti–6Al–4. (An area of striations have been marked by a black border). . . . 13
1.6 Photomicrographs showing fracture profiles, (a) pre-transition, $\Delta K = 10\,\mathrm{MPa}\sqrt{m}$, R_s=1.36 and (b) post-transition, $\Delta K = 18\,\mathrm{MPa}\sqrt{m}$, R_s=1.18. . . . 15
1.7 S–N curve for Spheroidal Graphite Iron tested at 20 kHz and 25 kHz (R=-1). . 16
1.8 A schematic illustrating the typical setup of an ultrasonic fatigue tester. . . . 17
1.9 A graph illustrating the safety coefficient employed to determine the maximum life of a component at a specific stress. . . . 18
1.10 Graphs that show the increase in temperature of the surface of a mesocantilever (a) at stress below failure (b) at stress that have caused failure. . . . 19
1.11 An example of fatigue defects in a specimen loaded at a stress amplitude of 410 MPa until 10^{10} cycles without fracture. . . . 20
1.12 An example of data that would be achieved using the staircase testing method for ultrafast high cycle fatigue testing. . . . 20
1.13 S–N curve for 2024/T3 aluminium alloy illustrating the two different failure modes. Mode A = Failure origin is an inclusion, Mode B = Failure origin are persistent slip bands. . . . 22
1.14 S–N curve for CP Ti and Ti–6Al–7Nb loaded in tension, torsion and tension/torsion at R=0.1 at 2 Hz. . . . 23
1.15 Dimensions of the two dogbone specimen designs (units = mm) used in tests by Sajadifar et al. . . . 24
1.16 Stress applied vs Cycles to failure for bulk CP Ti specimens with different specimen radii (as described in Figure 1.15). (a) coarse grain specimens, (b) ultrafine grain specimen. . . . 25
1.17 Schematic drawing and SEM image of a SiC double cantilever beam. . . . 26
1.18 SEM image of a double-clamp beam. . . . 27
1.19 CRSS vs beam width for CP Ti, Ti–6Al and Ti–6Al–4V microcantilevers (a) plot showing the fit to $\tau_y = \tau_0 + A w^n$ (b) power law plot. . . . 29
1.20 A schematic of a typical EBSD setup with detector and sample. . . . 31

1.21 An example of (a) an inverse pole figure map for CP titanium, (b) Kikuchi bands from the point indicated in the map in (a) and (c) the relevant inverse pole figure colour scale. 32
1.22 (a) Maps for 3D lattice strain tensor and lattice rotations around the dislocation measured by HR-TKD. (b) The forward calculation of the distribution of strain tensor and lattice rotation around a $[\bar{1}1\bar{1}/2]$ dislocation using an isotropic elastic forward model convolved with a 2D Gaussian probe function. Red arrows shows the direction of Burgers vector projection. The cross shown in the map is the place where reference pattern was taken. 36

2.1 (a) An array of mesocantilever specimens that were laser cut for ultrasonic fatigue testing and (b) an example of a single mescocantilever specimen. 38
2.2 A diagram of the tensile specimen design used in the tensile tests described in this chapter. 39
2.3 SEM images that show the different reference marks for (a) identifying the grain of interest during milling and (b) nanoindentation experiments. 41
2.4 An SEM image showing an example of a completed microcantilever. 42
2.5 Two polarised light micrographs illustrating the difference between a specimen (a) before electropolishing and (b) after electropolishing. 45
2.6 The setup of the ultrasonic fatigue rig highlighting (a) the sample location, (b) the camera to determine specimen status and (c) the laser used for calibration. . 48
2.7 Mesocantilever specimen holder made from a repurposed grub screw. 49
2.8 (a) The experimental setup for calibration depicting the laser hitting the hammer of the specimen before reflecting down, (b) shows the laser spot when the specimen at rest and (c) shows the deflection of the laser as the specimen is vibrated. 50
2.9 In-situ observation setup 53
2.10 An example of a mesocantilever that has begun to crack during fatigue testing. . 53
2.11 Schematic of the G200 Nanoindenter 54
2.12 (a) SEM image of two horizontal reference marks 4 μm and 2 μm with vertical marks from scanning tip. (b) Atomic force microscopy (AFM) topographical map of two reference marks. 56
2.13 Images that show (a) the SEM chamber for a standard TKD setup, (b) SEM general view image of the copper grid with specimen attached and (c) SEM image showing a close-up of the lift-out specimen attached to the copper grid. 59

3.1 An Abaqus model of a mesocantilever designed for examining short crack growth by Dr J Gong. Sharp corners cause stress concentration that dominate location of crack initiation. 63
3.2 An Abaqus model of the final mesocantilever design used in this project. The localised stress concentrations seen in Figure 3.1 are not present. 64
3.3 A model of the final mesocantilever shape used. 65
3.4 Three paths used to determine stress variation on the top surface of the mesocantilever (a) path along the centre of the beam, (b) path from one side of the beam to the other at the point of highest stress (c) path along one side of the beam from the fixed end to the hammer. 67

3.5 Convergence Studies for (a) Centre Path, (b) Transverse Path (c) Edge Path . . . 69
3.6 Design of experimental mesocantilevers used for initial tests in stainless steel 304L. 70
3.7 The final four mesocantilever designs tested with different resonant frequencies. Ti-Cantilever 1 - 24 kHz, Ti-Cantilever 2 - 28 kHz, Ti-Cantilever 3 - 33 kHz, Ti-Cantilever 4 - 40 kHz . . . 72
3.8 Grain area (μm^2) distribution in Grade 2 CP Ti Foil used in this thesis. (Bins which had less than 0.5% relative count were not included in the histogram, distribution determined with EBSD map from Figure 3.9. Step size of 0.5μm and boundary threshold of 5°) . . . 74
3.9 Example of grain shape in Grade 2 CP Ti foil used (EBSD pattern quality image, step size 0.5μm). . . . 75
3.10 A model of the final microcantilever shape used. . . . 75
3.11 Plots showing Microcantilever FEM Convergence Studies (a) difference in elastic response as a result of changing the depth of the base and (b) normalised stiffness of the different cantilevers. . . . 76
3.12 Plots showing Microcantilever FEM Convergence Studies (a) difference in plastic response as a result of changing the mesh size and (b) normalised final load of the different cantilevers. . . . 77

4.1 Images showing (a) the fine speckle pattern achieved for the majority of specimens (b) the 'coarse' speckle pattern for the samples tested at a strain rate of 2.0 x10^{-2}. . . . 80
4.2 Data showing how the stress response varies with strain rate and sample orientation with respect to the rolling direction in Grade 2 CP Ti. Samples cut parallel to the rolling direction at strain rates of (a) 1.8 x 10^{-4}, (b) 3.1 x 10^{-3}, (c) 2.0 x 10^{-2} and (d) sample cut perpendicular to the rolling direction tested at a strain rate of 4.3 x 10^{-3} . . . 81
4.3 A diagram of an hcp crystal with the <a> prism (green), <a> basal (blue and <c+a> first order pyramidal (grey) slip systems highlighted. . . . 84
4.4 Slip traces and associated load drop-strain burst plots for (a) <a> basal, (b) <a> prism, (c) <c+a> first order pyramidal. . . . 87
4.5 Examples of the ideal microcantilever orientation scenarios for the three examined slip systems (a)<a> basal, (b) <a> prism and (c) <c+a> first order pyramidal. 89
4.6 IPFZ maps indicating the nine grains selected to analyse the modulus of microcantilevers where specific slips systems are activated and the CRSS of three slip systems in question (<c+a>, <a> prism and <a> basal). . . . 91
4.7 Experimental and Finite Element Modelled load-displacement curves for microcantilevers for the **(a)** <a> basal, **(b)** <a> prism and **(c)** <c+a> first order pyramidal slip systems. . . . 93

5.1 The two points on the hammer between which displacement in the x and z directions are measured. . . . 97
5.2 Plots showing the deflection angle of the mesocantilever beam as a function of vibrational amplitude both (a) in a finite element model and (b) a representative experimental dataset. . . . 99

5.3 Plot showing maximum stress experienced by a mesocantilever as a function of deflection angle. . . . 100
5.4 Raw data for Stress vs Cycles to failure for CP Grade 2 Titanium in single-step Tests. . . . 103
5.5 Median and range for Stress vs Cycles to failure for CP Grade 2 Titanium in single-step Tests (raw data shown in Figure 5.4). . . . 104
5.6 Percentage of runouts at 10^9 cycles as a function of Stress (MPa) applied to mesocantilevers. . . . 105
5.7 Applied Stress vs Cycles to failure for CP Grade 2 Titanium in multi-step Tests. 106
5.8 Median and range for Stress vs Cycles to failure for CP Grade 2 Titanium in multi-step Tests (raw data shown in Figure 5.7). . . . 107
5.9 Combined raw data for single-step and multi-step data presented in Figure 5.4 and Figure 5.7. . . . 107
5.10 Combined plot of Stress vs Cycles to failure for CP Grade 2 Titanium in both single-step and multi-step tests. . . . 108
5.11 A cumulative step chart showing the failure of samples at (a) fixed stress single-step tests (b) fixed life multi-step tests. . . . 109
5.12 SEM images showing the difference in laser finish on two CP Ti mesocantilever specimens (a) accepted smooth finish (b) rejected rough finish. . . . 110
5.13 Comparison of performance difference between foil finishes 1 and 2 (a) number of cycles taken for a sample to fail at 300 MPa (b) cumulative step chart showing probability of failure at 300 MPa. . . . 111
5.14 Polarised light images of crack growth in a mesocantilever captured with a digital camera (a) mesocantilever at the beginning of the test (b) crack initiation (c) significant crack growth and second crack initiation site (d) failure of the specimen. 113
5.15 Crack growth of a mesocantilever tested at 371 MPa. . . . 114
5.16 Crack growth of a mesocantilever tested at 327 MPa. . . . 115
5.17 Time taken for a crack to initiate in a CP Ti mesocantilever as a function of stress. 116
5.18 Percentage of total life that is taken up by crack to initiate. . . . 117
5.19 SEM image of a CP Ti mesocantilever fracture surface tested at 350 MPa with a fatigue life of 1.45 x 10^5 cycles. . . . 118
5.20 SEM image of an example of striations in a CP Ti mesocantilever fracture surface and the crack growth direction. . . . 119
5.21 SEM images showing a CP Ti mesocantilever just before complete failure (a) top view (b) view along the beam of the remaining fracture surface. Sample tested at 420 MPa stopped at 2.64 x 10^4 cycles. . . . 120
5.22 SEM image illustrating the change in fracture mode through a mesocantilever beam during UHCF testing. Sample tested at 300 MPa with a fatigue life of 1.73 x 10^5 cycles. . . . 120
5.23 SEM image of striations and slip bands showing that crack initiation in a CP Ti mesocantilever begins at the surface corners. Sample tested at 350 MPa with a fatigue life of 1.45 x 10^5 cycles. . . . 121
5.24 SEM image of a failed CP Ti mesocantilever with multiple crack initiation sites (marked by boxes) tested at 300 MPa with a fatigue life of 3.32 x 10^6 cycles. . . . 122

6.1 Images showing different observations of a crack path in a CP Ti Grade 2 mesocantilever specimen. (a) Polarised light image of a crack growing through the mesocantilever (b) an IPFY map of the mesocantilever prior to testing with the crack path overlayed and (c) an IPFY map and pattern quality image of sample after failure. 128
6.2 Figures depicting the calculated Schmid factors for (a) Basal slip systems (b) Prism slip systems and the m' for (c) Basal slip systems (d) Prism slip systems for a fatigue crack initiation point. (Red arrows = slip plane direction, blue lines in the centre of the grain indicate the slip plane normal). 130
6.3 SEM image of a secondary crack in a CP Ti sample fatigued for 40,000 cycles at 275 MPa. 131
6.4 (a) SEM image of a primary crack in a CP Ti mesocantilever tested for 40,000 cycles at a stress amplitude of 275 MPa and (b) corresponding IPFY map. . . . 132
6.5 (a) Pole figure displaying the overall texture of the CP Ti mesocantilever presented in Figure 6.4 and (b) Pole displaying the local texture around the primary crack initiation point (information obtained from the area surrounded by the blue box in Figure 6.4. 133
6.6 Polarised light images of a CP Ti mesocantilever tested until failure at 365 MPa at (a) 0 cycles (b) 40,000 cycles (c) 50,000 cycles and (d) 160,000 cycles. 134
6.7 A schematic depicting the twisting and tilting angles (α and β respectively) of a crack travelling from grain 1 into grain 2. (Reproduced from Zhai et al [1]) . . 136
6.8 SEM image of a primary crack in a CP Ti sample fatigued for 40,000 cycles at 275 MPa. 137
6.9 Data quality maps achieved by cross-correlation analysis using XEBSD of the sample from Figure 6.8. The peak height map (right) shows the slip bands and crack present in the sample whilst the mean angular error map (left) shows small errors as well as picking up the primary crack and some of the slip bands. 138
6.10 GND Density map of area displayed in Figure 6.8 (Step size = 0.15 μm). 139
6.11 The components of (a) strain (b) stress as determined by cross-correlation of the primary crack present in the sample from Figure 6.10. 141
6.12 (a) Misalignment (m') between most likely active slip plains in grains for the lower crack portion marked in Figure 6.8 and the corresponding (b) argus image. (Red arrows = slip plane direction, blue lines in the centre of the grain indicate the slip plane normal). 143
6.13 Map showing the misalignment between activated slip systems for the crack displayed in Figure 6.8. (Red arrows = slip plane direction, blue lines in the centre of the grain indicate the slip plane normal). 144
6.14 Histogram showing the percentage of grains with varying misalignments between grains along the crack path for the crack displayed in Figure 6.8 and all the grains in the area. 145
6.15 A schematic of grain boundaries for the area displayed in Figure 6.8 and a series of randomly selected 'Virtual Cracks'. The white line indicates the grains each virtual crack intersected. 146

6.16 Histogram showing the percentage of grains with varying misalignments between grains along the crack path for the crack displayed in Figure 6.8 and a series of randomly selected 'Virtual Cracks' displayed in Figure 6.15. 147
6.17 Histogram showing the percentage of grains with varying global Schmid factors for both the grains along the crack path and for the crack displayed in Figure 6.8 and a series of randomly selected 'Virtual Cracks' displayed in Figure 6.15. . . . 147
6.18 An SEM of a large secondary crack originating from the side of a CP Ti mesocantilever tested at a stress amplitude of 365 MPa with a fatigue life of 1.6 x 10^5 cycles. 149
6.19 (a) Misalignment (m') between most likely active slip plains in grains and the corresponding (b) GND map for the crack displayed in Figure 6.18. (Red arrows = slip plane direction, blue lines in the centre of the grain indicate the slip plane normal). 150
6.20 Histogram showing the percentage of grains with varying misalignments between grains along the crack path for the crack displayed in Figure 6.18. 151
6.21 (a) SEM image of a large secondary crack originating from the side of a CP Ti mesocantilever tested at a stress amplitude of 365 MPa with a fatigue life of 1.6 x 10^5 cycles and (b) Lift-out at the crack tip (location marked by a red box). . . 151
6.22 GND Density Map of the crack area in Location 1 from the lift-out in Figure 6.21. (On-axis TKD configuration). 153
6.23 Electron channeling contrast images (dark field) showing dislocations around (a) the crack tip shown in Location 1 in Figure 6.21 (b) secondary crack from area in Location 2 in Figure 6.21. (On-axis TKD configuration). 154

List of Tables

1.1 A comparison between the time taken for a given number of fatigue cycles during ultrasonic high cycle fatigue testing (HCF) performed at 20 kHz and conventional HCF testing at 100 Hz. 15
1.2 Fatigue resistance parameters of laser welded Grade 2 CP Ti and Ti–6Al–4V. The endurance limit life was set at 2 x 10^6 cycles. 24

2.1 Composition of Commercially Pure Grade 2 Titanium Foil from Advent Research Materials Ltd. 37

3.1 Table displaying the number of elements in each Mesh ID. 68
3.2 Dimensions and Resonant Frequencies of Experimental Test Cantilevers in stainless steel 304L. 71
3.3 Stress Variation, Maximum Stress at 20 μm vibrational amplitude and Resonant Frequencies of Experimental Test Cantilevers tested in Grade 2 CP Ti. 72
3.4 Dimensions and Resonant Frequencies of Experimental Test Cantilevers tested in Grade 2 CP Ti. 73
3.5 Dimensions and Stiffness values for microcantilever FEM convergence studies. . 76
3.6 Mesh size and final load values for microcantilever FEM convergence studies. . . 78

4.1 A table showing the effect of strain rate on average Young's modulus, 0.2% Yield Strength and Ultimate Tensile Strength of CP Grade 2 Titanium foil. (RD = tensile specimens cut parallel to the rolling direction, TD = tensile specimens cut perpendicular to the rolling direction). 81
4.2 Target grain orientation in terms of Euler angles for activating <a> basal, <a> prism and <c+a> slip systems. 88
4.3 Orientations of grains selected for determining the modulus modulus of microcantilevers where specific slips systems are activated and the CRSS of three slip systems in question (<c+a>, <a> prism and <a> basal). 92
4.4 The calculated Critical Resolved Shear Stresses of <a> basal, <a> prism and <c+a> first order pyramidal slip systems. 92
4.5 The calculated Young's modulus of microcantilevers where <a> basal, <a> prism and <c+a> first order pyramidal slip systems were activated. 94
4.6 The experimentally determined Critical Resolved Shear Stresses for <a> basal, <a> prism and <c+a> first order pyramidal slip (τ_c) and corresponding extrapolated bulk values τ_0 95

5.1 Percentage of CP Ti samples tested using the single-step method that resulted in runouts 10^9 cycles. 103

Introduction

Extending the life of aero-engines and understanding how they behave towards the end of their service lives is something that has been at the front of the mind of every aerospace company. Engines typically go through millions of cycles in their lifetime and high cycle fatigue (HCF) is one of the primary causes of failure[2]. Aerofoils can also be subject to a large number of cycles in a short amount of time. This occurs if during operation the aerofoil passes through, or is held in, a resonant mode causing it to experience a high mean stress at a low amplitude but high frequency. Understanding the underlying mechanisms of HCF confers improvements not only in safety but also economically. One could prevent the early retirement of components and work on designing alloys with microstructures that would result in superior HCF properties. From a safety perspective, the European Aviation Safety Agency (EASA) requires engine designers to identify the modes of failure that lead to 'Hazardous Effects'[3]. These hazardous effects (engine fires, uncontained high energy debris etc) have to fulfil the 'Extremely Remote' condition. This condition, for engines, is that the probability of failure has to be less than 10^{-8} per hour of operation[3]. To meet such demanding criteria, understanding the mechanisms in operation during HCF is very important. Fatigue behaviour has long been known to be influenced by microstructure. However, there are certain aspects of fatigue and how they relate to the microstructure that continue to elude researchers, particularly, fatigue crack initiation (FCI). Though FCI has been previously linked with slip[4], the specific cause of FCI remains unclear. The link between crystal orientation and FCI will be investigated in this thesis.

Recreating service conditions to conduct tests would be economically and practically unreason-

able as it would take years to obtain results. To circumvent this, a method by which the test sample is vibrated at high frequencies was developed. This method is known as ultrasonic fatigue testing. A piezoelectric actuator excited by a power generator operating at 20 kHz transforms the electrical signal it receives into mechanical vibrations of the same frequency. A horn is put in place to amplify the vibration provided by the piezoelectric device to generate the displacement amplitude required to fatigue the specimen. By performing these fatigue tests at ultrasonic frequencies one can cause the specimen to experience 10^5 cycles in 5 seconds, 10^6 cycles in 50 seconds, 10^7 cycles in 8 mins 20 s and even data for the giga-cycle regime can be obtained in around 14 hrs. It is worth noting that existing HCF test methods that do not utilise the method previously outlined are significantly slower. One such example is rotating beam tests. These are performed at much lower frequencies (50 Hz[5]) but do use significantly larger specimens than those typically used for ultrasonic fatigue testing. There has also been HCF testing performed on specimens that had a gage section diammeter of 3.8 mm using a pneumatic actuator and electromagnetic shaker which reached frequencies of 70 - 400 Hz[6]. Frequencies of 1.8 kHz were achieved by The University of Dayton Research Institute using a magnetostrictive actuator[7] but all of these methods are far from the high frequencies that can be achieved using the ultrasonic fatigue testing method outlined above.

This project aims to improve the understanding of HCF crack initiation and how fatigue lives are linked to microstructure in hexagonal close packed (hcp) metals. In addition, the effect crystal orientation in neighbouring grains has on the crack path will be examined. Testing small sample volumes will lead to stronger variation in fatigue life making correlation with microstructure more obvious. This project will focus on demonstrating that a successful testing methodology has been developed as well as investigating the microstructural effects on fatigue performance of commercially pure titanium. The way this will be achieved is by demonstrating that ultrafast high cycle fatigue tests of mesoscale specimens can be, on average, representative of larger components. This methodology confers several significant advantages, namely – the ability to obtain representative S-N data in a very short amount of time from a small volume of

material, to examine the HCF properties of crucial components and specific areas (e.g. the joint in a linear friction welded (LFW) bladed disk or bladed ring).

Chapter 1

Literature Review

1.1 Titanium in the Aerospace Industry

The material investigated in this thesis is Grade 2 commercially pure titanium, which was selected as a relatively simple model system. It is important to understand why the focus is titanium, why high cycle fatigue and how these aspects are of interest to the aerospace industry. It wasn't until the Cold War that the use of titanium in the aerospace industry became popular. The drive for lighter and higher performance military aircraft during this period made titanium very attractive. When Pratt and Whitney used it in their J57 engine they were able to achieve a weight saving of 200 kg[8]. Since then, titanium has become synonymous with the aerospace industry. Titanium alloys now account for ~30% of the weight of a modern aeroengine. As a result a lot of investment has gone into the development of titanium alloys. Titanium's appeal lies in its high strength to weight ratio, high temperature performance and resistance to corrosion. However, the expensive nature of titanium makes its use limited to areas where it is deemed essential. With that in mind, titanium and its alloys still account for 9% of the total structural weight in aircraft such as the Boeing 777 (up from 0.5% in 1958 for Boeing's earlier 707 model). In military planes where weight savings provide a critical strategic advantage the use of titanium can be as high as 50% (by weight)[8]. Conventional titanium alloys fall into three categories; α alloys, α/β alloys and β

alloys with each of these having appreciably different mechanical properties. Fully understanding the microstructures of each alloy type and the effects it has on the aforementioned properties is key to the advancement of the industry. Due to the requirements of modern aircraft, α alloys are seldom used as their strength is inferior to that of the α/β alloys and β alloys. In the past, Ti–8Al–1Mo–1V was used in fan blades for medium bypass ratio aircraft turbine engines due to their high modulus of elasticity and good annealed strength [2]. However, this alloy is no longer used due to its susceptibility to stress corrosion cracking and expensive production process. α/β alloys are by far the most commonly used in the industry with Ti–6Al–4V (Ti–6–4) being the alloy of choice, making it widely known as the 'work horse' of the aerospace industry, and for good reason. α/β alloys are so desirable because, even if one was to normalise the properties based on density, they have comparatively high yield stresses and fatigue strengths. Its corrosion resistance and the ability to withstand higher temperatures is also superior when compared to other titanium alloys. Ti–6–4 is used in landing gear, bulkheads and aerofoils.

There has, however, been a trend in the industry towards replacing Ti–6–4 with β titanium alloys due to their superior strength. In fact, the Boeing 777 was the first commercial aircraft that contained more β Ti alloys than α. This was attributed to the use of Ti–10V–2Fe–3Al in the landing gear, it was almost entirely made of the β alloy with the exception of the outer/inner cylinders and axles that were made up of steel. By replacing a high-strength low-alloy (HSLA) steel, 4340 or 300M, with Ti–10–2–3 a weight saving of 580 kg was achieved[9]. Along, with the weight reduction there is also the significant matter of space economy. Aluminium would be the metal of choice for landing gear, as the cost is much lower than that of titanium, but due to the size this component would have to be to withstand the loads it would experience, it would no longer fit in the undercarriage of the aircraft. In addition to the reasons outlined above, titanium also has superior corrosion resistance and composite compatibility, when compared with aluminium alloys and low alloy steels [10].

The aerospace industry is continuously working towards developing engines that can operate at higher temperatures to improve their fuel efficiency and power output. This is where titanium

begins to struggle with the demands of the hottest parts of the modern engine. Ti–6–4 components are designed to operate at temperatures under 300°C and Ti–6–2–4–6, which is used in the intermediate compressor stages, operates at under 600°C [11]. At temperatures above this, oxidation becomes an issue, which results in the embrittlement of the titanium component. To allow for operation at higher temperatures there has been a drive to further develop thermal barrier coatings (TBC). TBCs were tested in aeroengines as early as the 1970s and entered the civil market a decade later [12]. A ceramic outer layer with low thermal conductivity is typically found in TBCs and is usually an yttria stabilised zirconia (YSZ) layer. Underneath this ceramic layer is a bond coating that can either be an 'overlay' coating, MCrAlY where M = Fe, Ni or Co, or a diffusion coating, Pt-modified aluminides. Between these two layers, a thermally grown oxide (TGO) appears during processing as well as in-service. This layer is thought to have a beneficial effect on the adhesion of the TBC to the substrate [13].

It is postulated that the next generation of engines will largely be made of composites as they confer significant economic advantages. Consequently, leading engine manufacturers have turned their attention to developing metallic matrix composites (MMC). Composites are lighter, can withstand higher temperatures and can even be stronger. In the context of fatigue, at 650°C titanium matrix composites (TMC) with a Ti–24Al–11Nb matrix has superior fatigue strength than the unreinforced matrix at 10^3 cycles by ~50%, though this drops to ~15% at 10^6 cycles [14]. It is thought that the improved fatigue performance comes from the increased resistance to crack propagation in the TMC, as illustrated by the S–N curve in Figure 1.1 where it is clear that the curves for the TMC and the unreinforced material will eventually intersect. However, the cost of making TMCs is quite high due to the inability to produce them on a large industrial scale. Once the manufacturing process is determined TMCs could be used as reinforced rings for rotating components of an aeroengine. Their superior strength and stiffness would result in bores of the disk being removed from the design and therefore allow a reduction in the size of the rotating stages, thereby conferring significant weight and volume reductions. Smaller engines but at the same thrust would give aircraft manufacturers more freedom in their future designs particularly

in regards to military aircraft, as the engine is usually incorporated into the airframe.

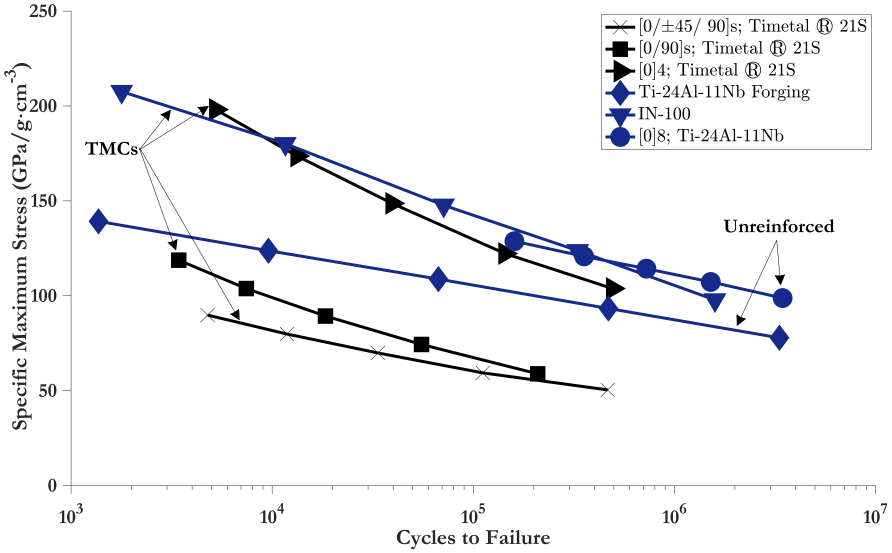


Figure 1.1: *Density normalised maximum stress (R = 0) vs. cycles to failure for TMCs and two unreinforced metallic alloys[14].*

1.2 Fatigue of Titanium and its Alloys

1.2.1 Lifing of Components

There are many considerations to take into account when lifing a component – material properties, mechanical and thermal stresses the component will experience and the environment in which the component will operate, amongst others. This is an important process that not only allows for cost- effective operation of the components but also minimises the risk of unexpected failure, thereby increasing safety standards. EASA in their latest amendment to the Joint Aviation Requirements (JAR) in 2010[3] state the requirements for establishing the approved life of critical parts, a typical process for which can be seen in Figure 1.2. Prior to installation, the use of engine critical parts must be determined as safe by the implementation of three plans – an engineering plan, a manufacturing plan and a service management plan[15]. Once the engineering plan is determined, the purpose of the manufacturing plan is to ensure that there is no deviation

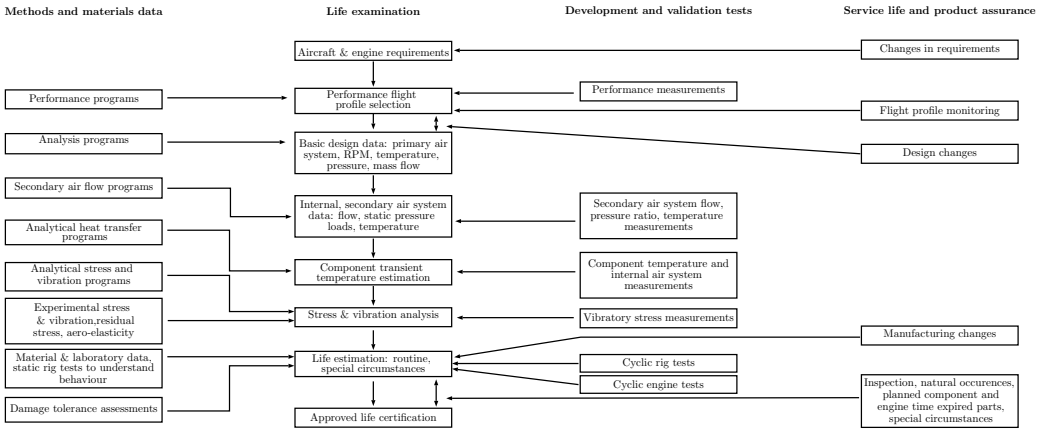


Figure 1.2: *Typical process for establishing the Approved Life of rotating parts. (Reproduced from EASA CS–E510[3]).*

from the established and accepted manufacturing process so that no processing anomalies are introduced that may affect the material's properties and, therefore, its life. The service management plan exists to enable the regular maintenance and, if needed, repair of components using EASA approved standards. The life of a critical component is determined to the 'first engineering crack', this is a result of the assumption that determining the growth rate of a crack in a critical component is impossible. A 'first engineering crack' is defined as 0.75 mm (surface length) with it also being assumed that the depth is 0.375 mm [36]. Traditionally, Goodman diagrams have been used as a way to determine a safe life[16] for HCF but this method has undergone significant changes in the past couple of decades. This method involves fatiguing a specimen at different mean stresses and stress amplitudes, load ratio – R (where R = $\sigma_{min}/\sigma_{max}$) and measuring the number of cycles at which the specimen fails. The fatigue limit, the stresses below which failure does not occur for a given number of loading cycles, is then plotted. An example of a typical Goodman diagram can be found in Figure 1.3. Points A, B and C denote the stress at which failure occurs after 10^7 cycles when R equals 0.7, 0 and –1 respectively.

1.2.2 Crack Initiation and Propagation

In 1958 Wood[17] first proposed mechanisms for fatigue crack initiation and is where the majority of modern mechanisms have been derived from[18]. Wood suggested that during cyclic

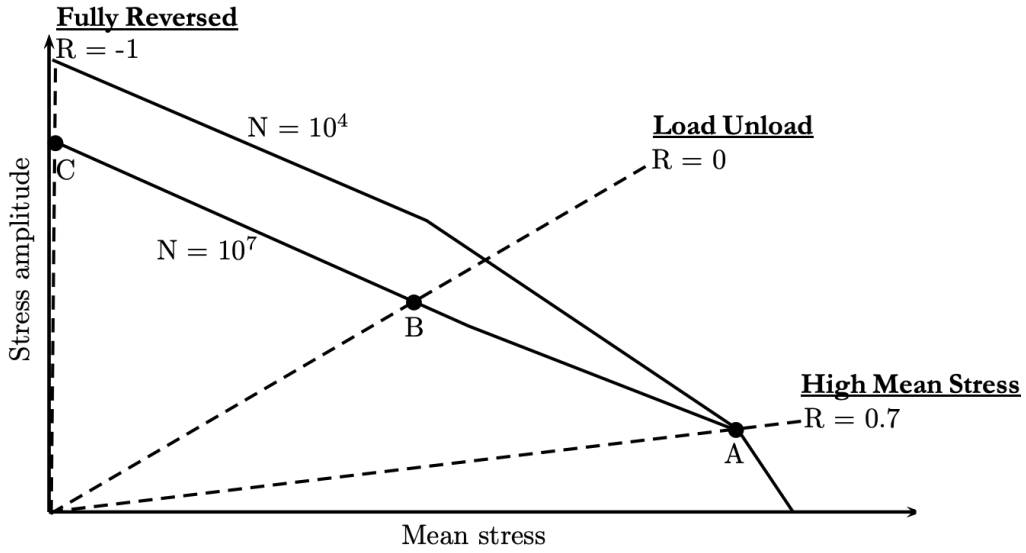


Figure 1.3: *Schematic of a Goodman diagram. (Reproduced from Nicholas[16]).*

fatigue the persistent slip bands that form introduce topographical changes to the material in the forms of 'hills' and 'valleys'. One can then effectively treat the 'valleys' as notches that generate an area of stress intensity and therefore where fatigue cracks will initiate. In his work, Wood also states that the cyclic fatigue performance is affected by the stress amplitude. The preferential nucleation of cracks at slip bands and grain boundaries during cyclic fatigue can be linked to constraints at grain boundaries with misorientation between the grains encouraging FCI. Work by Hu et al on Ti–6.8Mo–4.5Fe–1.5Al[19], using EBSD, supported the theory that higher misorientation between grains promoted crack initiation. They were also able to show that if the active slip plane in the next grain along the crack path was at low angles with the crack plane short crack growth was encouraged. This was explained by the 'elastic-plastic incompatibility' between grain boundaries. Work by Heinz & Neumann[20], on austenitic stainless steel, showed that in the case of face centred cubic (f.c.c.) metals the most important crack initiation sites in HCF were at twin boundaries. They suggested that this was as a result of elastic anisotropy causing local stress concentrations that promoted dislocation glide at grain boundaries. Likewise, in the case of f.c.c. twins is also a slip plane which, therefore, allows dislocations to travel large distances leading to stronger strain localisation than what is found at a 'regular' grain boundary. At LCF the

stresses are high enough to cause cracks to initiate at locations other than twin boundaries. It follows that at HCF, and therefore lower stress amplitudes, the proportion of total failure initiation sites attributed to twin boundaries increases. Bridier et al[21] have shown that grains oriented favourably for basal slip were the sites of crack initiation under tensile loading in both LCF[22] and HCF. Though, as Bridier et al state, both basal and primsatic slip were more prevalent than pyramidal slip it was prismatic slip that was the dominant mode, which is supported by the work of Patton, Baggerly and Williams[23] who showed that the critically resolved shear stress (CRSS) for prismatic slip is marginally lower than for basal slip at room temperature. It is worth noting that the CRSS is strongly dependent on temperature and alloy content. However, cracks still formed earlier during basal slip and propagated more quickly than for the cases of prismatic slip. Le Biavant et al[24] have suggested that local areas with coherent texture, also known as macrozones, that are also favourably oriented for basal or prismatic slip see multiple crack initiation sites in close proximity.

Przybyla and McDowell[25] conducted simulations on different Ti–6–4 microstructures and were able to show that a significant driving force for fatigue crack initiation were hard-soft grain interactions between primary α grains that were favourably oriented for pyramidal or basal slip. In their work they have suggested methods of estimating these driving forces, known as fatigue initiation parameters (FIPs). For example, McDowell[26] to estimate fatigue crack formation in metals as a result of plastic racheting (Equation 1.1) and reversed cyclic plasticity (Equation 1.2) used plastic shear strain-based FIPs.

$$(\Delta\varepsilon^{p}_{ij})_{\text{ratch}} = (\Delta\varepsilon^{p}_{ij})_{\text{end of cycle}} - (\Delta\varepsilon^{p}_{ij})_{\text{beginning of cycle}} \tag{1.1}$$

$$(\Delta\varepsilon^{p}_{ij})_{\text{cycle}} = (\Delta\varepsilon^{p}_{ij})_{\text{max}} - (\Delta\varepsilon^{p}_{ij})_{\text{ratch}} \tag{1.2}$$

Here, ε^{p}_{ij} is the component of the plastic strain tensor. McDowell and Dunne[27] examined the role of computable FIPs to determine the correlation between local microstructure and likelihood of cracks initiating. Fatigue crack initiation, as mentioned previously, has long been linked with

slip[4] but the specific cause behind fatigue crack initiation is still unclear. Grain orientation with respect to loading is also important during dwell regimes. Sinha et al[28] showed that when grains are oriented with their c-axis parallel to the loading direction they are more likely to be the sites of FCI. This was supported by later work from Bantounas et al[29] where it was shown that when the c–axis is less than 15° from the loading direction these grains act as paths for faceted crack growth.

This project's aim is to develop an understanding of the microstrucutral features that cause crack initiation. As mentioned previously, HCF strength is strongly based on a material's ability to withstand FCI and this in turn is dependent on the material's resistance to dislocation motion. It is understood that the size of the α colonies and lamellae, the α grain size, as present in the β phase that influence resistance to FCI. It is also seen that the smaller the a colonies and grain size the higher the resistance to FCI. However, a comprehensive model that can explain the reasons behind these observations is lacking. It is also well documented that FCI is affected by orientation of the grains. As can be seen in Figure 1.4 it is only once the cooling rate exceeds ~100°C/min that an appreciable difference in HCF strength can be seen as below 100°C/min. The thickness of the lamellae after a cooling rate of 1°C/min is in the region of tens of microns whilst beyond 100°C/min it is in the micron range. Nearer to 1000°C/min the microstructure becomes martensitic in nature, with the colonies now being the same width, a micron or so, as the individual lamellae. It is when the material begins to approach this microstructure that the aforementioned appreciable difference in HCF is seen. Crack propagation is also largely dependent on the microstructure of a material when the crack is relatively small, and thus slow. Short crack growth (SCG) is strongly dependent on the orientation between neighbouring grains, with cracks propagating more readily if neighbouring slip bands are closely oriented with that of the existing crack[19] and there being a low angle difference. Zhai, Wilkinson and Martin[1] were also able to show (in Al-Li alloys) the dependence of crack growth rate on the angle between slip planes in neighbouring grains, again demonstrating that the smaller the angle the more easily the crack propagates. Hu et al also found that the angle between the microcrack and the loading

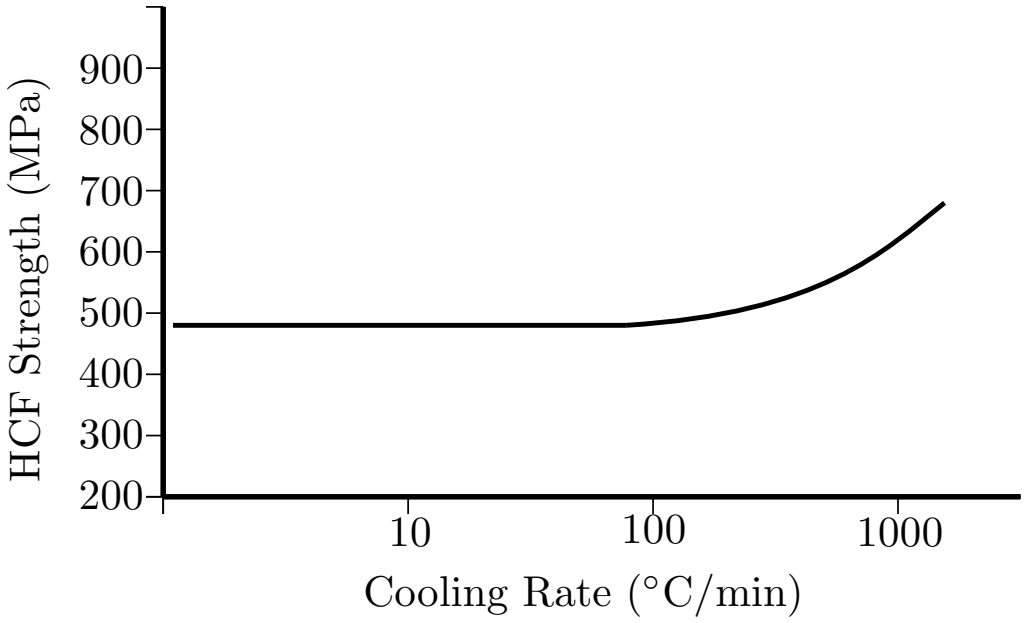


Figure 1.4: *Dependence of HCF strength (R = –1) of lamellar microstructures on cooling rate from the β phase field, Ti–6Al–4V (Reproduced from Lutjering and Williams [2]).*

axis is close to 90. It is worth noting that the behaviour of short crack growth is very different to long crack growth which is why SCG has garnered so much interest. As Nakajima et al[30] showed, finer microstrutures for α/β titanium alloys had lower fatigue strengths when loaded in a 'short life' regime where short crack growth was dominant. Larger grains in coarser microstructures acted as deflectors of the crack path, therefore, giving them their superior fatigue life in this regime.

1.2.3 Fractography

An important part of determining the origin of failure and the type of failure in a material is examining the fracture surface of the sample. For example, by counting striations one can glean how many fatigue cycles a sample has undergone and based on the direction of these striations where the origin of failure was (striations tend to point away from the origin site). An example of such striations can be seen in Figure 1.5 from Venkateswarlu et al[31]. As discussed previously, facets are a common origin of fatigue crack initiation sites but it was as a result of Sinha et al[32] using EBSD and quantitative tilt fractography that the orientations of these facets was

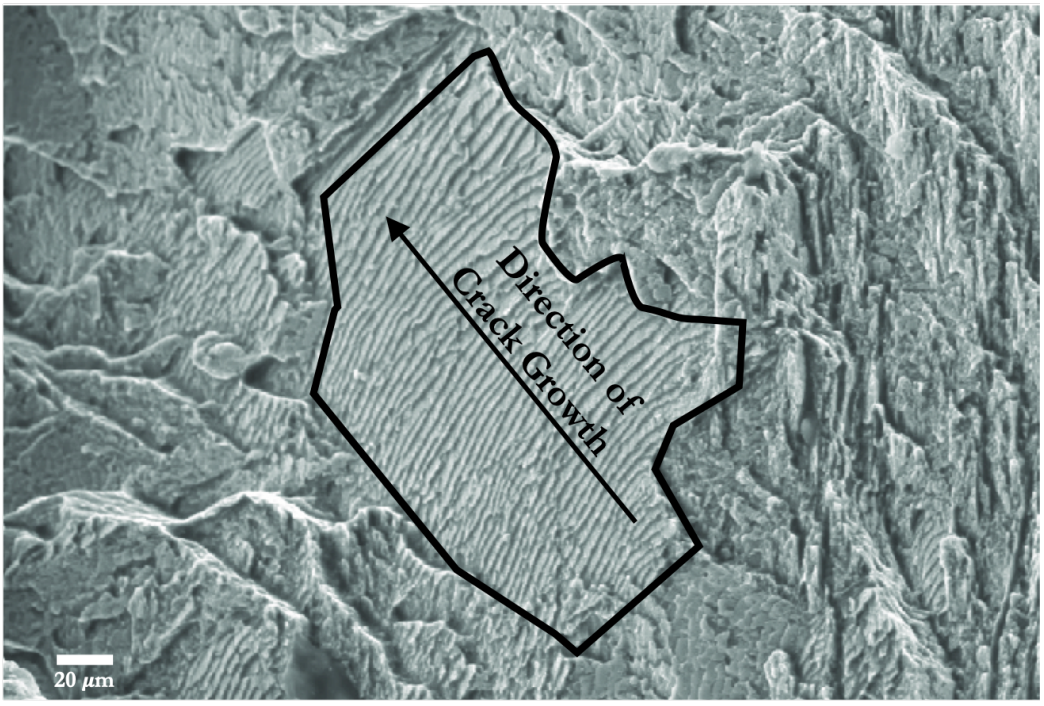


Figure 1.5: *An example of striations formed by cyclic fatigue in Ti–6Al–4[31]. (An area of striations have been marked by a black border).*

determined. They showed that in the case of non-dwell fatigue the facets are oriented at 5° with respect to the basal plane, in dwell fatigue they are 10–15° with respect to the basal plane and in static loading cases they are 20° with respect to the basal plane. This is a very useful result, as it indicates that by using fractography, coupled with EBSD, one can determine the site and/or cause of failure which is vital in aerocomponents that experience many different types of loading in service.

Using fractography, Bantounas et al[33] showed that some the larger the number of grains unfavourably oriented for fatigue (oriented for basal cracking) resulted in worse high-cycle fatigue performance. It is also interesting to note that the orientation of grains that cause initiation and those that simply encourage crack growth fall into different orientation windows. Grains between 15° and 40° were the initiation sites of crack growth (these grains required both a tensile component and shear stress to initiate) whilst grains between 0° and 90° aided faceted crack growth. Additionally, Bache et al[34] observed that if the cyclic stress was relatively low and fell between the cyclic and monotonic yield strengths, any facets that formed tended to be perpen-

dicular to the tensile axis.

As discussed above, though fractography is inherently a qualitative technique it can give indications to many quantitative phenomena. Namely, Wanhill et al[35] showed that with increasing ΔK the fracture profile becomes smoother. Increased roughness is the result of a material attempting to dissipate the strain energy in the material to multiple crack tips, this results in increased crack deflection and the effective ΔK is lower[36, 37]. Figure 1.6 shows an example of the difference in fracture profile roughness. These micrographs were taken of areas that are classified according to whether or not the crack growth is sensitive to microstructure or not[36]. These are defines as 'pre-transition' and 'post-transition' respectively. This transition has been correlated with the size of the cyclic plastic zone becoming equal to that of the α grain size. It is in this post-transition period that striations begin to form as well. In Figure 1.6, the value R_s is the surface roughness parameter that is calculated using[38]:

$$R_s = [4(R_1 - 1)/\pi] + 1 \tag{1.3}$$

R_1, the linear roughness parameter, is the ratio of the true length of the profile to the projected length across a specified reference direction[39].

1.3 Ultrasonic High Cycle Fatigue Testing

Ultrasonic HCF testing has advanced a great deal since its inception in the early 20th century when Hopkinson created a device that was able to test specimens at 116 Hz[40]. Current methods allow for tests to be performed at 20 kHz and data can be obtained in a very short amount of time when compared to conventional testing methods (see Table 1.1).

In 1925[41] and then again in 1929[42] with Lehmann, Jenkin made two significant advances to reach the kiloHertz regime of testing. However, it was in 1951 when Mason[43] introduced a piezoelectric transducer to his testing device that testing at frequencies of 20 kHz became possible. Around a decade later ultrasonic HCF testing was even performed at frequencies as high

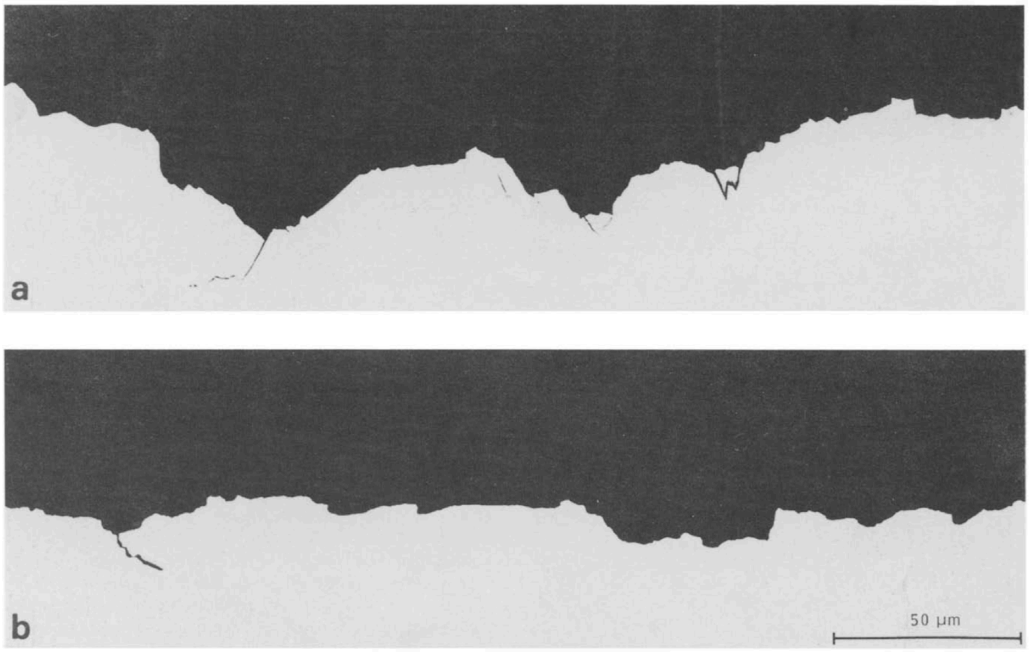


Figure 1.6: *Photomicrographs showing fracture profiles, (a) pre-transition, ΔK = 10 MPa$\sqrt{m}$, R_s=1.36 and (b) post-transition, ΔK = 18 MPa$\sqrt{m}$, R_s=1.18[35].*

Table 1.1: *A comparison between the time taken for a given number of fatigue cycles during ultrasonic high cycle fatigue testing (HCF) performed at 20 kHz and conventional HCF testing at 100 Hz.*

Number of cycles	Time taken	
	Conventional HCF tests (100 Hz)	Ultrasonic HCF tests (20 kHz)
10^5	16.6 min	5 s
10^6	2.7 h	50 s
10^9	3.8 months	13.8 h

as 92 kHz[44] and 199 kHz[45]. A typical setup can be found in Figure 1.8. Work by Wang et al[46] on ferrous alloys demonstrated that there is good agreement between results obtained by ultrasonic testing and conventional tests of 25 Hz (see Figure 1.7). Bathias & Paris[47] conducted a study on a nickel based alloy used in turbine discs and found that the fatigue strength is related to defects such as inclusions and porosity rather than short crack growth. However, an interesting discovery was that the effect of inclusions on fatigue performance was masked by that of porosity when load ratio was -1 (fully reversed loading) or 0 (load unload condition). Conversely, when the mean stress is high (load ratios of 0.8 and above) the role of inclusions becomes dominant.

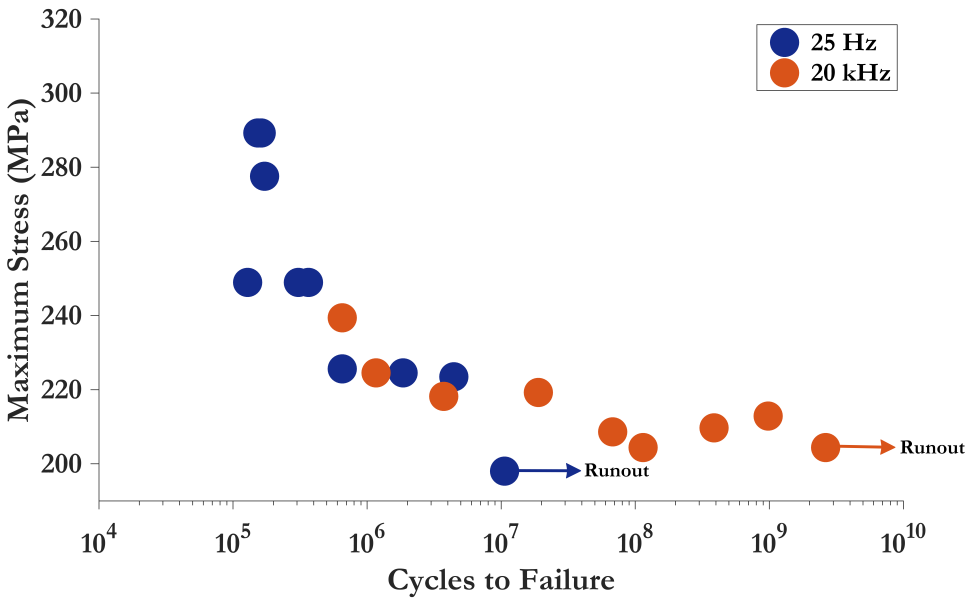


Figure 1.7: *S–N curve for Spheroidal Graphite Iron tested at 20 kHz and 25 kHz (R=-1) [46].*

In the modern setup a power generator transforms a standard 50/60 Hz electrical signal into a 20 kHz ultrasonic signal. This ultrasonic signal is then converted by the piezoelectric transducer into longitudinal ultrasonic waves and mechanical vibration of the same frequency which is then amplified by an ultrasonic horn to generate the required strain amplitude in the specimen. Prior to the advent of ultrasonic testing it was not practical to obtain a large amount of data for fatigue cycles above 10^7. As a result, it was largely assumed that the S-N curve became asymptotic[48], however, when this was shown to be incorrect in some systems the shortage of data on material performance in the gigacycle range became a more significant problem. This wasn't so much a problem in the mid 19th century when Wöhler stated that the fatigue limit of steels was 10^6 cycles as machines very rarely went beyond such lifetimes[49] but in the modern age obtaining representative data for the gigacycle regime is a very attractive prospect and will allow for more accurate lifing and, therefore, improved safety as well as maximising performance. In fact, it was only in the 1980s that it was shown steels could fail after 10^7 cycles[50, 51]. Testing in the giga-cycle regime revealed new failure mechanisms at stress levels below the extrapolated endurance limit. It was observed by both Bathias & Paris[47] and by Murakami & Endo[52] that fatigue

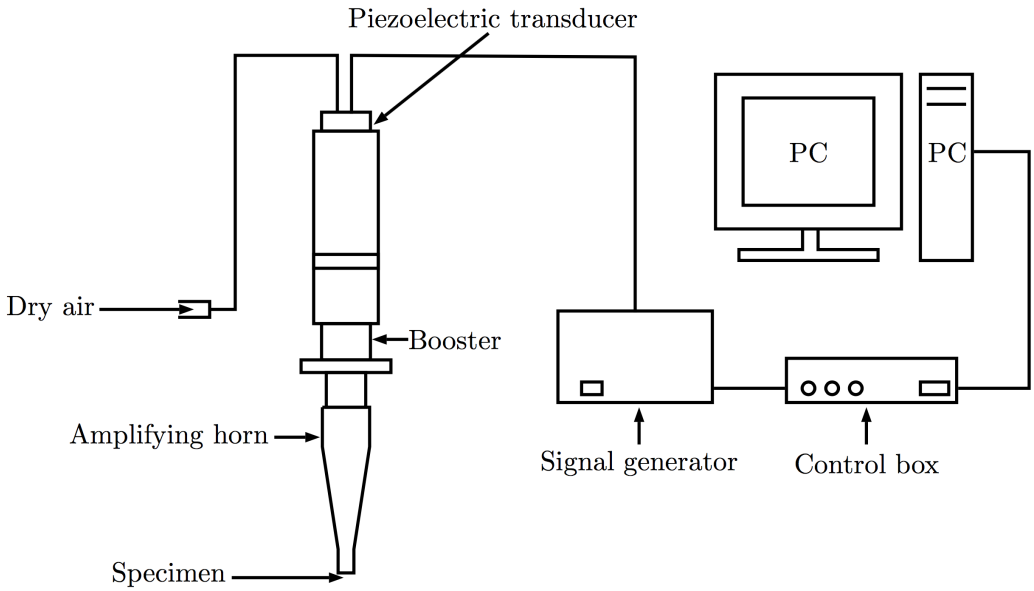


Figure 1.8: *A schematic illustrating the typical setup of an ultrasonic fatigue tester.*

cracks tend to initiate from within the material rather than the surface as is typical in LCF.

Ultrasonic fatigue tests aren't limited to room temperature but, by modifying the experimental setup, can be performed at high temperatures and at cryogenic temperatures. Using a high-frequency inductor a temperature of near 1000°C can be achieved[53]. Performing tests at high temperature allows for the experiment to more closely resemble in-service conditions, typically 300°C – 500°C for titanium alloys in aerospace. In astronautics, titanium alloys experience very low temperatures so recreating these conditions using ultrasonic testing equipment is useful as it not only allows for gigacycle data to be obtained much more quickly than using conventional testing methods but there is also a significant economic advantage. To generate such low temperatures liquefied gas is used and if these tests were performed at 100 Hz then a large amount of liquefied gas would be required, by performing these tests at ultrasonic frequencies, thereby reducing the duration of the experiment, the cooling agent is conserved. The importance of conducting HCF tests in the gigacycle regime has grown significantly. Many regulatory authorities are strongly considering the need to demand data concerning performance of components at 10^9cycles, with the United States military already moving towards operating in this regime. Being able to demonstrate that ultrasonic fatigue tests can be representative of industrial 'real-life'

scenarios would be a major advancement for the industry and will confer significant economic savings as well as improving the understanding of component performance and, therefore, overall safety standards in the aero-industry. Currently, as there is limited data at the gigacycle lifespan, a safety coefficient is used when identifying the maximum life of a component at a specific stress (see Figure 1.9). This coefficient is chosen so that the component, in theory, has an infinite life at the stresses indicated. There is no clearer illustration than this one that depicts the impact a better understanding of fatigue properties would have on industry. If the safety coefficient can be minimised then, due to our better understanding of material behaviour, travel will be safer and components will be able to perform at their maximum capabilities. To truly understand the intrinsic strengths of material and the effect microstructure has on mechanical properties one must probe the properties of individual grains, grain boundaries and macrozones. To do so, the use of cantilevers that are microns to a few hundred microns in length are required. These 'specialist' cantilevers have recently increased in popularity and in this work are categorised into two types known as microcantilevers, for those with a width less than a couple tens of microns, and mesocantilevers for those that are couple hundreds of microns in width. Mesoscale specimens can be cut with a laser and are used to probe larger areas of the microstructure than the microcantilevers. Mesocantilevers allow for the analysis of macrozones and therefore enables researchers to

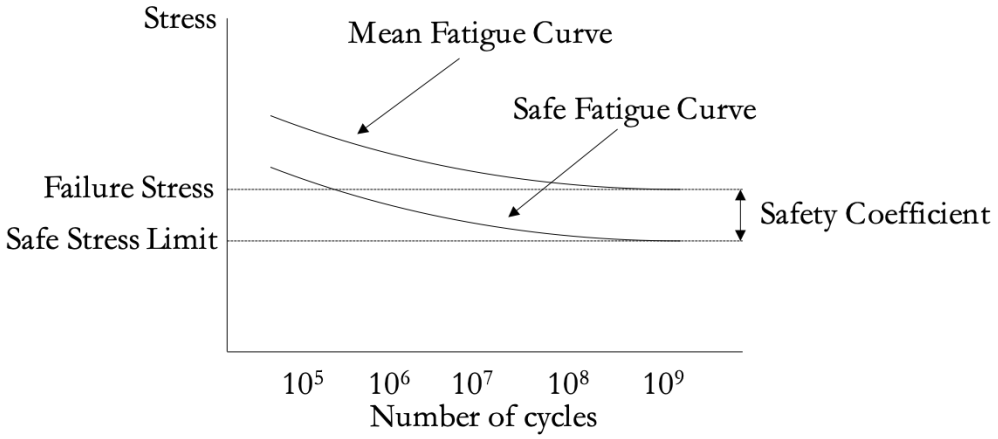


Figure 1.9: *A graph illustrating the safety coefficient employed to determine the maximum life of a component at a specific stress.*

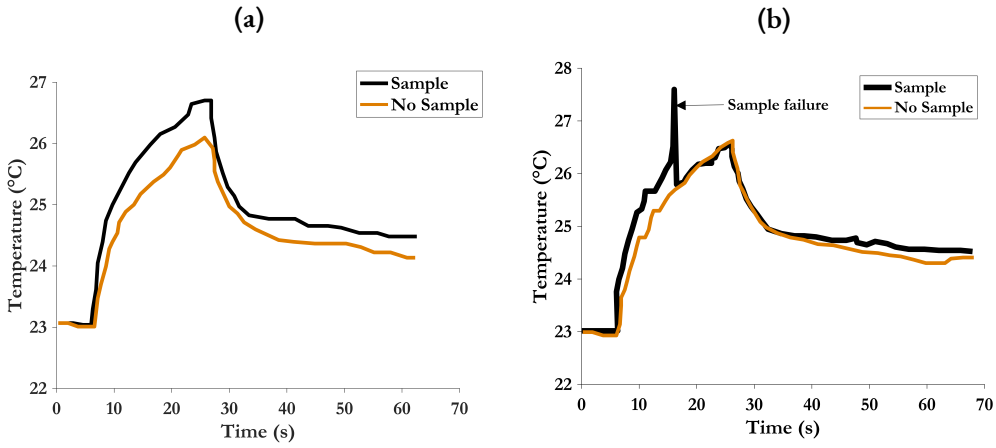


Figure 1.10: *Graphs that show the increase in temperature of the surface of a mesocantilever (a) at stress below failure (b) at stress that have caused failure.*

investigate the effect of texture and particular microstructural elements on fatigue crack initiaton and short crack growth. For both cases of cantilevers it is important to design a cantilever with a geometry that allows for the investigation of FCI by making FCI in the specimen independent of geometry. At the time of writing, there has not been much published work on ultrafast high cycle fatigue tests on a mesoscale. The majority of work has been on much larger test specimens than those used in this thesis. A typical example of the size of specimens is included in the work by Heinz and Eifler [54]. Here the test specimens have a gauge length and diameter of 4 mm with the entire specimen being 45.5 mm in length. At this size, tests need to be paused after loading to allow heat, caused by plastic deformation, to be dissipated in order to prevent an increase of more than 10 K. In the case of mesocantilevers, J Gong has demonstrated that temperature rise during testing is negligible (as shown in Figure 1.10).

Figure 1.10a shows that the temperature difference between an empty sample holder and one with a mesocantilever pinned inside during testing is minimal. Figure 1.10b shows that at sample failure there is a sharp peak in temperature before dropping down to the same as the case with no sample. In both of these cases the temperature does not go above 28 °C so it can be concluded that there is no significant temperature effect on sample during testing. This is due to the much larger surface area to volume ration of the specimens which allows the heat to dissipate quickly during testing. As a result, the time taken for each test is quicker and does

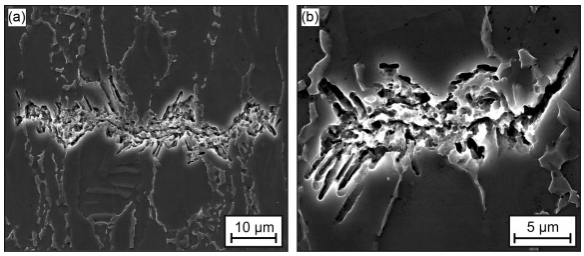


Figure 1.11: *An example of fatigue defects in a specimen loaded at a stress amplitude of 410 MPa until 10^{10} cycles without fracture[54].*

not cause the specimen to go through unnecessary ramp ups or ramp downs[i]. Heinz and Eifler were able to show that the stress amplitude that Ti–6Al–4V can tolerate decreases significantly beyond 10^8 cycles and, interestingly, the failure mode also changes. Beyond 10^7 cycles cracks almost exclusively form from below the surface of the specimen rather than on the surface, this could be due to the inhomogeneities Heinz and Eifler found in the phase distribution in their samples (Figure 1.11).

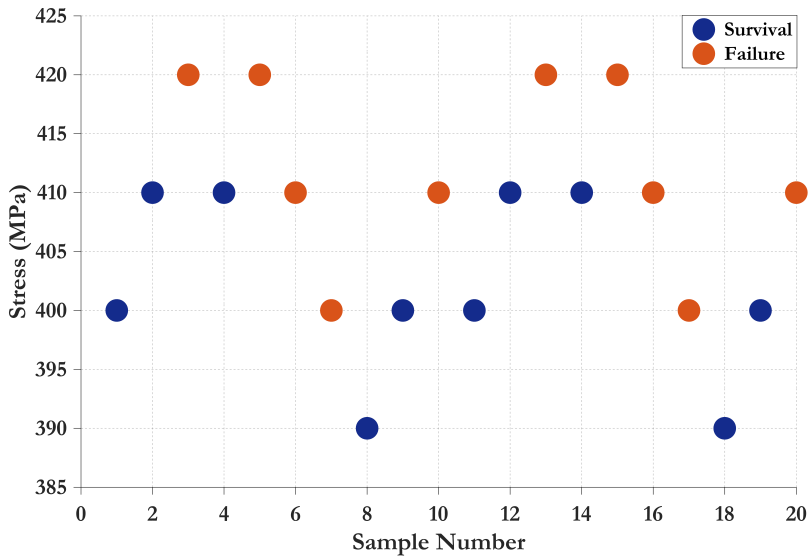


Figure 1.12: *An example of data that would be achieved using the staircase testing method for ultrafast high cycle fatigue testing. [55].*

There are several approaches to fatigue testing that can be used: the single-step, multi-step

[i]There is a short delay for the ultrasonic testing equipment to reach the stress amplitude targeted. This means there are periods of time where the sample is experiencing fatigue at stresses lower than the testing stress which can affect the final result.

and staircase methods. For the single-step method a testing stress is chosen and the sample tested at that stress for the desired number (i.e a runout limit) of cycles or until failure with the result recorded accordingly. Multi-step tests involve the sample being tested at various stresses and blocks of cycles prior to the 'target' stress. There have been questions of a 'training' or 'coaxing' effect on samples that undergo multi-step tests i.e samples that have been tested under their fatigue limit exhibit longer lives to samples that have not been tested at the same stress. These ideas stem from work done by Smith [56] and Moore[57] which suggested that specimens that experience this 'understressing' then perform better. However, as Nicholas[58] demonstrates there is no longer a scientific basis for this with one possible explanation being posited by Epremian and Mehl[59]. This theory suggests that when an apparent 'coaxing' effect is seen it is simply one due to skewed statistics. Samples failing under the fatigue limit results in a bias for specimens tested at higher stresses since the samples that have survived are inherently stronger than the average specimen and so longer lives are seen. The staircase method is almost a hybrid of the previous two methods described. It was first evaluated in 1948 by Dixon and Mood[60], for the purpose of explosives testing but it was Little and Jebe[61] who evaluated its use for fatigue testing. For this method, a stress is chosen and the sample tested at that stress for a pre-determined number of cycles or until failure (whichever is sooner). If the sample fails, this is noted and a new sample is tested at a slightly lower stress until failure or up to the same pre-determined number of cycles as before. If the first sample survived the test this is also noted and a 'fresh' sample is tested at a slightly higher stress until failure or up to the same number of cycles as the sample that survived. An example of the data set one would achieve is shown in Figure 1.12 from work done by Pollak et al[55]. Pollak et al conducted simulations to determine the viability of several approaches to the staircase method and although suggested that using non-uniform stress spacings between tests can result in more statistically efficient data the analysis that comes with that is far more tedious. Therefore, in that body of work only uniform spacing tests were considered and evaluated. The staircase method allows a distribution of the fatigue strength of a material to be determined with different approaches resulting in different standard deviations. In this thesis the single-step and

multi-step methods were used to gather statistical data on fatigue properties.

Marines et al[48] performed tests on an Al alloy using more than 100 specimens to demonstrate the limitations of the staircase method and the infinite life assumptions made. In their work the testing frequency was between 10 and 30 Hz (well below the ultrasonic frequency that this work uses) and tested up to 10^8 cycles at 13 different stress levels. Their results showed that there was a turning point in the cause of failure beyond 10^6 cycles. Below 10^6 cycles and at higher stresses the cause of failure was typically an inclusion (Mode A in Figure 1.13) whilst at lower stresses and beyond 10^6 cycles the cause was the presence of persistent slip bands (Mode B in Figure 1.13). The result is that if one were to plot two separate curves for these data groups the difference is pronounced (see Figure 1.13).

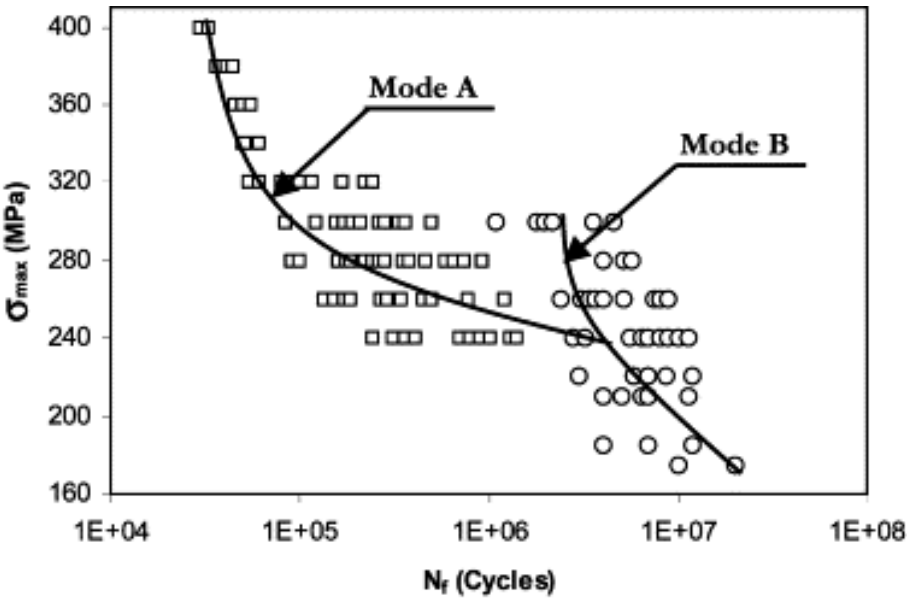


Figure 1.13: *S–N curve for 2024/T3 aluminium alloy illustrating the two different failure modes. Mode A = Failure origin is an inclusion, Mode B = Failure origin are persistent slip bands[48].*

There has also been work on various commercial purity grades of titanium. Kobayashi et al[62] performed fatigue tests of bulk specimens of commercially pure titanium (as well as Ti–6Al–7Nb) at 2 Hz and a load ratio, R, of 0.1. The grain size of CP Ti in these tests were 200 μm whilst the test specimen was a typical dogbone type specimen with a gauge length of 15 mm and gauge area of 7 mm^2. The size of these specimens, as well as the grain size, is much larger than

that of the mesoscale samples that will be described in Chapter 3 the fatigue behaviour associated with these differences will be discussed further in Chapter 5. Kobayashi et al performed tests investigated the difference in performance for pure tensile loading, pure torsion and a combination of tensile and torsion. Figure 1.14 shows the data obtained from their fatigue tests. Here, it can be seen that the fatigue strength of the specimens is higher in torsion rather than tension.

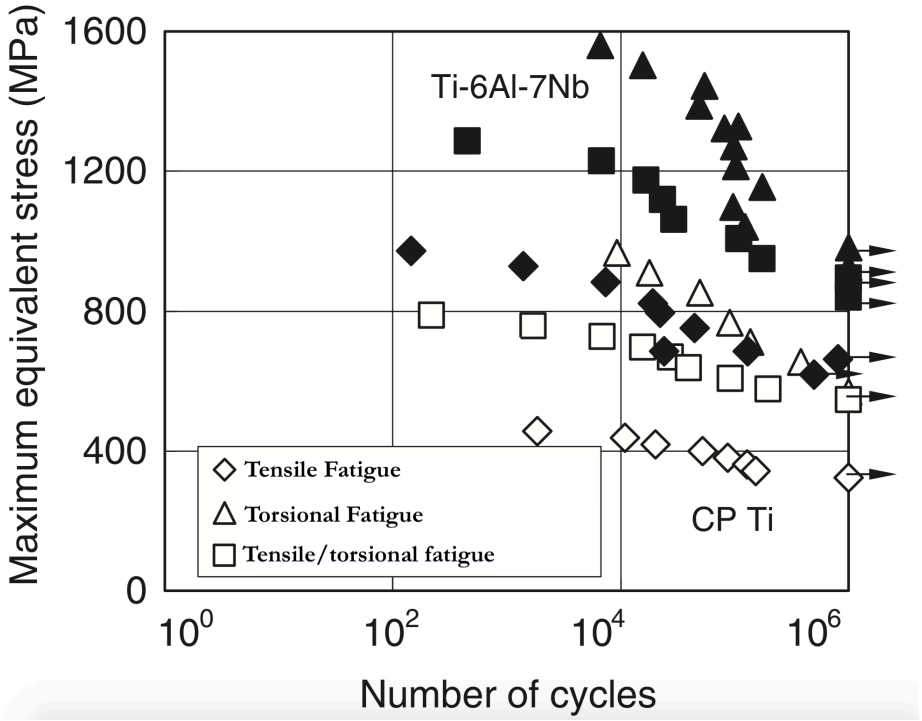


Figure 1.14: *S–N curve for CP Ti and Ti–6Al–7Nb loaded in tension, torsion and tension/torsion at R=0.1 at 2 Hz[62].*

Work by Casavola et al[63] on bulk specimens of laser welded joints of Grade 2 Ti and Ti-6Al-4V demonstrated the difference in strength as a result of alloying elements. The load ratio was 0.1, and the specimens tested at 10-15 Hz. Table 1.2 displays the fatigue coefficient and exponent as defined by Basquin's power law, $\Delta\sigma_a = \mathrm{S}(2\mathrm{N}_f)^b$, where $\Delta\sigma_a$ is the stress amplitude, S is the fatigue coefficient and b the fatigue exponent. There is no mention of grain size in these specimens so the effect of a grain size strengthening effect when comparing it to the data presented in this section or with data presented in Chapter 5 cannot be discussed.

There has also been work to compare the grain size effect on fatgiue performance by Sajadifar

Table 1.2: *Fatigue resistance parameters of laser welded Grade 2 CP Ti and Ti–6Al–4V.[63]. The endurance limit life was set at 2 x 10^6 cycles.*

Material	S (MPa)	b	Endurance Limit
Grade 2 CP Ti	609.5	-0.084	167
Ti–6Al–4V	1068	-0.099	232

et al[64]. In this work, coarse grain (46 μm) and ultrafine grain (0.3 μm) Grade 4 CP Ti was tested. Specimens were bulk specimens with a load ratio of -1 and tested at 1000 Hz. Two different specimen designs were utilised. One with a small radius that acted as a pseudo-notch and another with a larger radius as shown in Figure 1.15. Figure 1.16 shows that the smaller grain size material exhibits markedly higher fatigue strength. In addition, the effect of moving the stress concentration away from the pseudo-notch and spreading it more evenly across the sample resulted in higher fatigue strength with the effect being more pronounced for the ultrafine grain specimen.

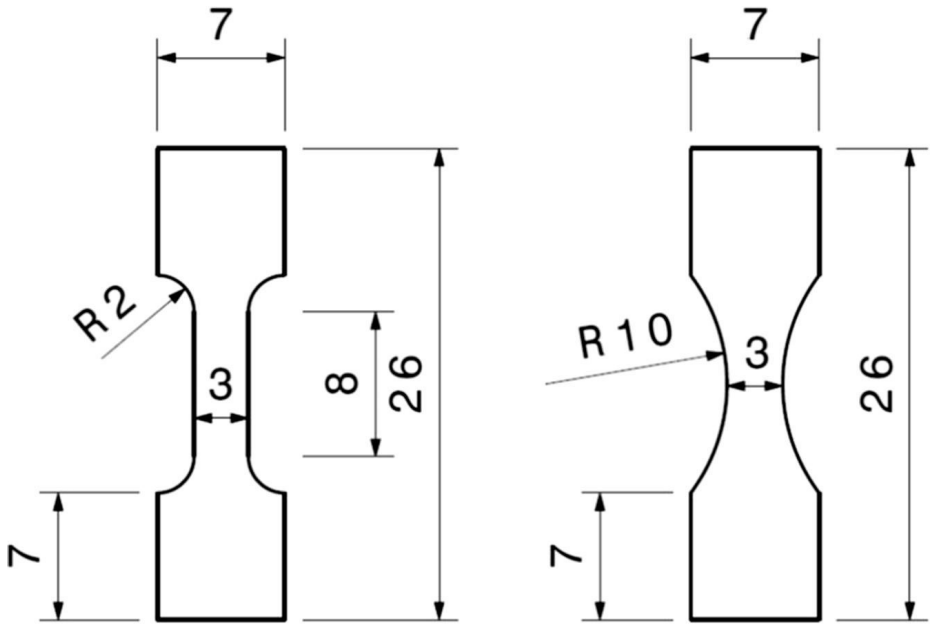


Figure 1.15: *Dimensions of the two dogbone specimen designs (units = mm) used in tests by Sajadifar et al[64].*

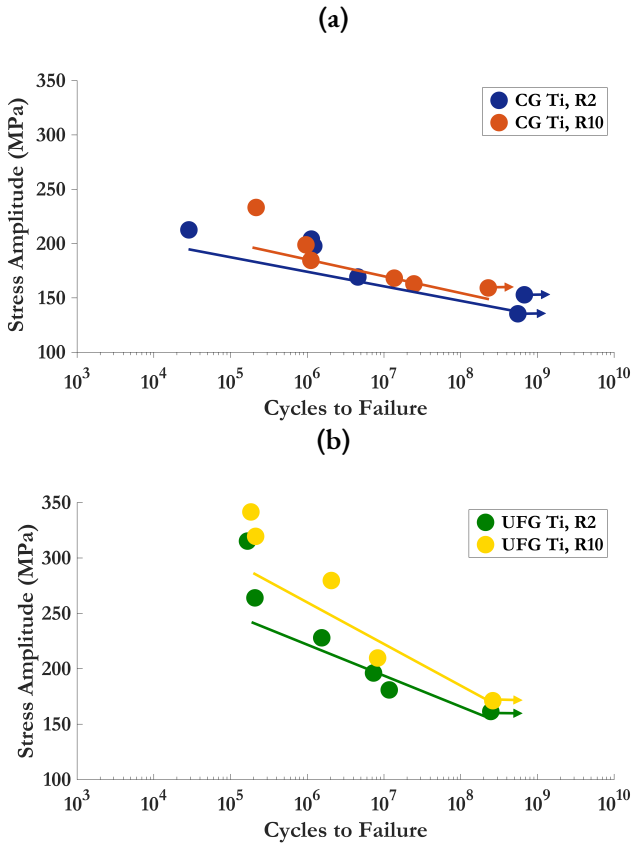


Figure 1.16: *Stress applied vs Cycles to failure for bulk CP Ti specimens with different specimen radii (as described in Figure 1.15. (a) coarse grain specimens, (b) ultrafine grain specimens. (Reproduced from Sajadifar et al[64]).*

1.4 Microcantilever Testing

To be able to contextualise the fatigue results at the mesoscale it is important to perform tests on several length scales. In Section 4.1 the results of millimetre-scale tensile tests are included. These tests are well understood and so a review of this method is not included here. Microcantilever tests, however, are still novel. Microcantilevers, due to their small size, can be used to measure the strengths of individual slip systems and strengths at grain boundaries [65]. In aerospace components, particularly those that are single crystal like turbine blades, understanding strength of grains in specific orientations is important. It is also important for polycrystals as local stresses and strains depend on crystal orientation and elastic-plastic anisotripy controls complex patterns of deformation. The failure processes depend on the extremes of the stress-strain patterns. The

elastic modulus of a single crystal depends on the lattice orientation with respect to the direction of stress. In 2005, Uchic and Dimiduk[66] developed a method using a focussed ion beam (FIB) to create specimens ranging from 2 to 20 μm in diameter initially in Ni alloys. These were micropillars that they tested in compression using a flat-tipped nanoindenter to determine the size effect on plastic behaviour. Differences in response were observed for micropillars of 2 μm and 5 μm in diameter. However, the mechanisms for this difference in behaviour was not known at the time. Since then, there has been significant progress with various microscale designs being used for tests. One such design is a double cantilever beam as developed by Liu et al[67]. This design, with a pre-notch created using a FIB, creates an environment that achieves stable crack growth. This is particularly useful for studies into fracture resistance as fracture in bending is usually very unstable. Figure 1.17 is an example of the design created by Liu et al. Another design developed to create suitable conditions for stable crack growth is that of Jaya et al[68]. The design, Figure 1.18, known as a double-clamped beam was created to probe the fracture resistance of (Pt,Ni)Al bond coats. Like the double cantilever design, a pre-notch created by a FIB is also present in the centre of the beam.

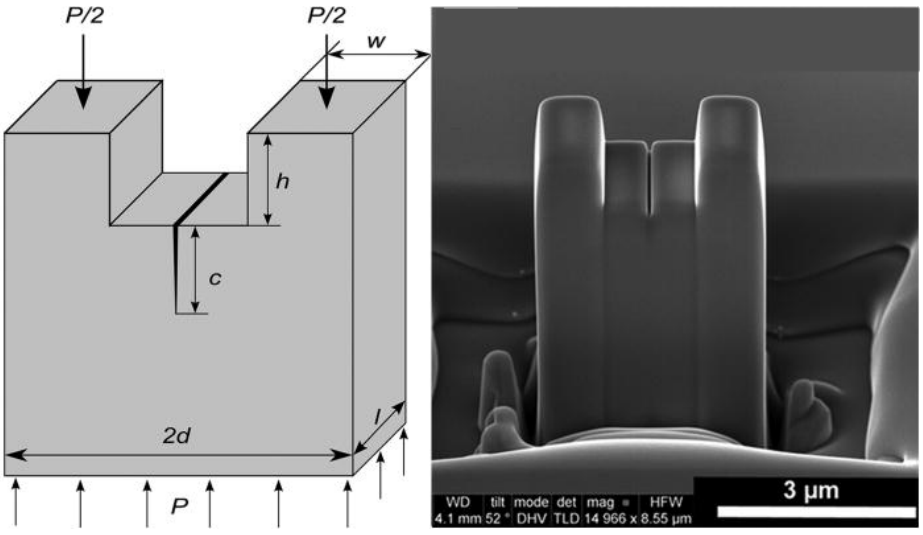


Figure 1.17: *Schematic drawing and SEM image of a SiC double cantilever beam[67].*

The focus in this body of work are microcantilevers that are tested using a nanoindenter to

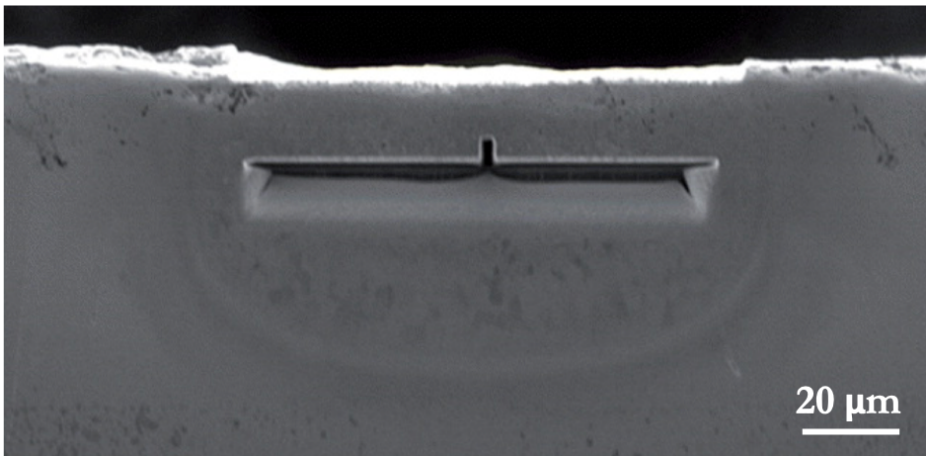


Figure 1.18: *SEM image of a double-clamp beam[68].*

bend the microcantilever to a fixed depth. Gong and Wilkinson [69] using EBSD and a FIB were able to isolate slip systems of α–Ti and study them. By performing crystal plasticity based finite element simulations of the microcantilever loading and fitting the model load-displacement data with experimental data the CRSS values were determined for the different slip systems. The same approach will be used in this thesis. Ding et al [70] performed more microcantilever tests and were able to show that<c+a> pyramidal dislocations cross-slip between $1\bar{1}01$ planes in compression of α–Ti, but not during tension which can be used to perhaps rationalise the reason behind the higher yield stress seen in compression. This work found that the yield stress of α–Ti in compression was in fact almost twice that in tension. By examining the microcantilevers post-bending under an SEM it was possible to see slip bands in some cases. For <a> slip on the prism planes and <c+a> on pyramidal planes one could see slip bands in the upper part of the microcantilever (where it is in tension). However, slip bands were not as clearly visible for <a> slip on the basal planes and, as suggested by Gong, is because basal slip is wavier than the two aforementioned slip cases. The static properties of three slip systems are investigated in this thesis - <a> basal, <a> prism and <c+a> first order pyramidal slip. As there is anisotropy in both plastic and elastic behaviour in hcp metals, it is important to determine the strength of these three slip systems as it will facilitate the understanding of the failure mechanisms in polycrystal cases.

In order to determine the elastic modulus and the CRSS for the three slip systems present in

hcp materials the method used by Gong and Wilkinson[69] is used in this thesis. Here, a three-dimensional finite element model is created in order to simulate the behaviour of the microcantilevers mentioned in the previous section. The microcantilevers are all within a single grain so the finite element model is of a single crystal and modified according to the slip system investigated. As with Gong and Wilkinson's work, the constitutive equation from Dunne's physically based crystal plasticity model[71] will be used in this thesis (Equation 1.4).

$$\mathbf{L}^p = \sum_j \rho b^2 v \exp\left(\frac{-\Delta F}{k_B T}\right) \sinh\left(\frac{\left(\tau^j - \tau_c^j\right)\Delta V}{k_B T}\right) \mathbf{s}^j \otimes \mathbf{n}^j \tag{1.4}$$

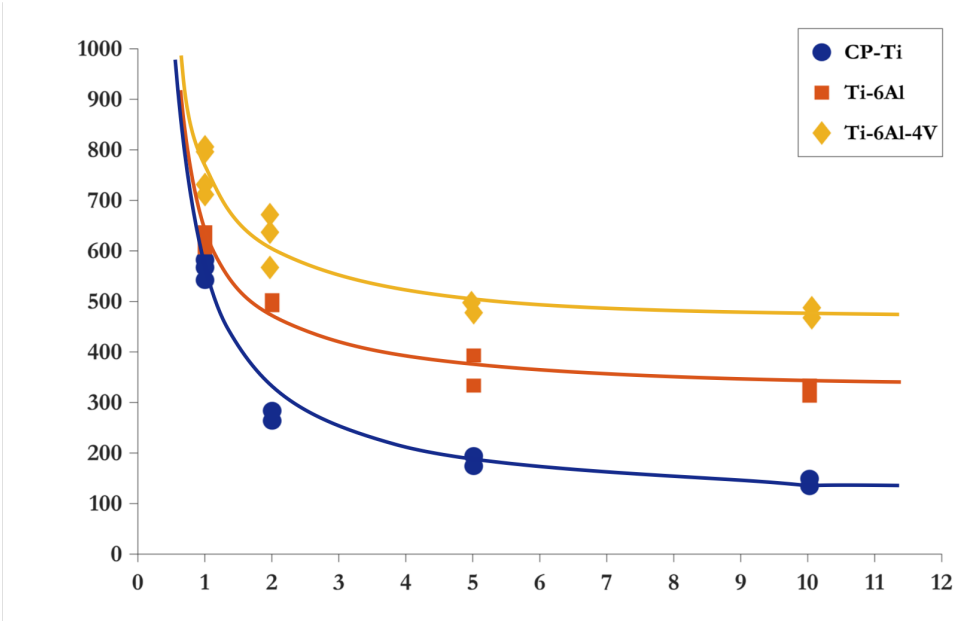
Here, $\mathbf{L}^p$ is the local plastic velocity gradient, ρ is the density of gliding dislocations, b is the magnitude of the Burgers vector, v is the jump attempt frequency of dislocations trying to pass energy barriers, k_B is the Boltzmann constant, T is the absolute temperature, ΔF is the Helmholtz free energy, ΔV is the activation volume, $\mathbf{s}^j$ is the unit slip direction and $\mathbf{n}^j$ is the unit normal to the slip plane of the jth slip system, which has a CRSS of τ_c^j and is under a shear stress of τ^j. Gong was able to demonstrate that this method gives rise to good agreement with literature for the Young's modulus and CRSS. In the final model it is important to take into account flexure at the 'fixed end' of the microcantilever. Armstrong et al[72] showed that if multiple tests along the beam are performed on a microcantilever (provided the beam has a ratio of 6:1 of length:width or greater) then using simple beam theory the flexure can be accounted for. Gong & Wilkinson[73] showed that this can also be achieved by just doing one test but using finite element modelling (FEM) instead.

Gong et al [74, 65] also demonstrated that there is a notable size effect on measured CRSS values once the width of microcantilevers decreases below 12 μm in both zirconium and titanium. The CRSS increases with decreasing microcantilever width, as shown in Figure 1.19.

It is clear that from this graph that the effect becomes more pronounced below 2 μm wide microcantilevers. As the microcantilever target width in this thesis is 2 μm, the importance of knowing the exact measurements is underscored as even a deviation of 10% in width can result

in a difference of ±50 MPa in the determined CRSS values. This relationship can be described

(a)



(b)

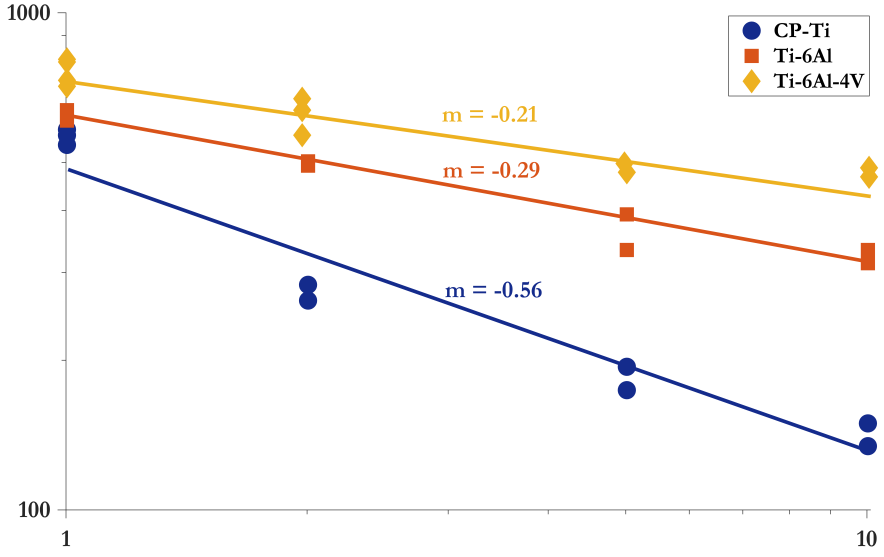


Figure 1.19: *CRSS vs beam width for CP Ti, Ti–6Al and Ti–6Al–4V microcantilevers (a) plot showing the fit to* $\tau_y = \tau_0 + Aw^n$ *(b) power law plot[74].*

using the equation:

$$\tau_y = B w^m \tag{1.5}$$

Here, τ_y is the CRSS value, B is a material strength parameter, w is width and m is an exponent dependent on the material. This simple power-law relationship is inadequate for describing the bulk properties of hcp metals as it results in incredibly small strengths. To resolve this, based on their work, Gong and Wilkinson determined that the above equation can be modified to include a size-independent term τ_0 that represents the CRSS of a bulk single crystal. This new equation is:

$$\tau_y = \tau_0 + A w^n \tag{1.6}$$

Gong and Wilkinson determined the exponent value, n, for CP Ti to be -1[75] and the material constant A to be 461 Pa m[74]. Gong et al also demonstrated that in zirconium the material constant, A, changes dependent on the slip system activated [65]. Here, it was shown that the higher the CRSS value for a particular slip system, the larger the corresponding value for A.

With all the above in mind, it was determined that performing single-loading microcantilever tests coupled with FEM is the best approach for this thesis along with the modified equation to determine bulk single crystal properties.

1.5 Electron Backscatter Diffraction

From just a few groups performing research with EBSD in the 1970s[76] the field has now become a near essential part of metallographic analysis, partly enabled by the full automation of EBSD in 1991 and advances in computing power. EBSD operates on the principle of having an electron beam, using a SEM, that rasters across the surface of a tilted specimen and diffracted electrons are detected by a fluorescent screen (that is in turn imaged with a charge-coupled device, CCD, camera). Figure 1.20 is an example of a typical EBSD setup. The backscattered electrons that impinge on the detector give rise to a diffraction pattern made up of Kikuchi lines. Each point on the surface of the material gives rise to a separate pattern from which the orientation of

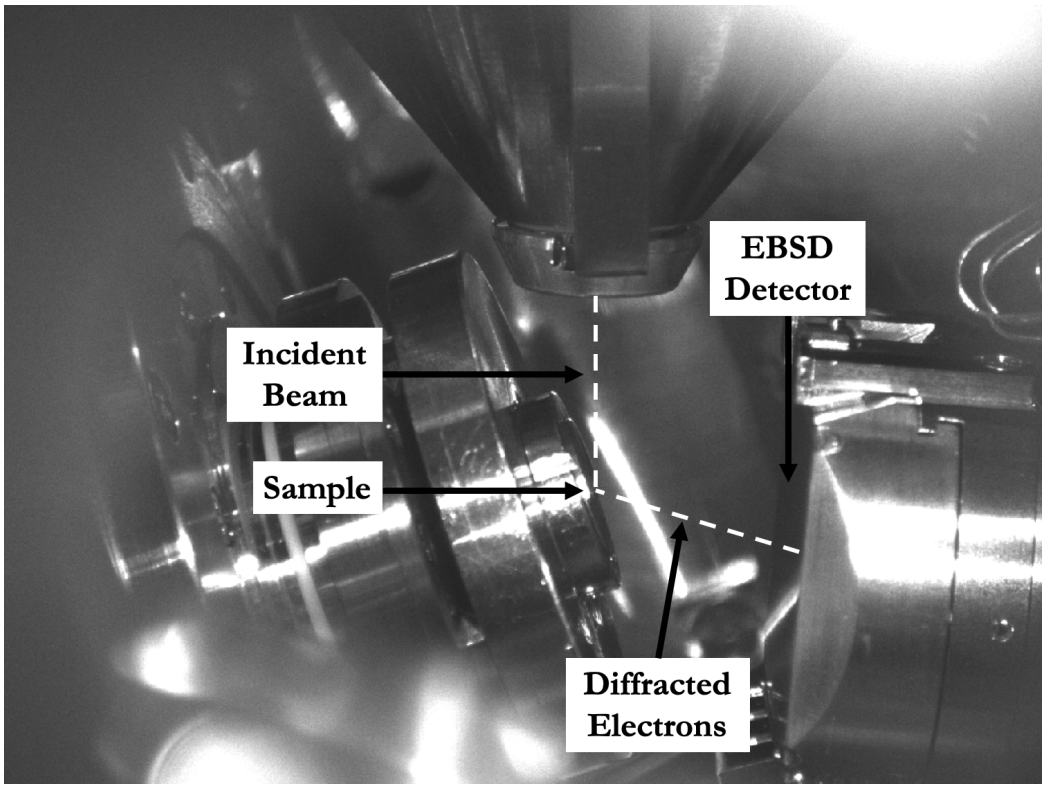


Figure 1.20: *A schematic of a typical EBSD setup with detector and sample.*

the grain can be gained, along with some related metrics. A point by point series of such measurements allows the creation of an EBSD orientation map. An example of the Kikuchi bands that are obtained, along with a typical orientation map for titanium, can be found in Figure 1.21.

The sample is typically tilted to 60°–70°as a result of Alam, Blackman and Pashley's work[77] that showed pattern contrast was highest when the incident beam was between 20°–30° from the sample surface. This was in opposition to previous work by both Boersch[78] and Meibom & Rupp[79] who found there was an increase in pattern contrast with increasing the angle between the sample surface plane and impinging beam. However, as Alam et al note in their paper, this was due to a failure to note the difference in camera length during their findings. In addition to sample tilt, prior to EBSD analysis the sample must be extremely well polished. This is paramount for obtaining not only 'clean' patterns that are able to be indexed accurately but is also important when one begins to use EBSD as a method for strain analysis.

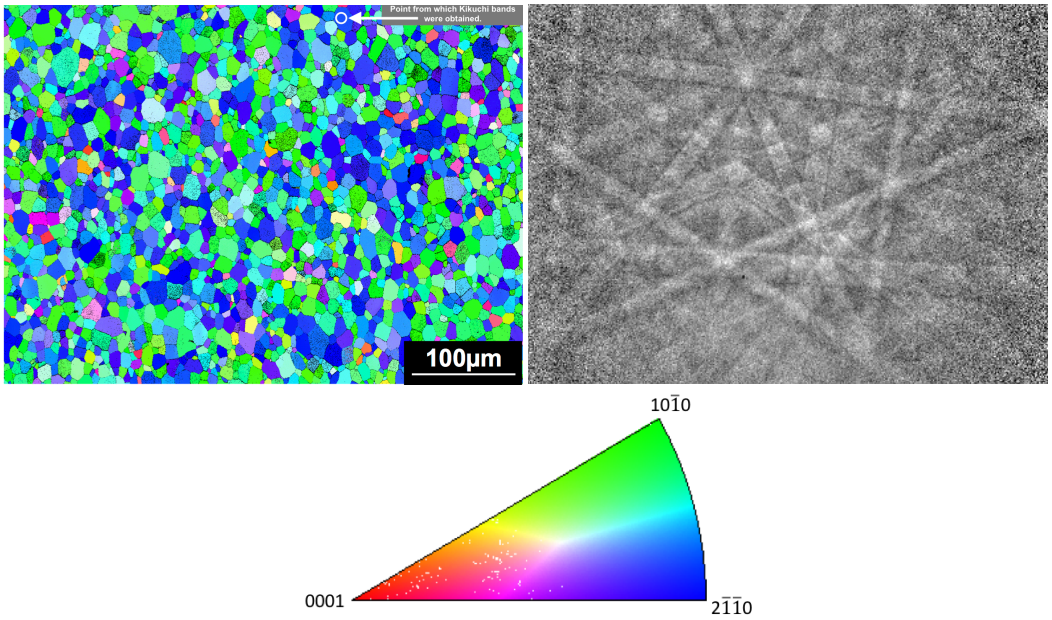


Figure 1.21: *An example of (a) an inverse pole figure map for CP titanium, (b) Kikuchi bands from the point indicated in the map in (a) and (c) the relevant inverse pole figure colour scale.*

EBSD Strain Mapping

Strain analysis using EBSD can be achieved by two methods: pattern quality and local rotations [80]. In the first approach, pattern diffusivity is the measure used as indicative of the dislocation contrent in the diffracting volume and this is further linked to the level of plastic strain throughout the material. Areas which are particularly low contrast or blurry contain many lattice defects as a result of plastic deformation. Immediately, the drawbacks of this method are visible as it is difficult to quantify the amount of strain present, though it is possible to obtain some quantitative information if one was to obtain a series of EBSD patterns from the material of interest and deform it to known plastic strains. Such work was done by Hendersen, Quested and McClean[81] on a nickel-based superalloy. In an attempt to improve the quantifiability of this technique, by removing the subjective analysis methods of a human operator, MacKenzie[82] sought to use Fourier analysis of the patterns. Wilkinson and Dingley[83] were subsequently able to improve on this method in 1991 and managed to achieve a sensitivity of 1% in the measurement of plastic strain distributions. However, this approach has the significant conceptual issue that although

there are general correlations between plastic strain, defect content and pattern quality, the detailed local associations need not be true. Using local lattice rotation gradients to determine the dislocation content in a material is better linked to high plastic strain gradient than high strain preferred as this method can be readiltquantified, as opposed to its previously mentioned counterpart. By measuring the misorientations within grains before and after deformation the levels of accumulated strain can be determined and, as shown by Prior[84], the misorientation angles can be determined to an accuracy of less than ±1°.

It is also possible to measure elastic strains in a material using EBSD. Again, there are two possible methods to achieve this: the measurement of Kikuchi line shifts and the measurement of zone axis shifts. The former was deemed unsuitable as the highest strain sensitivity achieved was 0.3 % [85] making it beyond the elastic limit of most metallic materials. Increased sensitivity of elastic strain analysis can be achieved by measuring the change in zone axis positions before and after the deformation of the specimen. Strain sensitivities using this method can be as high as ±2 x 10^{-4}[85]. Papers in 2012 by Britton & Wilkinson in 2012[86] and Maurice et al[87] demonstrated that remapping patterns provides the capability of being able to accurately distinguish small elastic strains that might have previously been lost due to the presence of larger lattice rotations. This opens up the possibility of examining intra-granular stress variations in deformed metals with greater resolution than previous methods. Both of these papers utilise cross-correlation-based analysis combined with the remapping of the pattern intensities. As was mentioned above, zone axis shifts are used to determine elastic strain differences and small lattice rotations in a material. Wilkinson et al[88, 89] showed that the magnitudes and directions of shifts from one diffraction pattern to the next can be written in terms of changes in the strain and lattice rotation states with the diffracting volume. A reference pattern is selected in each grain and cross-correlation measurements are made to determine pattern shifts and, hence, lattice strain in relation to this. This means that the results are not absolute strains, unless the strain at the location of the reference pattern is known. However, this method is still extremely important for determining lattice curvatures, that in turn can provide information on GND density, as well

as elastic strain gradients. With increasingly larger EBSD maps being captured, there have been significant developments that have resulted in automatic selection of reference points[90]. The usefulness of this cannot be understated, as in polycrystals multiple reference patterns need to be recorded in each grain and with areas that contain a large number of grains doing so manually would not be viable[91]. With particular relevance to this thesis, this method was demonstrated on the case of a fatigue crack in a nickel based superalloy[88]. When compared to using the Hough transform method to analyse the plastic zone the noise was too large to determine the size of the plastic zone with much accuracy. However, cross-correlation based analysis is able to determine that the plastic zone extends ~23 μm from the crack tip. Though it was also shown that both methods are unable to make measurements of high fidelity close to the crack as the patterns were too diffuse and low in contrast.

1.6 Transmission Kikuchi Diffraction

As was mentioned briefly in the previous section, on-axis transmission Kikuchi diffraction (on-axis TKD) is a technique that utilises the principles of EBSD but is performed quite differently to the standard method described above. A section devoted to the development and advantages of this technique allows for a comprehensive exploration. The most apparent advantage of TKD upon first glance is that the technique has a higher spatial resolution than convention EBSD (a few nanometres compared to tens of nanometres respectively)[92]. This is a result of the much smaller interaction volume of the beam and the sample (due to the greatly reduced thickness of a TKD sample). Prior to work by Fundenberger at al[93, 94] the EBSD detector would be positioned vertically, as in conventional EBSD, for TKD. This previous setup had much longer acquisition times due to the high scattering angles resulting in a decreased intensity of transmitted electrons which causes the need for longer acquisition times for an identical scan in the on-axis configuration [95, 96]. The on-axis technique can speed up acquisition by more than 20 times, or use 20 times lower doses (as demonstrated by Yuan et al[97]) In addition to faster acquisition,

a low scattering angle setup also gives rise to higher quality patterns. An example of the on-axis TKD setup is presented in Figure 2.13.

It is important to note that, like with any EBSD technique, the resolution is influenced by a number of other factors and not simply the setup. Among these are beam size, electron accelerating voltage, atomic mass of the material and the thickness of the specimen. Out of these variables, sample thickness has the greatest effect on pattern quality and resolution of the image. The thicker the sample the more broadening of the beam occurs, thus reducing lateral spatial resolution[95, 98, 99]. In addition to on-axis TKD being useful for materials with grain sizes less than 100 nm[100] the high spatial resolution is ideal for samples that have a high density of dislocations. Recent work from Hongbing et al[101] demonstrated the practical applications of the high resolution capabilities of conventional TKD technique by mapping the full lattice strain tensor of a single dislocation.

1.7 Aims of this Work

The aforementioned literature review highlights the gaps that exist in the field at the time of writing. This thesis aims to contribute knowledge to several of these gaps. The primary focus will be in demonstrating a significantly improved ultra high frequency fatigue testing method that is combined with advanced characterisation techniques such as SEM, HR-EBSD and TKD. Secondly, it will add to the data available on high cycle and very high cycle fatigue properties of CP Grade 2 Ti as well as improve the understanding of its behaviour during ultra high frequency fatigue testing. Thirdly, a contribution to the understanding of the effect microstructure has on fatigue crack initiation and growth in hcp metals will be made.

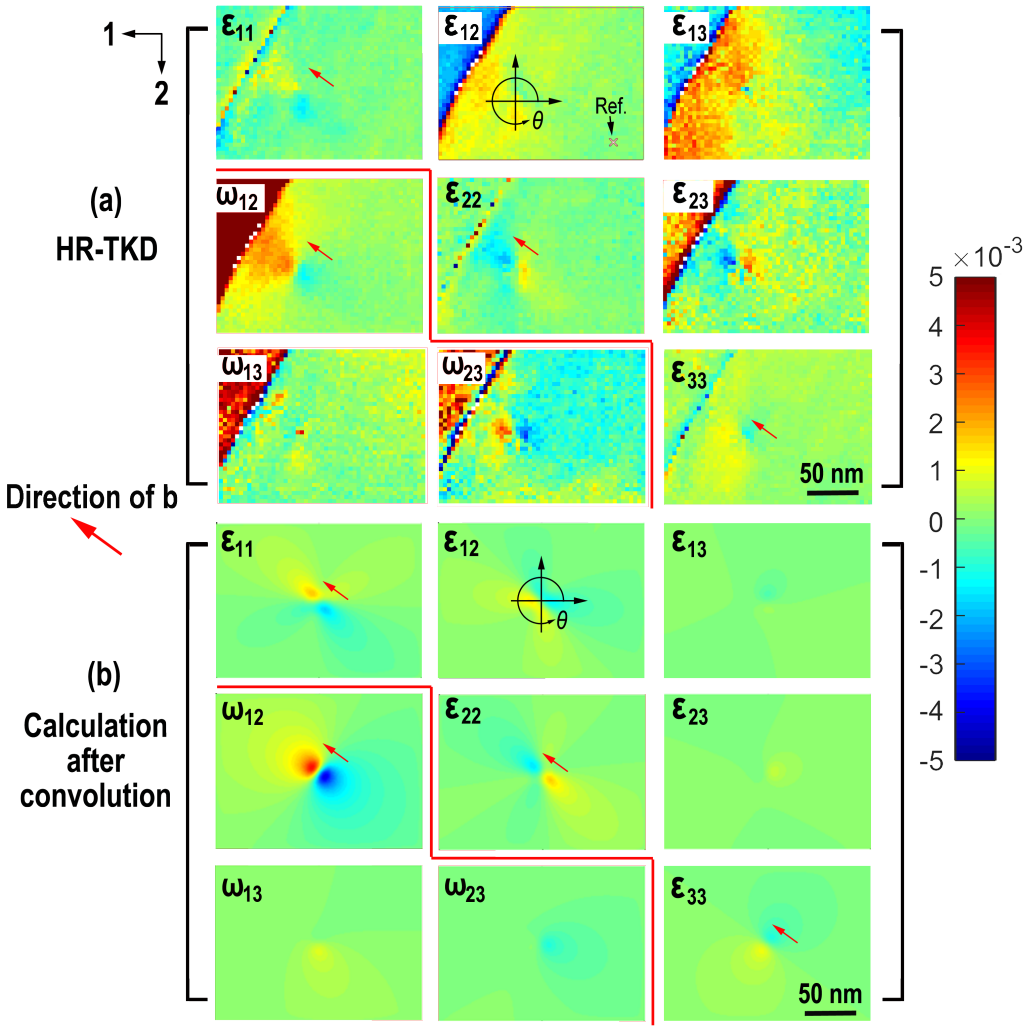


Figure 1.22: *(a) Maps for 3D lattice strain tensor and lattice rotations around the dislocation measured by HR-TKD. (b) The forward calculation of the distribution of strain tensor and lattice rotation around a $[\bar{1}1\bar{1}]/2$ dislocation using an isotropic elastic forward model convolved with a 2D Gaussian probe function. Red arrows shows the direction of Burgers vector projection. The cross shown in the map is the place where reference pattern was taken[101].*

Chapter 2

Materials and Experimental Methods

This section outlines the material investigated in this thesis and the experimental techniques employed. After the description of materials, the sample preparation techniques will be described; electropolishing, focussed ion beam (FIB) milling and laser cutting. The section will conclude with the characterisation techniques utilised - scanning electron microscopy (SEM), electron backscatter diffraction (EBSD)- and the testing methods - ultrasonic fatigue testing, conventional tensile testing and nanoindentation.

2.1 Materials

2.1.1 Commercially Pure Titanium

The material investigated in this thesis was commercially pure (CP) titanium. The 100 μm thick Grade 2 titanium foils were purchased from Advent Research Materials Ltd. Their composition is displayed in the table below.

Table 2.1: *Composition of Commercially Pure Grade 2 Titanium Foil from Advent Research Materials Ltd.*

Ti (wt%)	C (wt%)	Fe (wt%)	H (wt%)	N (wt%)	O (wt%)
Balance	0.002	0.07	0.0068	0.01	0.154

2.2 Sample Preparation

2.2.1 Laser cutting

To prepare mesocantilevers in the CP titanium foil the process was outsourced to a laser cutting company (Laser Micromachining Ltd.) that uses an ultraviolet laser with a femto-second pulse time. This pulsing of the laser prevents heating damage of the material by the laser whilst the small wavelength of the source provides high levels of accuracy and repeatability between samples. Figure 2.1 below shows the array of mesocantilevers as received from Laser Micromachining LTD.

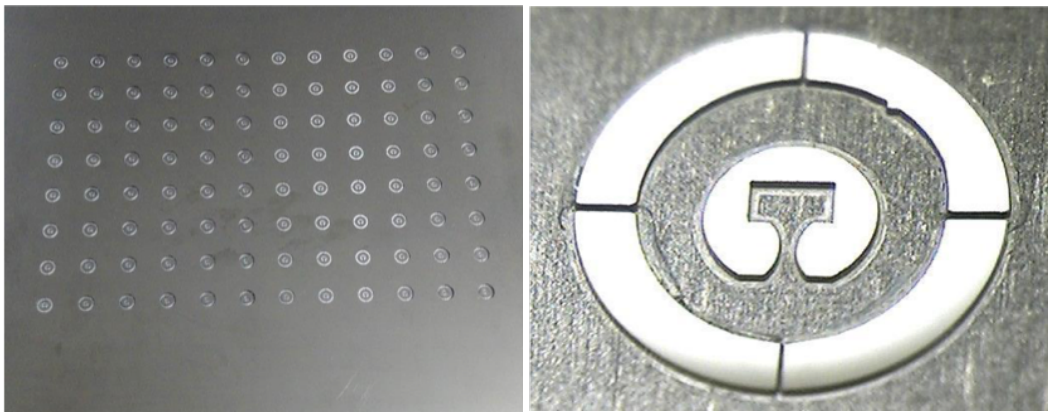


Figure 2.1: *(a) An array of mesocantilever specimens that were laser cut for ultrasonic fatigue testing and (b) an example of a single mescocantilever specimen.*

2.2.2 Water-jet cutting

To prepare the tensile test specimens in the CP titanium foil, water-jet cutting was performed. A typical dog-bone test specimen was used (Figure 2.2).

Test specimens were cut in two different orientations - parallel to the rolling direction and perpendicular to the rolling direction. This was to investigate the effect of cold-rolling in the material used on tensile properties.

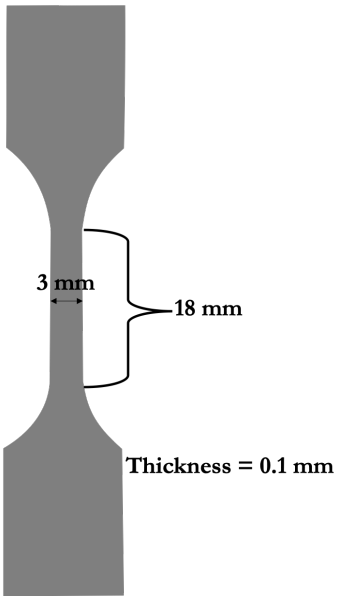


Figure 2.2: *A diagram of the tensile specimen design used in the tensile tests described in this chapter.*

2.2.3 Focussed Ion Beam Milling

In this project focussed ion beam (FIB) milling was used for two purposes - creating microcantilevers for mechanical testing and for performing 'lift-outs' to generate electron transparent specimens for material characterisation and analysis. The techniques involved for these two cases have been described below. FIB microscopes emit gallium (Ga^+) ions from a gallium liquid metal source, with accelerating voltages from 5-30 keV. Typically the emission current is around 2 μA. The Ga+ beam is rastered over the sample surface whilst secondary electrons are detected and an image produced. The FIB used in this thesis was the Zeiss® NVision 40 FIB-SEM. The method by which cantilevers are created is by focussing the ion beam on the area chosen and rastering the beam over the surface. The atoms on the surface are displaced from their original lattice site by the bombarding ions and removed. The Nvision is a dualbeam machine which means that it has both an ion beam and electron column. This allows for milling of the specimen at the same time as imaging thereby reducing the damage caused by Ga^+ bombardment.

Microcantilever manufacture

A FIB was used, as opposed to laser cutting, for the microcantilevers due to their dimensions being far smaller than the mesocantilevers (2 μm in width compared to the 100-150 μm width respectively). All microcantilevers machined in this thesis had triangular cross-sections. To manufacture our static microcantilevers the method used is described below:

N.B It is advisable to make reference marks (see Figure 2.3a) to ensure that the grain selected is always identifiable as redeposition during milling may make it difficult to locate.

(1) A 6.5 nA current beam at 30 keV was used to mill rough U-shaped trenches for the initial shape of the cantilever. Ensure the trenches are large and deep enough so that the nanoindenter tip does not collide with any other surface other than the cantilever. An example of a complete cantilever with the trenches desired is shown in Figure 2.4).

(2) Sample is tilted to 24° to begin the creation of a triangular cantilever.

(3) A 3 nA current beam at 30 keV was used to mill closer to the area of interest to leave a 6 μm wide cantilever. Milling at a stage tilt of 24° provides the first undercut to create a free-standing cantilever.

(4) A 1.5 nA current beam at 30 keV was used to mill even closer to the area of interest leaving a 4μm wide cantilever.

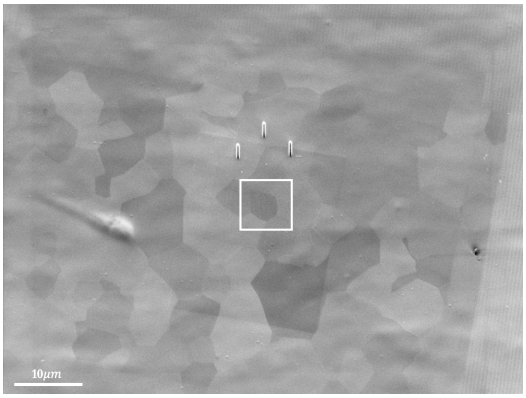
(5) A 300 pA current beam at 30 keV was used to achieve a near-final shape of the cantilever with a 2.5 μm wide cantilever.

(6) A 150 pA current beam at 30 keV was used for the final polishing step to create the final shape of the cantilever with a 2μm wide, 12 μm in length cantilever.

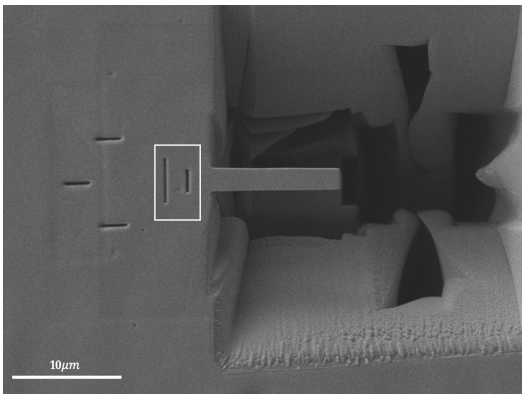
(7) A 80 pA current beam at 30 keV was used to make two reference marks to aid with locating the cantilever during nanoindentation tests. (See Figure 2.3b).

Throughout this process, the stage is rotated as appropriate to ensure milling from the relevant three sides.

The microcantilevers are 2 μm wide and 12 μm long so that their base falls entirely within a grain of interest and for it to still conform to standard beam theory (having a ratio of 6:1, length:width). An example of the final cantilever shape is shown in Figure 2.4.



(a) *Three reference marks to identify the grain of interest (marked by a white box) prior to milling of the microcantilever.*



(b) *Two reference marks for nanoindentation experiments. (Marked by a white box).*

Figure 2.3: *SEM images that show the different reference marks for (a) identifying the grain of interest during milling and (b) nanoindentation experiments.*

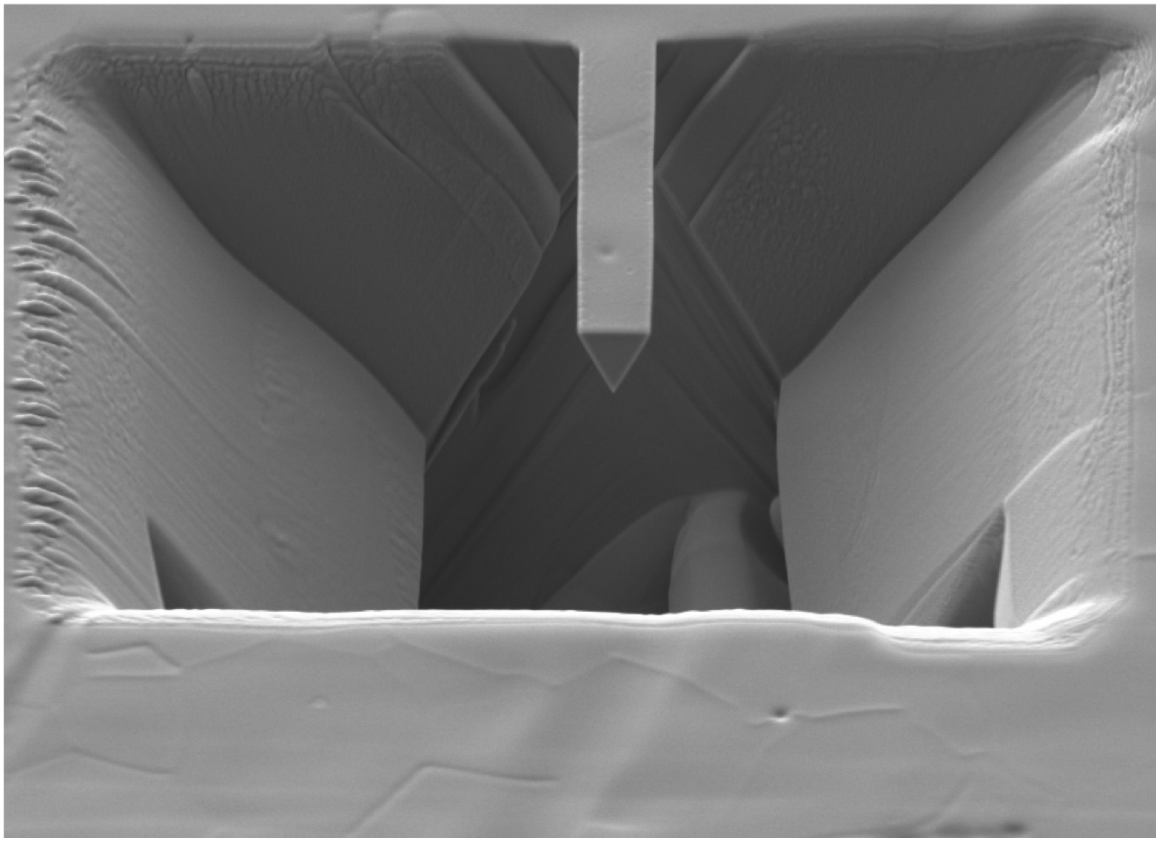


Figure 2.4: *An SEM image showing an example of a completed microcantilever.*

Lift-out

In order to perform certain characterisation and analysis techniques, the samples need to be electron transparent. Such is the case for on-axis Transmission Kikuchi Diffraction (TKD) which was described in detail in Section 1.6. To create such a sample one must mill away the surrounding area to generate a specimen thin enough. It is also important to protect the area of interest so a material that is highly resistant to electron bombardment is deposited on the surface of the area of interest. In the case of this project, the material deposited was platinum. The protocol for the lift-out experiments is described below:

(1) A layer of platinum is deposited on the surface above the area of interest

(2) The FIB is used to mill trenches around the area of interest

(3) The FIB is used to thin the section and then to leave a small bridge of material between the

section and the bulk

(4) The needle is brought in close to the section and platinum deposited to bind the needle to the section

(5) The FIB is used to sever the bridge between section and bulk

(6) The copper grid is brought in close to the section and platinum deposited to bind the needle to the copper grid

(7) The FIB is used to sever the platinum bridge between the needle and the section

2.2.4 Electropolishing

For both testing and characterisation of our specimens it is important to have smooth and damage free surface. In the case of testing, a smooth surface and edges helps even out the distribution of stress on the specimen during testing. Electropolishing removes any damage from the laser cutting on the edges of the cantilever as well as rounding off the edges. In the context of characterisation any marks on the surface from the rolling of the material or specimen preparation can affect the quality of the pattern obtained during EBSD analysis and will give incorrect measurements during strain analysis when using High Resolution (HR) EBSD. Figure 2.5 illustrates the difference of image quality between samples that were electropolished and those that were not. The method by which the samples were electropolished is described below:

The electrolyte used for electropolishing in this thesis was made up of:

- 6% Perchloric Acid
- 59% Methanol
- 35% 2-butoxyethanol

(1) A tub of methanol was prepared and cooled to -50 °C and placed onto a magnetic stirrer

(2) The electrolyte solution with a total volume of 250 cm^3 was made using the proportions above in a beaker and placed into a plastic tub

(3) A stir bar was introduced to the electrolyte solution and the magnetic stirrer switched to cause the stir bar to rotate gently

(4) Electrodes were set up and connected to a power supply.

(5) The power supply was set to 25 V whilst ensuring that the current was stable and at around 0.03 A during electropolishing

(6) A single titanium disc is taken and gripped by gold plated tweezers that were connected to the power supply and submerged into the electrolyte solution for 20 s

(6) The power supply is then switched off and the titanium disc is washed in pure methanol followed by distilled water before being dried using a pressurised air canister

(7) Each disc is inspected under a polarised light microscope to ensure that the electropolishing was sufficient (See Figure 2.5b for an example of an electropolished specimen)

(8) If electropolishing quality is deemed insufficient, the sample is electropolished once more

(N.B) The quality of the electrolyte solution changes as the experiment proceeds. It has been observed that is best to polish two 'blank' discs using the method above to 'age' the solution and reach peak performance. It is also important to note that after 6-8 samples the solution starts to underperform and polishing is of a lower quality meaning a new solution needs to be prepared.

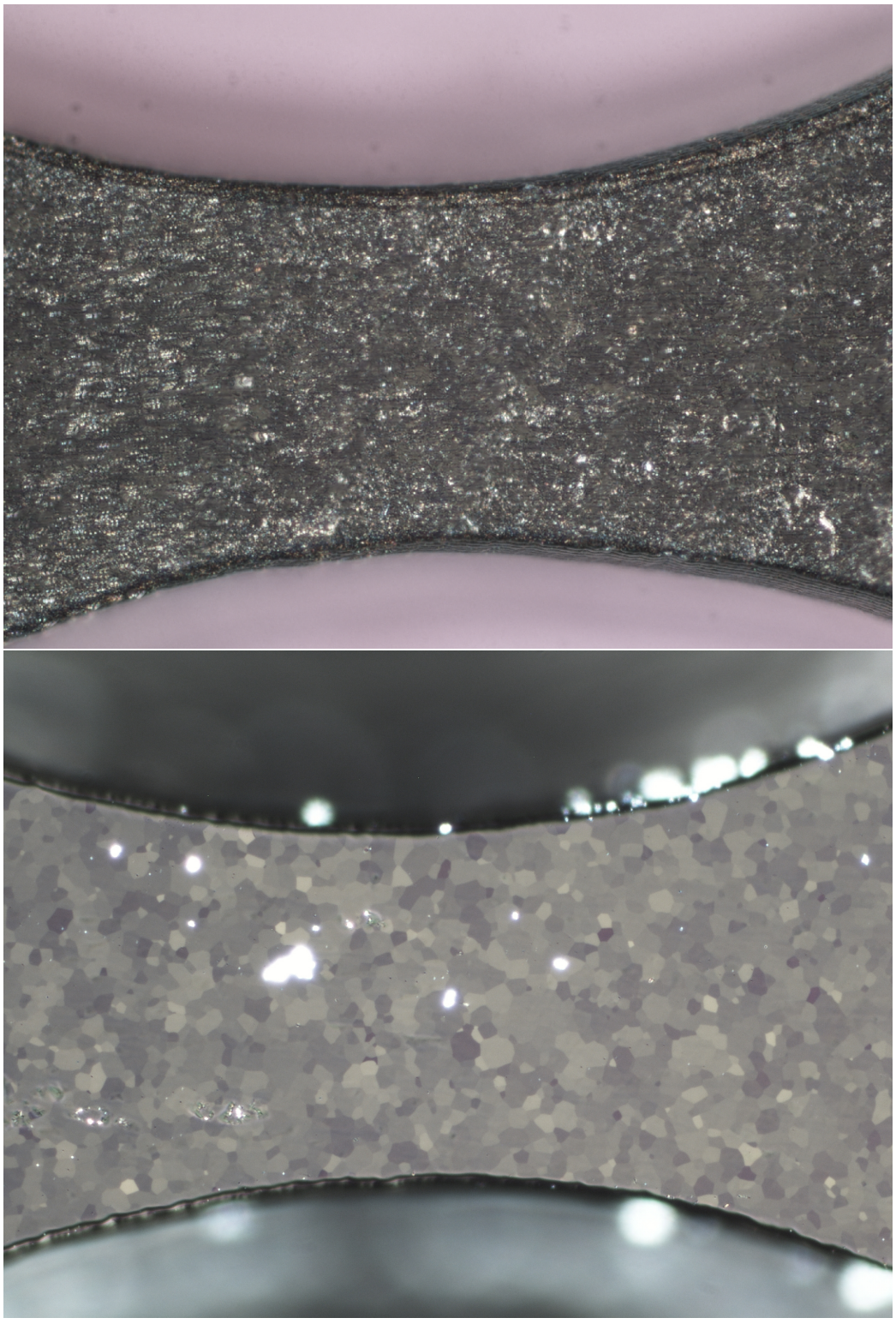


Figure 2.5: *Two polarised light micrographs illustrating the difference between a specimen (a) before electropolishing and (b) after electropolishing.*

2.3 Testing

For this thesis several techniques were employed to achieve the results outlined. These were chosen to probe several micromechanical properties of the titanium foil, namely grain strength, the properties of individual slip systems, elastic properties and fatigue properties. These tests were also used to investigate the microstructural effect on crack initiation, path growth and growth rate.

2.3.1 Tensile Testing

To give context to the results obtained in this project it was important to determine mechanical properties on a macroscale. This was achieved by performing tensile tests on specimens significantly bigger than the micro- and mesoscale specimens. In this thesis, tensile tests were dual purpose. They were used to determine tensile strength of the specimen as well as determining the stress-strain relationship using digital image correlation (DIC). The protocol for this experiment is outlined below:

(N.B) Prior to testing, the samples were coated with a speckle pattern to allow the camera used for DIC to track the change in strain in the sample.

(1) The test specimen is fixed into the grips tightly taking care not to apply load or twist the thin sample.

(2) The camera is aligned to ensure the centre of the gauge length is in view and that the area that fractures will be captured.

(3) Desired stroke speed (dependent on the desired strain rate) is set in the software.

(4) Pre-load of 5N is applied to ensure the sample is taut.

(5) Once pre-load is reached the test and image recording is started simultaneously until the specimen fractures.

2.3.2 Ultrasonic Fatigue Testing

The history and purpose of this method was discussed in detail in Section 1.3 and so will only briefly be recapped here. The main purpose of ultrasonic fatigue testing, in addition to being able to have a high throughput of samples, is to investigate the effect microstructure has on the initiation sites of cracks, the path the crack takes and the fracture surface. The specimens used for these tests were the mesoscale specimens prepared by laser cutting (as discussed in Section 2.2.1). For this experiment, several considerations had to be taken into account. Namely, the design of the specimen, the pinning of the specimens, the testing protocol and in-situ observation techniques. The design of the specimen is discussed in extensive detail in Chapter 3 as a significant amount of work was undertaken to create the final design. All other considerations are described in detail below. The experimental setup is depicted in Figure 2.6.

Pinning of the Specimen

Due to the nature of the protocol and the experiment, it was decided that mechanical pinning of the specimen was the best option. This is because it allows for quick and damage-free removal of the specimen and there are several advantages to this sort of removal. One can then perform 'interrupted' tests where a crack has grown but the cantilever hasn't fully broken off, allowing for analysis of the crack tip using electon backscattered diffraction, EBSD. It also preserves the shape of the specimen after complete failure so that the fracture surface and surrounding area is not affected. Of course, this method isn't without its disadvantages. As mechanical pinning is exactly that mechanical, there can be issues with ensuring the specimen is perfectly pinned. If the pinning is too loose, the specimen doesn't receive the stress intended and results are, therefore, unreliable. Too tight and there is a risk of damaging the specimen. In both cases the holder and the rig are at risk of being damaged.

The specimen holder itself was made from a modified grub screw (shown in Figure 2.7). Here, the lid is used to pin the specimen to the inner part of the grub screw. Both the lid and main grub screw are made of stainless steel. The hole through the bottom is made so that the

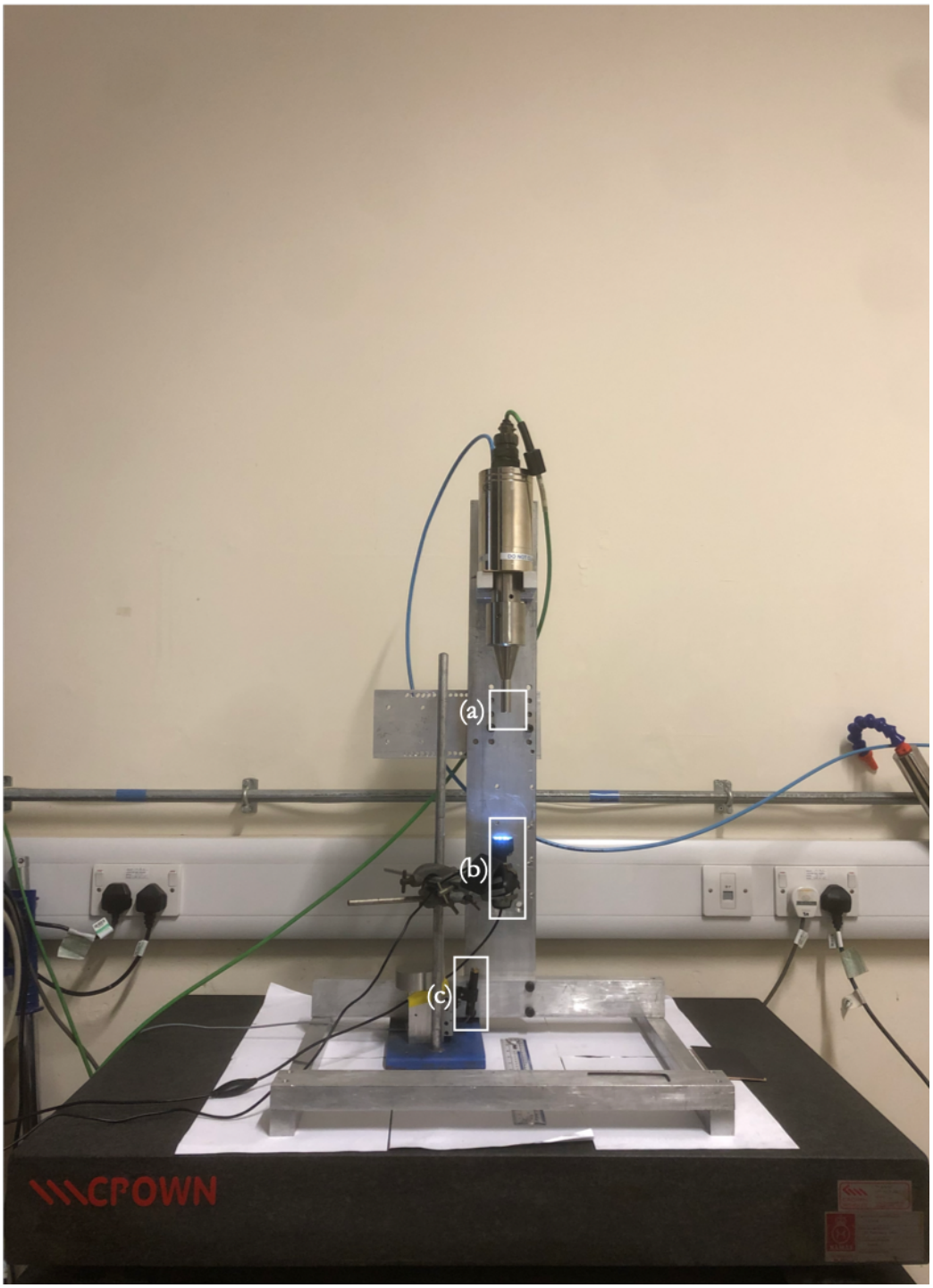


Figure 2.6: *The setup of the ultrasonic fatigue rig highlighting (a) the sample location, (b) the camera to determine specimen status and (c) the laser used for calibration.*

sample is visible from below. In addition to providing space for the cantilever to vibrate up and down unimpeded it also allows for the laser to reflect off the hammer of the specimen for calibra-

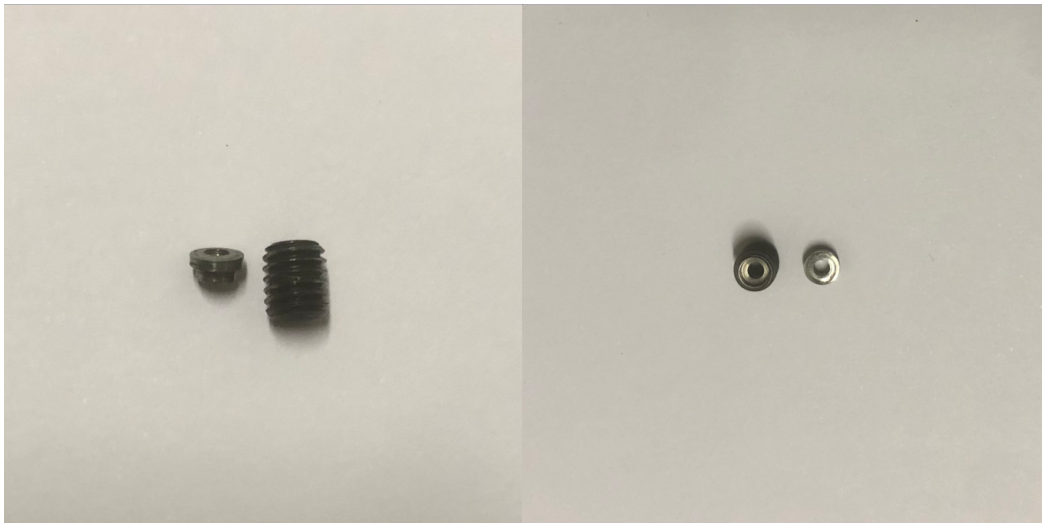


Figure 2.7: *Mesocantilever specimen holder made from a repurposed grub screw.*

tion (further discussed in Section 2.3.2).This setup also provides a line-of-sight for the camera in order to perform in-situ observation of the crack growth. It is important to make the hole large enough so that the cantilever does not come in contact with the grub screw at any point but also for the integrity of the grub screw to remain. Likewise, ensuring the hole diameters in the grub screw and lid match prevents over/underbites and risk of failure of the grub screw.

Calibration Protocol

Though care is taken to ensure that pinning and sample dimensions are kept constant throughout, the nature of both sample preparation and mechanical pinning make that impossible. As such, every sample is calibrated to ensure that the stress it experiences is what is intended when using the LabView control software. The setup for calibration is shown in Figure 2.8 whilst the protocol is outlined below:

(1) The sample is placed into the holder and screwed into the bottom of the fatigue rig to sufficient tightness

(2) The rig is rotated so that the hammer points left and the laser switched on at a lower intensity so that the entire spot is visible on the centre of the hammer

(3) The laser's intensity is increased so that its reflection is visible on the detector below and the laser focussed if required to ensure minimal scatter on the detector

(4) The ruler is positioned parallel to the deflection movement to track maximum deflection at each vibration amplitude

(5) The camera is positioned to capture the deflection and recording initiated

(6) Background scatter of the laser is measured and then four calibration tests for 1 s each

(N.B) Amplitudes chosen are such that the maximum is well below the stress that the cantilever would see during testing so as not to influence the results. In this case, the amplitudes chosen were 5 µm, 10 µm, 15 µm, and 20 µm. These give a good variation of stresses to ensure calibration is as accurate as possible.

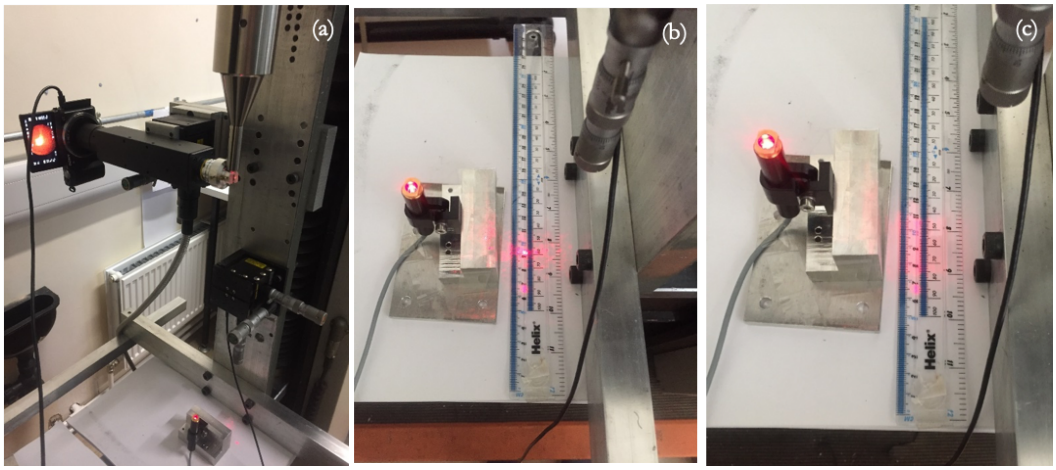


Figure 2.8: *(a) The experimental setup for calibration depicting the laser hitting the hammer of the specimen before reflecting down, (b) shows the laser spot when the specimen at rest and (c) shows the deflection of the laser as the specimen is vibrated.*

It has been observed there is a maximum of 10% variation in selected amplitude and actual stress conferred between specimens. The maximum amplitude chosen in calibration is less than 200 MPa.

Testing Protocol

The various testing protocols used in fatigue testing have been outlined in the literature review at the beginning of the thesis (Section 1.3) so will not be discussed here. Several protocols were trialled before it was decided that the best protocol for the purposes of this thesis is outlined below. For single-step tests, to ensure representative data was obtained once a sample reached the pre-determined 'run-out' life, the specimen was retired and noted as a run-out. There are slight differences to the testing method dependent on the observations one wishes to make. One protocol stream is just for determining the life of a specimen whilst the second stream is to monitor crack growth and determine initiation sites, the former is an 'uninterrupted' test whilst the second is an 'interrupted test'. Differences between the two tests are pointed out where relevant in the final protocol chosen outlined below:

(N.B) Sub-level 'a' is the protocol for uninterrupted tests, whilst sub-level 'b' is the protocol for interrupted tests.

(1) The sample is placed into the holder and screwed into the bottom of the fatigue rig to sufficient tightness

(2) A vibration amplitude that corresponds to the desired stress level is set in the LabView software and the pulse time is set:

(a) Pulse time is set to 50,000 s as that is the maximum test length before the specimen is considered as a run-out.

(b) Pulse time is set to 1% of the life targeted. E.g. If the crack growth of a specimen with a targeted life of 10^6 is being investigated then each pulse is set to 10^4 (0.5 s)[i]

(3) The compressed air for cooling is switched on and final checks before testing initiates are carried out:

[i]The caveat here is that there is a minimum amount of time that is required for the rig to reach the desired stress level during ramping up. As such, 0.5 s is the minimal pulse time to ensure the actual stress desired is reached. Therefore, when probing fatigue properties for lifetimes below 10^6 the pulse time set does not go below 0.5 s.

(a) The rig is rotated so that the hammer points left and the entire hammer is positioned on the screen to be in the field of view for the failure detection software.

(b) The rig is positioned so that the middle of the cantilever is in the field of view of the camera in order to capture crack initiation and growth

(4) Testing is initiated and runs:

(a) Until failure or run-out

(b) If observing crack growth until failure then the test runs until failure, otherwise the test is stopped when a crack of the desired length forms

(5) Sample removed and stored for further analysis

In-situ Observation

As was briefly touched upon in the previous section, the way in-situ observation is conducted depends on the purpose of the test. The two different set ups for uninterrupted tests and interrupted tests are shown in Figure 2.9. The key difference here, is that during uninterrupted tests to allow for easier detection of the crack and growth of the crack, a polarising filter is used. At the correct angle, the microstructure becomes visible and the crack becomes brighter than the surrounding surface of the cantilever. (Figure 2.10).

2.3.3 Nanoindentation

Developed in 1983 by Pethica, Hutchings, and Oliver[102], nanoindentation is a mechanical testing technique used for investigating the mechanical properties of small volumes of material. Using this technique it has been possible to examine the mechanical properties of individual grains in the titanium foil used in this thesis. This has been important in contextualising the fatigue properties observed on the mesoscale. The mechanical properties extracted by nanoindentation in this thesis are the elastic modulus and the critically resolved shear stress (CRSS).

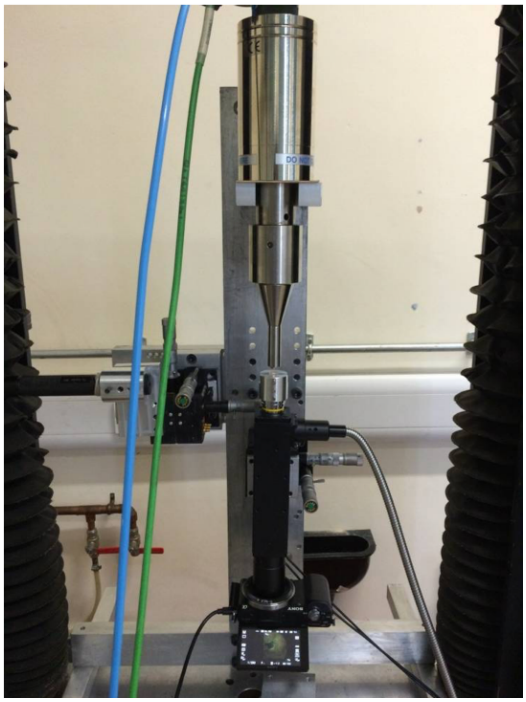


Figure 2.9: *In-situ observation setup*

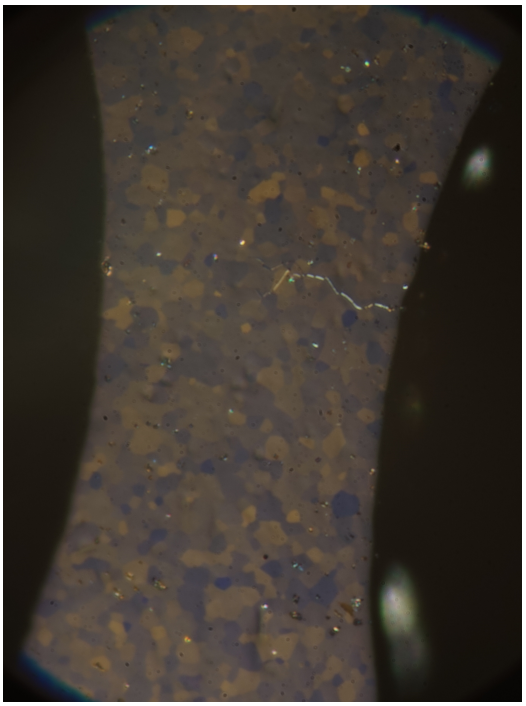


Figure 2.10: *An example of a mesocantilever that has begun to crack during fatigue testing.*

This section will describe the basic operation of the nanoindenter used - NanoVision® scanning stage using a Keysight® G200.

To determine the mechanical properties outlined above, a diamond Berkovich tip is pushed against the surface of a microcantilever at a specified rate up to a determined depth. A schematic of the nanoindenter setup is shown in Figure 2.11. Here, the coil magnet assembly responsible for applying a specified load to the indenter shaft is shown. A capacitance gauge measures the displacement of this shaft. The G200 Nanoindenter has a resolution of 0.01 nm with regard to displacement and 50 nN with regard to force[103]. Figure 2.11 shows the typical setup of the G200 Nanoindenter.

NanoVision® Scanning Stage

As the microcantilevers measure only 2 μm x 12 μm aligning them for testing with only the use of the optical microscope is not viable. To ensure optimal alignment for testing several steps are

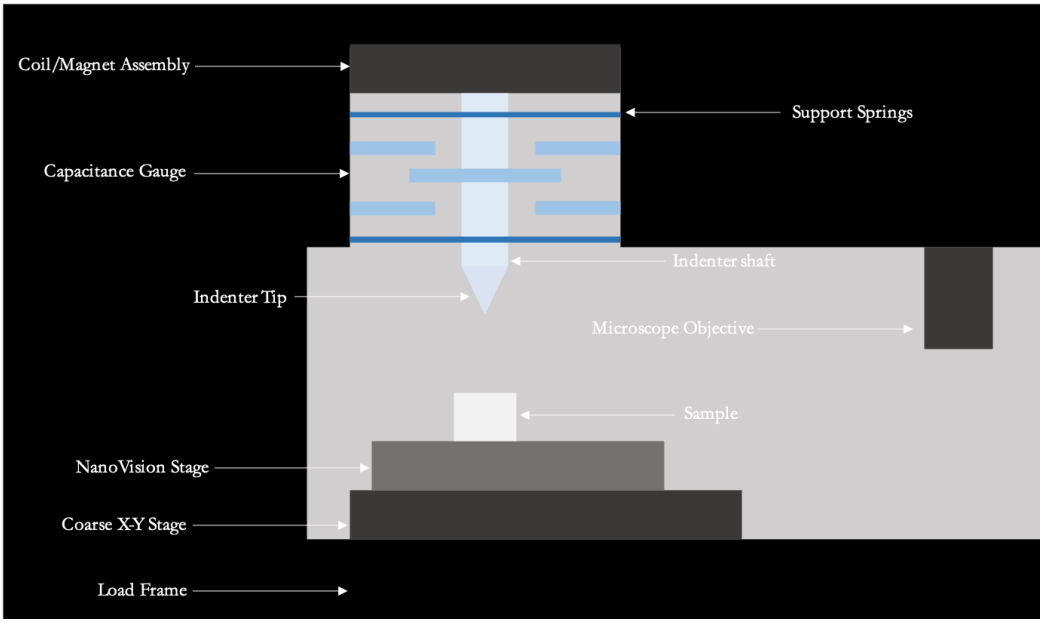


Figure 2.11: *Schematic of the G200 Nanoindenter*

taken. The first of which was to make reference marks using the FIB (as described in Section 2.2.3). After loading the sample into the nanoindenter and the tip position is calibrated with the objective the cantilever is aligned with the free end pointing up and the fixed end down. The orientation of the tip is also ensured to be such that the tip points upwards)[ii]. The tip is then lowered until contact with the sample surface is made and rastered across the surface around the area of the FIB reference marks. Care is taken to ensure that the tip does not raster across the cantilever as this can cause damage and, therefore, affect the final result of the bend test. The damage to the sample surface caused by this rastering of the tip across the surface can be seen in Figure 2.12a.

Upon observing this image it is clear to see why the reference marks are made as opposed to rastering the tip across the cantilever to determine its location. After this step it is possible, using offset control, to bend the microcantilever with the point of contact being at 90% along the length of the beam from the fixed end (this is to ensure the behaviour of the beam corresponds to simple beam theory and that the bending response is consistent amongst all tests).

[ii] The reason for this is due to the shape of the tip. As it is a Berkovich tip if either the tip or microcantilever direction was reversed there would be a risk of the tip hitting the cantilever twice during bending. Orienting both in the manner outlined above minimises this risk.

Microcantilever Bend Test Protocol

(1) Perform microscope to indenter calibration to ensure these are aligned.

(2) Scan sample surface at reference marks to determine location from which offset is calculated for the tip's contact with the microcantilever.

(3) The test parameters for all tests were as follows:

- **Depth Limit** – 2000 nm
- **Displacement Rate** – 20 nm/s
- **Frequency Target** – 42 Hz
- **Harmonic Displacement Target** – 2 nm
- **Poissons Ratio** – 0.280
- **Spacing in X** – 0 nm
- **Spacing in Y** – Determined based on distance of reference mark to target area of microcantilever
- **Strain Rate Target** – 0.05 s^{-1}
- **Surface Approach Detection Stiffness** – 60 N/m
- **Surface Approach Distance** – 6000 nm
- **Surface Approach Velocity** – 30 nm/s

2.4 Characterisation and Specimen Analysis Techniques

In order to fully evaluate the results of testing, several characterisation techniques will be employed in this project. These consist of - Scanning Electron Microscopy, Electron Backscatter Diffraction, Electron Channelling Contrast Imaging and Fractography. These are all described below.

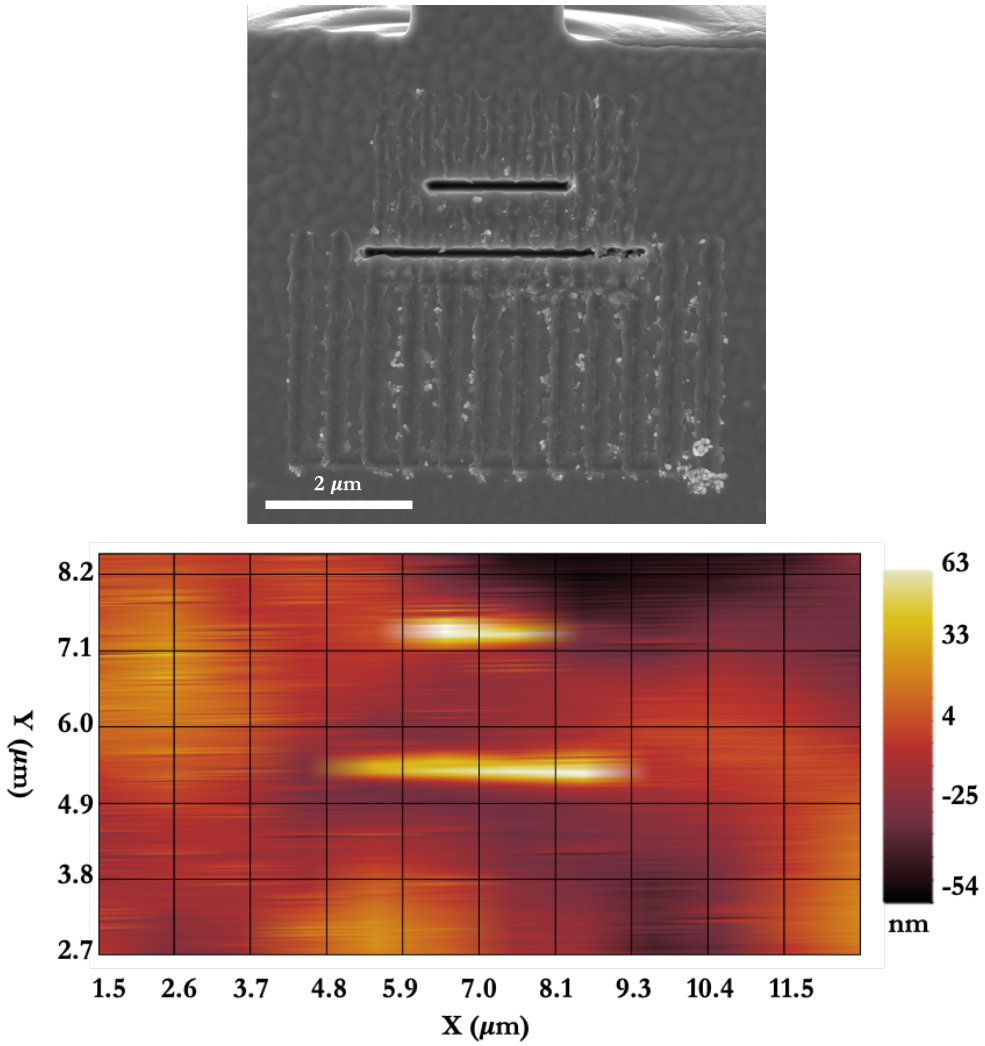


Figure 2.12: *(a) SEM image of two horizontal reference marks 4 μm and 2 μm with vertical marks from scanning tip. (b) Atomic force microscopy (AFM) topographical map of two reference marks.*

2.4.1 Scanning Electron Microscopy

Scanning Electron Microscopy (SEM) is a technique in which an electron beam is rastered across the surface resulting in various signals being produced. These signals provide the user with information regarding the topography, elemental composition and much more with the help of advanced techniques such as electron backscatter diffraction and electron channelling contrast imaging (both of which are discussed in the following sections). The technique most frequently used involves the emission of secondary electrons by atoms that have been excited by the incident

beam. These electrons then hit a detector and following processing an image is displayed. The following sections will outline the conditions used for various techniques that employed the scanning electron microscope and any changes to standard setup where appropriate. Prior to analysis, all specimens were plasma cleaned to remove any organic contaminants from the surface.
N.B Dwell times and other imaging conditions will be included in the results section alongside images as these sometimes differed from sample to sample.

2.4.1.1 Electron Backscatter Diffraction

The standard imaging setup for the EBSD maps obtained in this thesis are described below:

- **Stage Tilt**[iii] – 70°
- **Working Distance (Sample to Beam)** – 18 μm
- **Working Distance (Sample to Camera)** – 16 μm
- **Probe Current** – 5.0 nA
- **Beam Voltage** – 20 kV
- **EBSD Detector Tilt**[iv] – 4°

2.4.1.2 Transmission Kikuchi Diffraction

The setup for Transmission Kikuchi Diffraction imaging is described below.

- **Stage Tilt** – 0°
- **Working Distance (Sample to Beam)** – 5 μm
- **Working Distance (Sample to Camera)** – 16 μm

[iii] Throughout this thesis any reference to stage tilt is with respect to the floor. Here 0° would mean the stage is perpendicular to the incident beam whilst 90° would mean it is parallel to the incident beam.

[iv] Throughout this thesis any reference to the tilt of the detector is with respect to the incident beam. 0° is parallel to the incident beam whilst 90° would mean it is perpendicular to the incident beam.

- **Probe Current** – 1.0 nA
- **Beam Voltage** – 30 kV
- **EBSD Detector Tilt** – 90°

Figure 2.13 shows the setup used for TKD mode. As previously mentioned, samples to be analysed by TKD are required to be electron transparent. As such, the sample was prepared as described in Section 2.2.3. Figures 2.13b and 2.13c show the electron transparent specimen ready for TKD and attached to a copper grid.

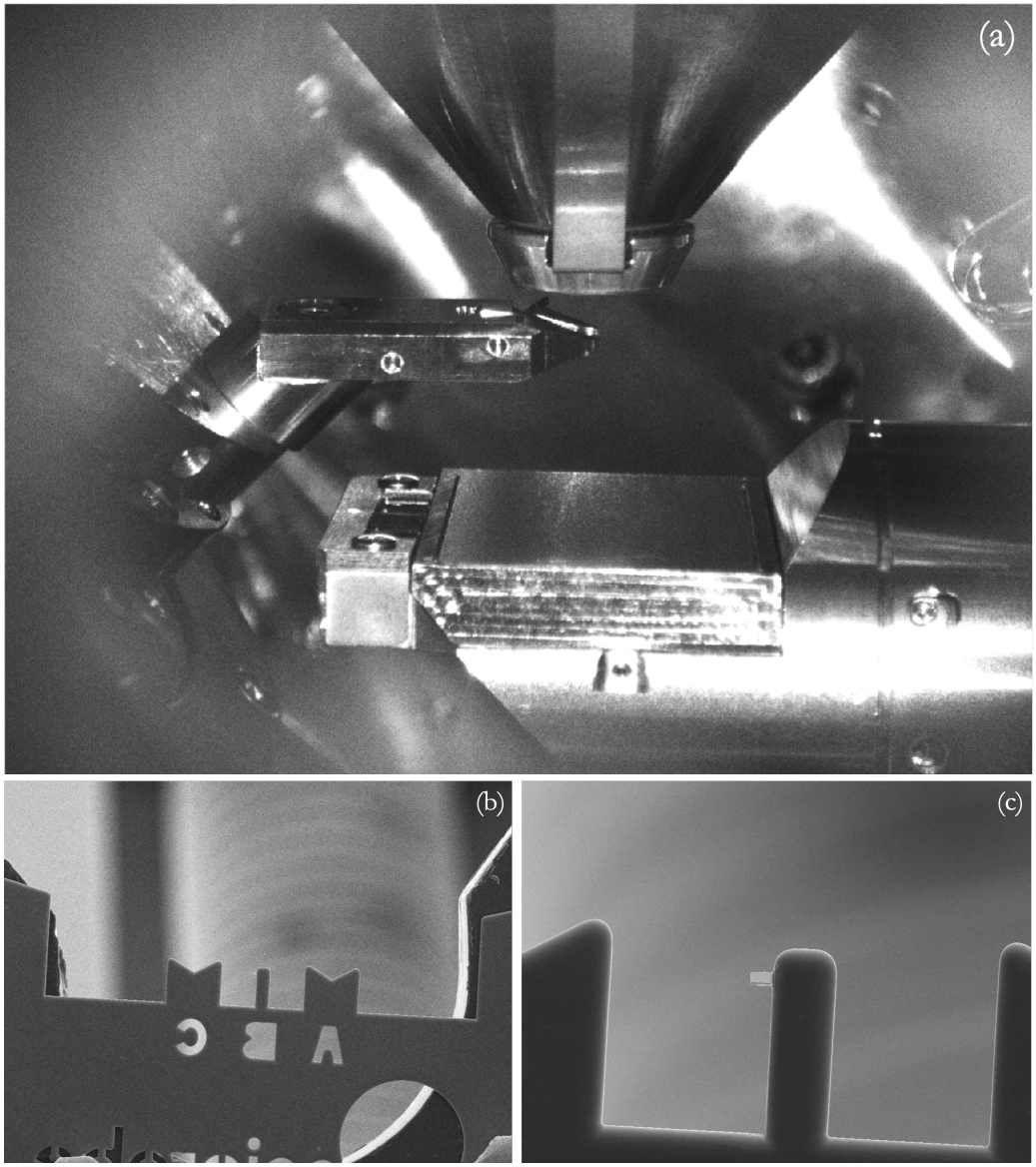


Figure 2.13: *Images that show (a) the SEM chamber for a standard TKD setup, (b) SEM general view image of the copper grid with specimen attached and (c) SEM image showing a close-up of the lift-out specimen attached to the copper grid.*

Chapter 3

Cantilever Specimen Design

For the purposes of this project, it was important to create a suitable specimen design in order to successfully probe the properties of the material outlined in the introduction. As mentioned in the earlier chapter, the main testing methods will use cantilevers deformed by ultrasonic testing and nanoindentation experiments. The different types of cantilevers that were used in this project can be split into two main types – mesocantilevers and microcantilevers. The microcantilevers were used for static type testing while the mesocantilevers were used for cyclic testing. Mesocantilevers were 150 μm in width, whilst the microcantilevers were 2 μm in width. These widths were chosen as in the case of mesocantilevers, each specimen would contain a large enough number of grains so as to be representative of the microstructure and, therefore, probe the effects of microstructural features (such as macrozones) on fatigue properties. In the case of microcantilevers the width was small enough to allow the fixed-end to be located within a single grain and thus ensure only the desired slip system was probed. Both specimens were cut out of a foil of 100 μm thickness. The mesocantilevers spanned the entire thickness of the foil and the microcantilevers were 1.73 μm thick. Figure 3.2 is a diagram illustrating the final mesocantilever design and Figure 3.10 shows the microcantilever design used in the final experiments.

Selecting these final designs was a result of finite element modelling combined with experimental validation of several variations of the designs shown here. There were several criteria the

design needed to fulfil to be deemed suitable. Namely, the mesocantilever's resonant frequency had to be as far as possible from 20 kHz as the closer it was to 20 kHz the greater the risk of it achieving resonance during testing since the ultrasonic generator oscillates at 20 kHz. One also needs to bear in mind that the overarching goal of this project was to investigate the effect of microstructure on FCI and as such the design had to ensure failure was microstructurally dependent and not sample geometry dependent. Previous work by Dr J Gong was geared towards examining SCG rather than FCI and this is evident when one examines his cantilever design (Figure 3.1).

The sharp corners result in very localised areas of stress concentration causing cracks to always initiate there, barring any severe defects in the middle of the beam. The first task of this project was to create a cantilever design that gave rise to a more uniform area of stress concentration towards the middle of the beam. Since obtaining HR-EBSD patterns before and after fatigue testing was desired, in order to perform cross-correlation analysis, the area of high stress concentration that was targeted was 100 μm x 150 μm. This allowed for an area of stress concentration that was representative in terms of microstructure but was also practically observable. HR-EBSD maps for this area typically take around 24 hrs, therefore performing more than one map on each sample with the hundreds of samples being tested was decided to be not economically or practically viable. The final Abaqus model of the cantilever used in this project is shown in Figure 3.2.

The aim of this work was to move fatigue crack initiation sites away from geometric features and instead have cracks form as a result of microstructural features. The most time and cost effective way to do so was to model several designs in Abaqus and perform finite element analyses rather than create designs and have them cut into the target material and perform physical experiments. This allowed many iterations of the design to be created before settling on a final few for testing to confirm modelling results. The first step was to move failure away from the sharp corners where the cantilever joins the fixed end. As it is well known that cracks form primarily in areas of high stress concentration, and according to fracture mechanics the smaller the radius of a corner the higher the stress concentration at that location. Therefore, Dr J Gong's model

was taken as a starting point and work began on tapering the corners to move the area of the highest stress to the centre of the beam. Though these did indeed slightly move the stress away from the corners it was not enough for the purposes of this project. As such, a design similar to typical dog-bone tensile specimens was explored. These proved to be far better than the previous attempts with the area of high stress pushed to the thinnest part of the mesocantilever. With this design the size of the area of maximum stress could be controlled by modifying the length of the beam and the radius of curvature for the beam. The size of the hammer (the location of which is depicted in Figure 3.10) and beam controlled the stress the beam experienced and the resonant frequency of the mesocantilever.

As with any modelling experiment it is important to determine whether or not the model captures all phenomena of the material under the chosen conditions. To do so, several things need to be taken into account - the material properties, the boundary conditions, the design of the model and the mesh size. The first property can be taken from database values as a good starting point and the second is dependent on the experimental setup so is usually intuitive. The latter two require fine-tuning during the modelling process. This is known as convergence studies i.e do the results achieved change appreciably if the mesh size is made finer or if the model design changes. The details of the models and convergence studies for the meso- and microcantilevers modelled in this thesis are discussed in Sections 3.1.1 and 3.1.2 respectively. The mesh type used in both of these models was the solid 3D eight-node type (C3D8R) as this met the requirements for accuracy in determining the stress response. The modelling performed in this body of work will be elastic and isotropic. It is assumed that due to the large strains the specimen undergoes in LCF the stress as a result of plasticity will have redistributed and therefore elastic anisotropy will not be present[104]. In the case of determining the resonant frequency, anisotropic modelling is more accurate as it takes into account the texture of the microstructure in the material. However, anisotropic modelling is very complex whilst the isotropic value provides a good estimate of the resonant frequency. When determining the stress response using a model, an elastic isotropic model is used as in the HCF regime, the behaviour of a mesocantilever is near elastic. There-

fore, the elastic modulus input in the model is the most important value when determining the mesocantilever model's response. As will be shown in Chapter 4 the modulus is dependent on a material's texture with respect to the loading axis. This is also supported by literature that shows that as the c-axis of the crystal is inclined towards the loading direction the Young's modulus increases[105]. In the case of the texture present in the material used (Figure 6.5) the alignment of the c-axis is such that the data sheet value of 105 GPa for CP Grade 2 Ti is a good approximation for the overall elastic modulus. In addition to literature data, the tensile tests performed and included in Chapter 4 show that the average Young's modulus for monotonic tensile tests, with the loading direction in the same direction as that in the mesocantilevers, is ~105 GPa. It is clear when looking at Figure 3.2 that the distribution of maximum stress is far more even than in the cantilever in Figure 3.1 as well as moving from the fixed-end corners and to the centre of the cantilever.

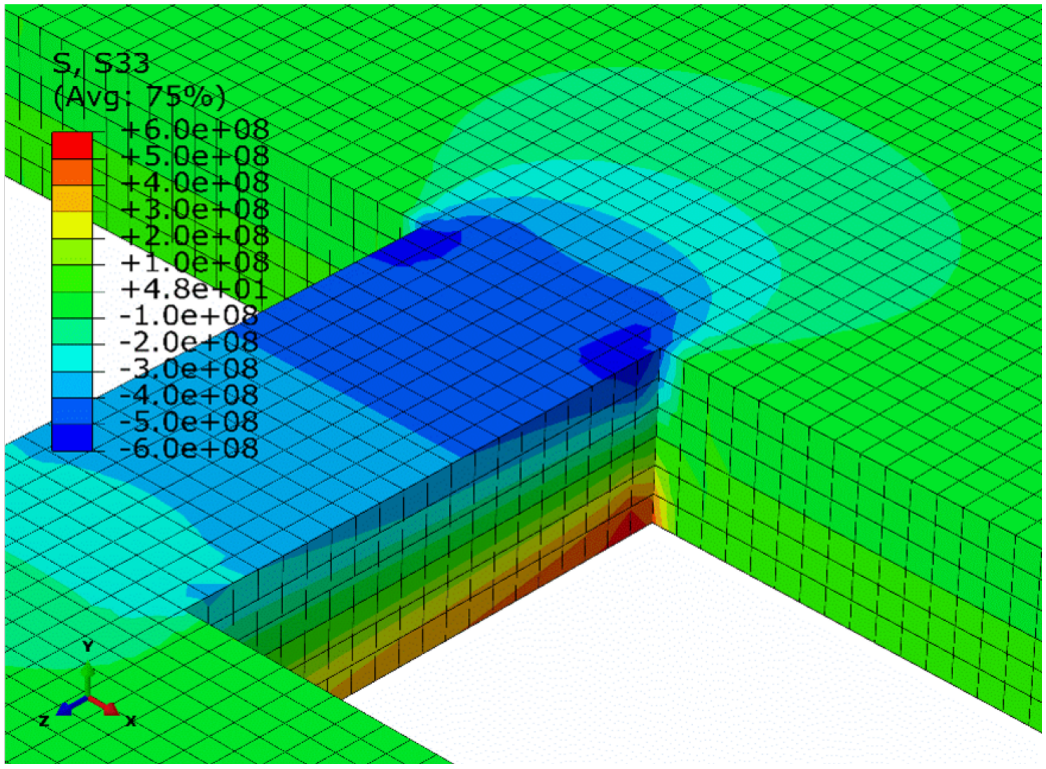


Figure 3.1: *An Abaqus model of a mesocantilever designed for examining short crack growth by Dr J Gong. Sharp corners cause stress concentration that dominate location of crack initiation.*

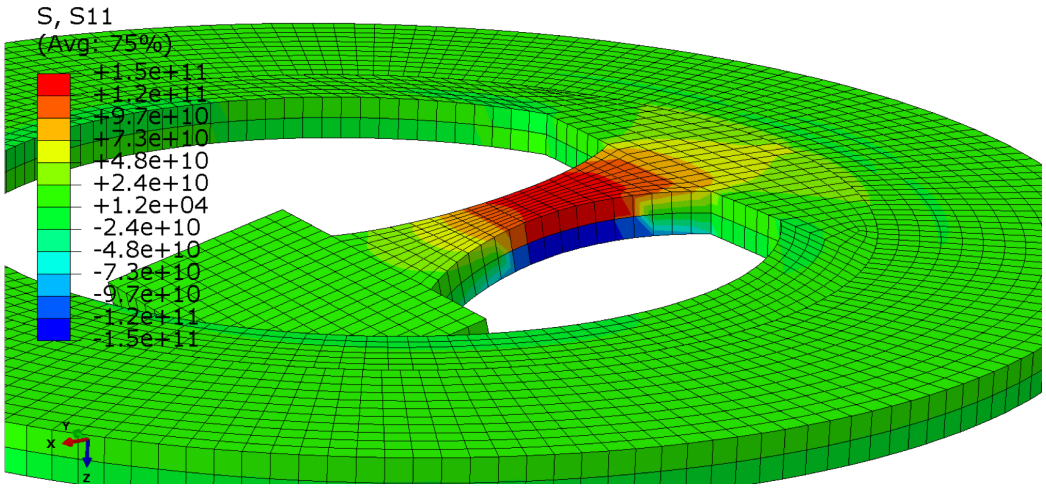


Figure 3.2: *An Abaqus model of the final mesocantilever design used in this project. The localised stress concentrations seen in Figure 3.1 are not present.*

3.1 The Model

3.1.1 Mesocantilevers

Dimensions and Conditions

For the mesocantilever models it was important to model the entire 3 mm diameter test specimen to replicate experimental conditions. This was because a difference in the response of the mesocantilever in terms of stress and resonant frequency was seen if simply the cantilever and part of the base was modelled. The entire model can be seen in Figure 3.3 The boundary conditions for the model depended on the type of analysis run. The analyses were either to determine the resonant frequency or the stress response at the experimental vibrational amplitude. When determining the resonant frequency for the model, the Lanczos algorithm was used to determine 20 eigenvalues. The Lanczos algorithm allows for the automatic reduction of a Hermitian matrix to determine lower frequency modes.This is achieved by solving an eigenvalue problem. When initially described by Cornelius Lanczos, it was numerically quite unstable, however, Ojalvo and Newman[106] were able to correct and introduce numerical stability to the algorithm. The boundary conditions were encastre around the areas pinned by the grub screw in experiments

(indicated as Zone 2 in Figure 3.3). The frequency of the first resonant mode is selected as it is the relevant value for the conditions of this experiment. This mode corresponds to simple out of plane bending as depicted by the arrows in Figure 3.3. For examining the stress response, the boundary conditions are again on Zone 2 but this time it is a displacement/rotation type boundary condition linked to the steady-state dynamics step implemented (x and y displacements, as well as all rotations, are set to zero). The steady-state step runs through three frequencies 19 kHz, 20 kHz and 21 kHz and the boundary condition dictates a displacement of 10 μm in the Z direction, as a sine wave, to simulate the vibration of the ultrasonic horn. A direct dynamic analysis method to achieve steady state vibration immediately is used as the full dynamic method requires a significant amount of computational time (nearly one month). The difference in final calculated resonant frequencies and stresses, however, are minimal. Likewise, experiments performed by Dr J Gong and Tinger Wen have shown that time taken for the mesocantilever to reach steady state is 0.05 seconds. This was achieved by tracking laser reflection movement as a result of cantilever deflection (using a similar method to the calibration method outlined in Section 2.3.2) and noting down the time before the laser reflection spread became stable.

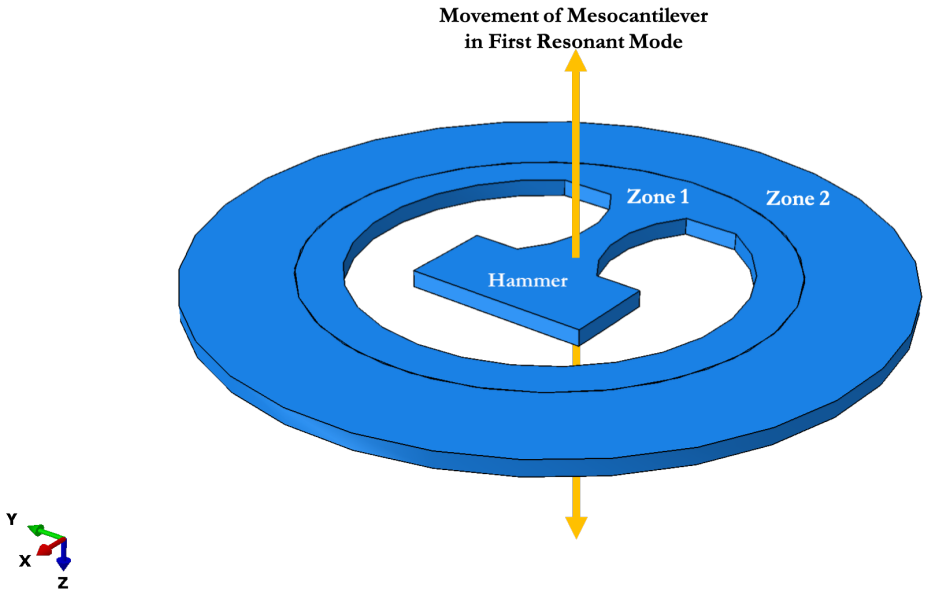


Figure 3.3: *A model of the final mesocantilever shape used.*

Convergence Studies

The finer the mesh size the more details regarding the specimen's response to certain conditions are captured. However, with finer mesh comes more computational load. It is, therefore, cost and time efficient to find a balance between model accuracy and time taken for the model to run. These are called convergence studies as at some point the difference in mesh size doesn't result in an appreciable difference in the result of the model i.e the results converge. The values compared for the convergence studies were the variations in stress along three paths on the top surface of the beam: (a) the centre of the beam, (b) from one side of the beam to the other at the point of highest stress and (c) along one side of the beam from the fixed end to the hammer. The paths used are displayed in Figure 3.4. These paths are referred to as the centre path, the transverse path and the edge path respectively.

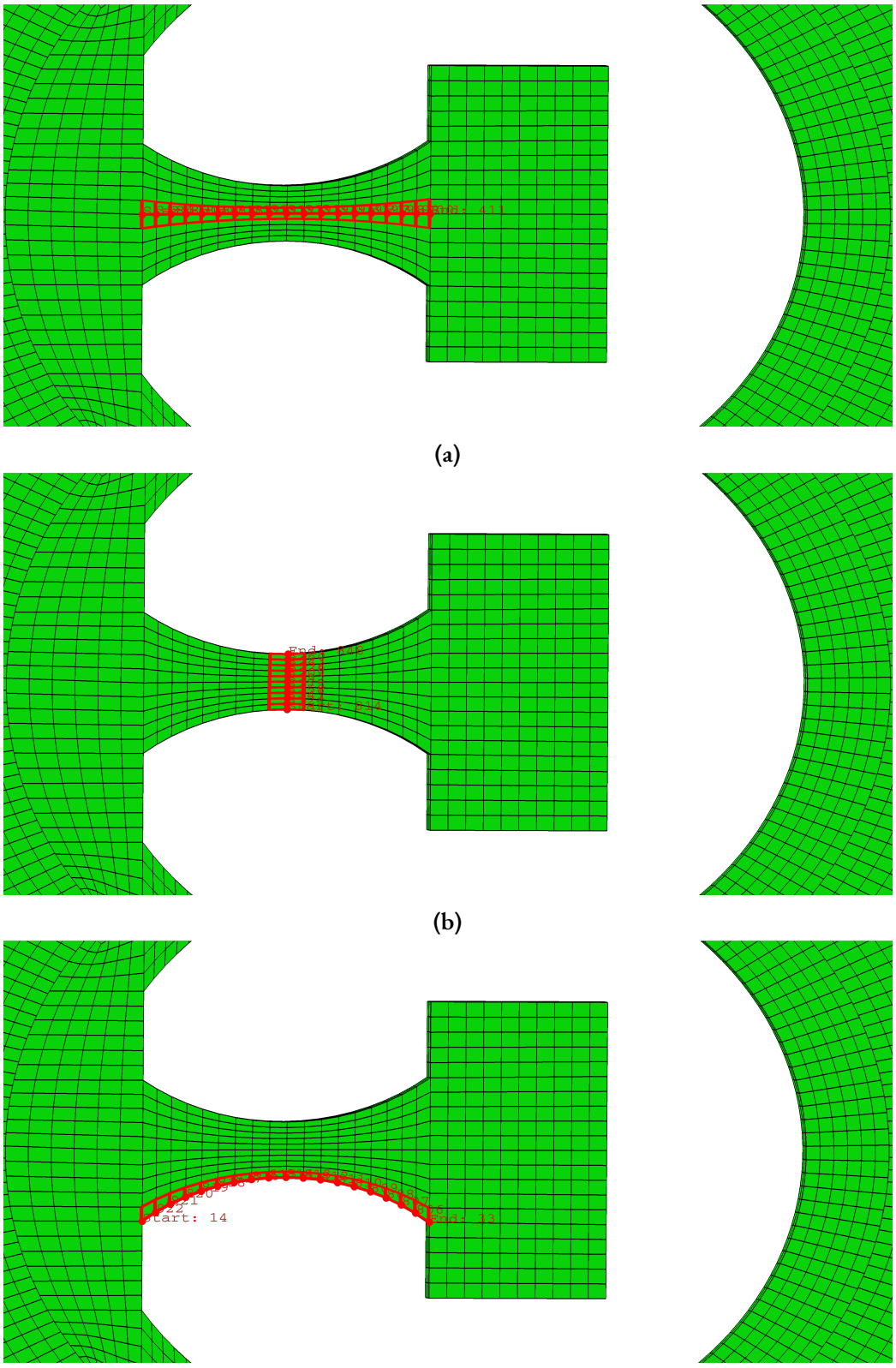


Figure 3.4: *Three paths used to determine stress variation on the top surface of the meso-cantilever (a) path along the centre of the beam, (b) path from one side of the beam to the other at the point of highest stress (c) path along one side of the beam from the fixed end to the hammer.*

The red boxes in each of the paths in Figure 3.4 are the elements in the model with the numbers signifying the nodes from which the stress data in the convergence studies are obtained. Figure 3.5 shows the convergence studies done for the mesocantilever. These plots show that the calculated stress values begin to converge by CS 6 (the finest mesh with 311850 elements, table of meshes with their respective number of elements presented in Table 3.1). The computational load and time taken to perform analysis with a CS 6 mesh was not so high that it was not practical to do so. As such, the CS 6 mesh was used to model mesocantilevers going forward.

Table 3.1: *Table displaying the number of elements in each Mesh ID.*

Mesh ID	Number of Elements
CS 1	458
CS 2	656
CS 3	1114
CS 4	2490
CS 5	23690
CS 6	311850

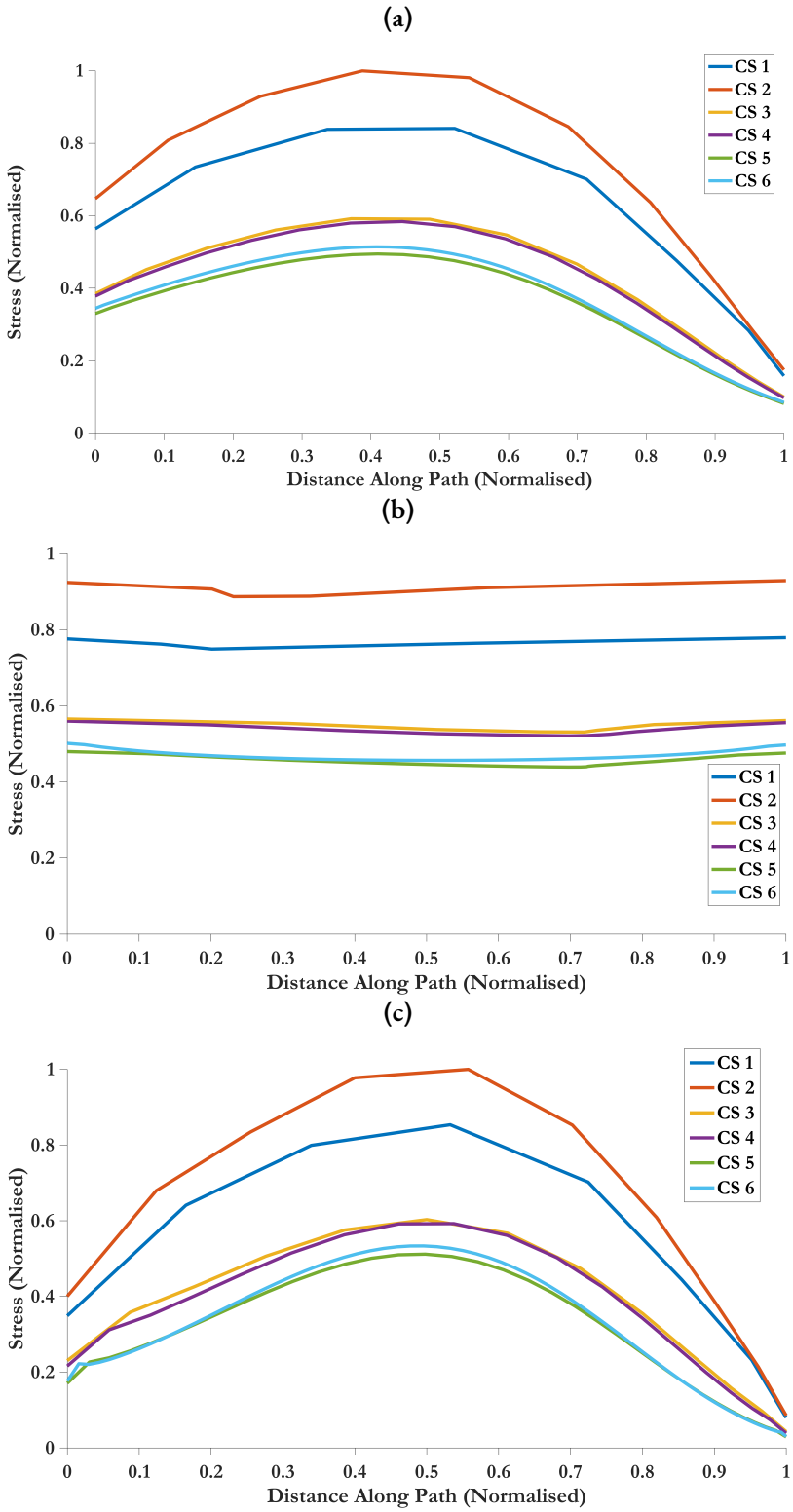


Figure 3.5: *Convergence Studies for (a) Centre Path, (b) Transverse Path (c) Edge Path*

Selection of Final Design

Once the convergence studies determined that the model design was indeed appropriate for experiments to be conducted. Mesocantilever models were cut out using a femto laser (as described in Section 2.2.1). To ensure that the mesocantilever model design was the best option for the aims of the project several designs that differed slightly were created as well for experimental testing. The array of mesocantilevers used for this first stage are displayed in Figure 3.6 with their dimensions displayed in Table 3.2. This set are referred to as SS-Cantilevers as they were cut into stainless steel (304L) sheet of 100 μm thickness.

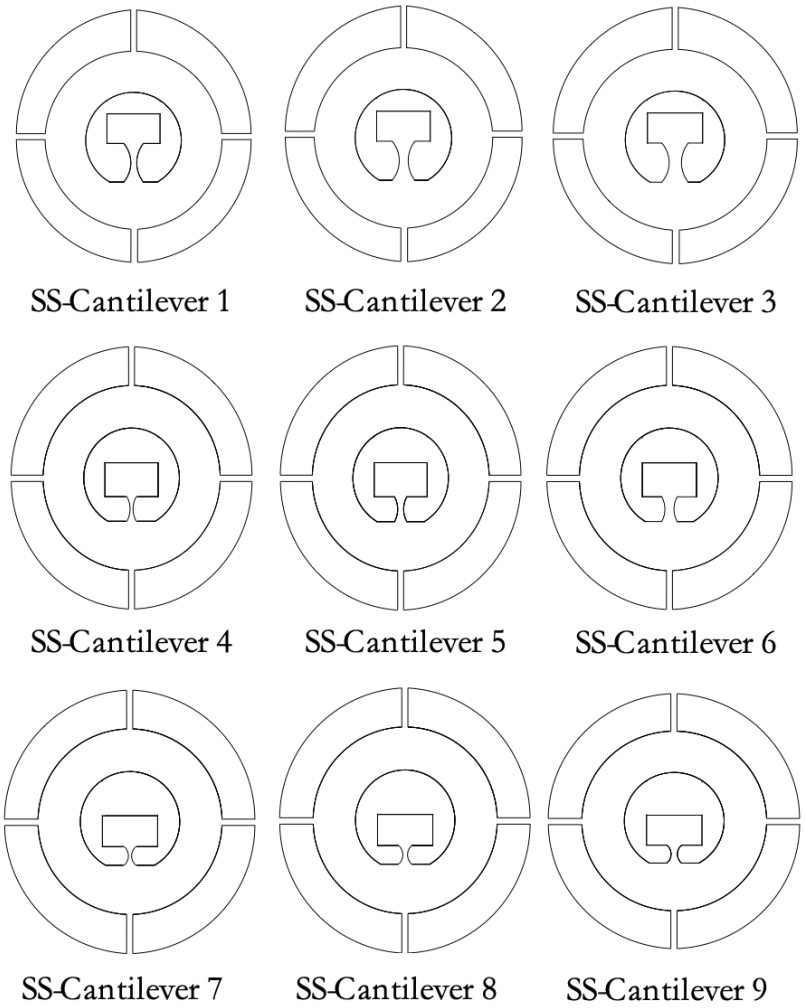


Figure 3.6: *Design of experimental mesocantilevers used for initial tests in stainless steel 304L.*

Table 3.2: *Dimensions and Resonant Frequencies of Experimental Test Cantilevers in stainless steel 304L.*

	Hammer		Beam		Calculated Resonant Frequency (kHz)
	Height (μm)	Width (μm)	Length (μm)	Width (μm)	
SS-Cantilever 1	900	500	650	100	21.11
SS-Cantilever 2	900	500	650	150	23.73
SS-Cantilever 3	900	500	650	200	26.92
SS-Cantilever 4	900	550	400	50	15.49
SS-Cantilever 5	900	550	400	100	27.87
SS-Cantilever 6	900	550	400	150	31.79
SS-Cantilever 7	900	500	300	50	20.69
SS-Cantilever 8	900	500	300	75	32.35
SS-Cantilever 9	900	500	300	100	37.31

There were several metrics of the sample's behaviour during testing that were most important for the purposes of this thesis. Firstly, the vibrational amplitude at which the sample failed after 10^6 cycles had to be in the middle of the capabilities of the equipment (amplitudes from 10 μm to 60 μm). This is because tests at shorter lives would require larger vibrational amplitudes and tests at longer lives would require smaller vibrational amplitudes. Secondly, the width of the mesocantilever would be large enough for the path of a crack to not only be observed during testing but the operator would have time to stop the test before the sample failed completely. After these tests it was determined that the cantilevers with a width of 150 μm were the best performing if the metrics outlined were taken into account. Consequently, moving to the target material (CP Ti) four more experimental designs were physically tested all with 150 μm widths but with different hammer sizes and beam lengths. The variation of stress in the area of maximum stress along with the resonant frequencies and maximum stress value for these four beams were determined prior to selection for experimental tests. These values are shown in Table 3.3.

It was decided that a maximum variation of 10% was tolerable and that the resonant frequency needed to be at least 4 kHz above the oscillation frequency (20 kHz) of the piezoelectric actuator in the tester. This was because the frequency of the actuator could vary slightly during ramp up and operation. A margin of 4 kHz was deemed safe enough to be outside of the win-

Table 3.3: *Stress Variation, Maximum Stress at 20 μm vibrational amplitude and Resonant Frequencies of Experimental Test Cantilevers tested in Grade 2 CP Ti.*

	Calculated Resonant Frequency (kHz)	Maximum Stress (MPa)	Stress Variation (%)		
			Centre	Transverse	Edge
Ti-Cantilever 1	24	386	6.70	8.39	6.39
Ti-Cantilever 2	28	285	7.12	10.22	6.34
Ti-Cantilever 3	33	169	8.87	8.48	6.41
Ti-Cantilever 4	40	101	7.41	7.29	6.20

dow of variation in the equipment. This margin also took into account any changes in resonant frequency of the sample that could come about from either the laser cutting process or electropolishing. As can be seen in Table 3.2 with decreasing cantilever width the resonant frequency drops significantly. The stress targets were in the order of 10^2 MPa as the exact stress coupled into the mesocantilever during experiments was not known at this stage but rough values had been determined in previous experiments. Since the values fell within the desired parameters, all four designs were cut out in the target material - Grade 2 CP Ti (Referred to as Ti-Cantilevers in this section). The dimensions and resonant frequencies of these four mesocantilevers are outlined in Table 3.4 with the four designs used shown in Figure 3.7. From these it was determined that the mesocantilever with a resonant frequency of 33 kHz should be used for final testing. This was because it performed the best for all the metrics desired. Its failure amplitude for 10^6 fell in the middle of the allowable range for the equipment, the crack growth was the easiest to track and the location of crack initiation varied more greatly from sample to sample.

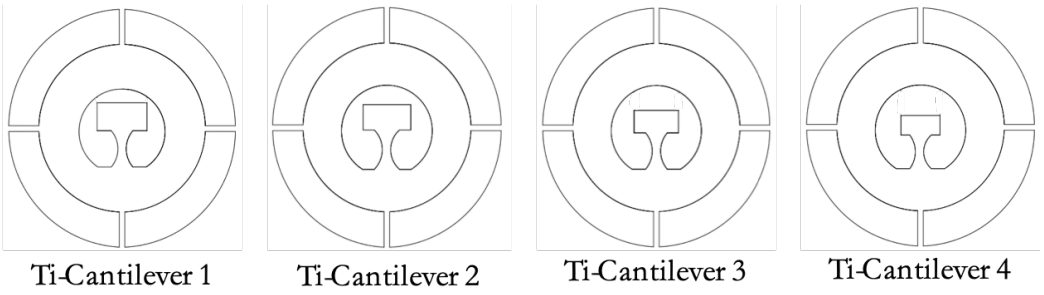


Figure 3.7: *The final four mesocantilever designs tested with different resonant frequencies. Ti-Cantilever 1 - 24 kHz, Ti-Cantilever 2 - 28 kHz, Ti-Cantilever 3 - 33 kHz, Ti-Cantilever 4 - 40 kHz*

Table 3.4: *Dimensions and Resonant Frequencies of Experimental Test Cantilevers tested in Grade 2 CP Ti.*

	Hammer		Beam		Calculated Resonant Frequency (kHz)
	Height (μm)	Width (μm)	Length (μm)	Width (μm)	
Ti-Cantilever 1	900	500	650	150	24
Ti-Cantilever 2	850	450	700	150	28
Ti-Cantilever 3	800	400	650	150	33
Ti-Cantilever 4	700	350	600	150	40

3.1.2 Microcantilevers

Dimensions and Conditions

With regards to the microcantilevers, as was previously discussed, it was key to have microcantilevers that allowed for the probing of strengths in three slip systems. To do so, the microcantilevers needed to be smaller than the grains of the material examined. The majority of grains in the foil had an area of 20 μm^2 (Figure 3.8 shows the grain size variation in the titanium foil used in this thesis). The small grain size means that the size of the microcantilevers is limited to ensure the fixed end is wholly within the target grain and as much of the beam is within the grain to ensure slip occurs in the target grain. As such, it was decided that microcantilevers of 2 μm in width would be made. With the width determined, it was also important to ensure that the microcantilevers still followed beam theory and as such a length:width ratio of 6:1 was opted for. Work by Armstrong et al[72] showed that if the fabricated microcantilever length:width ratio went below 6, it resulted in a noticeable underestimation of a material's Young's modulus. In addition, though the foil was cold rolled the majority of grains tend to be quite equiaxed with there only being a few elongated grains. Figure 3.9 shows the grain shape of a typical area of the foil. This is quite advantageous for the purposes of this project as it allows for microcantilevers to be milled in most orientations within a grain. The shape of the microcantilevers used here are all equilateral triangular prisms. This ensures that there is consistency for stress concentration

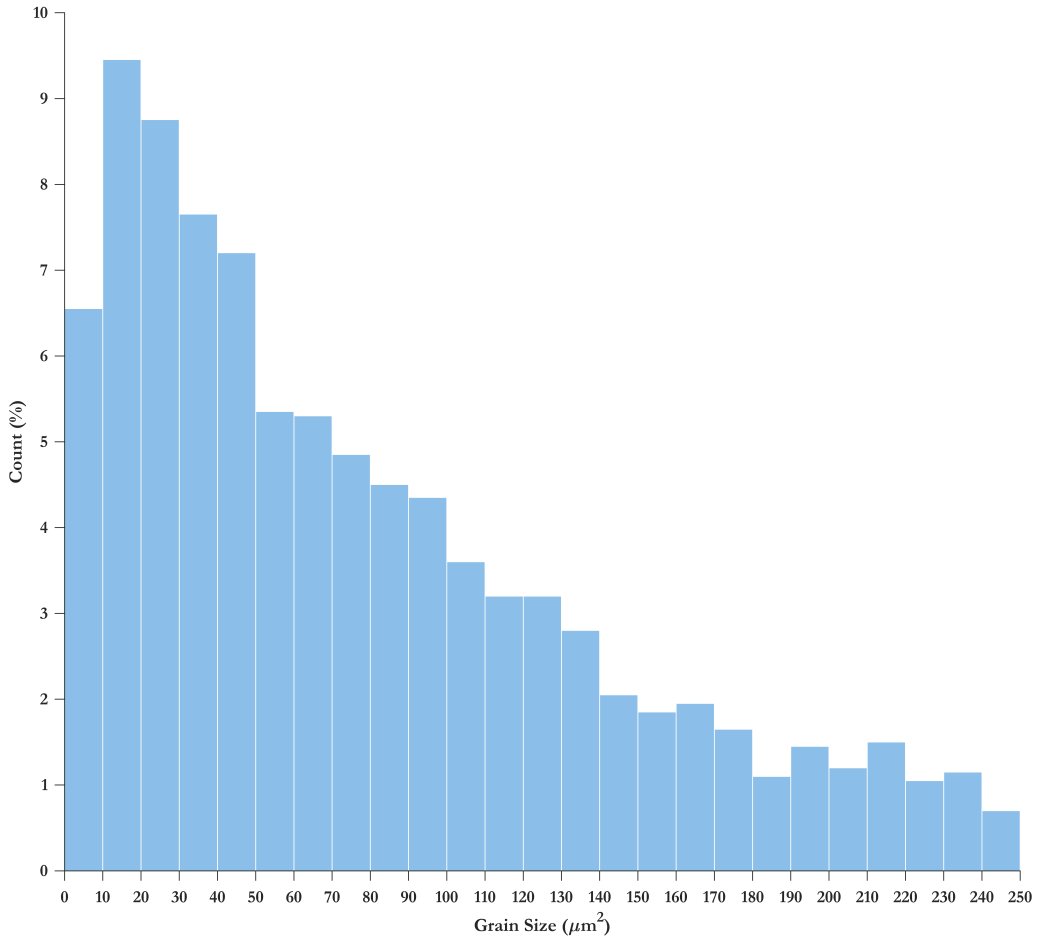


Figure 3.8: *Grain area (μm^2) distribution in Grade 2 CP Ti Foil used in this thesis. (Bins which had less than 0.5% relative count were not included in the histogram, distribution determined with EBSD map from Figure 3.9. Step size of 0.5μm and boundary threshold of 5°)*

locations between samples and it is a relatively simple shape to mill using a FIB. It also allows for the freedom of making the microcantilever at any location and orientation with respect to the surface.

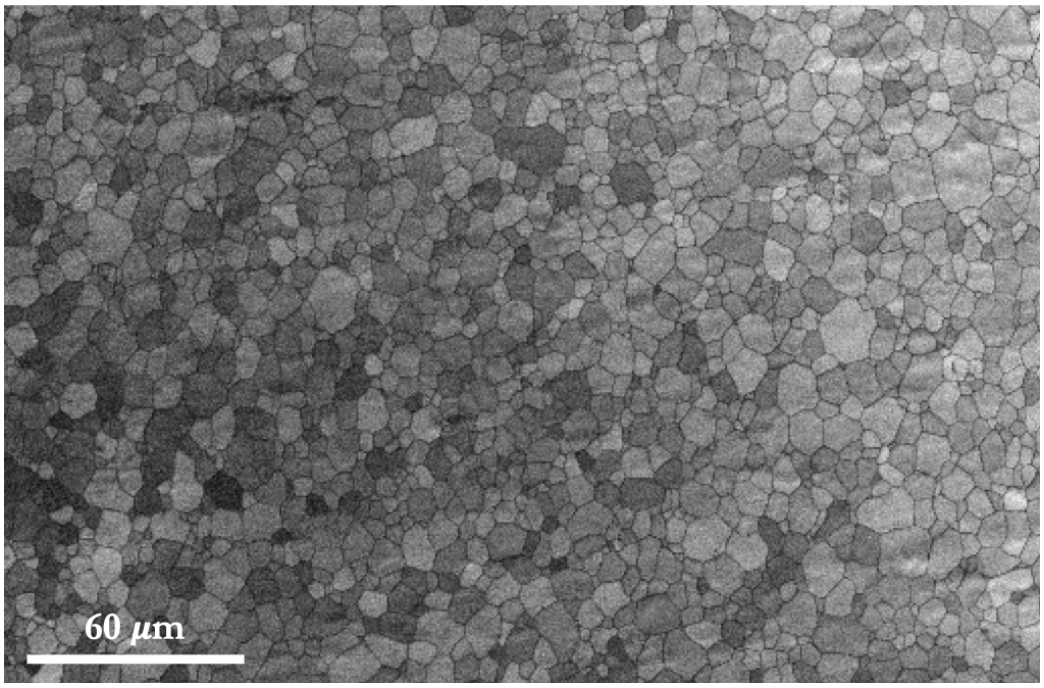


Figure 3.9: *Example of grain shape in Grade 2 CP Ti foil used (EBSD pattern quality image, step size 0.5μm).*

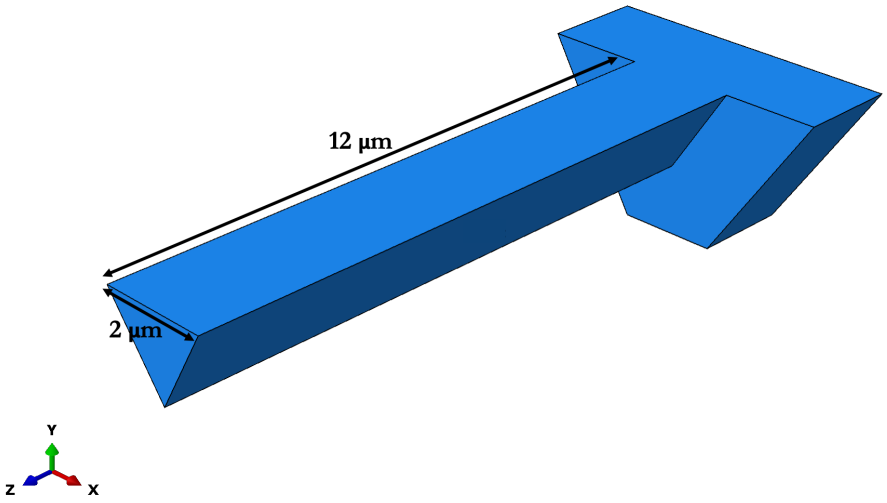


Figure 3.10: *A model of the final microcantilever shape used.*

Convergence Studies

As with the mesocantilever, it is vital to perform convergence studies on the microcantilever model to determine its validity. However, whereas previously the mesh size was the only vari-

able when determining a convergence point, here both the mesh size and the size of the bulk material portion (the base) need to be examined. Once there was only a 1%–2% difference in the result it was accepted that the results converged. Figures 3.11 and 3.12 show the results of these convergence studies. To maximise efficiency of the process, it is best to perform convergence for the size of the base prior to performing convergence of the mesh as that ensures that the number of elements modelled when determining the mesh size is minimal.

When performing convergence studies for the base it is the elastic response of the cantilever that changes most so the difference in stiffness is compared. Conversely, for mesh convergence it is the plastic region that is affected most and so the final load value is compared.

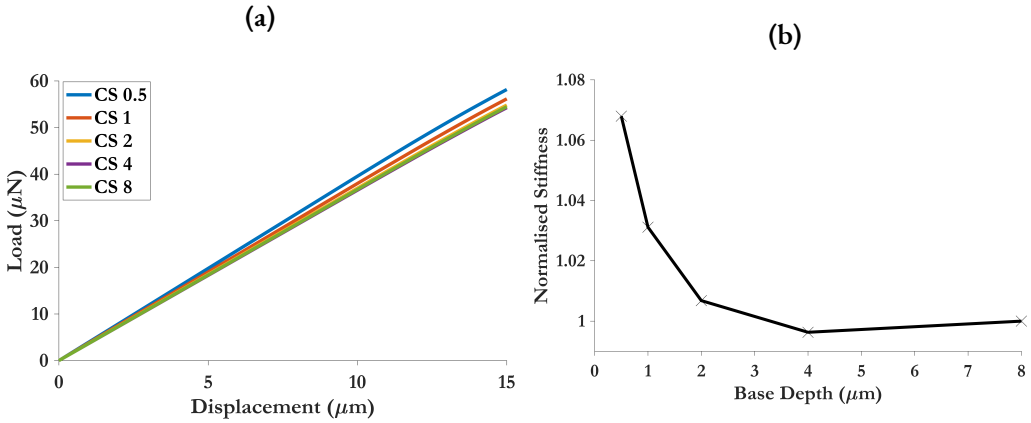


Figure 3.11: *Plots showing Microcantilever FEM Convergence Studies (a) difference in elastic response as a result of changing the depth of the base and (b) normalised stiffness of the different cantilevers.*

Table 3.5: *Dimensions and Stiffness values for microcantilever FEM convergence studies.*

Cantilever	Base Depth	Normalised Stiffness
CS 0.5	0.5	1.068
CS 1	1	1.0312
CS 2	2	1.0068
CS 4	4	0.9963
CS 8	8	1.000

The base convergence was performed with a mesh size of 0.5 μm so as to perform the analyses quickly. From the data in Table 3.5 it can be seen that the difference in stiffness value drops

below 1% once the depth of the base is 2 μm. Therefore, the extra computational time to model a cantilever with a base of 4 μm or 8 μm is unnecessary as there is no significant pay-off in the accuracy of the result. This is useful, as at finer meshes the extra 2 μm can result in a lot more computational work to run an analysis. From Table 3.6, it can be seen that the difference in final load value drops to near a 2% discrepancy at a mesh size of 0.12 μm. At this point, each model begins to change from taking tens of minutes to run to several hours. This makes it not practically viable to perform FEM analysis that tries to fit modelling data to experimental to determine the Young's modulus and CRSS values of the slip systems examined. There is only a difference of 2.4% in the final load calculated between it and the model with a mesh size of 0.07 μm and the time taken to run the analysis is at least an order of ten faster. Therefore, it was decided that the finest mesh size that would be used is 0.12 μm.

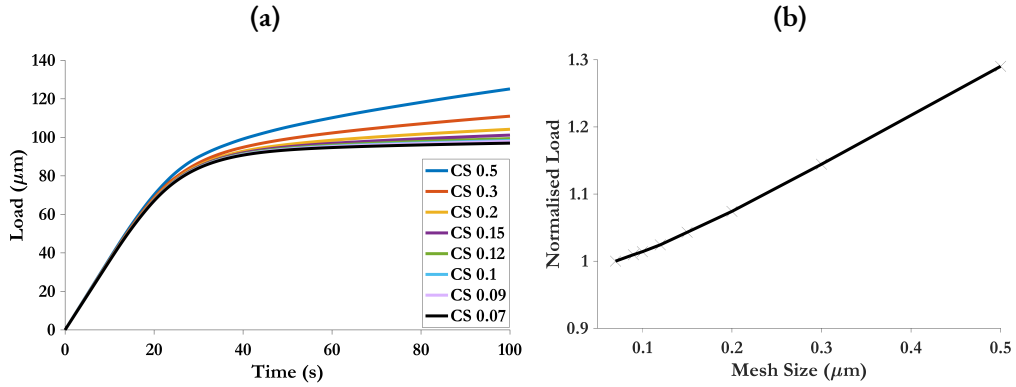


Figure 3.12: *Plots showing Microcantilever FEM Convergence Studies (a) difference in plastic response as a result of changing the mesh size and (b) normalised final load of the different cantilevers.*

Table 3.6: *Mesh size and final load values for microcantilever FEM convergence studies.*

Cantilever	Mesh Size (μm)	Normalised Final Load
CS 0.5	0.5	1.290
CS 0.3	0.3	1.144
CS 0.2	0.2	1.074
CS 0.15	0.15	1.043
CS 0.12	0.12	1.024
CS 0.1	0.1	1.014
CS 0.09	0.09	1.001
CS 0.07	0.07	1.000

3.2 Summary

With a combination of finite element modelling (FEM) and experimental testing, an optimal mesocantilever design for investigating high cycle fatigue properties was obtained. This design is suited to testing conditions and providing information regarding microstructural effects on fatigue properties, as well as, crack initiation sites and the effect on crack path. By using FEM the final design was reached much faster, and at a much lower cost, than if a trial and error method using experimental specimens. In addition, convergence studies were performed on the microcantilever design to ensure that FEM analysis to be conducted in the following chapter were accurate and time efficient.

Chapter 4

Static Loading Material Behaviour

As was mentioned in the testing section of this thesis (2.3) it is important to determine the static properties of the material to give context to the cyclic fatigue properties. In this chapter, the results of macroscale (tensile) testing and microscale (microcantilever) testing will be discussed.

4.1 Tensile Tests

The purposes of these results are two-fold. To measure the static loading behaviour of the material investigated in this thesis (i.e tensile strength) and to determine the strain rate effect on these properties. During cyclic loading, since the tests are performed at 20 kHz, the strain rates are very high ~160/s. As such, it is important to measure this effect so that results from fatigue tests at this speed are evaluated appropriately.

The samples used for tensile testing are the typical dogbone type specimens (Figure 2.2 as shown in the experimental chapter) and are prepared by water-jet cutting. The orientation of the samples are such that the tensile loading direction is parallel to the rolling direction to replicate the orientation of the mesocantilever specimens. Tensile properties are affected by the angle of tensile loading direction to the rolling direction as shown in Table 4.1. Due to the samples for tensile testing being so thin (0.1 mm) and small, attaching strain gauges to them is not possible. Therefore, to measure strain reliably, digital image correlation (DIC) is used. A speckle pattern

(Figure 4.1) is sprayed onto the surface of the sample and the test run as described in Section 2.3.1. A python toolbox, pydic[107], for cross-correlation is used to determine the strain changes in the sample and ParaView[108], also open source, was used to visualise the data produced by pydic. Pydic, uses a reference image (an image of the specimen just before testing begins) to measure the difference in location of detected spots between it and subsequent frames. This displacement is then used to calculate the strain change between frames. As the camera's frame rate (30 ms) during the experiment is known, this strain/frame can be converted into strain/s. The window size used to track points in each frame during DIC analysis was 50 x 50 pixels. In the case of the fine speckle pattern, Figure 4.1(a), this proved to be sufficient to capture speckles as they were smaller than the window size. However, in the case of the 'coarse' speckle pattern, Figure 4.1(b), the area analysed had to be selected so as to ensure a sufficient number of smaller points were captured.

Several tests were performed at several strain rates (pseudo-controlled by the stroke speed) until failure of the specimens. Figure 4.2. The results from these graphs are summarised in Table 4.1.

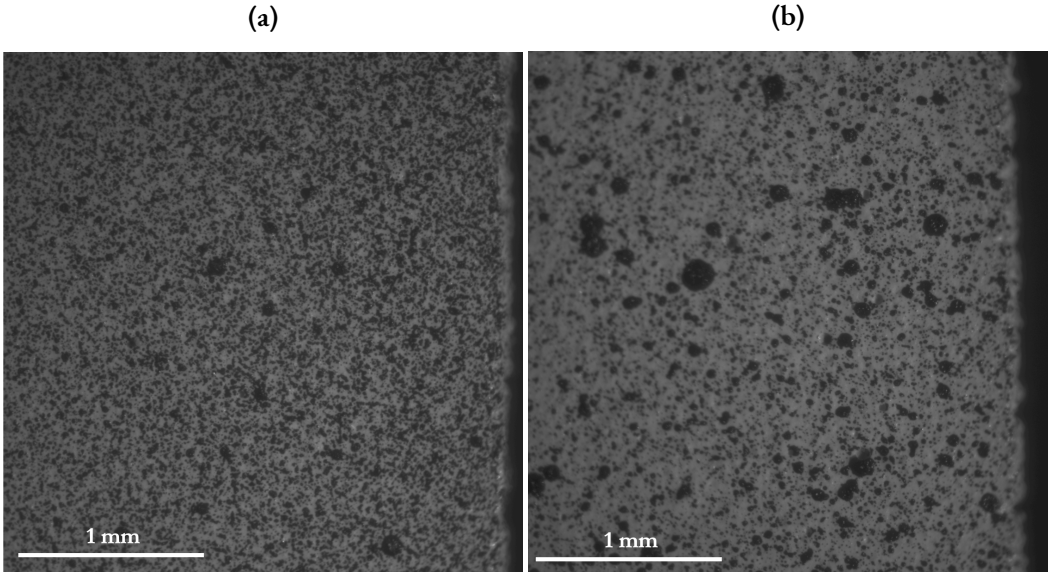


Figure 4.1: *Images showing (a) the fine speckle pattern achieved for the majority of specimens (b) the 'coarse' speckle pattern for the samples tested at a strain rate of 2.0 x10^{-2}.*

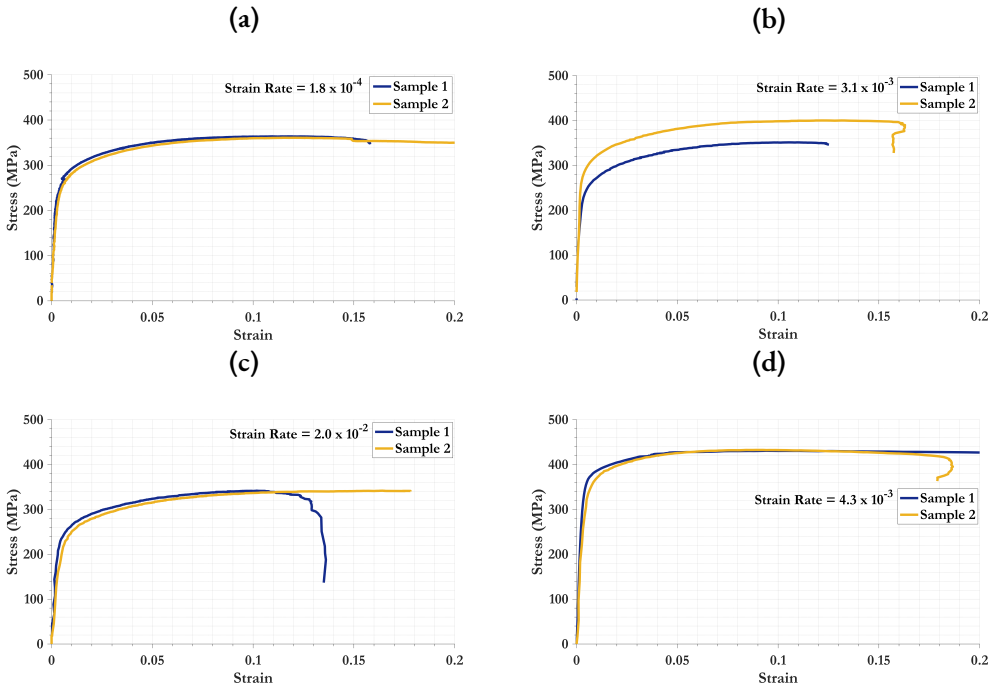


Figure 4.2: *Data showing how the stress response varies with strain rate and sample orientation with respect to the rolling direction in Grade 2 CP Ti. Samples cut parallel to the rolling direction at strain rates of (a) 1.8 x 10^{-4}, (b) 3.1 x 10^{-3}, (c) 2.0 x 10^{-2} and (d) sample cut perpendicular to the rolling direction tested at a strain rate of 4.3 x 10^{-3}*

Table 4.1: *A table showing the effect of strain rate on average Young's modulus, 0.2% Yield Strength and Ultimate Tensile Strength of CP Grade 2 Titanium foil. (RD = tensile specimens cut parallel to the rolling direction, TD = tensile specimens cut perpendicular to the rolling direction).*

	Young's Modulus (GPa)		0.2% Yield Strength (MPa)		Ultimate Tensile Strength (MPa)	
Strain Rate (%/s)	Average	Std Dev	Average	Std Dev	Average	Std Dev
RD 1.8 x 10^{-4}	82	14.50	243	8.49	363	2.12
RD 3.1 x 10^{-3}	115	3.54	265	38.18	376	34.65
RD 2.0 x 10^{-2}	117	-	222	-	342	0
TD 4.3 x 10^{-3}	128	9.90	326	34.64	432	1.41

It can be seen from both Table 4.1 and Figure 4.2 that with an increase in strain rate there is an increase in the Ultimate Tensile Strength (UTS) and 0.2% Yield Strength between the tests performed at a strain rate of 1.8 x 10^{-4} and 3.1 x 10^{-3} as is expected. However, unexpectedly, the samples tested at the fastest strain rate (2.0 x 10^{-2}) has the lowest UTS and 0.2% Yield Strength values. There is also an unexpected discrepancy in Young's modulus. The sample tested at the slowest strain rate has a significantly lower measured Young's modulus compared to the other two strain rates. This is unexpected, as Young's modulus is an intrinsic material property that is not expected to decrease with decreasing strain rate.

The unexpected results outlined above could be due to several issues during testing. UTS could have been affected by damage variation during water-jet cutting of the tensile specimens. Since the specimens are only 100 μm thick any variation in edge finish will have significant impact on the measured UTS between specimens. In addition, the specimens are comparatively long compared to their thickness. This means that during the setup of the experiment there is an increased risk of unintentional straining and torsion that will have a negative effect on the 0.2% Yield Strength and UTS values measured. In regards to the anomalous Young's modulus measurement, this may be a result of the limitations of the experimental method used to determine this value. One such limitation is that of the camera used. The tests that produced the anomaly were performed first and the camera may not have been fully operational at this stage as it was still in the process of 'warming up'. This could have resulted in the capture of images being unstable and not in fact being at 30 ms as input in the software but, rather, slightly quicker. If, for example, the frame rate was just 3 ms faster than the intended frame rate the measured Young's modulus would be 10% lower than the actual value.

4.1.1 Strain Rate Sensitivity

In order to best put into context the results obtained in the ultra-fast high cycle fatigue experiments outlined later in this work, it is important to consider the strain rate sensitivity of the material being examined. Literature has shown that titanium experiences strain rate sensitivity

that can appreciably alter the measured flow stress at different strain rates. Both Meyers et al[109] and Chichili et al[110] showed that with increasing strain rates there is an increase in flow stress. Chichili et al's work on α-titanium showed that at strain rates in the order of 10^0 s^{-1} the flow stress was ~500 MPa whilst at strain rates in the order of 10^3 s^{-1} the flow stress was ~600 MPa. This is a significant increase. By first calculating the strain rate sensitivity of the tested CP-Ti, it will then be possible to determine the flow stress at the ultrasonic testing strain rate of 500 s^{-1} using the equation:

$$\ln\sigma = m \cdot \ln\varepsilon + c \tag{4.1}$$

Here, σ is the flow stress, m is the strain rate sensitivity, ε is the strain rate and c is a constant. The strain rate sensitivity measured from the tensile tests described above was 0.0124 (with c = 6.0579). This is in line with literature values for titanium and titanium alloys[111][112]. The strain rate sensitivity measured by Lee et al[113] was 0.019 for Grade 2 CP-Ti. The grain size in their Grade 2 CP-Ti was of a similar scale as the one tested in this work (13.8 μm). This finding is in good agreement with the strain rate sensitivity determined in this work. Luan et al[112] found that the strain rate sensitivity ranged from ~0.006 to ~0.070. This strain rate sensitivity was also found to be dependent on grain size and texture. Where soft grains were more dominant then the strain rate sensitivity was lower, whilst hard grain dominant microstructures had the higher strain rate sensitivities. Lee et al[113] also found that with increasing presence of oxygen there was a decrease in strain rate sensitivity. Using the value for strain rate sensitivity outlined above (0.0124) the flow stress as estimated for the ultrasonic test strain rate was 455 MPa. This result is noticeably lower than the HCF strength measured in chapter 5. This suggests that the tensile test to determine the SRS was not successful and that a more accurate method should be used instead due to the nature of the specimens involved. It will be recommended in the future work section at the end of this thesis that strain rate jump tests should be performed directly on the mesocantilevers themselves as this will provide a more accurate SRS value.

4.2 Microcantilever Tests

On the other end of the size scale in this thesis are microcantilevers that provide useful information in regards to individual grain strength in different orientations. In this section, the <c+a> first order pyramidal, <a> basal and <a> prism slip systems are investigated. Figure 4.3 is a diagram of an hcp crystal with the slip systems investigated highlighted.

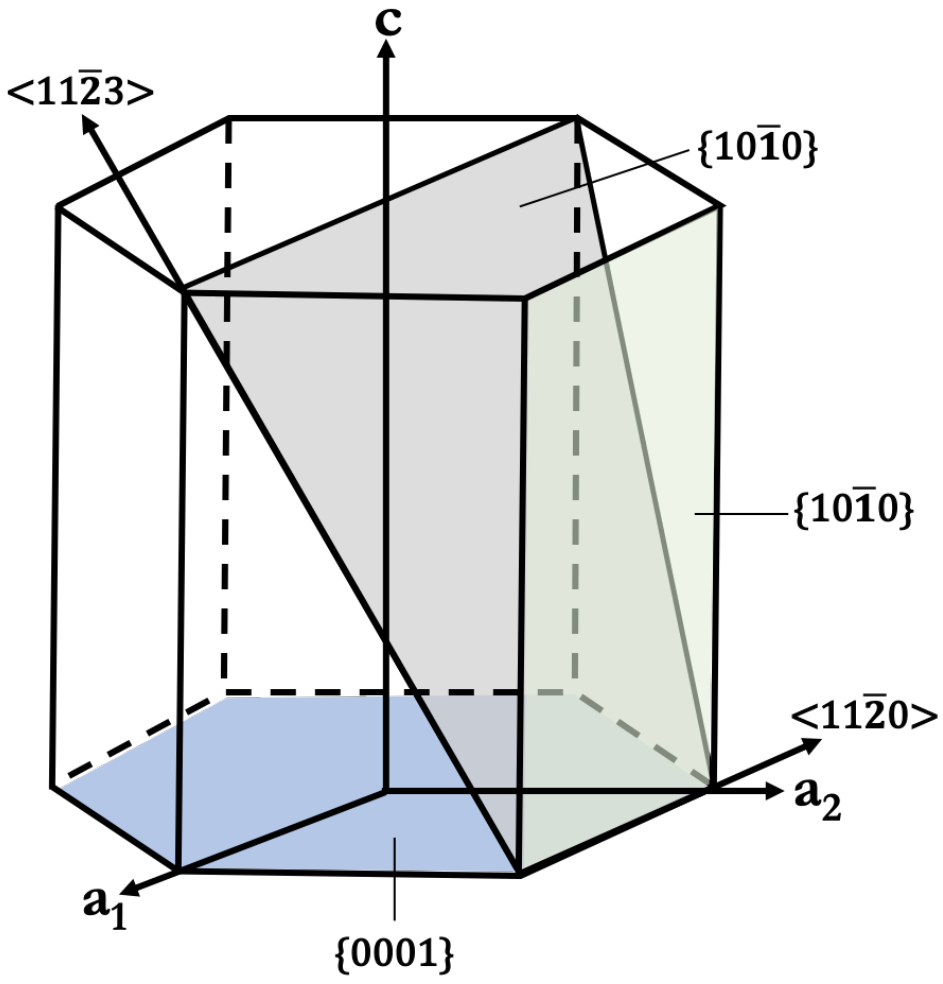


Figure 4.3: *A diagram of an hcp crystal with the <a> prism (green), <a> basal (blue and <c+a> first order pyramidal (grey) slip systems highlighted.*

Understanding the strengths of these individual grains is important when rationalising the overall performance of the material. Particularly when attempting to contextualise the fatigue properties measured in Chapter 5. To simply use the data from macro-specimens like those

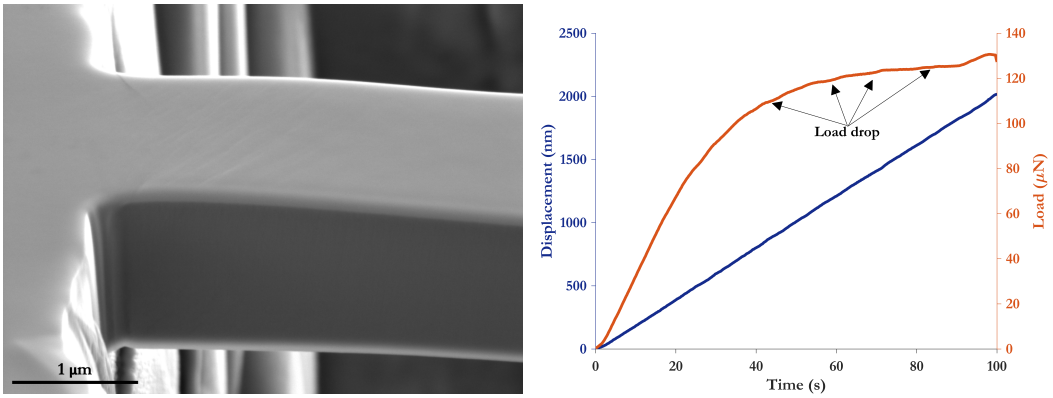
used for tensile testing would not give a true picture of the materials strength as by their nature their stress and plastic behaviour is heterogeneous. This is due to local microstructural effects, namely the 'hard-soft' grain interactions mentioned in the literature review. It is precisely this heterogeneity that is a major factor in the failure process. Therefore, to determine the critical resolved shear stress (CRSS) of each individual slip system microcantilevers must be prepared within grains of the correct orientation using a focussed-ion beam. All microcantilevers machined in this thesis had a triangular cross-section. This provides the user with two degrees of freedom and, therefore, allows for a greater choice of grains to be selected as the long axis of the beam can then point in any direction parallel to the sample surface plane. To ensure that the desired slip system was activated, it was key to maximise the Schmidt factor of the target whilst minimizing the resolved shear stress for the others.

For <a> prism slip – $<11\bar{2}0>10\bar{1}0$ – the beam direction was perpendicular to the <c> axis whilst one of the prismatic planes was at 45° to the beam direction. This meant the resulting Schmidt factor was 0.5 for this slip system with the next highest Schmidt factor (0.25) also belonging to an <a> prism system. For <a> basal slip – $<11\bar{2}0>0001$ the <c> axis was 45° to the beam direction as was one <a> slip direction. With this orientation, the Schmidt factor was 0.5 for <a> basal and, as with <a> prism oriented grains, the second highest Schmidt factor (0.25) was for an <a> prism slip system. For <c+a> first order pyramidal slip – $1/3\ <11\bar{2}3>10\bar{1}1$ – the beam direction was parallel to the <c> axis with an <a> slip direction perpendicular. In the case of microcantilevers machined to test <c+a> first order pyramidal slip, even though the direction and plane are not angled at 45° away from the beam direction it still has the highest Schmidt factor (0.40). Furthermore, the Schmidt factor for any <a> type slip system is 0. To confirm activation of all three slip systems after testing, SEM images were taken to observe the slip traces formed and match them appropriately. These images can be seen in Figure 4.4. The formation of these slip traces can also be associated with load drops and strain bursts as is also shown in Figure 4.4. As slip bands form, load is shed as a result, the larger the load drop, the more intense the resulting slip band. At the same time, there is a corresponding strain burst as a result of this plastic

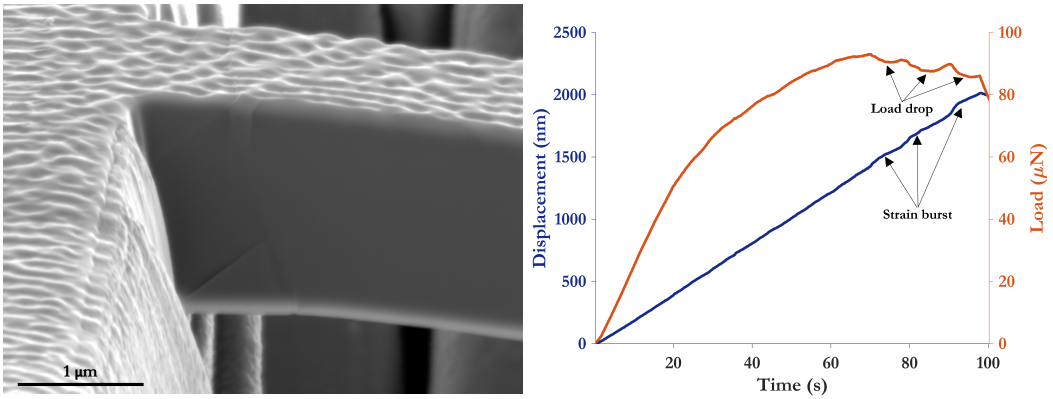
response. This was observed in the cases of the microcantilevers tested in this work. In Figure 4.4(a), the load drop and strain bursts in the <a> basal microcantilever are comparatively low and are harder to notice on the plot than those of <a> prism. Prior to yielding, the stiffness was 0.18 $\mu N\ nm^{-1}$ whilst just after the load drops it was a significantly lower 0.05 $\mu N\ nm^{-1}$. This affirms that the microcantilever is still undergoing plastic deformation after the slip band forms. There are multiple points that could be associated with slip band formation and this is reflected in the SEM image where there are multiple faint slip bands on the tensile surface of the microcantilever. In the case of the <a> prism cantilever, Figure 4.4(b), there are three clear points on the plot that can be defined as load drops/strain bursts, these may also correspond with the three intense slip bands observed for this microcantilever. The larger load drops correspond with higher measured post-drop stiffnesses. The first load drop has a post-drop stiffness of 0.021 $\mu N\ nm^{-1}$ whilst the second, larger, load drop's post-drop stiffness is 0.033 $\mu N\ nm^{-1}$. The post-drop stiffness as a proportion of the stiffness in the elastic region is lower for the <a> prism microcantilever than the <a> basal microcantilever. This suggests that there is a positive correlation between the intensity of slip bands and the size of the load drop but an inverse correlation between slip band intensity/load drop size and the post-drop stiffness. Consequently, it can be theorised that with the formation of larger slip bands, the plastic response that occurs after this event is greater than before the appearance of slip bands. These correspond with the three intense slip bands that are seen in both the tensile and compressive surfaces of the microcantilever. One is confined to the tensile surface, one to the compressive and one appears to extend from one surface to the other. For <c+a> first order pyramidal slip, the load drops and strain bursts are lower than <a> basal but slightly higher than the <a> prism slip case. However, they are again small drops/bursts and there are significantly more of them as can also be confirmed by the larger number of faint slip traces in the corresponding SEM image. The displacement vs time plot also confirms that the actual displacement rate is very close to the target displacement rate of 20 $nm\ s^{-1}$, outside of the strain burst moments.

The target Euler angles for the three slip systems are outlined in Table 4.2. Following Euler

(a)



(b)



(c)

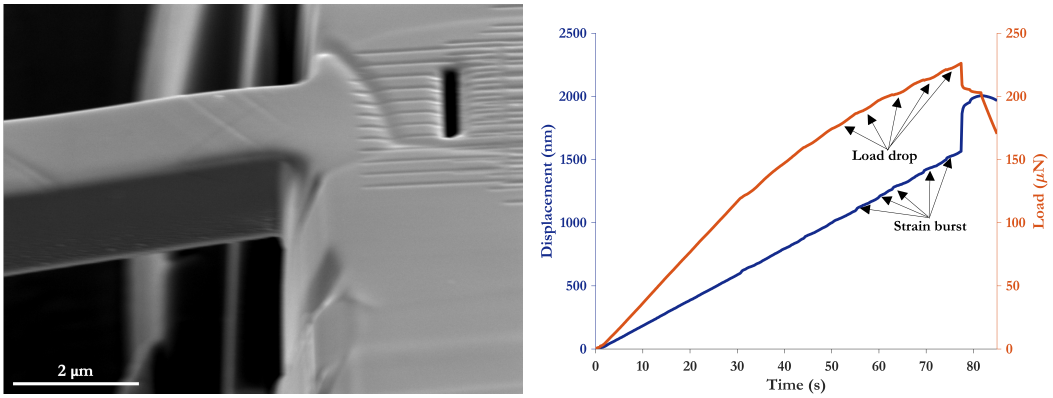


Figure 4.4: *Slip traces and associated load drop-strain burst plots for (a) <a> basal, (b) <a> prism, (c) <c+a> first order pyramidal.*

notation convention, phi 1 is rotation around the y–axis (see Figure 4.5 for axis directions), PHI is a rotation around the newly defined x–axis and phi 2 is a rotation around the newly defined

Table 4.2: *Target grain orientation in terms of Euler angles for activating <a> basal, <a> prism and <c+a> slip systems.*

	Euler Angles (degrees)		
Slip System	phi 1	PHI	phi 2
<a> basal	0–360	45	30, 90, 150 210, 270, 330
<a> prism	0–360	90	15
<c+a> first order pyramidal	0–360	90	0

y–axis. In all cases, a positive rotation corresponds to a an anti-clockwise rotation. As the foil used was cold rolled it was quite textured in nature and as such it was difficult to find grains well oriented for activation of <c+a> first order pyramidal and <a> prism slip. Likewise, finding grains perfectly oriented for <a> basal was also improbable. Therefore, a slight deviation in targeted Euler angles was accepted. For <a> prism slip systems this tolerance was ±2° for PHI and ±2° for phi 2. For <a> basal slip it was ±3° for PHI and ±3° for phi 2. For <c+a> first order pyramidal slip it was ±3° for PHI and as high as ±10° for phi 2 due to the difficulty of finding grains oriented for this type of slip. In one case, due to constraints in finding a suitably oriented and sized grains for <a> basal slip systems, the phi 2 angle was 15° away from the target. However, this posed no issue as the PHI angle was more important in maximising the chances of activating the <a> basal slip system and the activation was confirmed using slip trace analysis. Examples of the ideal orientation scenarios for each slip system can be seen in Figure 4.5.

4.2.1 Determining the Elastic Modulus and Critical Resolved Shear Stress

To determine the critical resolved shear stress (CRSS) and the elastic modulus a combination of experimental data and finite element modelling can be used. This is achieved by fitting modelling data to experimental data. The microcantilever model was created using ABAQUS and the constitutive equation included in the literature review(Equation 1.4) from Dunne's physically based crystal plasticity model[71] was written into a user element subroutine.

The cantilevers are manufactured using a FIB as described in Section 2.2.3. The target di-

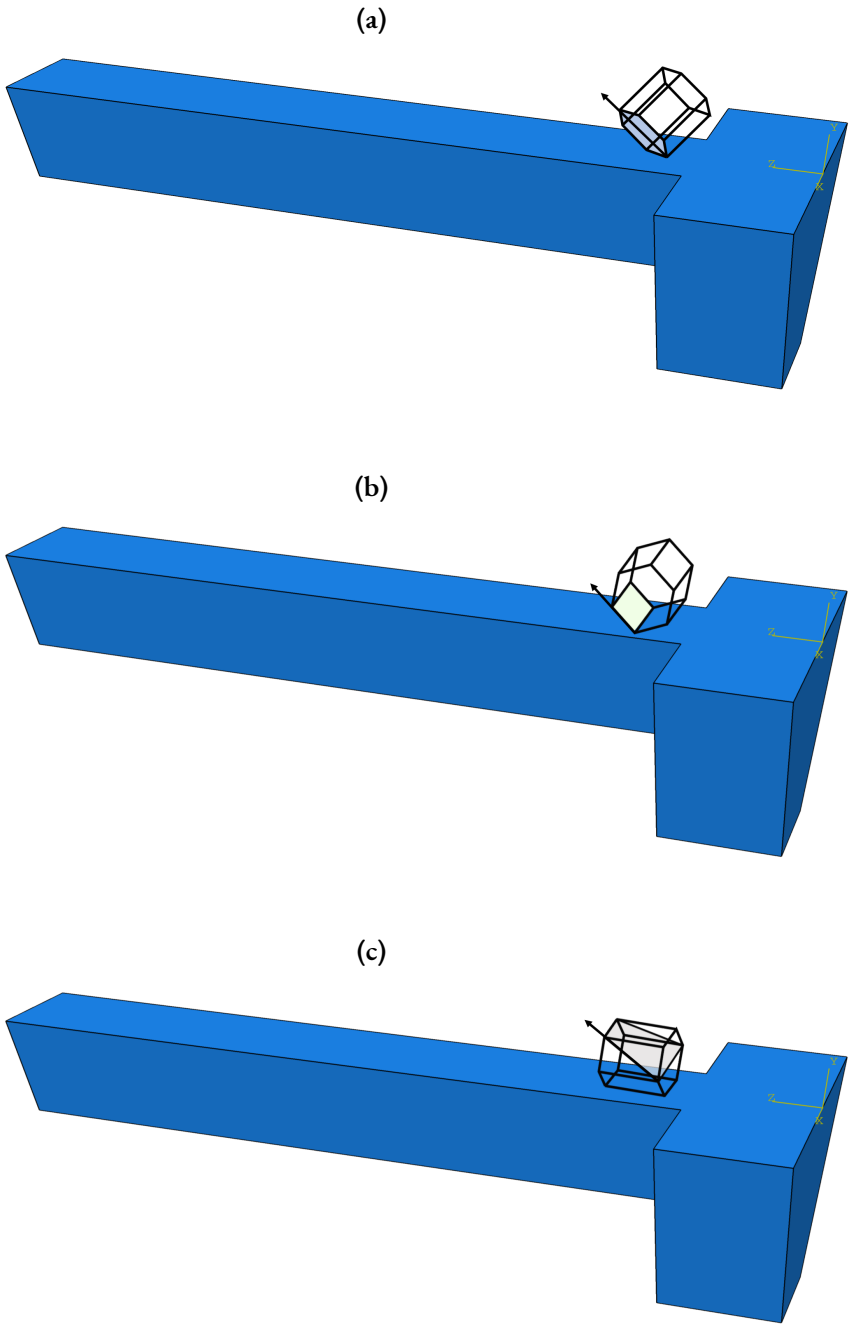


Figure 4.5: *Examples of the ideal microcantilever orientation scenarios for the three examined slip systems (a)<a> basal, (b) <a> prism and (c) <c+a> first order pyramidal.*

mensions of the microcantilevers are 2 μm x 12 μm x 2 μm (Width x Length x Thickness, W x L x B). Using a combination of nanoindentation, for reference marks, and EBSD analysis grains were carefully selected in order to test the target slip systems. The nanoindent reference marks

were made at a depth as shallow as possible to minimise the size of strain fields in the surrounding grains. Nevertheless, microcantilevers were made as far from the reference marks as possible and never in the grains immediately surrounding these indents. Figures 4.6 show the EBSD maps with the grains tested outlined and Table 4.3 shows the orientation information for the grains tested. Though care was taken to get final microcantilevers machined into as close to the target dimensions as possible, machine/gallium source performance means that the final dimensions vary slightly between microcantilevers. In all cases, a maximum variation of ± 5% in the width and length was tolerated. As such, it was vital to take final measurements to determine the width, length and thickness of the microcantilever as variation in the final thickness has a large effect on the load/displacement response of the microcantilever. Consequently, every model's dimensions were changed to fit those of the experimental microcantilever exactly to ensure accurately determined CRSS and elastic modulus values. Fitting of the model to the experimentally obtained data was a two-step process. The first step was to fit the elastic region and the second the plastic region. Both steps utilised an iterative process of fitting. For elastic fitting the model was run for a time period that corresponded to a deflection of 0.3 μm. This captured the majority of the elastic response whilst also minimising computer work-load to enable multiple iterations to be run quickly. Once the calculated stiffness of the model cantilever was within 1% of the experimental value it was accepted. This modulus value was then taken forward into the fitting of the plastic region. Fitting for the plastic region was conducted by determining the CRSS value that gave the smallest root mean squared difference between the model and experiment's load-displacement curves. The equation used was:

$$\eth = \left\{ \frac{\int_0^D \left[P_{\text{exp}}(x) - P_{\text{model}}(x) \right]^2}{D} \right\}^{\frac{1}{2}} \tag{4.2}$$

Here, P_{exp} and P_{model} are the experimental and model loads at a deflection of x of the microcantilever. D is the maximum deflection in the process and is set at 1.1 μm to avoid influence of the load drops seen at larger strains. Up to this deflection point, plasticity only occurred in the

compressive part of the microcantilever (i.e the bottom part). The goodness of fit for the plastic region was evaluated by determining which CRSS value gave the lowest root mean squared deviation. Once the root mean squared deviation was at its minimum the CRSS value was accepted.

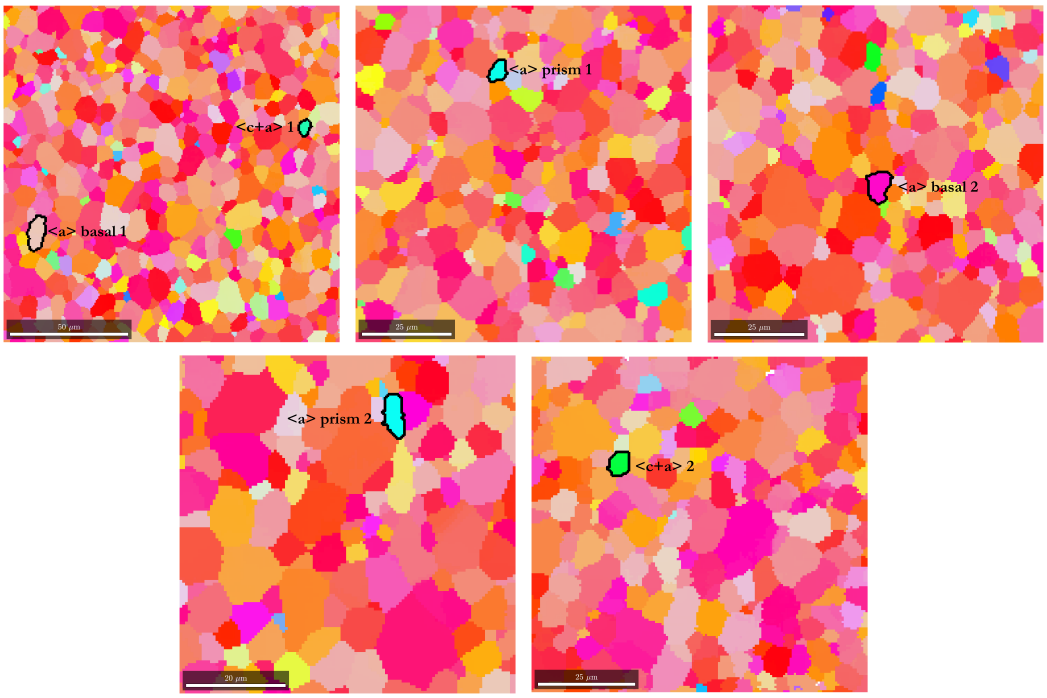


Figure 4.6: *IPFZ maps indicating the nine grains selected to analyse the modulus of microcantilevers where specific slips systems are activated and the CRSS of three slip systems in question (<c+a>, <a> prism and <a> basal).*

Two cantilevers were made for each slip system. Using a nanoindenter, each microcantilever is deflected to a depth of 2000 nm. Contact between the indenter tip and the microcantilever beam is targeted at 90% along the length of the beam from the fixed end (10.8 μm) to ensure that the beam's behaviour did not deviate strongly from simple beam theory.

The load vs displacement curves along with the FEM fitting for each slip system can be seen in Figure 4.7. In Figure 4.7 the elastic and plastic responses of the microcantilever beams to loading can be seen. In the case of <a> basal slip (Figure 4.7a) at ~0.4 μm deflection the cantilever begins to visibly yield as the microcantilever begins to experience plastic deformation. Up to this yield point the behaviour of the microcantilever is elastic as categorised by the linear relationship between load and displacement. By calculating the gradient of this portion, the elastic modulus

Table 4.3: *Orientations of grains selected for determining the modulus modulus of microcantilevers where specific slips systems are activated and the CRSS of three slip systems in question (<c+a>, <a> prism and <a> basal).*

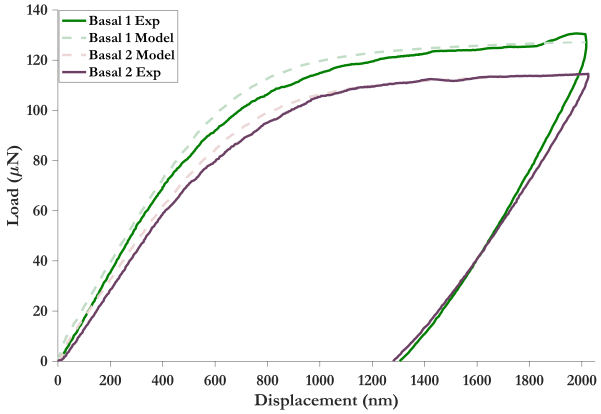
Grain ID	Slip System	phi 1 (degrees)	PHI (degrees)	phi 2 (degrees)
<a> prism 1	<a> prism	7	91	346
<a> prism 2		13	91	347
<a> basal 1	<a> basal	353	43	30
<a> basal 2		336	46	14
<c+ a> 1	<c+a>	1	87	352
<c+ a> 2		357	90	2

Table 4.4: *The calculated Critical Resolved Shear Stresses of <a> basal, <a> prism and <c+a> first order pyramidal slip systems.*

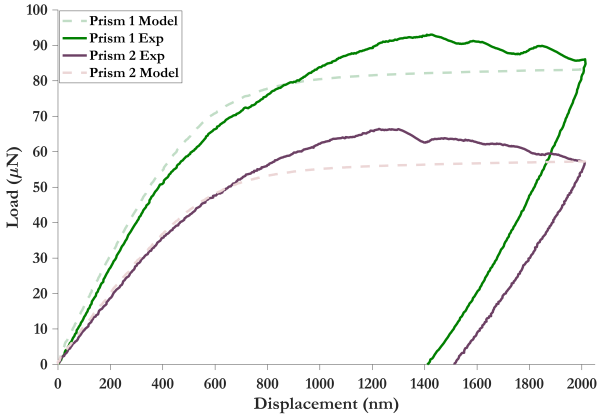
	Critical Resolved Shear Stress (MPa)			Standard Deviation (MPa)
Slip System	Cantilever 1	Cantilever 2	Average	
<a> basal	526	530	528	3
<a> prism	360	380	370	14
<c+a>	1025	860	943	117

of the microcantilever can be obtained. When the <a> basal and <a> prism slip systems were activated the average elastic moduli of the microcantilevers measured were 114 GPa (±5.66 GPa) and 102 GPa (±5.66 GPa). For microcantilevers where <a> prism slip was activated, Figure 4.7b, the elastic response is quite similar to that of microcantilevers where <a> basal slip is activated with the elastic region of the former ending shortly before the observed response of the latter. This was seen to be at ~0.38 μm. In the case of microcantilevers where <c+a> first order pyramidal slip is activated, the elastic region is much larger than that of microcantilevers where <a> basal and <a> prism slip systems are activated. This is due to the well-documented elastic anisotropy of hexagonal materials. In addition to choosing grains with the appropriate orientation, to activate <c+a> first order pyramidal slip cantilevers were tested along the <c> axis, whereas to activate <a> basal or <a> prism slip cantilevers were tested along the <a> axis. Literature has shown that materials tested along the <c> axis are much stiffer than those tested along the<a> axis[73, 114]. The final determined CRSS of the slip systems and Young's modulus of the microcantilevers investigated are displayed in Table 4.4 and Table 4.5 respectively.

(a)



(b)



(c)

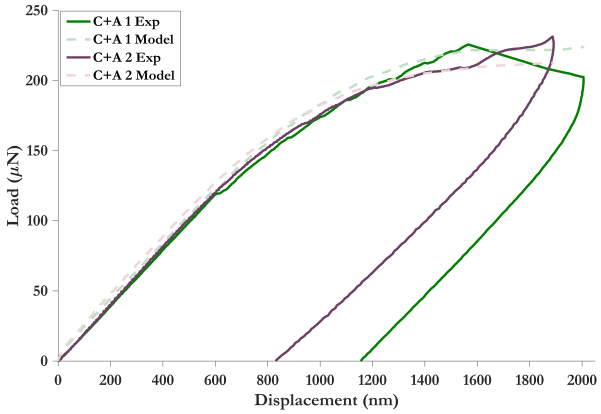


Figure 4.7: *Experimental and Finite Element Modelled load-displacement curves for microcantilevers for the* ***(a)*** *<a> basal,* ***(b)*** *<a> prism and* ***(c)*** *<c+a> first order pyramidal slip systems.*

Table 4.5: *The calculated Young's modulus of microcantilevers where <a> basal, <a> prism and <c+a> first order pyramidal slip systems were activated.*

	Young's Modulus (GPa)			Standard Deviation (GPa)
Slip System activated	Cantilever 1	Cantilever 2	Average	
<a> basal	118	110	114	6
<a> prism	96	108	102	8
<c+a>	158	166	162	6

As was demonstrated by Gong and Wilkinson[74], there is a clear relationship between microcantilever width and measured CRSS. As was mentioned in Section1.4 of the literature review, the equation that relates the size effect with CRSS is:

$$\tau_y = B w^m \tag{4.3}$$

τ_y is the CRSS value, B is a material strength parameter, w is width and m is an exponent dependent on the material. The modified equation,that elucidates the bulk single crystal CRSS, determined by Gong and Wilkinson is:

$$\tau_y = \tau_0 + A w^n \tag{4.4}$$

The exponent value, n, for CP Ti was determined to be -1 and the material constant A to be 461 Pa m[74]. These are the values that will be used when extrapolating the CRSS of bulk specimens from the results achieved in these microcantilever tests. Table 4.6 summarises the bulk CRSS values obtained from the microcantilever tests. The calculated bulk CRSS value for <a> prism slip is slightly higher to that achieved by Gong and Wilkinson[74] but this is expected as their work was on Grade 1 CP Ti, whilst the slightly higher oxygen content of the Grade 2 CP Ti used in this thesis results in slight hardening.

Table 4.6: *The experimentally determined Critical Resolved Shear Stresses for <a> basal, <a> prism and <c+a> first order pyramidal slip (τ_c) and corresponding extrapolated bulk values τ_0*

	Critical Resolved Shear Stress (MPa)	
Slip System	Average τ_c	τ_0
<a> basal	528	298
<a> prism	370	130
<c+a>	943	795

4.3 Summary

By conducting both macroscale tensile tests and microcantilever bending tests the static properties on these two length scales has been determined for the CP Grade 2 Titanium foil investigated in this thesis.

Macroscale tensile tests provided important data for comparing the results obtained in the later fatigue tests of mesoscale specimens. Investigating the effect of strain rate on tensile properties, using DIC, showed that an increase in strain rate from the order of 10^{-4} to 10^{-3} resulted in a higher measured 0.2% Yield Strength and UTS. Literature has supported this observation[115]. However, in the case of the strain rate tests conducted at 10^{-2} this trend is not seen. Some literature suggests that there can be a slight reduction in tensile properties before increasing again at higher strain rates[116]. It will therefore, be assumed that at the much larger strain rates of the ultrasonic fatigue tests, tensile properties will be higher than those presented for the static loading cases here. A combination of finite element modelling and experimental data for microcantilevers determined the elastic and plastic strengths of three individual slip systems - <a> basal, <a> prism and <c+a> first order pyramidal. These results, showed that <a> prism is the weakest of the three (with an elastic modulus along the length axis of the cantilever of 102 GPa and bulk CRSS of 130 MPa) and that slip is most likely to occur in <a> prism grains first. This is further supported by the failure mechanism in macroscale tensile tests with the fracture being at 45° to the load direction along the sample surface. The microcantilever tests also gave rise to bulk properties for each slip system. This data can also be used to contextualise the data that will be presented in Chapter 5.

Chapter 5

Fatigue Properties

In this chapter the high cycle fatigue properties will be discussed i.e how specimen life varies with applied stress. In addition, data on crack growth rate will be presented before concluding with analysis of the fracture surfaces and how they can give insight into crack initiation sites and the path the crack took through the bulk before failure.

5.1 Stress-Life Data (S-N curves)

As was mentioned in previous chapters, the route to obtaining S-N data required multiple steps prior to the results presented here. Specimen designs were determined by a combination of FEM and experimental testing, as described in Section 3.1.1. If samples were to be analysed using EBSD they were first electropolished as described in Section 2.2.4. Not all samples were electropolished or were analysed using EBSD prior to testing as this would require a great deal of time that would not be practical for the ~250 specimens that were tested. It was also vital to perform calibration studies (described in Section 2.3.2) for each specimen as sample thickness and finishing varied, particularly for samples that were electropolished, which would result in different stresses being experienced at the same vibrational amplitude. All mesocantilever samples were prepared by laser cutting as described in Section2.2.

5.1.1 Calibration of Cantilever Deflection

The applied vibrational amplitude should have a linear relationship with deflection of the mesocantilever. Spreading of a laser reflection spot was used to measure this deflection providing a calibration of amplitude requested in the computer software with the real amplitude experienced by the sample. In order to calculate this, however, FEM analysis needs to be performed on a mesocantilever to determine the deflection angle of the beam and maximum stress experienced at a given applied vibration amplitude. The FEM model was run at two different vibrational amplitudes - 10 μm and 40 μm. To determine the deflection angle of the beam in the model, the distance between the nodes at the end of the hammer and the beginning were measured. (These locations are shown in Figure 5.1).

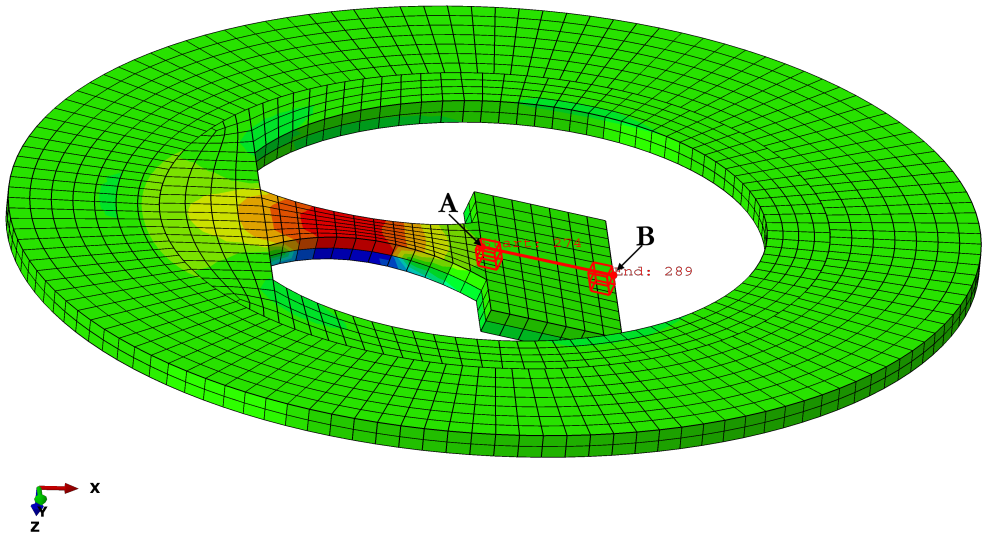


Figure 5.1: *The two points on the hammer between which displacement in the x and z directions are measured.*

The differences in distance along the x–axis and along the z–axis of the two nodes (A and B in Figure 5.1 were obtained for the FEM model at maximum deflection and the deflection angle obtained from:

$$\text{FEM Deflection Angle} = \arctan\left(\frac{\text{z displacement}_A - \text{z displacement}_B}{\text{x displacement}_A - \text{x displacement}_B}\right) \tag{5.1}$$

Likewise, to measure the experimental deflection angle the following equation is used:

$$\text{Experimental Deflection Angle} = \arctan\left(\frac{L_{amp}}{L_{WD}}\right) \tag{5.2}$$

Here L_{amp} is the deflection amplitude of the laser spot after reflecting from the sample hammer and L_{WD} is the distance between the laser and the sample hammer (in the case of this thesis L_{WD} was kept fixed at 46.3 cm). Figure 2.6 in Chapter 2 depicts the setup used. Looking at Figure 5.2 it can be seen that the relationship between deflection angle and vibrational amplitude in both the model and experimentally are linear.

With a larger deflection angle it follows that there is also an increase in maximum stress as the sample is going through larger amounts of deformation. Understanding the relationship of this change is key in determining the stress the mesocantilever experiences at each vibrational amplitude. Therefore, the change in maximum stress as a function of deflection angle in the FEM was plotted (Figure 5.3).

Using the gradients of these three plots, the stress applied experimentally can be determined using the equation below.

$$\sigma_{exp} = DA_{exp} \times n_{model\sigma vsDA} \tag{5.3}$$

Here, σ_{exp} is the experimental stress at a given amplitude DA_{exp} is the deflection angle seen in the experiment for a given amplitude and $n_{model\sigma vsDA}$ is the relationship between stress and deflection in the model (i.e the gradient of the plot in Figure 5.3).

As can be seen in Figure 5.2b the representative experimentally determined value of n, 2.4 x 10^{-3} radians is different from the value determined by the model – 2.6 x 10^{-3} radians. This was seen across all physical specimens regardless of whether it was electropolished or not. The physical specimens also exhibited a scatter in deflection angles (ranging from 2.2 x 10^{-3} radians to 2.8 x 10^{-3} radians at the same vibrational amplitude). This observation could be the result of several aspects, namely - variations in sample thickness or dimensions, pinning of the specimen

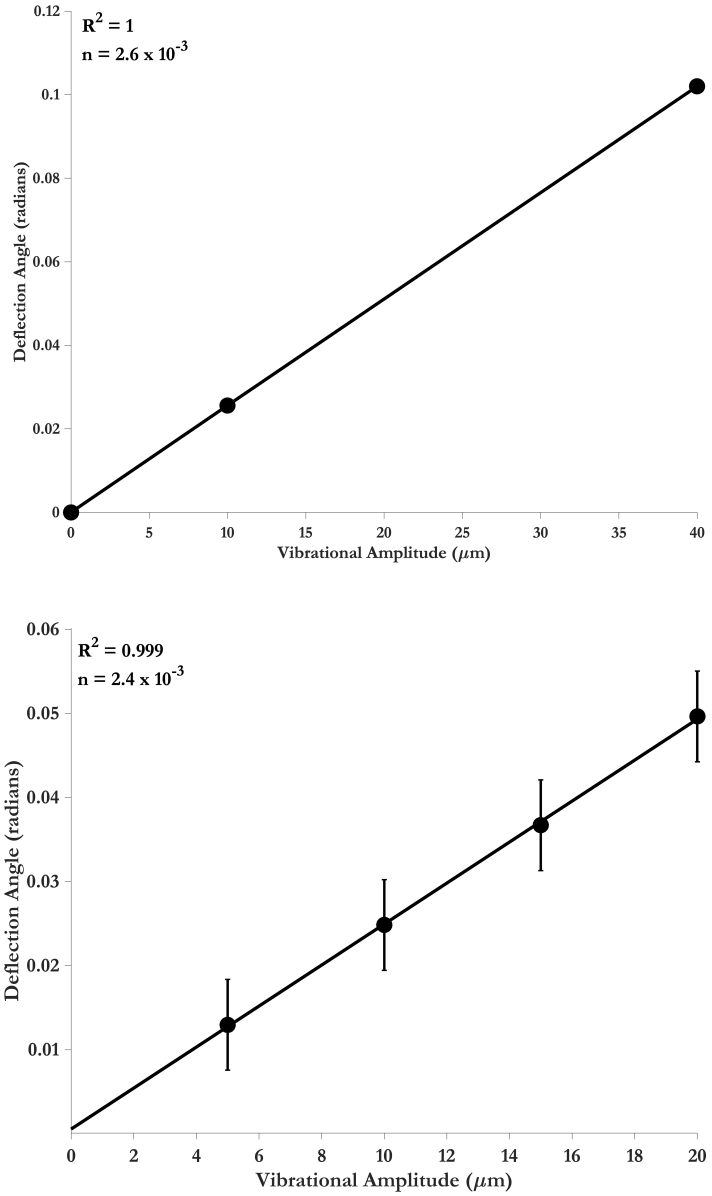


Figure 5.2: *Plots showing the deflection angle of the mesocantilever beam as a function of vibrational amplitude both (a) in a finite element model and (b) a representative experimental dataset.*

and even individual sample density and stiffness. The larger the deflection the thinner or less stiff the sample was. The mean deflection angle was 2.4 x 10^{-3} radians with a standard deviation of 2.50 x 10^{-4} which corresponds to ~10% variation in stresses applied. The mean deflection angle being slightly smaller than that of the model suggests that the issue lies with clamping of the specimen. This deviation is quite large and Figure 5.4 shows how this variation in stress can

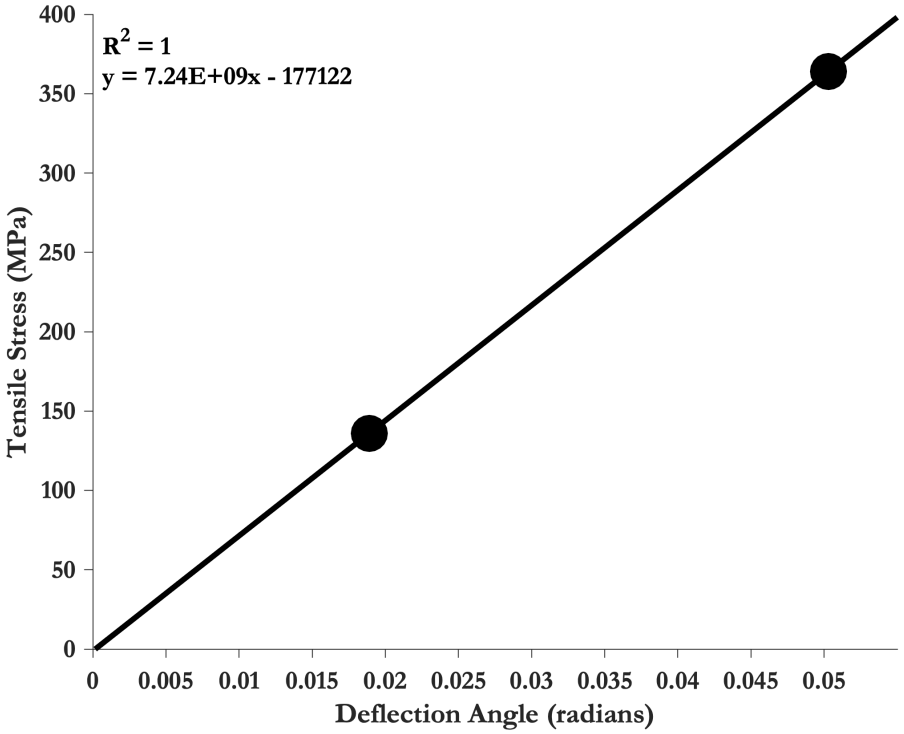


Figure 5.3: *Plot showing maximum stress experienced by a mesocantilever as a function of deflection angle.*

shift the measured fatigue life an order of 10 away from its actual value if the stress applied is either over- or underestimated. It is, therefore, necessary to calibrate each sample individually to determine DA_{exp} in order to ensure accurate values of stress are recorded. If samples were removed from the holder during tests they were then calibrated once more upon reclamping.

5.1.2 Ultrafast High Cycle Fatigue Results

In this thesis two testing methods were employed to correlate stress applied to a specimen with its fatigue life. These were the multi-step and single-step methods. There has been previous work to show there is little or no training effect [58, 59] but there is still disagreement over its existence. Therefore, the purpose of using both methods is both to further assess whether there is a training effect and to evaluate each method's suitability for the purposes of achieving a high throughput of data using an ultrasonic tester and mesoscale specimens. The accuracy and the efficiency of

the methods will be evaluated in this subsection.

Single-Step Testing

The protocol followed for these tests was as described in Section 2.3.2. The run-out life in all single-step tests was 10^9 cycles. This was chosen as a compromise between allowing a large number of cycles to be applied but still allowing for a high throughput of specimens. Each test to 10^9 cycles takes ~14 hours to run and at this point of the Failure Stress – Cycles until Failure graph the curve begins to flatten out and there is a high possibility that the sample was being tested at a stress below its fatigue limit and would have a theoretically infinite life. The testing stresses ranged from 500 MPa to 250 MPa in order to obtain data at lower lives of 5 x 10^3 cycles up to the runout limit of 10^9 cycles. Due to the nature of the testing equipment, tests shorter than 5 x 10^3 cycles were not performed as these tests take 0.25 s to run at 20 kHz. At lives shorter than this, the ramp up time begins to take up a significant portion of the testing time and there is no longer confidence in the target stress being applied for the majority of the test. This is the same reason for pulse times during pause testing for crack observation was never below 0.25 s.

In fatigue testing there can be significant scatter due to microstructural effects on performance, therefore a minimum of three tests were performed at each stress level to failure to determine this deviation. The exception for this was 250 MPa as 90% of specimens resulted in runouts. Figure 5.4 is a plot of failure stress against cycles until failure. In Figure 5.4 and Figure 5.5 runouts as well as samples that have failed are plotted and considered in the determination of the range. The number of runouts at each stress level are indicated on the plot and are displayed in terms of percentage of samples tested in Table 5.1. From Figure 5.5 the fit follows the Basquin power law and results in a calculated fatigue strength coefficient, S, of 675 MPa and fatigue exponent of -0.0480. A second Basquin power law fit that ignored runout values was also plotted ($\Delta\sigma_{a2} = S_2(2N_{f2})^{b_2}$) with S=1408 MPa, b=-0.1235. These specific values, are comparable to those seen in literature [63] as well as the general trend in the fatigue performance[62, 64]. However, when comparing it to data discussed in the literature review included in this thesis, the fatigue strengths

measured in these tests are higher. When comparing it with the work of Kobayashi et al on CP Ti (Figure 1.14) the fatigue strength of the Grade 2 CP Ti presented in Figure 5.5 is significantly higher. Kobayashi found that in the tensile fatigue regime, that CP-Ti had a fatigue strength of around 400 MPa at 10^4 cycles, whilst in the data presented here the fatigue strength at 10^4 cycles is between 450 - 500 MPa. This is most likely due to the testing conditions employed in the tests described in this thesis. Here, strain rates are very high whereas in the work by Kobayashi et al the strain rates are significantly lower and, as has been discussed previously, a higher strain rate results in higher measured tensile strengths. It is important to note that the HCF strength presented here is higher than the yield stress measured during conventional tensile tests. Meanwhile, Kobayashi et al's tests (having been performed at 2 Hz) are closer to the regime of testing of the conventional tensile tests. As such, their test results are in good agreement with what is expected at slower strain rates. Likewise, the load ratio of R=0.1 employed by Kobayashi et al results in the specimens experiencing an overall higher mean stress when compared with the load ratio of R=-1 employed in these tests. In addition, the larger grain size in the specimens used by Kobayashi et al is also a reason for the significantly lower measured strengths. For the work by Casavola et al [63] (also discussed in the literature review), the measured fatigue coefficient and fatigue exponent is comparable if runouts are taken into account. Casavola et al found that their fatigue coefficient was 600 MPa whilst the one presented in this work is 675 MPa. The fatigue exponent in Casavola et al's work was -0.084 whilst the one presented in this work was -0.0480. An explanation for this work having a higher measured fatigue coefficient is again due to the load ratio difference (Casavola et al tested at R=0.1, which meant their specimens were subject to a higher mean stress) and the strengthening effect higher strain rates of testing have on specimens (Casavola et al tested at 10-15 Hz). Work by Medvedev et al[117], tested Grade 2 CP-Ti with a similar average grain size as the material used in this thesis (~20 μ) which makes for a good comparison in terms of minimising the microstructural effect on performance. Medvedev et al's tests were performed at more conventional testing frequencies of 20 Hz but the load ratio was the same as those used in this work (R=-1). Therefore, strain sensitivity aside, Medvedev et al's work

is a near ideal comparison for contextualising the results present here. Medvedev et al found that the fatigue strength of Grade 2 CP-Ti, was ~280 MPa at 10^5 cycles, which is slightly lower than the ~300-350 MPa determined in this work. Again, this difference is most likely due to the increased fatigue strength as a result of the higher strain rates. Most interestingly, however, it that a seeming fatigue limit can be seen at ~250 MPa in Medvedev et al's work which is very similar to the result found in this work that will be discussed in more detail in the subsequent paragraphs.

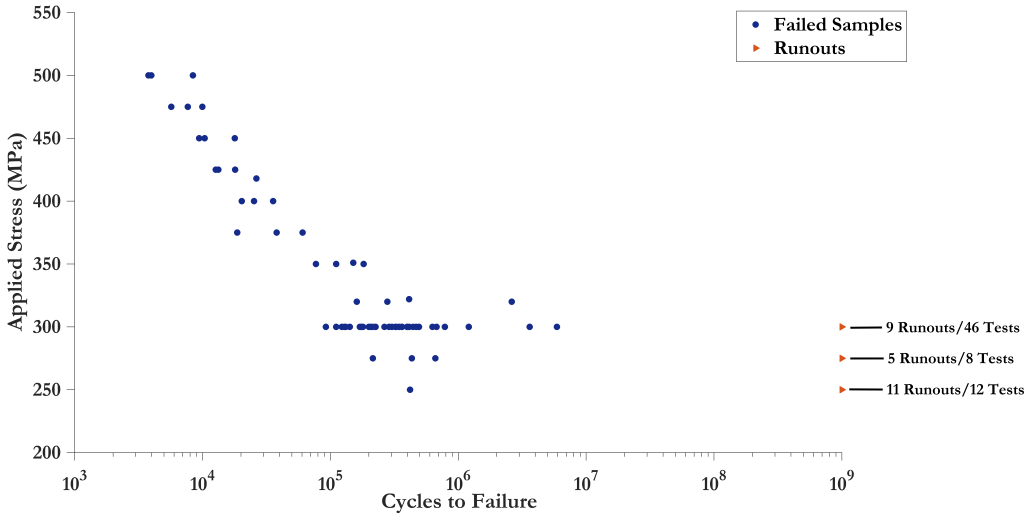


Figure 5.4: *Raw data for Stress vs Cycles to failure for CP Grade 2 Titanium in single-step Tests.*

Table 5.1: *Percentage of CP Ti samples tested using the single-step method that resulted in runouts 10^9 cycles.*

Stress (MPa)	Number of Failures	Number of Runouts	Runout Percentage
300	37	9	19.6
275	3	5	62.5
250	1	11	91.7

As could be expected, the percentage of runouts increased dramatically with a decrease in applied stress. In fact, the plot in Figure 5.6 suggests the relationship between percentage of runouts at 10^9 cycles and stress is close to linear.

Though as demonstrated by previous literature[48, 118], one should view trends that indicate no failure below a certain stress value critically. The graph may indicate that there will be no

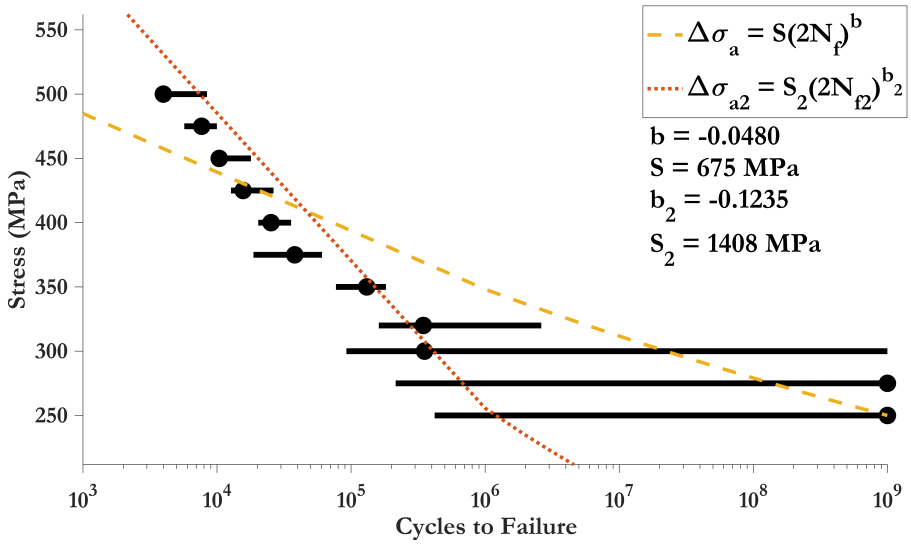


Figure 5.5: *Median and range for Stress vs Cycles to failure for CP Grade 2 Titanium in single-step Tests (raw data shown in Figure 5.4).*

failure for these specimens at ~240 MPa but there may be many reasons why a specimen could fail at that stress. Inclusions, surface damage or even an unfavourable grain orientation could cause a sample to fail at these stresses within 10^9 cycles. At this point it is also important to restate that these runouts were limited to 10^9 cycles and that beyond this number of cycles there is a significant probability that the sample will eventually fail. The results presented here are in good agreement with the macro- and microscale results for static strength in the previous chapter. The stress below which Figure5.6 shows there should not be cyclic failure is ~240 MPa, whilst the bulk CRSS calculated from microcantilever tests for the <a> prism slip system (the softest of the slip systems and the one most likely to activate during loading) is 130 MPa. The calculated CRSS value is a response to shear and if the von Mises criterion in Equation 5.4 for pure shear is used:

$$\text{CRSS} = \frac{\sigma_y}{\sqrt{3}} \tag{5.4}$$

Then the bulk σ_y calculated from these tests is 225 MPa. Likewise, in the macroscale monotonic tensile tests the 0.2% yield strength measured was in the range of 222 MPa - 265 MPa dependent on strain rate. The slight discrepancy is likely due to the effect of strain rate on strength and

size-effects (as shown in both the microcantilever tests and tensile tests).

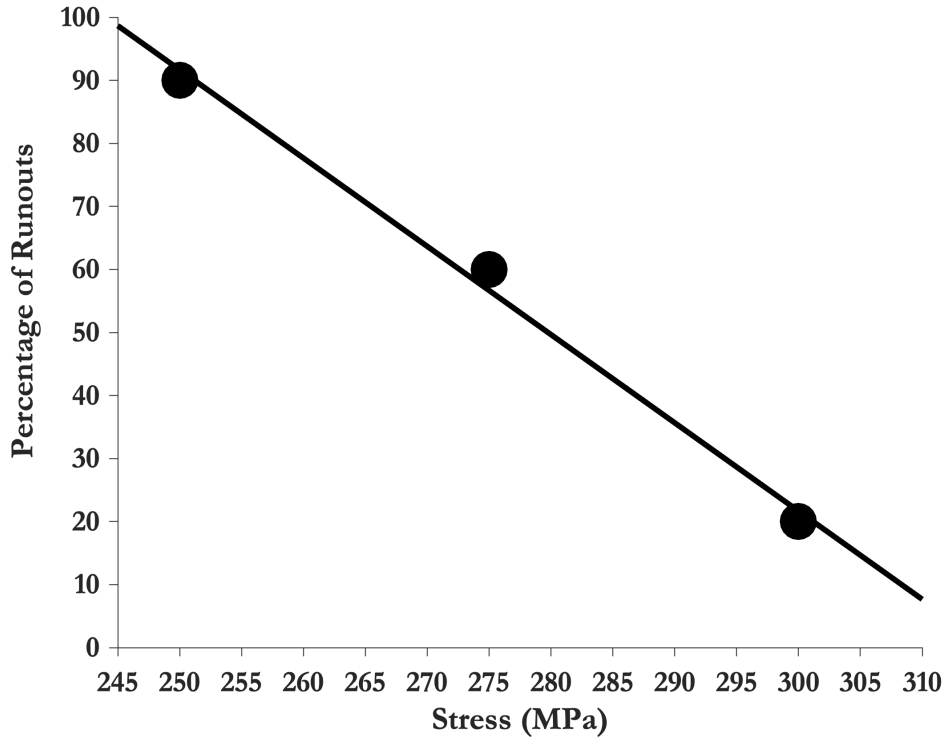


Figure 5.6: *Percentage of runouts at 10^9 cycles as a function of Stress (MPa) applied to mesocantilevers.*

Multi-Step Testing

The protocol followed for these tests was as described in Section 2.3.2. In these tests rather than there being a fixed stress for testing it was the life that was fixed (i.e a target life of 10^5 cycles was chosen and the specimen was vibrated at a set amplitude for 10^5 cycles). If the sample survived, then the vibrational amplitude is increased and the sample is tested again for 10^5 cycles. This process is repeated until failure and the stress at which failure occurs vs target life is recorded. In the case of this thesis, the starting stress for all samples was 250 MPa and the increments increased by only 5 MPa each time to maintain a degree of accuracy. Figure 5.7 exhibits the data obtained using this method. Looking at this figure it is clear that the scatter after 10^5 cycles begins to increase and the curve begins to flatten out. There is significant overlap of the ranges (Figure 5.8) at this point but there is no overlap with multi-step tests that had a target of 10^4 cycles. This is

in good agreement with data of typical S-N curves of metals in literature. Figure 5.9 shows the raw data from both single-step and multi-step tests. Here, the similar trend in measured fatigue performance from both methods is evident. A Basquin power law fit was also plotted for the multi-step data and it can be seen that S=411 MPa and b=-0.0165. Due to the nature of multi-step testing, there are no runouts to affect the fit. As seen in both literature and the data presented here, it can be seen that in the HCF regime there is significant overlap of results as stress decreases and life increases. This coupled with the stress uncertainty causes the S and b values measured in multi-step tests to be further away from those expected in literature compared to single-step tests. A closer look at the two different testing methods is investigated in the following section.

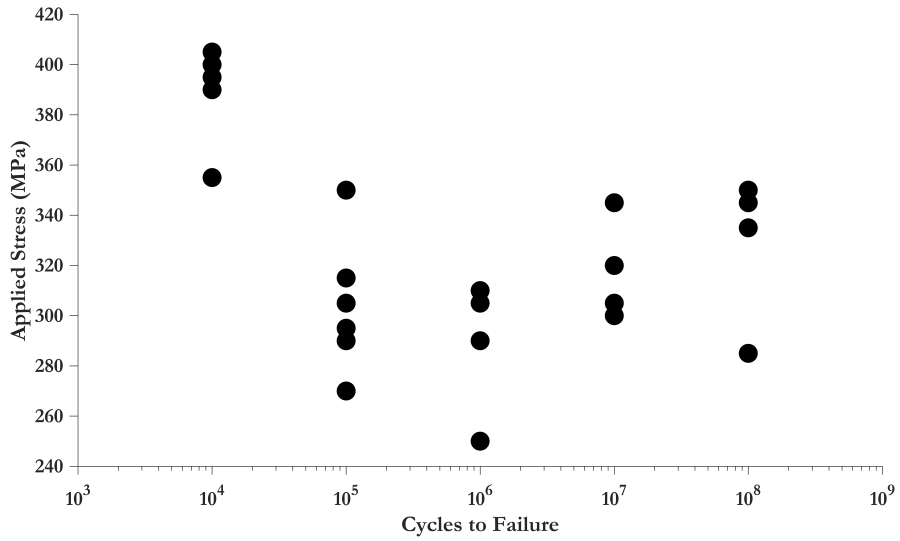


Figure 5.7: *Applied Stress vs Cycles to failure for CP Grade 2 Titanium in multi-step Tests.*

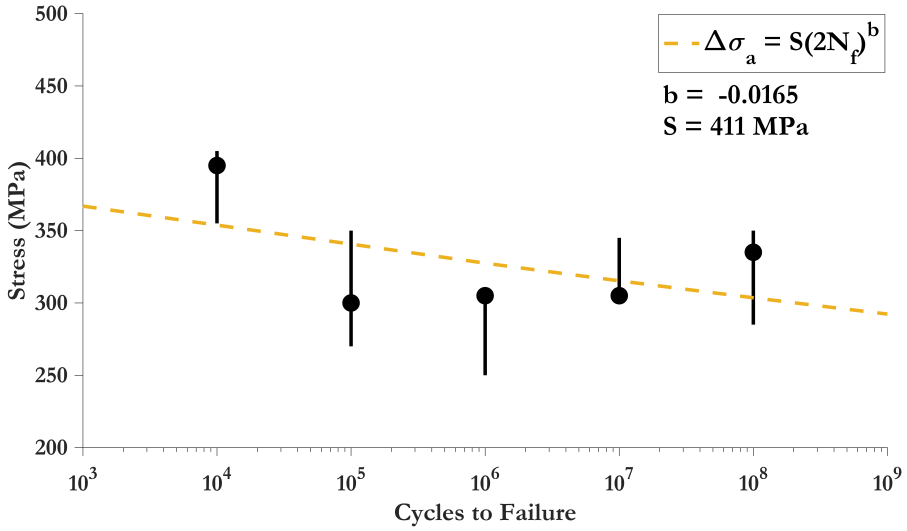


Figure 5.8: *Median and range for Stress vs Cycles to failure for CP Grade 2 Titanium in multi-step Tests (raw data shown in Figure 5.7).*

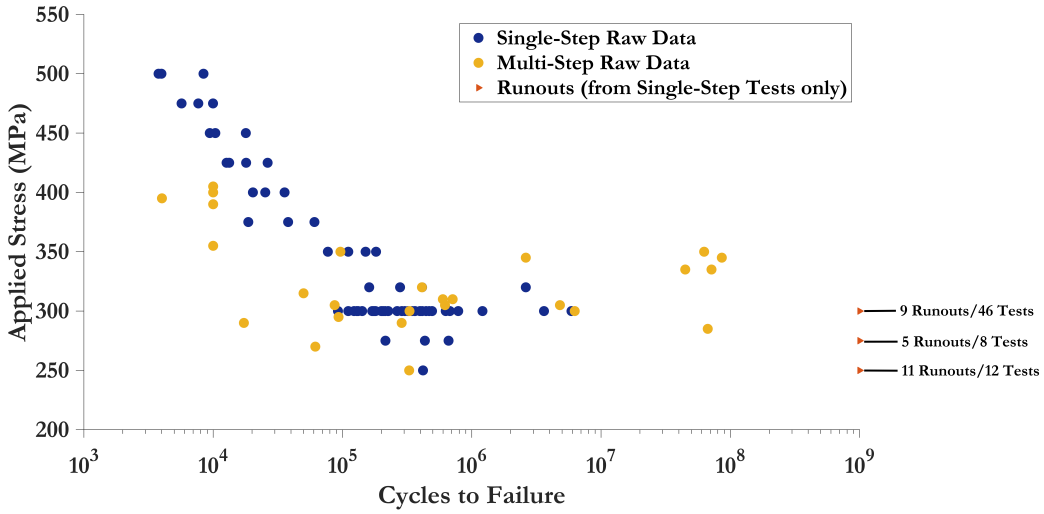


Figure 5.9: *Combined raw data for single-step and multi-step data presented in Figure 5.4 and Figure 5.7.*

Comparing Single/Multi-Step Testing

The results reported in this subsection were obtained from tests performed on a different foil sample to the earlier tests (which had led to data from Figure 5.4 to Figure 5.9). As such, the samples presented here had a different laser finish that resulted in comparatively worse fatigue

performance compared with the first foil. However, amongst itself the data is sensible and follows the same trend as the first foil. The ability to measure this performance is discussed at the end of this section.

The purpose of combined single/multi-step tests was to determine the statistical spread of life at a given stress and stress at a fixed life. To perform such a study using conventional testing, like much of the data presented in this chapter, would have been infeasible. Understanding this property provides important quantitative insight into the effect microstructure can have on fatigue properties. Single-step tests were performed first to determine the fixed life the multi-step tests would be run to. As the focus of this work was to investigate high cycle fatigue performance, a stress amplitude that has previously been seen to result in failure upwards of ~10^6 cycles was desirable. However, what was seen in tests was that too low a stress resulted in a high percentage of runouts. As such, a compromise was made to test at 300 MPa as this resulted in a low percentage of runouts but also a high fatigue life (as seen in the previous section). A life where just under ~80% of samples failed was chosen (a life with a plotted data point was chosen to maximise confidence) - 3.09 x 10^5 cycles. Figure 5.10 below shows the overlap of single-step (blue markers) and multi-step (green markers) tests and Figure 5.11 shows the cumulative probability of (a) the cycles to failure at a fixed stress of 300 MPa (b) the failure stress at a fixed life of 3.09 x 10^5 cycles.

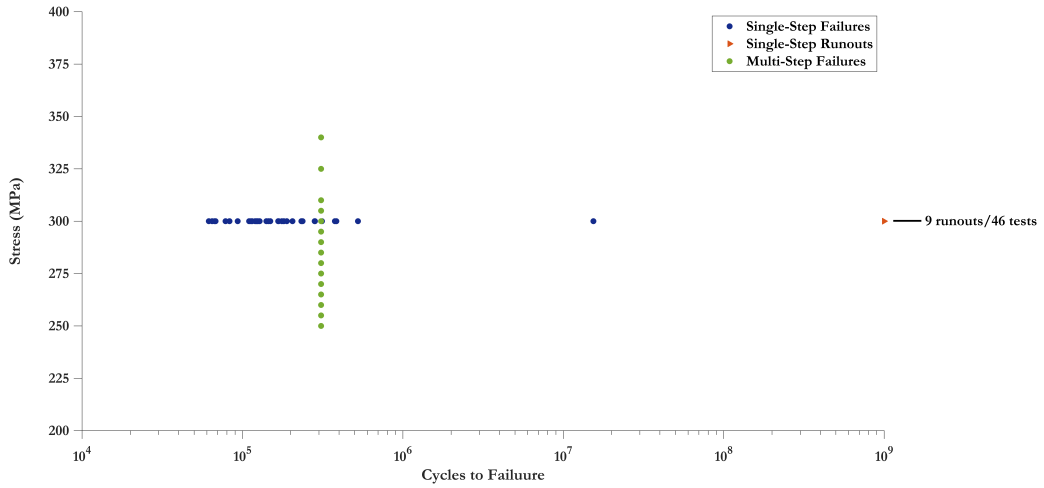


Figure 5.10: *Combined plot of Stress vs Cycles to failure for CP Grade 2 Titanium in both single-step and multi-step tests.*

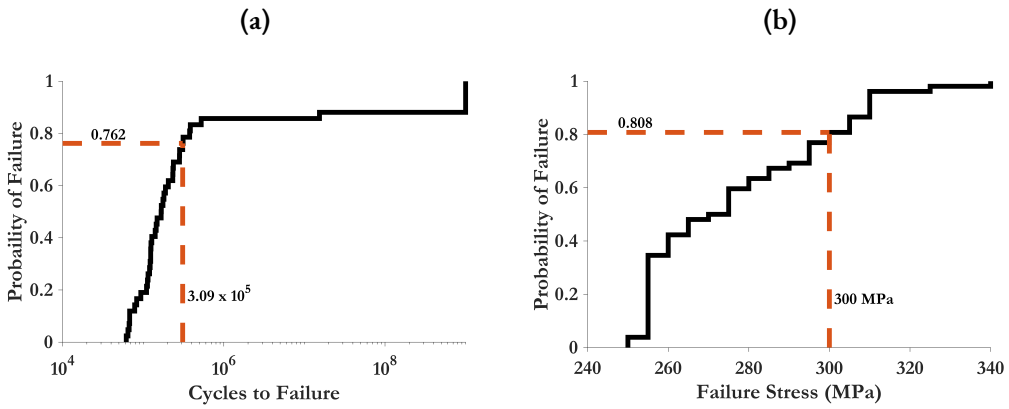


Figure 5.11: *A cumulative step chart showing the failure of samples at (a) fixed stress single-step tests (b) fixed life multi-step tests.*

From Figure 5.11(a), it can be seen that for a fixed stress of 300 MPa, the probability of the sample failing before 3.09 x 10^5 cycles is 76.2%. This was used to guide the setup of the multi-step testing which used a target life of 3.09 x 10^5 cycles and stress increments of 5 MPa. The probability of the sample failing by 3.09 x 10^5 cycles at stresses lower than 300 MPa is 80.8% as can be seen in Figure 5.11(b). This discrepancy of ~4% is minimal and can be accounted for by variation in actual testing times due to computer latency issues or stress tested at due to equipment performance.

All the data obtained in independent single-step testing and independent multi-step testing used samples that had been laser-cut in the same foil in the same session. For the joint single-step and multi-step study in this chapter samples were taken from a different foil. It was important to keep studies of fatigue performance within a single foil because a discrepancy in sample performance between foils was observed. This was a result of laser finish on the specimens, specimens with rougher edges had worse fatigue performance than those with smoother edges. Figure 5.12 shows the difference in laser performance between foils. Likewise, a tapering effect can be seen in this figure as the laser is fired from one side only resulting in one side of the mesocantilever beam being slightly wider than the other. This means there is a slightly higher stress concentration on one side than the other and, therefore, there is a higher chance of cracks nucleating on this side than the other. It is this thinner side that is observed during fatigue testing in order to

best capture physical crack nucleation and growth.

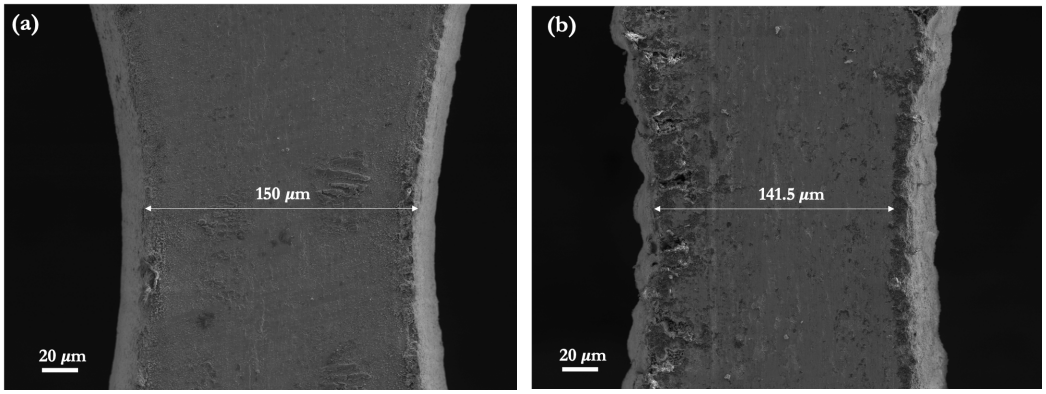


Figure 5.12: *SEM images showing the difference in laser finish on two CP Ti mesocantilever specimens (a) accepted smooth finish (b) rejected rough finish.*

The target finish was that of Figure 5.12(a) but slight variation between foils was accepted. The exact laser cutting conditions used are not known and, therefore, cannot be discussed here as it is proprietary knowledge of Laser Micromachining Ltd. As such, it would not have been appropriate to compare methods as there would be no confidence in the cause of any difference measured. However, what this enabled was the chance to determine whether or not this method is accurate enough to pick up on surface defects. Figure 5.13 shows the measured difference in performance between CP Ti foil 1 and CP Ti foil 2. Foil 1 had a smoother finish to foil 2.

In these figures, it is clear there is a noticeable difference between the two foils. The percentage of runouts of total samples tested in each foil are 19.6% for foil 1 and 11.9% for foil 2, which shows that samples are 1.6 times more likely to runout with the smoother finish in foil 1 than in foil 2. A similar trend is seen if one looks at the data displayed in Figure 5.13(b). Here the performance gap is relatively consistent with foil 1 outperforming foil 2 by ~2.1 times in terms of number of cycles survived. As the number of cycles is increased the difference in probability of a sample failing by a certain number of cycles decreases. This suggests that at lower lives it is sample finish that is the factor that affects failure more, as cracks initiate much faster when a surface is more rough, whilst at longer lives microstructure is the limiting factor. This small laser finish difference was easily picked up by the testing method and a measure of the performance margin was determined. The difference in performance at higher cycles is less affected by surface roughness than samples that

failed at lower cycles. Reaching the very high cycle regime at 10^7 cycles there is an 80% chance foil 1 will have failed by this point whilst for foil 2 there is an 85%. This suggests there is a 5% deficit in very high cycle fatigue performance due to specimen surface roughness.

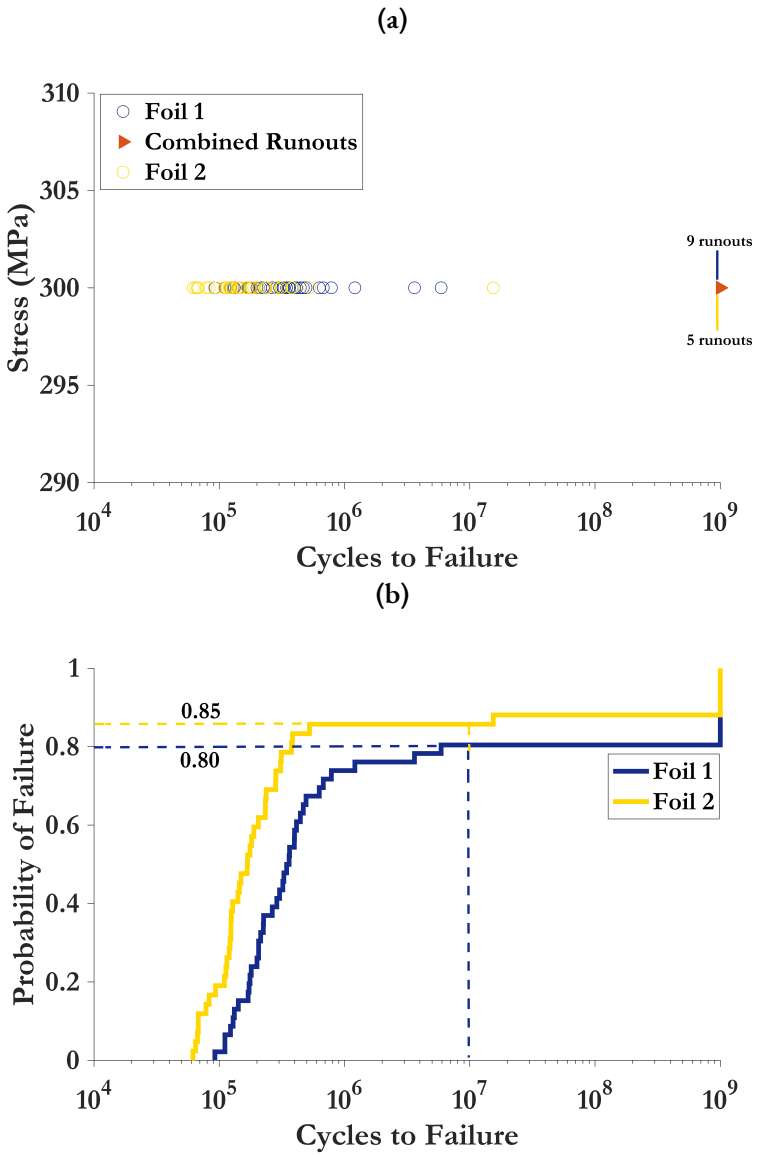


Figure 5.13: *Comparison of performance difference between foil finishes 1 and 2 (a) number of cycles taken for a sample to fail at 300 MPa (b) cumulative step chart showing probability of failure at 300 MPa.*

5.2 Crack Growth Rate

One of the main aims of this body of work was to determine whether or not ultrafast testing of mesoscale specimens would allow for accurate observations of crack growth. To investigate this, single-step tests that were pulsed at set intervals were conducted. The intervals chosen were based on numerous studies to find a balance between pulses that can capture crack growth and the increase in time taken for the test. All samples imaged in pulse testing (unless otherwise specified) were electropolished in order to reveal the microstructure and make it easier for crack detection. A polarising filter is used to observe crack growth as the crack shines brightly under the right conditions due to them scattering light more strongly than the smooth, polished surface. As the sample is vibrating at extremely high speeds and relatively high vibration amplitude during testing it is important to allow it to 'settle' for focussing prior to taking images. In addition to this, as there can be drift of the specimen in or out of the plane of focus (z–axis) of the camera during testing, a piezo–stage is used to move the camera +/- a few microns in the z–axis and several images taken to maximise the chance that an in-focus image is recorded. Another issue, was the low level of light during imaging. As such, the exposure time was set to ensure a bright enough image was taken. Taking a series of images and required pause time, though only ~8 seconds, adds an inefficiency of an order of magnitude to the resulting testing time if the pulse time is set at 0.5 s (i.e 10^4 cycles). This would mean that a test at 10^7 cycles would take just over two hours rather than 8 minutes and becomes more taxing at higher lives and shorter pulse times. These pulse time studies concluded that 0.25 s is the optimum for capturing crack growth in samples with a target life of ~10^5/10^6 cycles. Figure 5.14 is an example of the observations possible using this setup.

Here, the life of the crack is captured from (b) initiation to (c) near failure to (d) failure. Not only can the crack growth rate be measured (as will be presented later) but the crack path direction is clear as well. The crack path direction and the microstructural features that affect it will be discussed in Chapter 6, in this section only crack growth rate will be discussed in detail.

As was discussed, in the literature review, an important measure of high cycle fatigue resis-

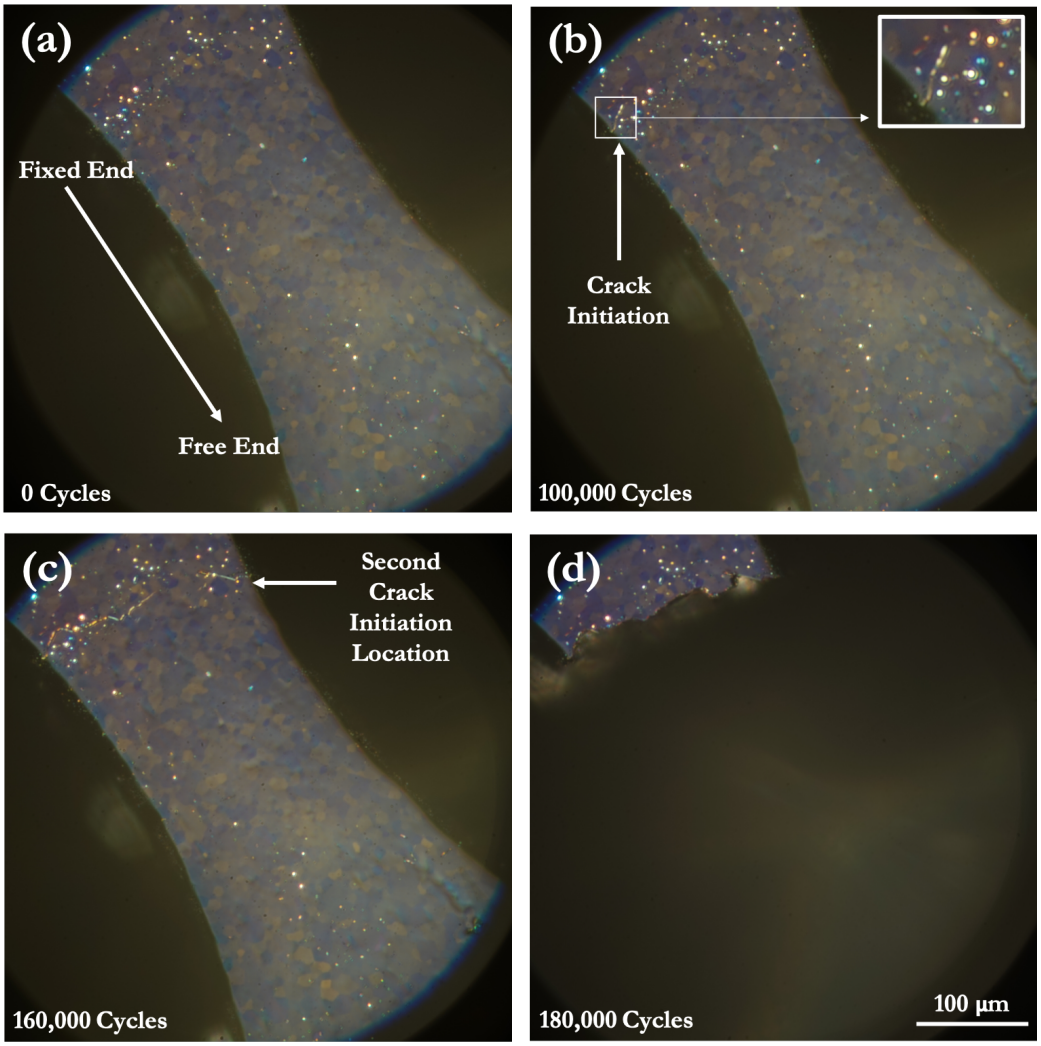


Figure 5.14: *Polarised light images of crack growth in a mesocantilever captured with a digital camera (a) mesocantilever at the beginning of the test (b) crack initiation (c) significant crack growth and second crack initiation site (d) failure of the specimen.*

tance is a material's resistance to the initiation of a crack. Using this observational setup, the time taken for a visible crack to initiate can be determined. This property can be measured as a function of stress as well as using microstructure to explain differences in performance. By measuring the length of the crack path as seen in images (i.e along the crack path), such as those in Figure 5.14, against time a plot can be made that depicts growth rate as well as clearly illustrating the time taken for the crack to initiate. Figure 5.15 shows the measurements achieved for a sample that failed after 175,000 cycles at a stress of 371 MPa.

From this graph it can be seen that the number of cycles until the crack visibly initiates on

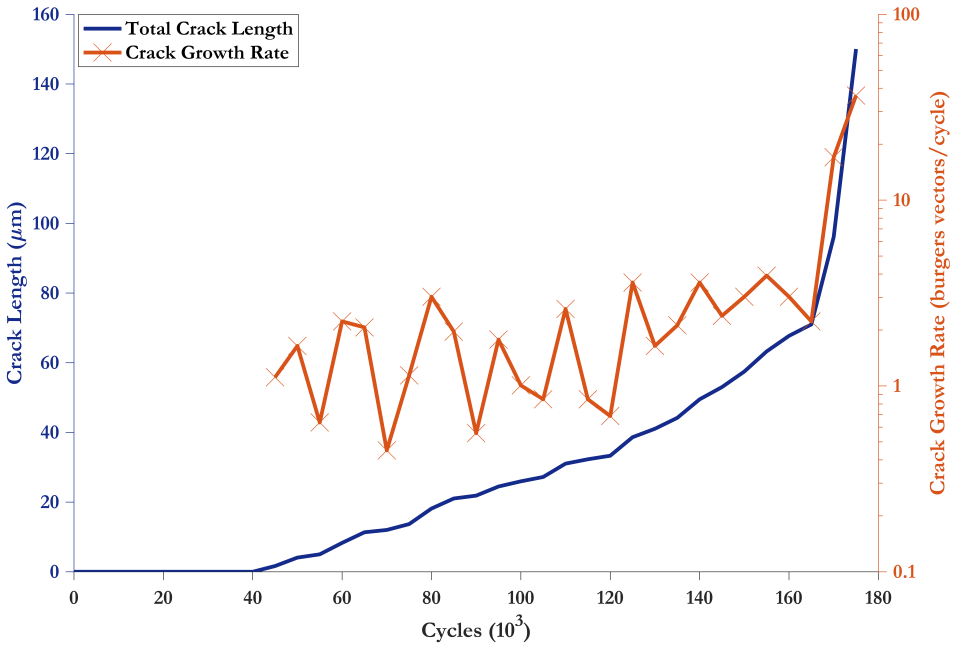


Figure 5.15: *Crack growth of a mesocantilever tested at 371 MPa.*

the surface is 45,000, meaning the initiation stage takes up 26% of the specimen's life. After this point, crack growth rate is stable at ~1 burgers vector per cycle until ~160,000 cycles where the growth becomes orders of magnitude quicker until complete failure of the mesocantilever. If one compares the growth rate behaviour to the total crack length across the beam it is seen that growth is fairly stable up until just beyond halfway across the beam before becoming unstable and growing very rapidly between the 0.25 s pulses.

Observing the crack growth rate using this method also showed that the crack rate does not continuously increase as the crack would slow down or stop at grain boundaries between pulses. This is to be expected as between grains there can be significant misorientation. These misorientations mean that cracks need to twist or tilt to move from the slip plane in the first grain to the next and this requires both energy and time. This phenomena will be explored further in Chapter 6. Occasionally, pauses that last several pulses are observed. Figure 5.16 is an example of such an occurrence.

The drop off in crack growth rate to zero indicates that the crack has stopped growing, at least visibly along the surface. At these arrest points, the cracks may grow into the beam as it is

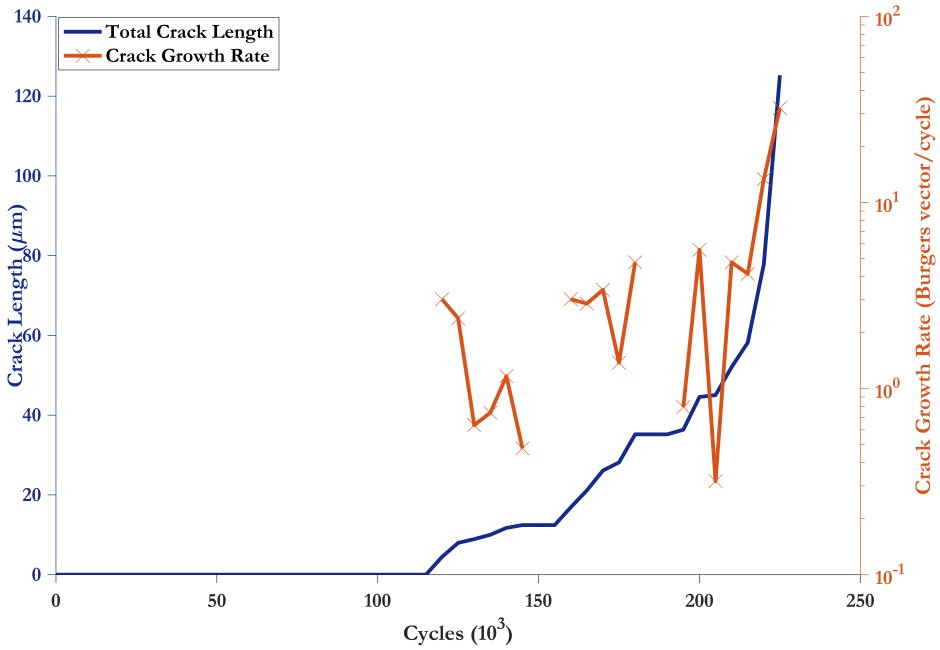


Figure 5.16: *Crack growth of a mesocantilever tested at 327 MPa.*

not energetically favourable for it to progress to the next grain along the surface. Fracture surface analysis shows that the crack indeed grows down from the surface and tests paused just before full failure show how the crack front progresses in the next section (Figure 5.21). It's clear that the last part of the mesocantilever that remains attached is the opposite surface to the surface where the crack initiated. This was seen on all samples tested to just before failure.

The two plots in Figure 5.15 and Figure 5.16 show that the physical nucleation of a crack indeed takes up a large proportion of a specimen's life. The ability to perform a large number of tests in a short amount of time, whilst observing crack initiation, allowed for the investigation of the effect stress has on the time taken for a crack initiate and the proportion of a specimen's life is attributed to initiation. Once the crack initiates it is not long before the crack growth rate becomes rapid until failure. Figure 5.17 shows that there is perhaps a relationship between stress and time taken for a crack to initiate with higher stress resulting in typically fewer number of cycles for a crack to initiate. Initiation points were determined by examining the set of images taken for each sample. These images were taken at evenly spaced intervals/testing pulses. The error bars present reflect the fact that testing pulses were 0.25 s which is the equivalent of 5,000

cycles. What is also observed, is that there is a high scatter in this data. This could be because of stress calibration issues but is more likely to be the result of microstructural effects. If grains are less favourably oriented for slip relative to the loading direction then it is more difficult for cracks to initiate. Looking at Figure 5.18 a relationship between the proportion of the specimen's life taken up by crack initiation and stress is also seen. With an increase in stress, the proportion of a specimen's life taken up by crack initiation decreases. The reasons for scatter are the same as those mentioned above. By comparing Figure 5.17 and Figure 5.18, it can be seen that their trend is comparable, i.e the effect stress has on both the time taken for a crack to initiate and the proportion of a specimen's life taken up by crack initiation is intrinsically linked. It follows, therefore, that the importance of crack initiation resistance increases linearly with a decrease in stress/increase in desired ultimate life.

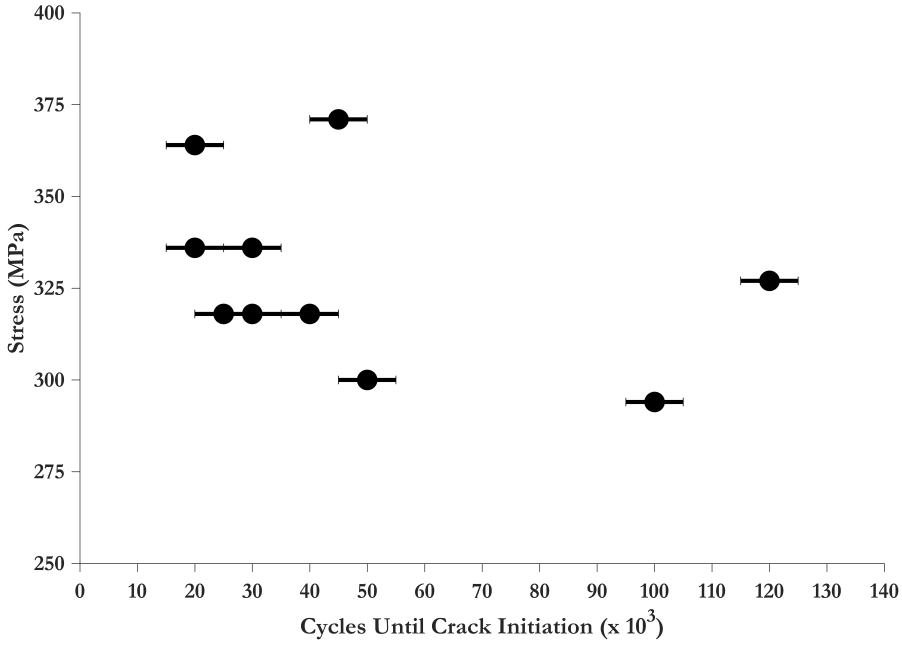


Figure 5.17: *Time taken for a crack to initiate in a CP Ti mesocantilever as a function of stress.*

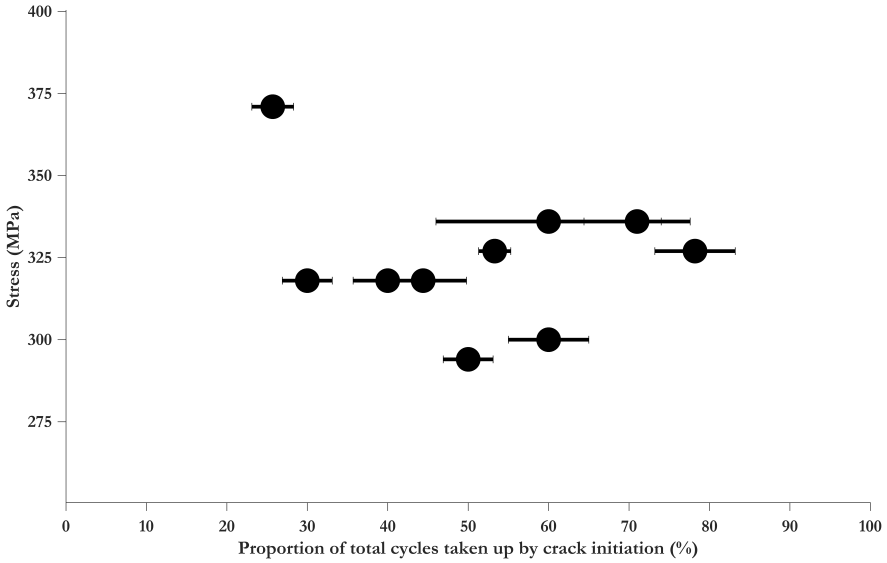


Figure 5.18: *Percentage of total life that is taken up by crack to initiate.*

5.3 Fracture Surface Analysis

Another benefit of using mesoscale specimens for analysing fatigue performance is that the resulting fracture surface is much more manageable for imaging than conventional macrosamples. In the case of the mesocantilevers used in this thesis, the fracture surface area is never larger than around 100 µm x 150 µm. This means that the entire fracture surface can be captured in a high resolution image, in an SEM, orders of magnitude smaller in terms of file size for an image of a macrosample at the same resolution. An example is shown in Figure 5.19.

As mentioned in the literature review at the beginning of this thesis (Section 1.2.3), fractography can provide useful information regarding the failure mechanisms in a specimen. Of most interest in this body of work is the location of the initiation site because it is resistance to initiation that is most important for components that are designed to withstand a high number of cycles. A good understanding of the location of fatigue crack initiation (FCI) is also important in the context of this work as one of the original aims was to determine whether or not this method and combination of sample design can allow for the study of microstructural effects on FCI. The aim was to produce fatigue cracks that would initiate at different locations in different samples

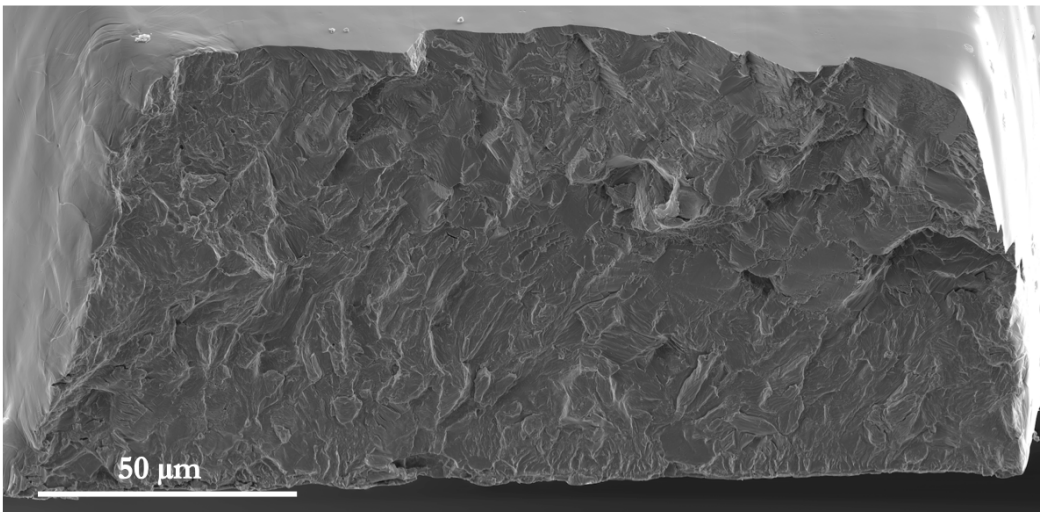


Figure 5.19: *SEM image of a CP Ti mesocantilever fracture surface tested at 350 MPa with a fatigue life of 1.45 x 10^5 cycles.*

and, perhaps, even have multiple crack initiation sites within the same sample.

Features like striations can be used to determine the location of these fatigue crack initiation sites. Striations are formed as a result of slip behaviour at the crack tip that results in plastic deformation during a loading cycle. As such, striations can be used to estimate the crack growth rate and the number of cycles a specimen has experienced. It is precisely because striation formation is a direct consequence of the crack path direction that the origin of the crack can be traced. It is important to note that the match up between striation spacing and number of striations is not a one-to-one match with growth rate and number of cycles as during near threshold conditions it can take multiple cycles to generate a striation. Likewise, when a crack approaches a grain boundary and striations accumulate near the boundary, using them to estimate the growth rate is inaccurate. As such, it is better to use striations in the middle of grains to estimate growth rates. An example of the striations seen in the mesocantilevers is in Figure 5.20. Here, the distinct ridges and equal spacing of striations are clearly visible. By measuring the size of the facet (highlighted in the Figure 5.20 and the spacing between each striation, the local crack growth rate can be determined. In the case of this specimen, the length of the facet is 2880 nm, whilst there are 53 striations present and the average spacing between them is 54 nm. Assuming one striation per cycle is fair (54 nm x 53 =2862 nm), therefore, in this area there have been 53 cycles in this local

area with a stable growth rate of 54 nm per cycle. This is in the correct order of magnitude for the stable crack growth region seen in titanium alloys[119]. This area of the fracture surface was found near the middle of the cantilever, suggesting that the crack growth rate had become more stable than at the slower initiation point and faster growth rates typically seen near the end of a crack.

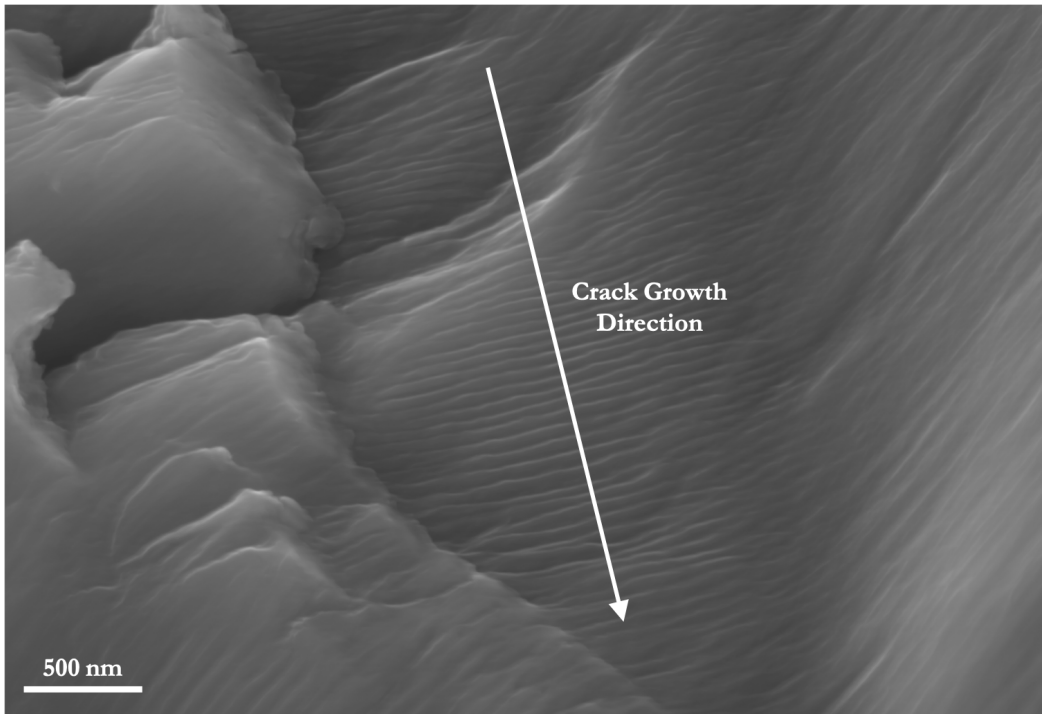


Figure 5.20: *SEM image of an example of striations in a CP Ti mesocantilever fracture surface and the crack growth direction.*

As was briefly mentioned, in the previous section the progression of the crack front from one surface to the other can clearly be seen. In the majority of cases the crack initiates at the surface that is less wide. This difference in width of the beam from one side to the other is due to laser cutting. There is a tapering effect the deeper into the material the laser travels and results in the 'top' side of the cantilever (i.e the surface closer to the laser source) being thinner than the bottom. This causes there to be a slighter greater stress concentration at this surface rather than the wider surface. It is precisely for this reason that when crack growth observation experiments are performed the thinner surface is oriented to be facing the camera as there is a higher probability that cracks will initiate there. What can also be seen on fracture surfaces is a distinct change from

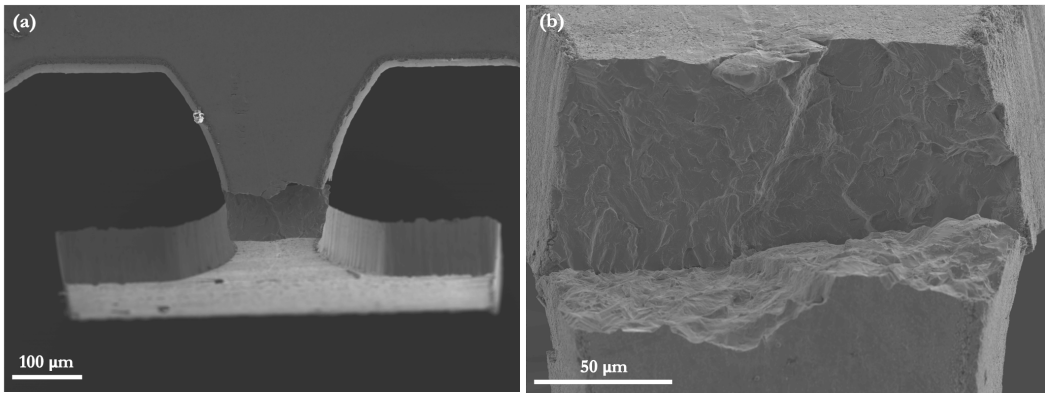


Figure 5.21: *SEM images showing a CP Ti mesocantilever just before complete failure (a) top view (b) view along the beam of the remaining fracture surface. Sample tested at 420 MPa stopped at 2.64 x 10^4 cycles.*

a relatively smooth fracture into a relatively rough fracture surface. This is also near the wider side of the mesocantilever (as seen in Figure 5.22). By studying the fracture surface carefully a clear change in fracture mode is seen to occur. At the beginning, the crack grows relatively slowly by fatigue and results in the formation of a lot of smooth facets with striations. There is a clear step across the cantilever in the area surrounded by the white box suggesting that the crack travels from the top surface down to this point before full failure of the mesocantilever.

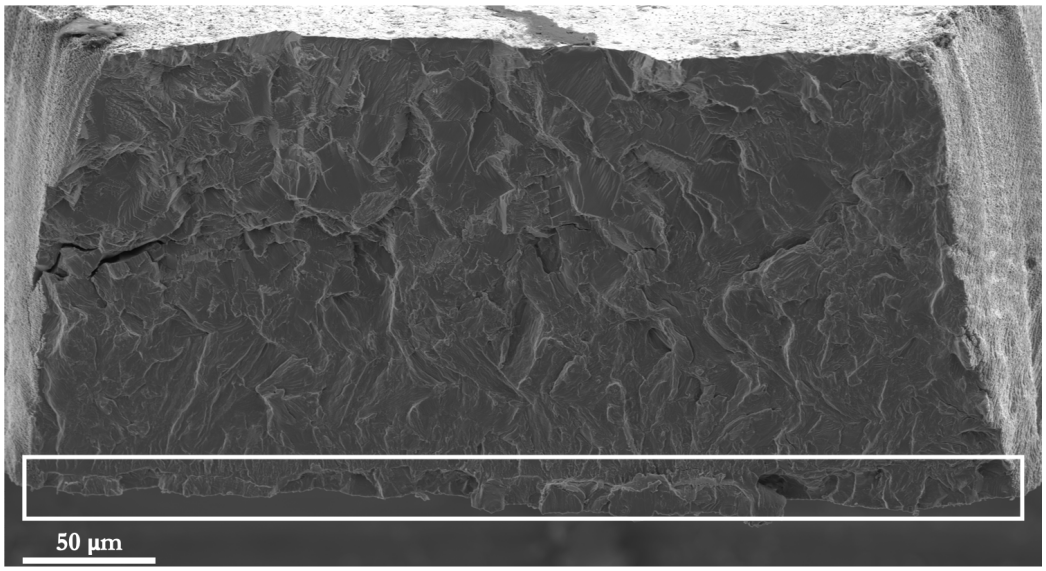


Figure 5.22: *SEM image illustrating the change in fracture mode through a mesocantilever beam during UHCF testing. Sample tested at 300 MPa with a fatigue life of 1.73 x 10^5 cycles.*

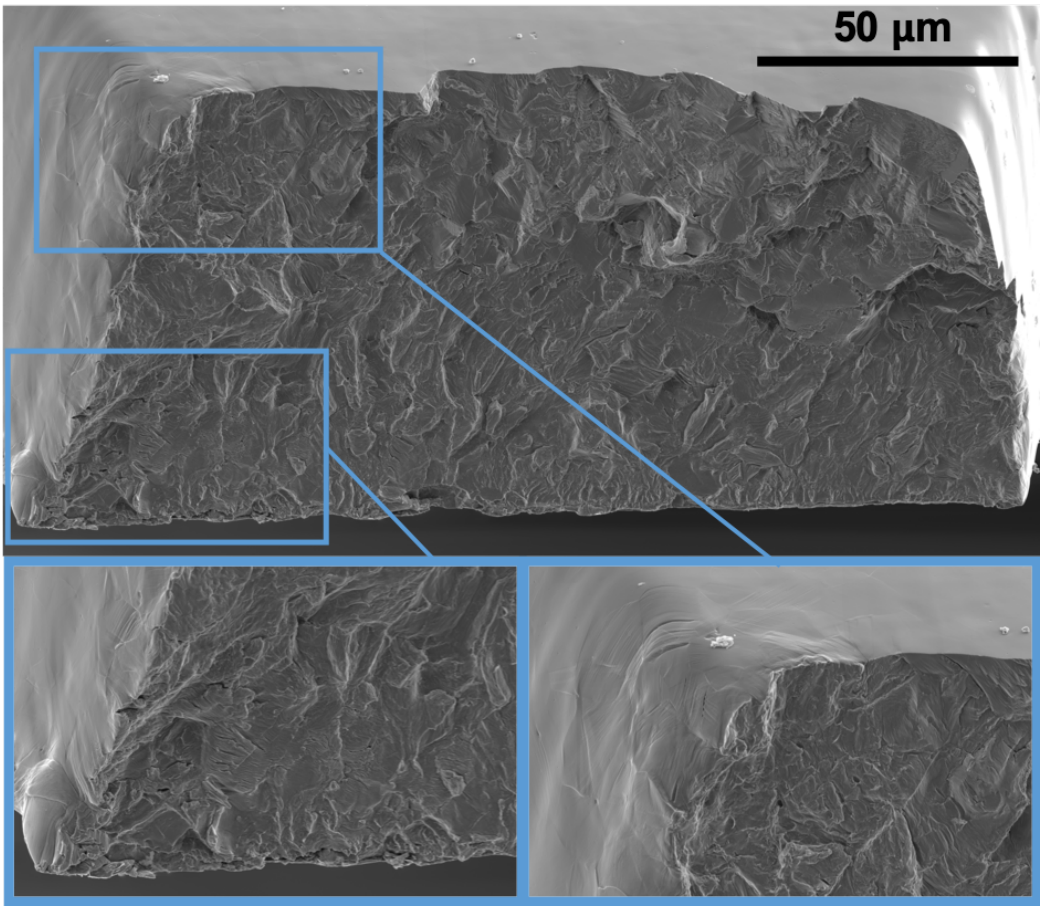


Figure 5.23: *SEM image of striations and slip bands showing that crack initiation in a CP Ti mesocantilever begins at the surface corners. Sample tested at 350 MPa with a fatigue life of 1.45 x 10^5 cycles.*

From these fractography studies it is shown, by observing the striations and their direction, that most cracks initiate at the surface and at the edges. Figure 5.23 shows this in more detail. There is also clearly a larger concentration of slip bands at the corner of the sample that the striations indicate is the point of crack origin. This further confirms that the point of crack initiation was indeed there. This evidence is important for the next chapter's crack path analysis as that is the assumption made in most cases, unless otherwise stated. It is also important to note that though the majority of striations point away from the primary crack origin there are several groups of striations present that point in different directions. This suggests the presence of multiple secondary crack initiation sites. Evidence of multiple initiation sites is supported by the second crack initiation depicted in Figure 5.14 and the presence of cracks that are not connected

at the surface in Figure 5.24.

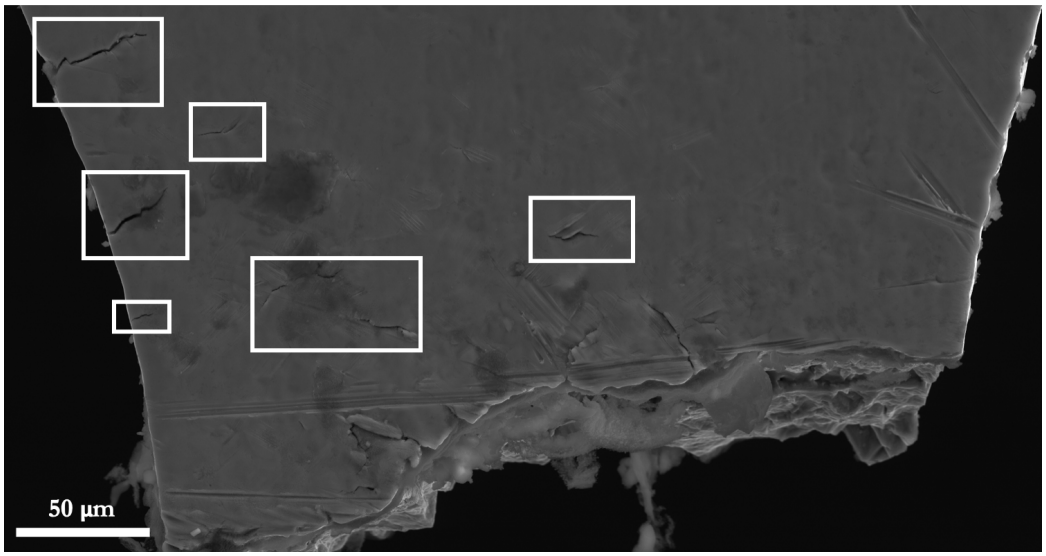


Figure 5.24: *SEM image of a failed CP Ti mesocantilever with multiple crack initiation sites (marked by boxes) tested at 300 MPa with a fatigue life of 3.32 x 10^6 cycles.*

5.4 Variation in Crack Growth Rate

If we compare the crack growth rate ascertained from the previous two sections (Section 5.2 and 5.3) there is an order of magnitude difference between them. Crack growth rate is very sensitive to local microstructure and can be affected by grain size, orientation, the presence of grain boundaries and the misorientation between grain boundaries. However, it is far from clear how sensitive it is. This effect is particularly noticeable during short crack growth where microstructural features play an even larger role in the measured crack growth rate. Crack growth rate is also affected by the load ratio with higher (positive) load ratios resulting in higher crack growth rates[119]. Literature also shows that as cracks growth in length, nearing the end of the fatigue life, their growth rate also increases[120]. These aforementioned factors, explain the varying growth rates measured as not only do varying microstructures cause this observation but also the life cycle of the crack. It is unclear at what stage of the fatigue life the striations were observed but, as was mentioned earlier, due to their location within the crack surface it is likely that it was towards the

end of the fatigue life of the specimen. As such, the measured crack growth rate is an order of magnitude higher than the average crack growth rate measured during the stable growth period depicted in Figure 5.15. Figure 5.15 also shows that the exponential increase in crack growth rate occurs at ~90% of the fatigue life fraction and is in good agreement with the step-change observed in literature[120]. As was demonstrated by King et al[121] local crack growth rates in magnesium can vary by an order of magnitude ($4\ nm^{-1}$ to $40\ nm^{-1}$) as a result of grain and crack orientation. It was shown that cracks tended to be oriented with the basal plane and this orientation match was typically associated with higher growth rates. Brown and Hicks[122] also found similar results when investigating the titanium alloy IMI 685. They were able to show that the microstructure present ahead of the crack tip could result in dramatically different crack growth rates. Pilchak[123] performed tests on single-phase Ti-7Al and determined that fatigue crack growth rates could increase by two orders of magnitude between areas of striation crack growth and faceted growth. Turnbull and de los Rios[124] examined the effect grain size has on fatigue crack growth rates in an aluminium magnesium alloy (Al-5754) and showed that when the crack length is less than 5-10 grains in length there is noticeable variation in rate. In such cases, crack growth rates are intermittently fast and slow. Once the crack length exceeds this size, the variation in rate decreases before increasing monotonically. This trend was also observed in all the previously described samples present in this work. The grain size, as mentioned earlier in this work, in the samples tested are ~20 μm^2 and from looking at Figure 5.15 and Figure 5.16 it can be seen that up to crack lengths of between 40 μm to 50 μm (i.e. 5-10 grains) the variation in rate is relatively high before settling once the crack exceeds this length the variation in rate decreases before increasing monotonically.

5.5 Summary

Using mesoscale and ultrafast high cycle testing, the fatigue properties of Grade 2 titanium has been probed. By calibrating individual samples and ensuring high levels of finish on the speci-

mens results are more accurate and reproducible. Fatigue performance, as displayed by the S-N curves in Figure 5.5 and Figure 5.8 show similar trends to that seen in bulk fatigue tests seen in literature. Using a Basquin power law fit, the fatigue exponent (b) and fatigue coefficient (S) of single-step tests were -0.048 and 675 MPa respectively. These were comparable with values seen in literature (e.g b=-0.084, S=609.5 MPa [63]) with discrepancy in values explained as a result of load ratios used and strain rates experienced by the specimen during testing. It was also seen that multi-step tests, though in good agreement with single-step tests in regards to general fatigue performance trends can underestimate the values of b and S as a result of the uncertainty in stress, particularly in the HCF-VHCF regime.

These mesoscale tests also have good agreement with the monotonic macroscale and microscale tests. The extrapolated stress at which zero failures will occur during fatigue tests is ~240 MPa whilst the calculated bulk yield strength from microscale specimens was 225 MPa and the macroscale tensile tests indicated an average 0.2% yield stress of 243 MPa. This demonstrates that data achieved by ultrafast mesoscale tests of Grade 2 CP Ti is representative of bulk material behaviour. The results presented also reaffirm that results achieved by both single-step and multi-step tests are comparable. The probability of failure of a sample in the HCF regime, whether single-step or multi-step tests are employed, are very similar. This shows that there is either no coaxing effect or it is negligible. In addition, this testing method has demonstrated its ability to measure difference in sample condition and determine the deficit in performance as a result of rough sample surface.

By observing crack growth the microstructural effect on crack growth rate is evident. Cracks are seen to stop at grain boundaries and grow into the beam prior to continuing along the surface. The importance of initiation resistance in high cycle fatigue has been underscored by showing the longer the target life the more important crack initiation resistance is. It has been shown that the lower the stress applied, the longer the time taken for a crack to initiate and the more of a specimens life is taken up by the initiation stage.

Fractography has proved to be invaluable in ascertaining the crack initiation points. It has also

confirmed that there are multiple initiation sites within and along the cantilever beam as desired. It also allows for determination of local crack growth rates by striation counting. As the crack extends into the middle of the beam, and away from the surface, crack growth rate becomes more steady state. It has also shown that this testing method, coupled with sample design, generates multiple crack initiation points which will allow for crack path and crack tip analysis using the advanced characterisation techniques that will be discussed in the following chapter.

Chapter 6

Effect of microstruture on crack initiation and short crack growth

In this chapter, understanding the driving forces behind crack initiation and propagation are key. As Krupp states, even in the case of a 'perfect' material that cyclic deformation will lead to crack initiation if the required amount of localised irreversible plastic slip is present. This is due to the generation of a 'slip step' as a result of dislocations appearing at the surface. This slip step, exposes the fresh metal surface to the air and therefore, most importantly, oxygen. Any oxygen that adheres to the metal surface prevents the 'rewelding' of the slip step during the load-reversal phase of the cyclical loading (i.e crack closure). It is in this instances that cracks begin to initiate at slip bands. Literature has shown that in the case of short fatigue crack growth, as is described in this chapter, crack growth is primarily driven by slip. It follows, therefore, that the higher the Schmid factor the greater the driving force for growth[125]. Work by Hunsche and Neumann[126] showed that crack formation is a result of slip localisation that is present in persistent slip bands (and corresponding dislocation pile-up) and that the crack and the persistent slip bands are well aligned. This is accompanied by higher concentrations of plastic strain which is also a major driving force for crack formation. This is especially evident in cases where the dislocations present in persistent slip bands cannot cross grain boundaries resulting in an ac-

cumulation of dislocations at these boundaries that leads to intergranular cracking[127].

By using high resolution electron backscatter diffraction (HR-EBSD), SEM imaging and MATLAB analysis the role of microstructure on crack initiation and crack path will be discussed. This chapter is separated into two sections - crack initiation and crack path analysis. In order to analyse the microstructure, MTEX an open-source toolbox for MATLAB was used to analyse EBSD data. The toolbox reconstructed grains using the orientation information gathered by the EBSD detector and Bruker software. Using a combination of polarised light images, EBSD maps taken before and after fatigue testing the initiation location of a crack and subsequent path can be investigated. The inverse pole figure (IPF) map that is of most interest in these studies is one showing the crystal axis parallel to the loading axis. This is so that slip system orientation can be discussed with respect to the loading axis. Figure 6.1 shows a typical specimen for which all three observations were made. Figure 6.1a is a polarised light image during testing with a crack formed but the sample not fully failed whilst Figure 6.1b shows an IPFY map with the primary crack laid over and Figure 6.1c shows an IPFY map and pattern quality image of the failed mesocantilever. It is clear from looking at this set of images that the fatigue crack is mixed intergranular and intragranular in nature (i.e it goes along grain boundaries as well as through the grain). In this chapter the reasons for this behaviour will be elucidated. In a polycrystal, there is a varying misalignment of the crystal between grains and this results in misalignment between the slip systems that can be activated from grain to grain as the crack propagates across the microstructure. This misalignment can significantly hinder crack growth and have a noticeable effect on its path. These effects can be measured both quantitatively, through GND density and crack deflection, and qualitatively, though observed slip band formation. In this chapter, the misalignment (m') between potentially active and activated slip systems will be measured and the effect that high or low m' has on the crack's behaviour will be described. An m' of 1 would signify there is no misalignment between active slip systems (they are parallel to each other) in neighbouring grains whilst an m' value of 0 is maximum misalignment between active slip systems (i.e the slip systems are perpendicular to each other).

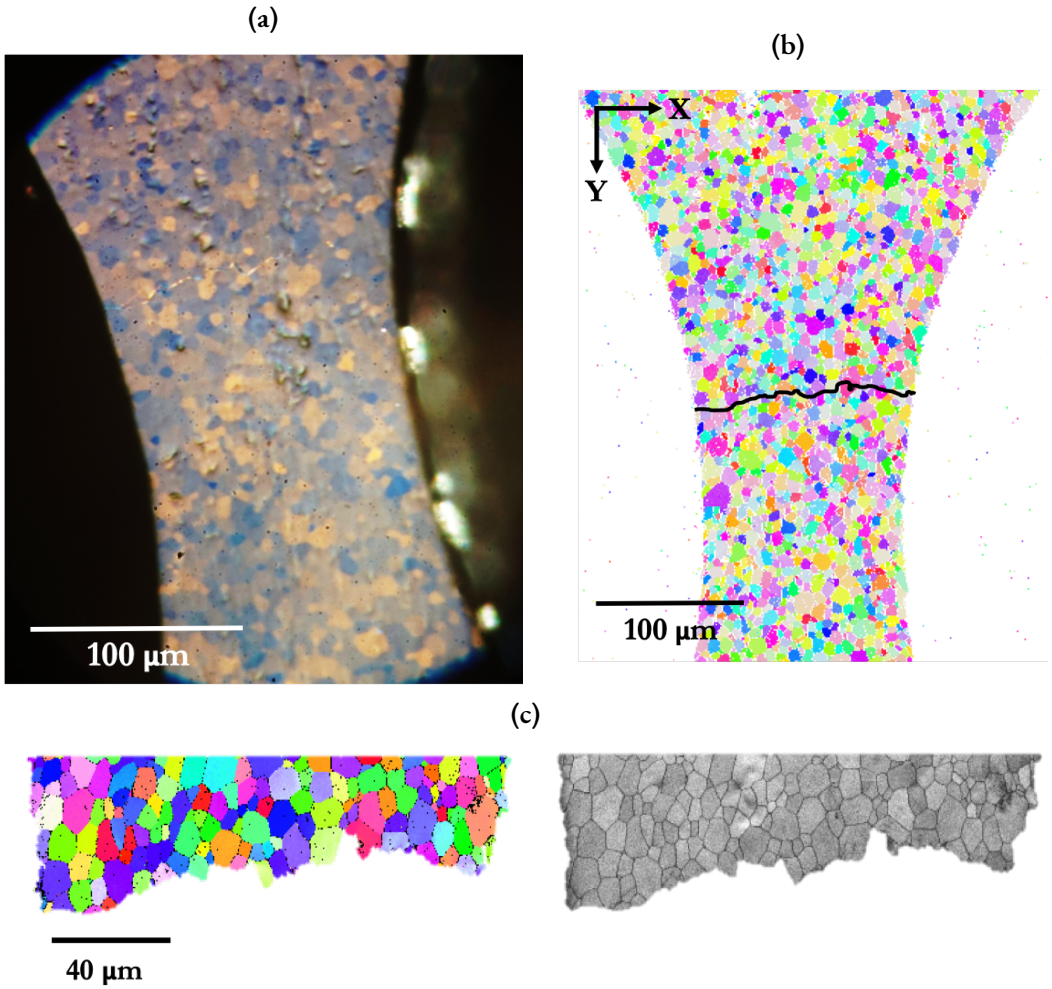


Figure 6.1: *Images showing different observations of a crack path in a CP Ti Grade 2 mesocantilever specimen. (a) Polarised light image of a crack growing through the mesocantilever (b) an IPFY map of the mesocantilever prior to testing with the crack path overlayed and (c) an IPFY map and pattern quality image of sample after failure.*

6.1 Initiation

As mentioned in the Chapter 5, initiation is of prime concern in high cycle fatigue as it takes the dominant part of fatigue life. It has been shown, by looking at fracture surfaces and capturing crack initiation in polarised light images (Chapter 5) that cracks tend to initiate at the edges of the mesocantilever. However, there is significant variation along the edge of the beam. By studying the mean orientation of the grains in which cracks initiate, as well as neighbouring grains, a link between microstructure and fatigue crack initiation locations can be determined. To do so, the

Schmid factor of the potentially active slip systems are calculated. The slip systems determined to be most likely to activate (due to their lower critically resolved shear stresses) are the <a> prism and <a> basal slip systems. The Schmid factor is calculated with respect to the tensile loading direction which in the case for all samples discussed in this chapter is along the y-axis when viewing the surface from above, as shown in Figure 6.1b. By performing this analysis at the initiation sites to determine the slip system activated (along with the majority of other grains along the crack path) it is clear that due to the multiplicity of prism slip systems and the overall texture present in the material that the prism slip system is most likely to be activated (as shown in Figure 6.2). From the maps that illustrate the Schmid factor of the basal slip systems and prism slip systems it can be seen that the majority of prism slip systems have a Schmid factor of above ~0.4 whereas the majority of basal slip systems have a Schmid factor of below ~0.3. As there are in total three different prismatic slip systems present in HCP metals, it was important to perform analysis on all three to determine which of the three had the best alignment to the crack path. MTEX allows the user to perform analysis of these different prismatic slip systems and as such the figures contained within this thesis include only the specific prism slip systems that align best with the crack path. In Figure 6.2 and the subsequent figures in this thesis that concern m' values, superimposed in the centre of each grain is a red arrow and blue line.

Figure 6.2 shows that it is easier, and therefore more likely, for slip to occur on the prism plane. Combining this with the SEM image (Figure 6.3) to determine the actual direction of the crack path and the m' maps, the alignment of the slip systems in the prism plane (and the actual crack path) is much better than that of the basal plane. Of the samples analysed to determine the slip system active in the grain where the fatigue crack initiated 79% of these were prism slip and 21% were basal slip (nine samples analysed). This is most likely a result of the orientation of the grains in this material being preferentially oriented for prismatic slip. It was also observed that in all cases, the crack originated within a grain rather than at a grain boundary. This is perhaps due to the edge of the cantilever being present within the grain and thereby promoting crack growth from within the grain rather than the grain boundary. To determine if there was any

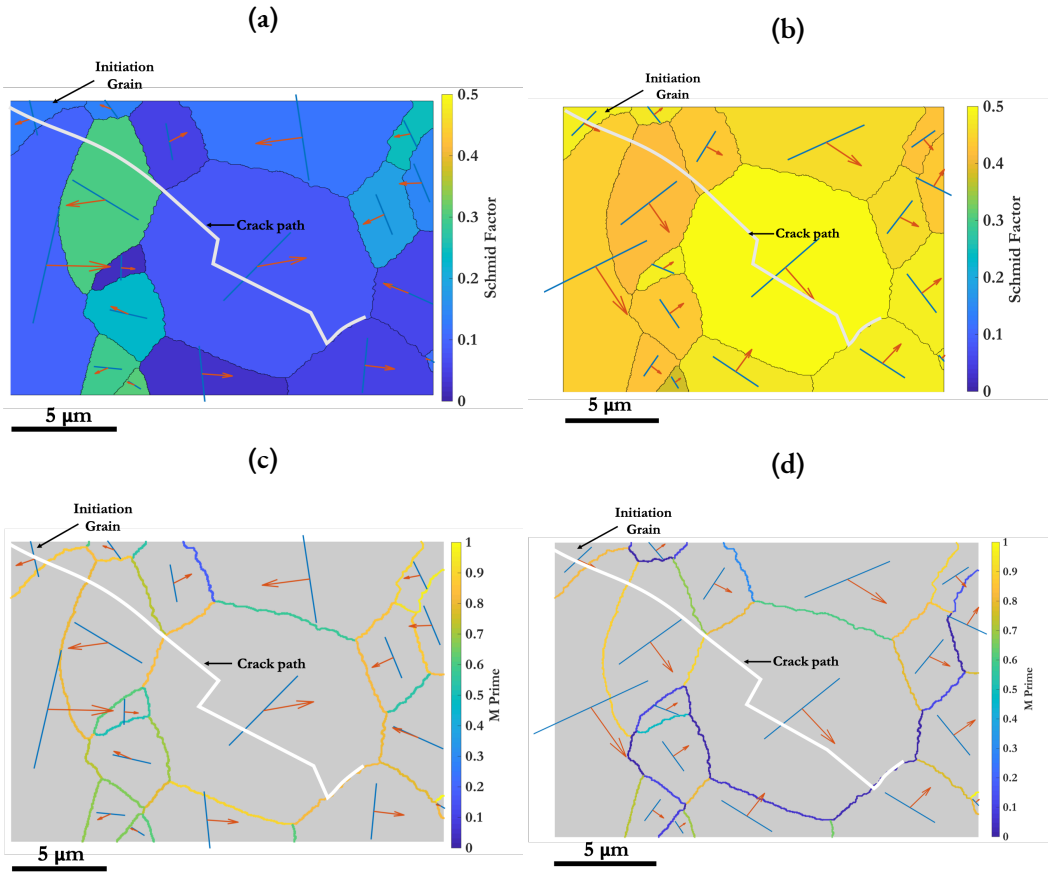


Figure 6.2: *Figures depicting the calculated Schmid factors for (a) Basal slip systems (b) Prism slip systems and the m' for (c) Basal slip systems (d) Prism slip systems for a fatigue crack initiation point. (Red arrows = slip plane direction, blue lines in the centre of the grain indicate the slip plane normal).*

effect on the initiation point as a result of the local texture, it was compared to the global texture of the sample. Local texture in this case is defined as the 10 neighbouring grains surrounding the grain in which the crack initiated. Due to the grain size, 10 grains were chosen as it was a large enough number to be representative of the crack initiation area but small enough so as to elucidate any local texture properties. Figure 6.4 is an example of specimen where a primary crack has initiated but the mesocantilever is still intact. This provided the ideal sample upon which to perform local texture analysis (Figure 6.5). As demonstrated by Figure 6.5, and as was seen in all the samples examined, the local texture as not dramatically different to the global texture. As this sample is cold-rolled, commercially pure titanium this is not surprising as there is no chance of the formation of macrozones that are sometimes seen in titanium alloys. This suggests there is

no clear relationship between the fatigue crack initiation point and texture.

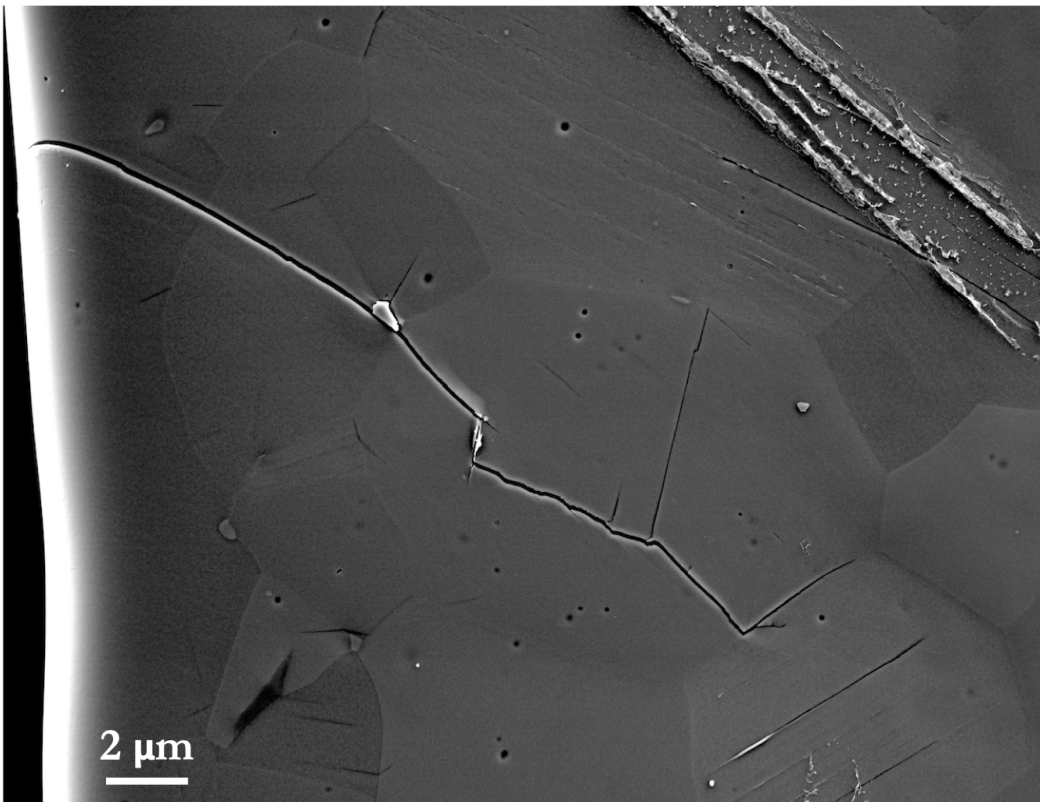
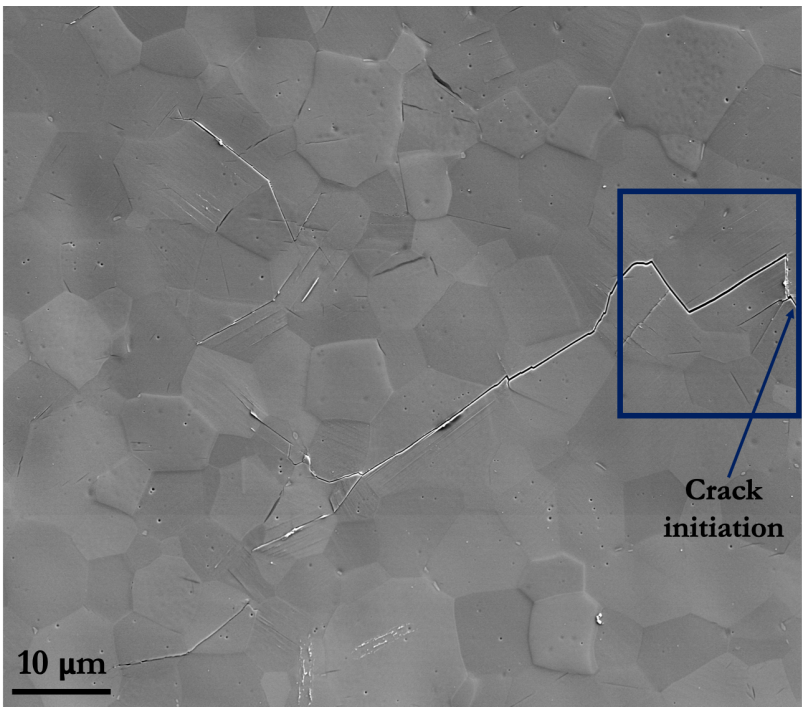


Figure 6.3: *SEM image of a secondary crack in a CP Ti sample fatigued for 40,000 cycles at 275 MPa.*

(a)



(b)

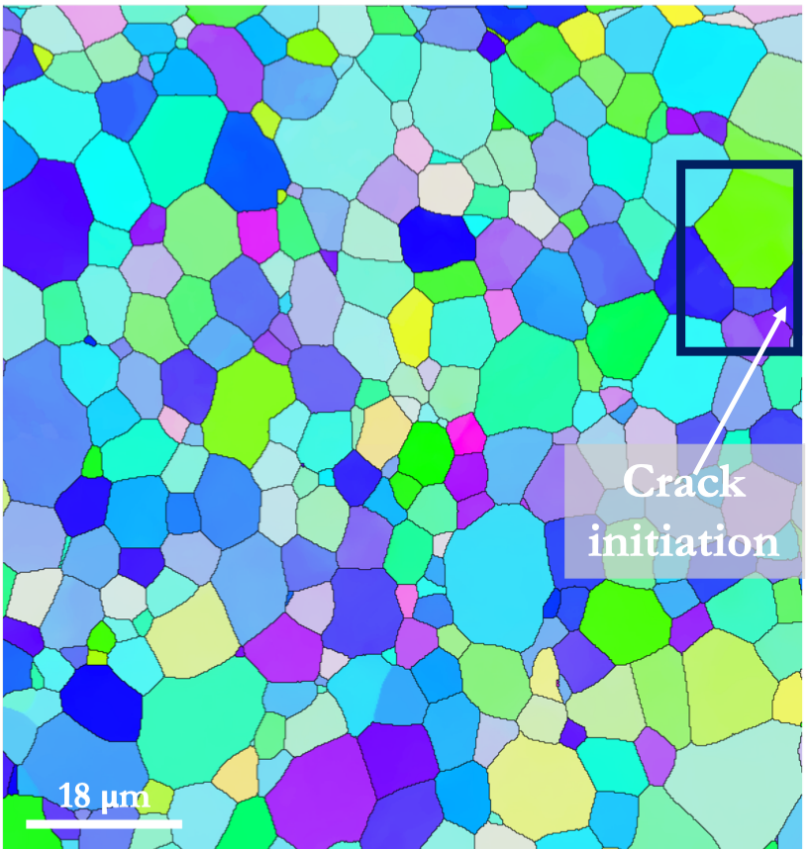


Figure 6.4: *(a) SEM image of a primary crack in a CP Ti mesocantilever tested for 40,000 cycles at a stress amplitude of 275 MPa and (b) corresponding IPFY map.*

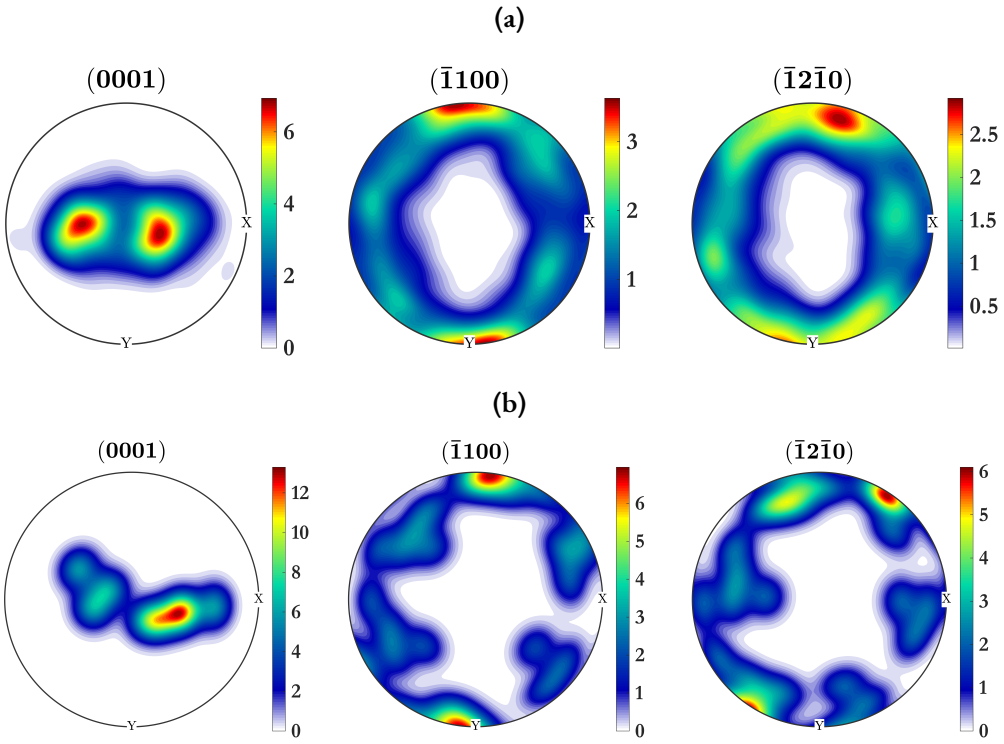


Figure 6.5: *(a) Pole figure displaying the overall texture of the CP Ti mesocantilever presented in Figure 6.4 and (b) Pole displaying the local texture around the primary crack initiation point (information obtained from the area surrounded by the blue box in Figure 6.4.*

As mentioned previously, there are several instances where multiple cracks initiate along the length of the beam of the same sample. In the majority of cases these cracks are relatively small compared to the primary crack. However, in some cases the growth of these secondary cracks is significant and their initiation times are relatively close to that of the primary crack. Figure 6.6 is an example of such a case, where the primary crack initiated after 40,000 cycles where as the two secondary cracks labelled (A and B) initiated at 50,000 cycles and 70,000 cycles respectively. In the case of these three initiation points, their second Euler angles (Phi) that dictate the inclination of their c-axes towards the plane of the surface of the mesocantilever are 26°, 164°and 13.6°respectively. As Schmid factor is highest when the slip plane is 45°to the loading direction, the closer these grains are oriented for that to happen the higher the chance a crack initiates at that location. The grain in which secondary crack A begins has the highest Schmid factor of the three initiating grains (0.48) as it is the most well oriented, whereas the primary crack initiating grain

has a Schmid factor of 0.47. These aren't far from each other and there be other reasons (perhaps the effect of grains underneath the surface) that cause the primary crack to initiate where it does. The similarity in Schmid factor, however, can explain why secondary crack A initiates so soon after the primary crack, only 10,000 cycles. This is in contrast to secondary crack B which initiates a further 30,000 cycles after the primary crack (the grain in which secondary crack B initiates has a Schmid factor of 0.43).

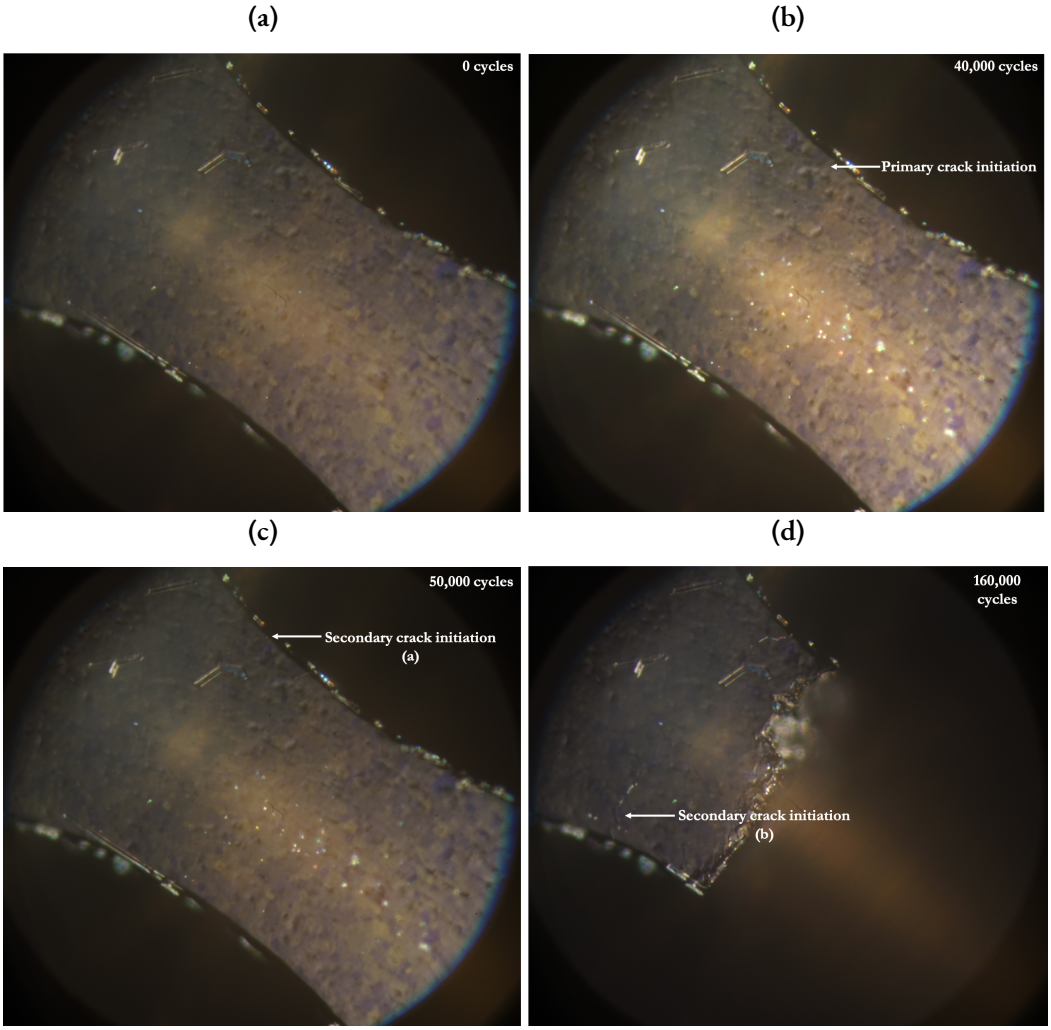


Figure 6.6: *Polarised light images of a CP Ti mesocantilever tested until failure at 365 MPa at (a) 0 cycles (b) 40,000 cycles (c) 50,000 cycles and (d) 160,000 cycles.*

6.2 Crack Path Analysis

As with the previous section, calculation of m' is key in understanding the crack's path. This will be combined with GND density data obtained using HR-EBSD analysis and SEM images that have captured slip bands on the surface. As was discussed in the literature review, the change in direction of the crack between grains can be described by either a tilting or twisting change. Figure 6.7 illustrates the angles associated with each type of direction change. In this schematic the path of a crack can be seen travelling from one grain into another. The activated planes in each grain intersect at the grain boundary between the two grains and it is the angles required for the crack to twist (α) and tilt (β) to move onto the activated slip plane in grain 2 that are measured. $\alpha = \psi_1 - \psi_2$ and $\beta = \theta_1 - \theta_2$. The hypothesis is that the larger the α and β angles, the more resistance there will be to crack progression. This can result in a crack changing direction and branching or even stopping at the boundary completely. Understanding the underlying mechanisms that cause a crack to stop at a certain point in the material is important as it will provide insight into the growth behaviour of a crack during cyclic loading. To investigate the phenomena at the crack tip, HR-EBSD, Electron Channeling Contrast /Imaging (ECCI), Transmission Kikuchi Diffraction (TKD) and SEM imaging were used. Cross-correlation analysis was performed on data obtained from HR-EBSD and TKD using XEBSD code produced by Britton and Wilkinson. This allows for the study of the geometrically necessary dislocation (GND) distribution at the crack front. The principles underlying cross-correlation analysis are described in detail in Section 1.5 of the literature review. By examining the crack tip, it is possible to gain a better understanding of crack development in much more detail than before. At the crack tip there is information regarding the plastic strains and related GND density that is present. This can give information such as the size of strain present and the potential future direction of the crack path. These phenomena can then be related to the surrounding microstructure. Once the crack grows further, this information is lost due to stress relaxation induced by the presence of the crack. As such, it is not possible to investigate these properties in samples that have fully failed. In this section the link between grain orientation and crack tip properties will be explored. The crack tips observed in this thesis can

be categorised in to two types - the 'surface' crack tip and the 'bulk' crack tip. The surface crack tip is the tip as visible on the surface of the mesocantilever whilst the bulk crack tip is that which extends into the depth of the mesocantilever. The 'bulk' crack tip is investigated by performing a FIB lift-out (as described in Section 2.2.3) of the area where the crack-tip is thought to extend to from the surface. The crack tips investigated were of both primary cracks and secondary cracks.

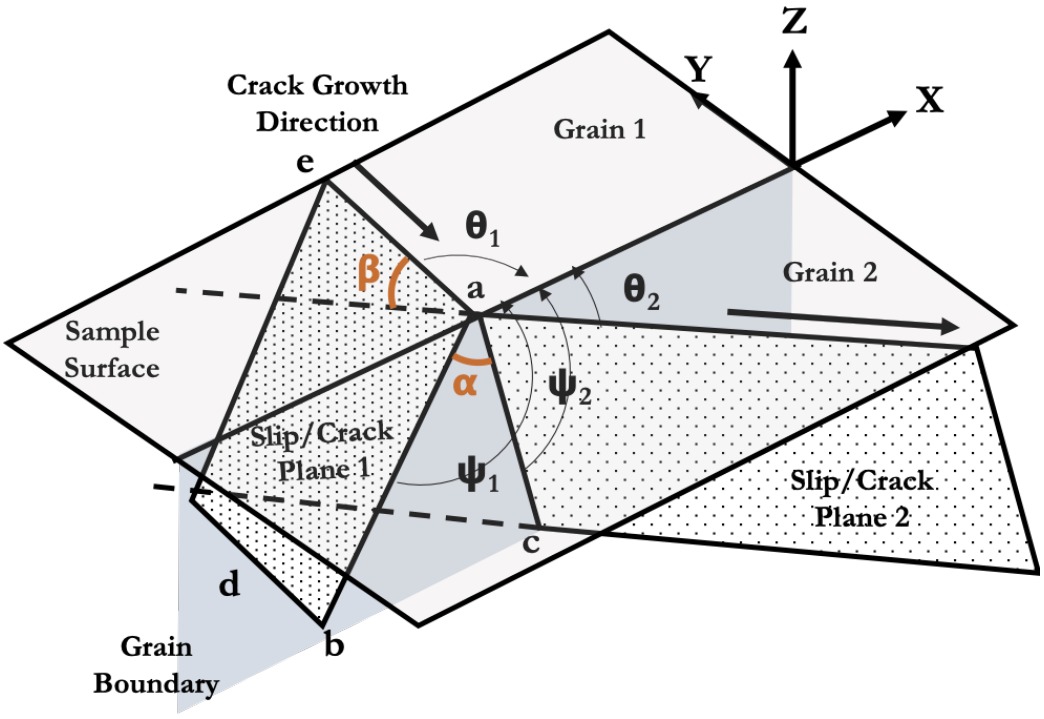


Figure 6.7: *A schematic depicting the twisting and tilting angles (α and β respectively) of a crack travelling from grain 1 into grain 2. (Reproduced from Zhai et al [1])*

Figure 6.8 is an SEM image of a CP Ti mesocantilever sample that was fatigued for 40,000 cycles at a stress amplitude of 275 MPa. This image shows a large amount of features that are of interest – slip bands minor crack branching and a major crack bifurcation point (these features are labelled in the figure). To probe these features further a HR-EBSD map was obtained and cross-correlation analysis using XEBSD was performed. The first step of cross-correlation analysis was to confirm that the cross-correlation analysis matched the test and reference pattern and that the solution for lattice rotation and strain was well-defined. This validation is presented in Figure 6.9. Here, it can be seen that there is a good match between the analysis and the test and reference

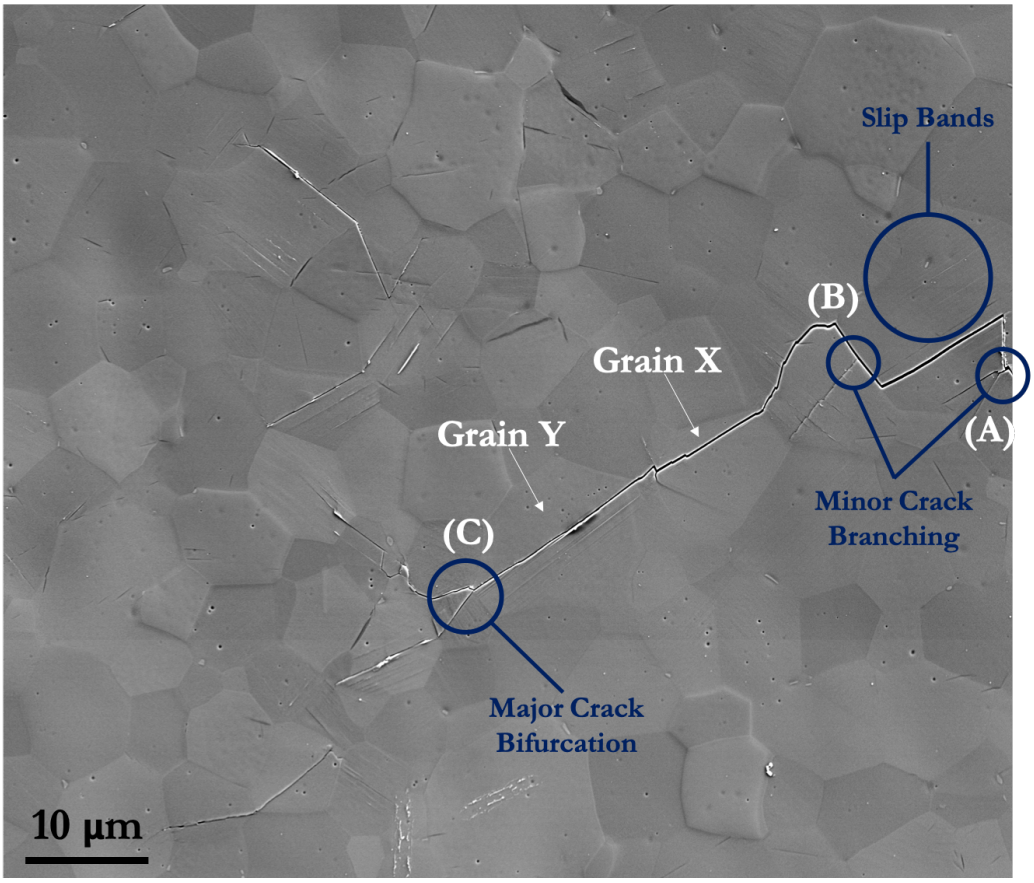


Figure 6.8: *SEM image of a primary crack in a CP Ti sample fatigued for 40,000 cycles at 275 MPa.*

pattern (the peak height is close to 1) and the small mean angular error confirms that the solution for lattice rotation and strain is indeed well-defined. There are a few grains that seem to have 'dropped' out of the analysis i.e they are incorrectly indexed/analysed due to poor pattern quality. As such, they are omitted from final GND density calculations and appear white in Figure 6.10.

In this sample it can be seen that the crack initiates within a grain and continues straight before reaching the next grain boundary, at a triple junction, where there is a slight deflection before continuing with intragranular growth until reaching a grain where there is a sharp deflection. This deflection does not correspond with the prismatic slip plane that was predicted to be most likely to be active, nor with the basal slip plane. What has been observed for primary cracks in a number of samples is that at the initiation point the global Schmid factor is insufficient in determining the active slip plane and that there are other factors that affect crack direction at this point.

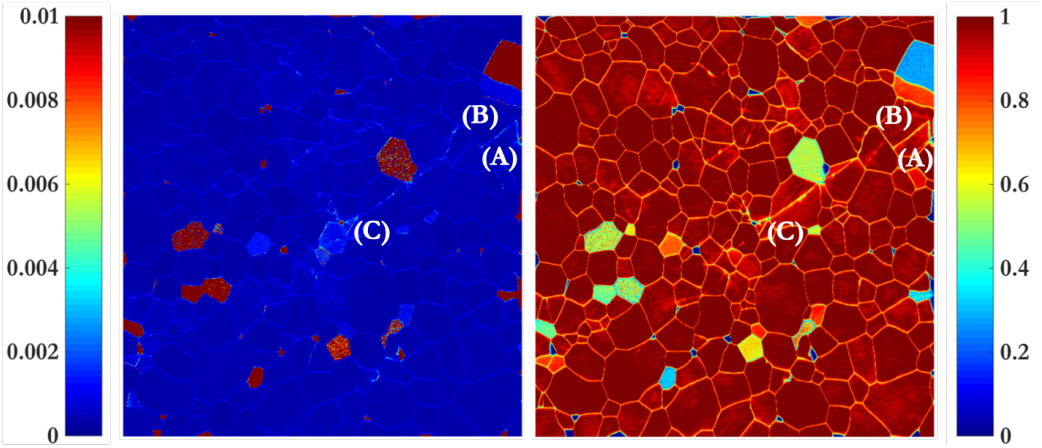


Figure 6.9: *Data quality maps achieved by cross-correlation analysis using XEBSD of the sample from Figure 6.8. The peak height map (right) shows the slip bands and crack present in the sample whilst the mean angular error map (left) shows small errors as well as picking up the primary crack and some of the slip bands.*

However, after the crack has travelled across the sample and through several grains its direction begins to follow the slip directions determined more closely. This behaviour is also captured by the GND density map in Figure 6.10 where a higher density accompanies the parts of the crack path where the m' between grains is low (i.e poor alignment of slip systems). Figure 6.10 is an HR-EBSD map of a primary crack along with the XEBSD analysis of the area that shows higher GND density present alongside the crack and the tip. The crack can be easily picked up in the GND density map as there are significantly higher concentrations surrounding the crack path compared to the rest of the sample. What is also noteworthy is that the GND density appears to be higher at points where the crack path changes direction abruptly as well as at the points where the crack has minor branches, the major bifurcation point and at the tips of each path (these points are indicated accordingly in the figure). One of the points at which GND density is highest is in fact at the point at which the crack path bifurcates.

From Figure 6.11(a) it can be seen that in the case of the in-plane components of the elastic strain tensor (ε_{11}, ε_{12} and ε_{22}) the areas of larger strain activity are aligned with the high GND density areas in the map from the same sample in Figure 6.10. Meanwhile, in comparison, there is much less activity present in the out-of-plane components of the strain tensor (ε_{13}, ε_{23} and

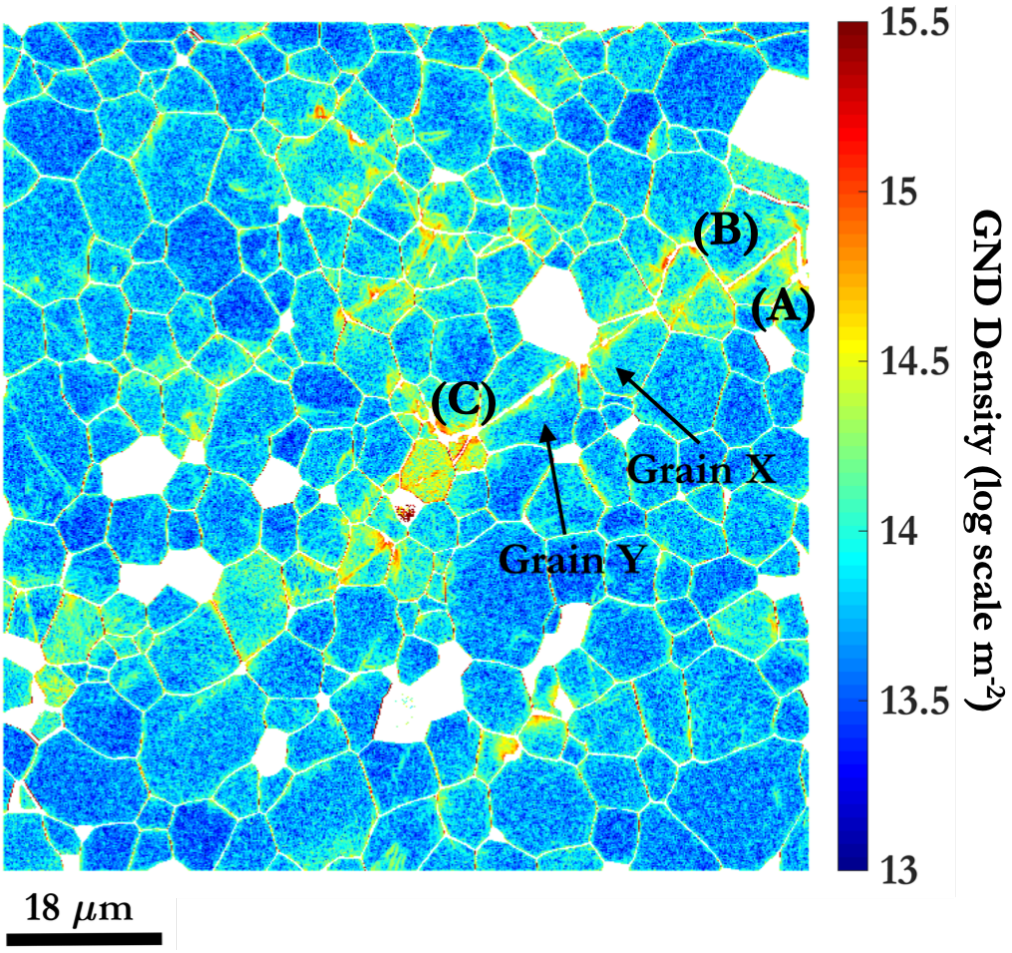
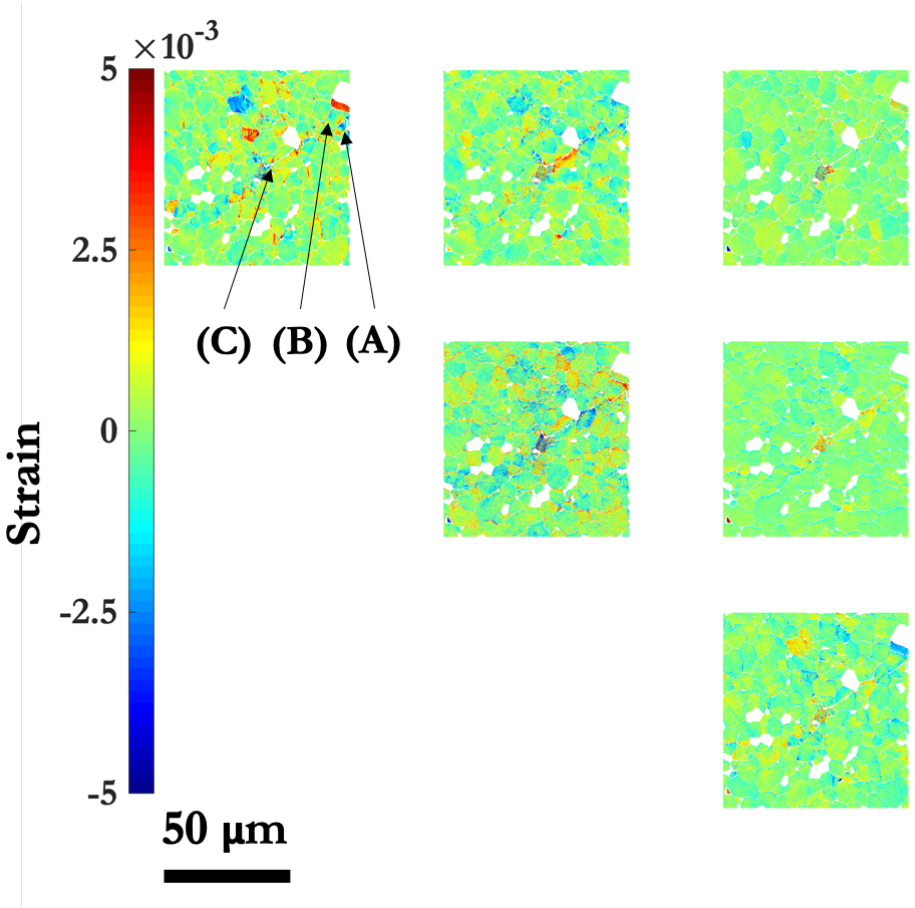


Figure 6.10: *GND Density map of area displayed in Figure 6.8 (Step size = 0.15 μm).*

ε_{33}). It is clear that even after testing has ended, there is a heterogeneous distribution of elastic strain present in the sample as a result of the plastic deformation that has occurred during fatigue testing. The distribution of stress, Figure 6.11(b), is also heterogeneous and in good agreement with the distribution of elastic strain. There are still significant 'hotspots' of stress at the crack tips and the divergence point. This is because as the crack grows it results in stress relaxation around it whilst the residual stresses remain high at the crack front.

(a)



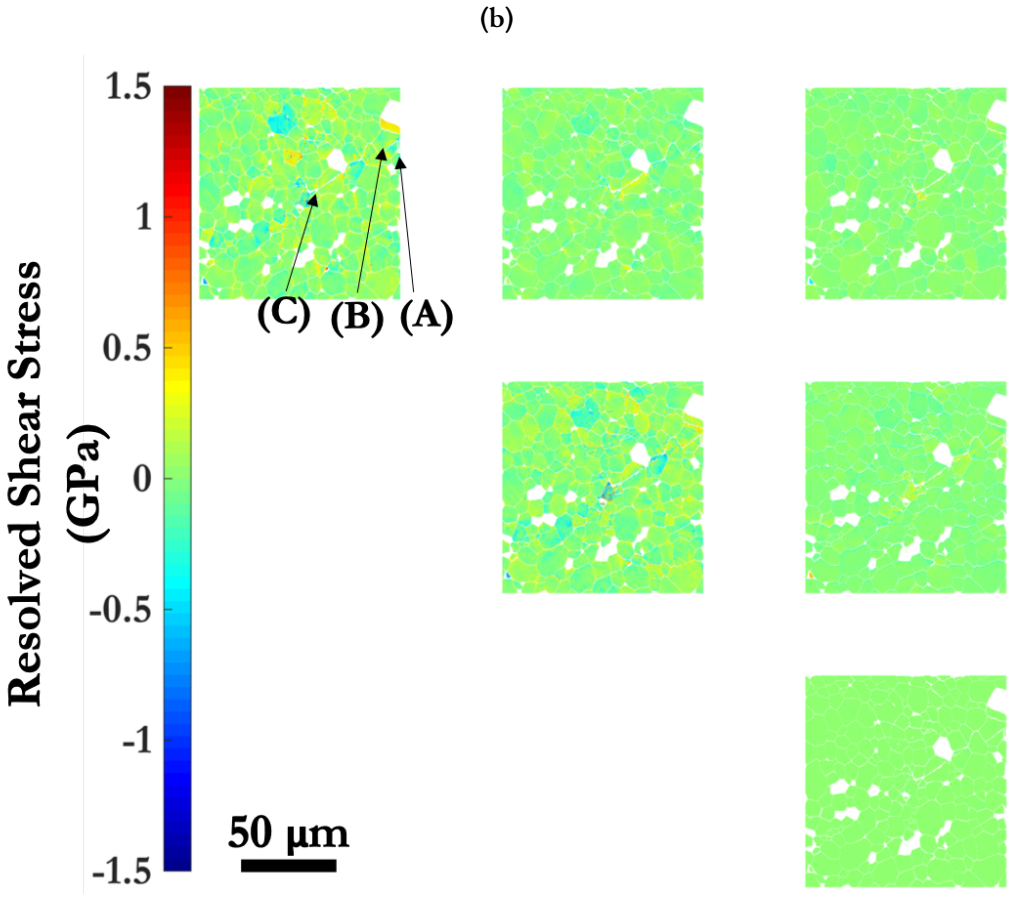


Figure 6.11: *The components of (a) strain (b) stress as determined by cross-correlation of the primary crack present in the sample from Figure 6.10.*

In the case of Grain X and Grain Y in Figure 6.8 it can be seen there is little deflection of the crack. It travels along a small grain boundary in between, the two grains but emerges into Grain Y in roughly the same direction as in Grain X. This small deflection in crack direction is also reflected in the GND density map (Figure 6.10) where there is a relatively low GND density when compared with other areas of the crack. There are also no slip bands related with this section of the crack. Conversely, there is significant misalignment between Grain Y and the major bifurcation point (m' of 0.48). One path moves through the grain along the higher Schmid factor basal plane (0.42) rather than the prism plane (Schmid factor of 0.28). This misalignment results in slip bands forming in the grain as the crack attempts to progress. Looking at the crack bifurcation point more closely in the SEM image it can be seen that the lower crack disappears on the surface. It is highly possible that it has diverted into the bulk due to the large misalignment between potential slip systems in the neighbouring grains. The m' values for the corresponding grains are visualised in Figure 6.12. The blue line represents the slip plane normal as it intersects with the sample surface whilst the red arrow represents the Burgers vector / slip direction if viewed from above in 2D. The argus image, which displays the slip bands in the area clearly, shows a large number of slip bands at the boundaries where m' is low. This suggests that the poorly oriented planes result in the build up of plastic deformation at these points due to the cracks inability to travel further along the surface. The slip bands also indicate how poorly aligned the slip systems are between Grains 1 and 2 as it can be seen that the slip band traces in Grain 2 are ~74°to those in Grain 1. The crack then re-emerges in Grain 3 ~28°away from parallel. This is also rationalised by the GND density map where there is a visibly higher GND density at the points the crack disappears and reappears. This is a prime example of the effect misalignment between grains can have on the crack path and the build up of plastic strain at these points. The crack then progresses into the next grain (Grain 4) that has a near maximum m' which is accompanied by no clearly visible slip bands at the boundary (the m' here is 0.83). The crack stops at the boundary, though the alignment here is also good (m' = 0.89). There are visible slip bands beginning to appear at this point as the grain after Grain 5 is poorly aligned for the continuation of the crack (m' = 0.38).

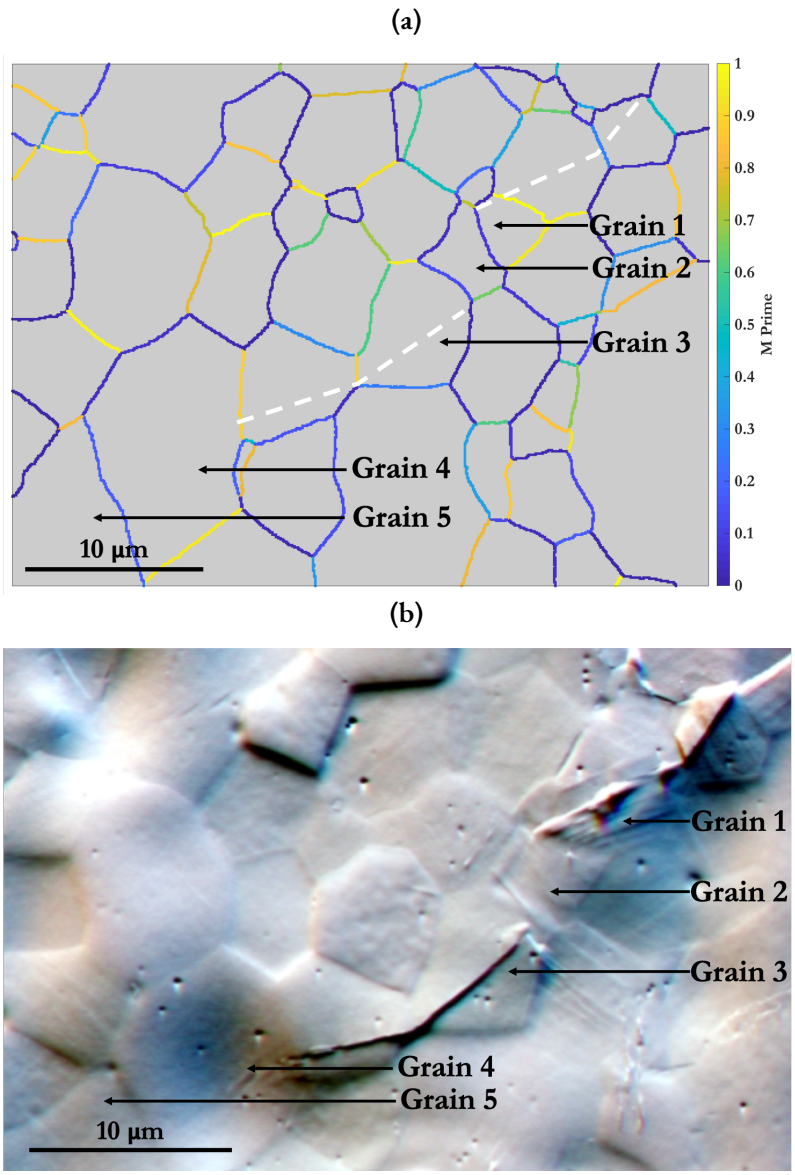


Figure 6.12: *(a) Misalignment (m') between most likely active slip plains in grains for the lower crack portion marked in Figure 6.8 and the corresponding (b) argus image. (Red arrows = slip plane direction, blue lines in the centre of the grain indicate the slip plane normal).*

In the case of the other branch of the crack, when comparing the GND density map, the overall m' map (Figure 6.13) and the SEM image in Figure 6.8, the link between the larger misalignment of the active slip systems from grain to grain corresponds with the more visible slip bands and rougher surface as well as a higher GND density (particularly at the start of the bifurcation of the crack). In every case that the crack disappears from the surface it does so at a grain

boundary with which there is very large misalignment. Figure 6.14 is a histogram that shows the percentage of grains along the crack path with specific misalignments compared with the misalignment between all grains in the area mapped. This figure shows that there is better alignment of slip systems along the crack path than the general area. In the case of the crack path grain boundaries, over 50% of grains have an m' greater than 0.5 whilst in the case of all grain boundaries within the area mapped 60% of grains have an m' less than 0.5 and more than half fall in the lowest alignment bucket (0 to 0.25). This suggests that the alignment along the crack path is greater than that of the average alignment between grains in the sample. However, it also indicates that nearly 50% of grains have an m' of less than 0.5 between slip systems, relatively high misalignment, which is why the crack grows along the grain boundary along most of the path.

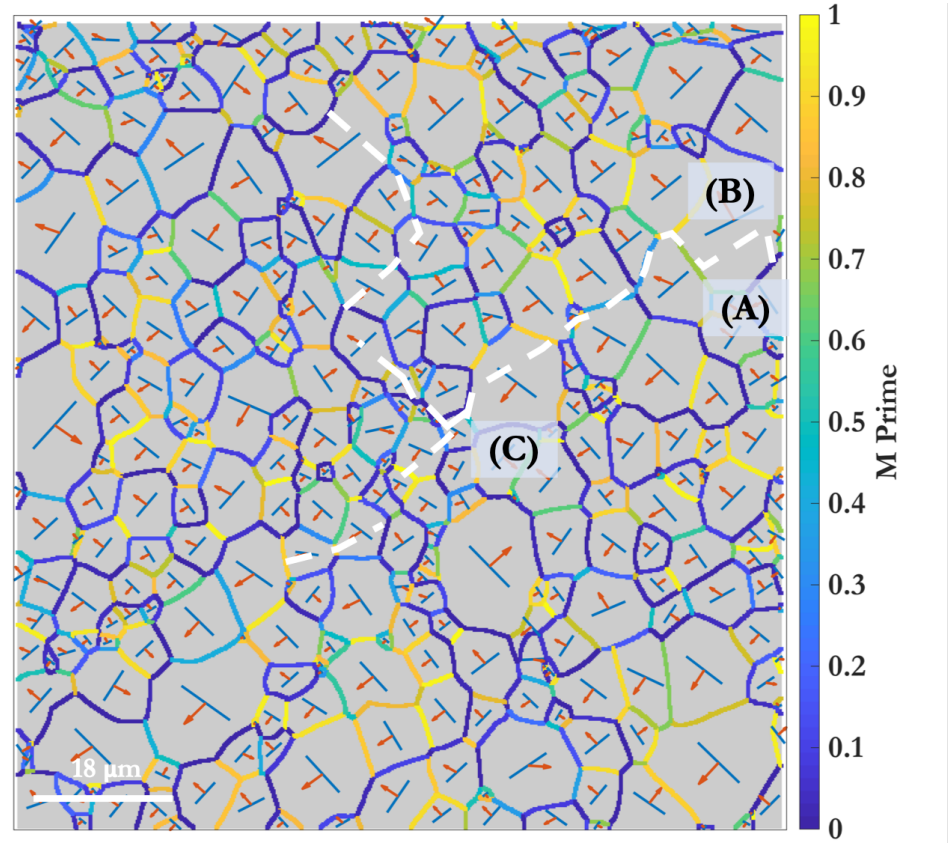


Figure 6.13: *Map showing the misalignment between activated slip systems for the crack displayed in Figure 6.8. (Red arrows = slip plane direction, blue lines in the centre of the grain indicate the slip plane normal).*

To further validate the above histogram results, several 'virtual' cracks were created by ran-

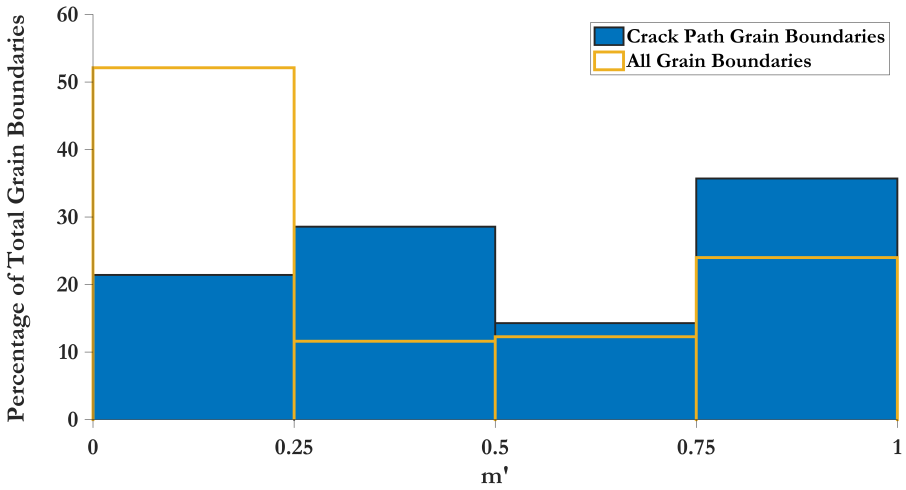


Figure 6.14: *Histogram showing the percentage of grains with varying misalignments between grains along the crack path for the crack displayed in Figure 6.8 and all the grains in the area.*

domly selecting a series of connected grains in the transverse direction to replicate the crack growth direction of the real crack observed. These virtual cracks were chosen according to specific criteria to ensure they were representative of potential crack paths similar to the original. Firstly, they needed to originate from the same side as the real crack. Secondly, the 'length' of the crack needed to be similar to the real crack and as such there are seven to eight grains in each virtual crack. Thirdly, they needed to be independent of each other to ensure enough grains were sampled (i.e. each virtual crack had unique grains selected when compared to the others). The randomly selected virtual cracks are displayed in Figure 6.15. The aim of these virtual cracks is to demonstrate that the better m' values seen in the real crack path compared to the overall m' values were not due to sampling. As such, a histogram comparing the m' of these virtual cracks and the real crack are shown in Figure 6.16. From this figure, it can be seen that the percentage of grains that have significant misalignment (m' between 0 and 0.25) is nearly 60%. This is nearly three times higher than the crack path grains with a similar m' and slightly higher than the value seen for all grain boundaries across the sample (Figure 6.14. Likewise, the number of grains that fall into the buckets of better alignment (0.5 to 0.75 and 0.75 to 1) are both considerably lower than the real crack path (20% and 30% lower respectively). Therefore, it can be concluded that

cracks do indeed follow a path with higher alignment between the grains.

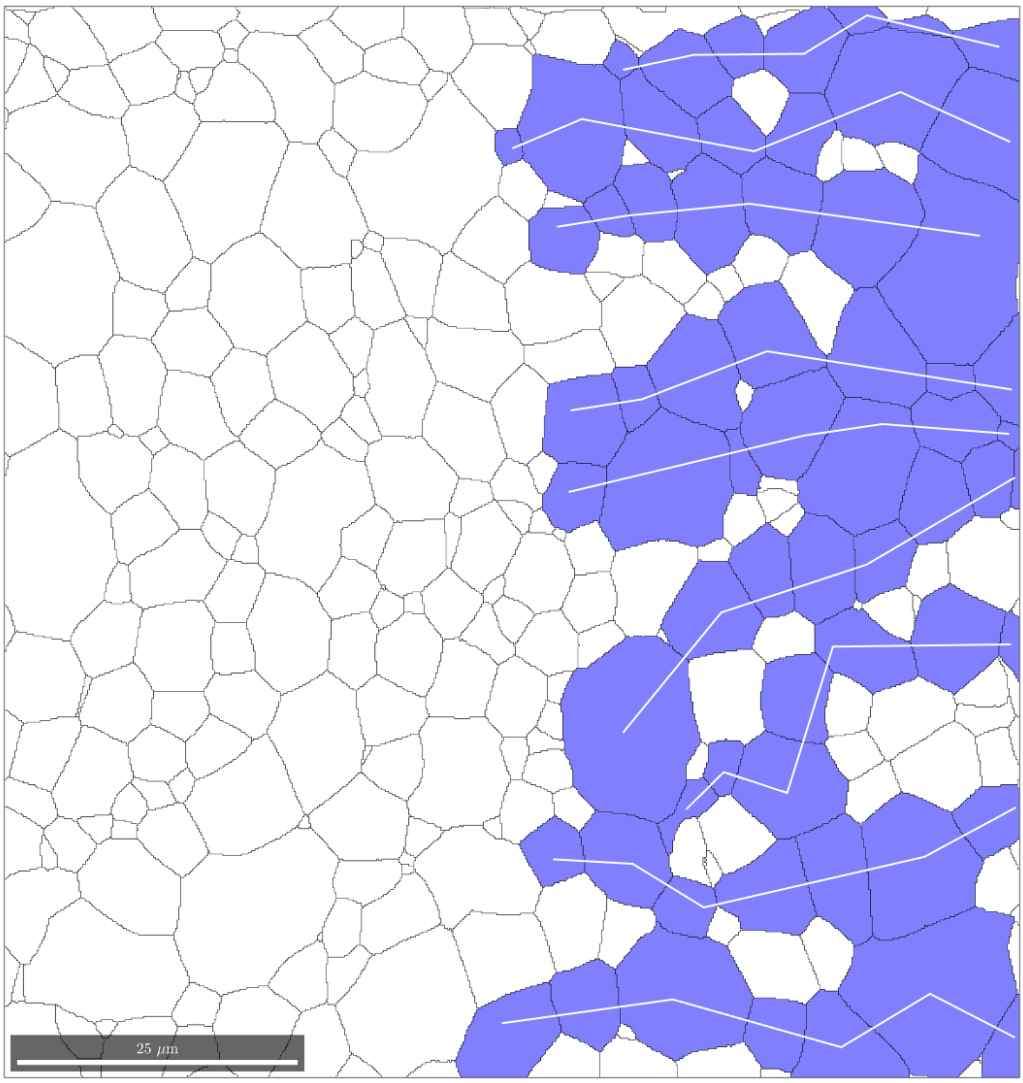


Figure 6.15: *A schematic of grain boundaries for the area displayed in Figure 6.8 and a series of randomly selected 'Virtual Cracks'. The white line indicates the grains each virtual crack intersected.*

As can be seen in Figure 6.17, there is no clear correlation between the Schmid factor and the path the crack chooses to take. Largely, the grains along the real crack path and the virtual crack path have a high global Schmid factor (between 0.4 and the maximum of 0.5) and there appears to be a fairly random distribution between observed Schmid factors between these values. However, it is important to note that the Schmid factor values calculated here are global Schmid factors with the assumption that the tensile direction is in the y-axis (as was described earlier in this chapter). At a more local level, there may be significant tensile stresses on each grain (particularly as a crack

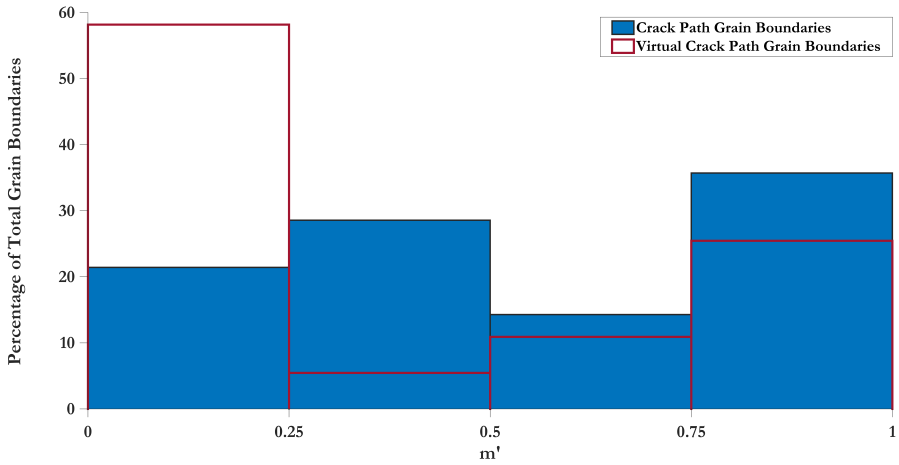


Figure 6.16: *Histogram showing the percentage of grains with varying misalignments between grains along the crack path for the crack displayed in Figure 6.8 and a series of randomly selected 'Virtual Cracks' displayed in Figure 6.15.*

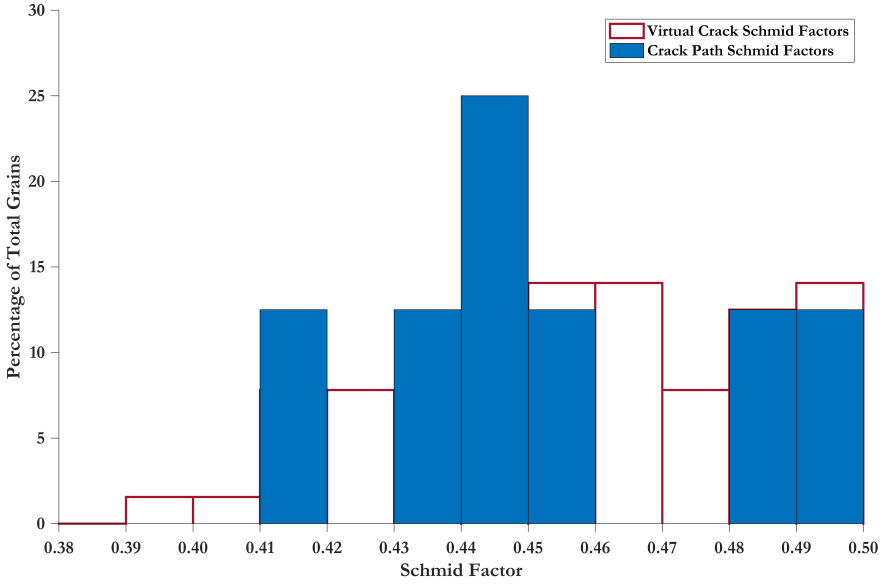


Figure 6.17: *Histogram showing the percentage of grains with varying global Schmid factors for both the grains along the crack path and for the crack displayed in Figure 6.8 and a series of randomly selected 'Virtual Cracks' displayed in Figure 6.15.*

begins to form) that would have a greater effect on the measured Schmid factor than the global tensile stress. To determine this, requires a significant amount of modelling and characterisation. This modelling will be suggested as future work at the end of this thesis.

In a sample that had been tested at 365 MPa and had a full fracture after 1.6 x 10^5 cycles sev-

eral secondary cracks were observed. These were also analysed by HR-EBSD. In the case of one secondary crack (Figure 6.18) there is clearly a relatively high GND density (Figure 6.19) surrounding the crack and at each crack deflection point. If one compares the overall GND density for this secondary crack, to the primary crack in Figure 6.10, it is clear that there is a greater deal of plasticity further away from the crack. This is due to the greater misalignment of potentially active slip systems along the crack path for the secondary crack when compared to primary crack. This greater misalignment results in more resistance for the crack to progress and, therefore, more pile-up of dislocations along the crack path. The significant misalignment between grains along the crack path can be seen in Figure 6.19a. Here, the m' map is overlaid on the SEM image of the crack and the very low compatibility between active slip systems when compared with that of the primary crack is evident. This is further supported by the large amount of visible slip bands in Figure 6.18 whereas in the primary crack there are less fewer slip bands on the surface except for in the instances where there is poor alignment between neighbouring grains. The high misalignment between grains along the crack path also results in the crack preferentially travelling along the grain boundaries rather than through the grain. In the cases where the crack extends into the grain and grows through it is when the m' is close to 1. These differences of m' between the primary and secondary crack paths explain quantitatively why a certain crack, once initiated, grows more favourably than others and is then the cause of failure in a sample. What is also evident from both cases is that when alignment is poor between slip systems in neighbouring grains, the crack will grow along a boundary. The crack does stop at a triple junction before bifurcating along the boundaries of two grains that have low m' with respect to the previous grain. In the case of this secondary crack a histogram plot illustrating the percentage of grains along the crack path with specific misalignments compared with the misalignment between all grains in the area mapped was also produced (Figure 6.20. As with the previous example in Figure 6.14 the plot shows that there is significantly better alignment between slip systems in neighbouring grains along the crack path than the overall alignment of slip systems in all grains. However, in this case the alignment for the crack path grains is noticeably better than that in Figure 6.14. This is also reflected in the

path of the actual crack seen in Figure 6.18 as it is more transgranular than the crack in Figure 6.8.

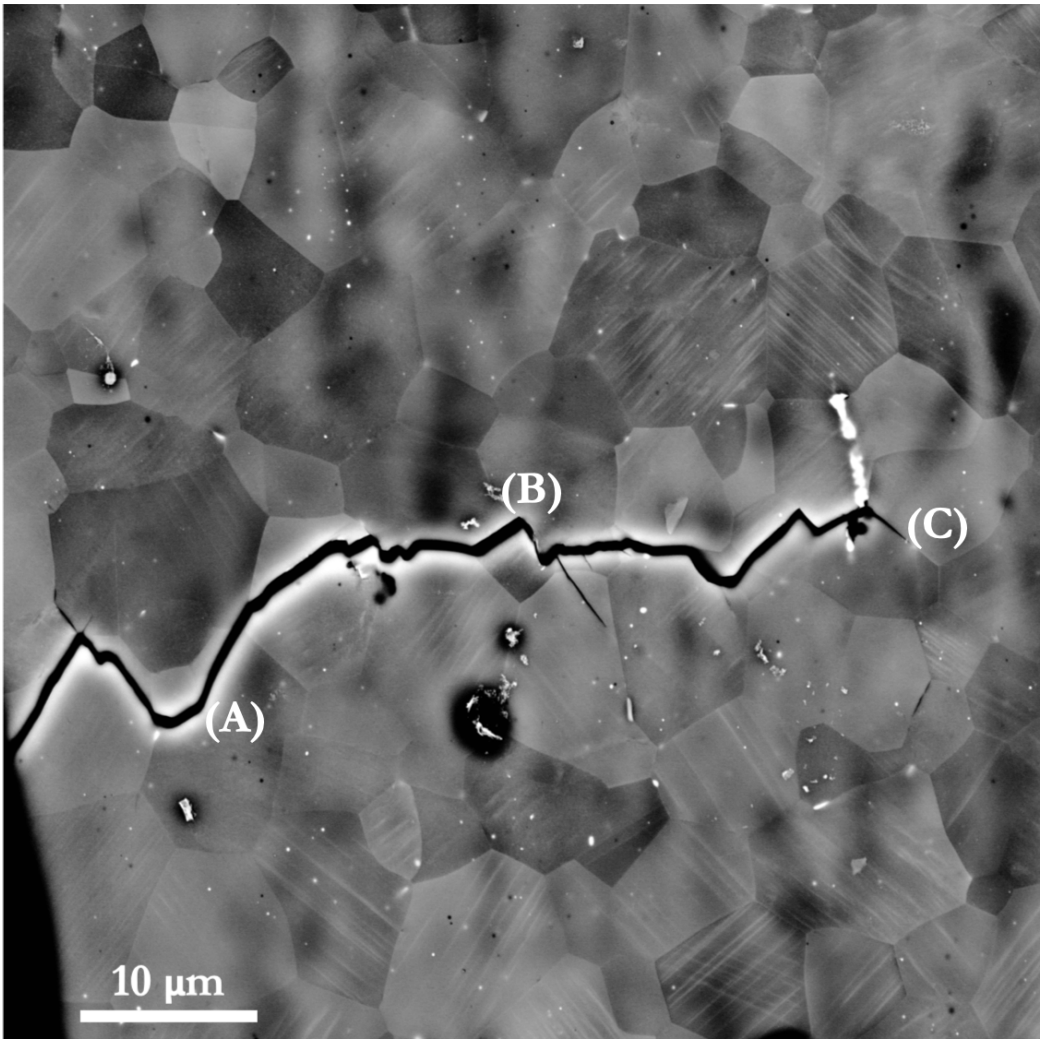


Figure 6.18: *An SEM of a large secondary crack originating from the side of a CP Ti mesocantilever tested at a stress amplitude of 365 MPa with a fatigue life of 1.6 x 10^5 cycles.*

So far, the discussion regarding crack tip phenomena has focussed on the surface tips of the crack but as was seen in the fractography analysis in Chapter 5 the crack grows into the bulk from the surface. As such, lift-outs were performed of the area near the crack tip (the process for which was described in Chapter 2) to examine the direction of crack growth into the bulk and the phenomena present at this 'bulk' tip. By testing at a high stress amplitude, 365 MPa, a large secondary crack was introduced into a specimen that had a fatigue life of 1.6 x 10^5 cycles. A

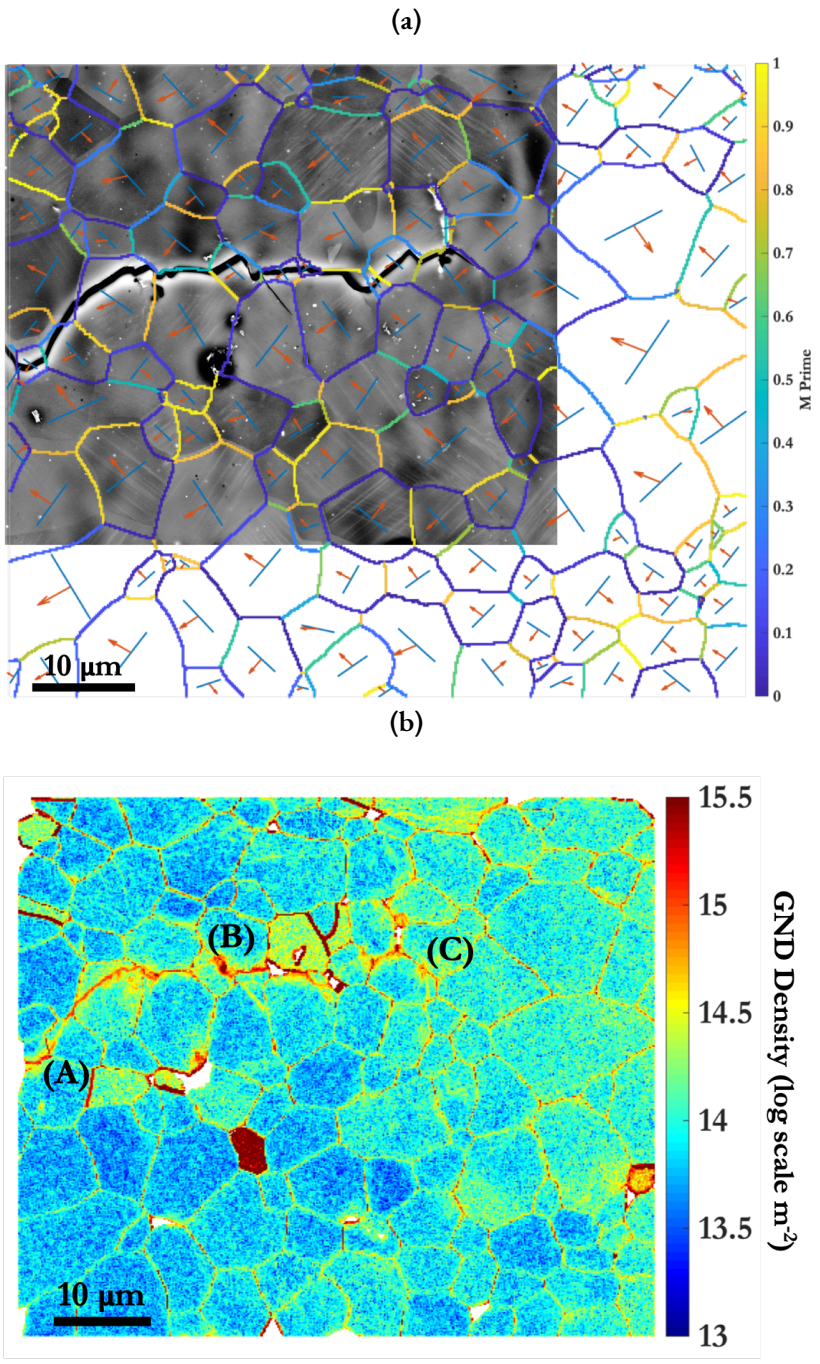


Figure 6.19: *(a) Misalignment (m') between most likely active slip plains in grains and the corresponding (b) GND map for the crack displayed in Figure 6.18. (Red arrows = slip plane direction, blue lines in the centre of the grain indicate the slip plane normal).*

FIB lift-out was obtained from the crack tip of this secondary crack to investigate the 'bulk tip'. Figure 6.21 shows an SEM image of this secondary crack, the lift-out location as well as the cor-

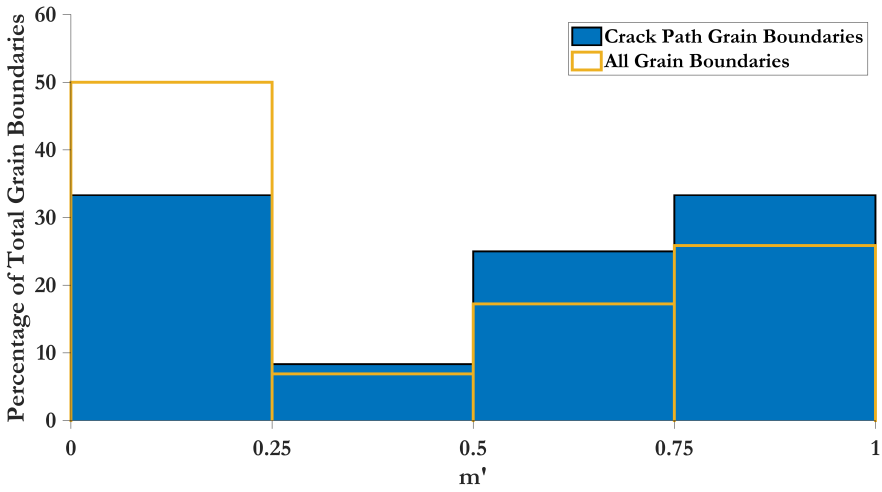


Figure 6.20: *Histogram showing the percentage of grains with varying misalignments between grains along the crack path for the crack displayed in Figure 6.18.*

responding 'bulk tip'. The SEM image of the lift-out (Figure 6.21b) shows that the crack stops

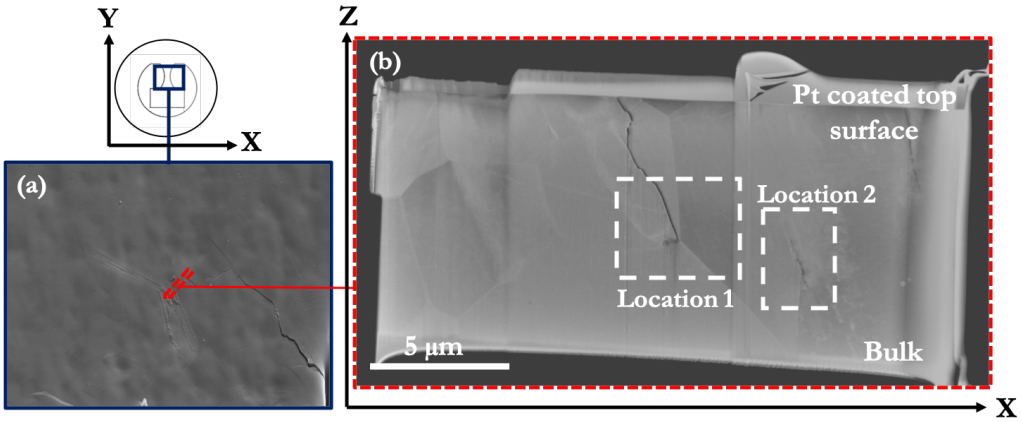


Figure 6.21: *(a) SEM image of a large secondary crack originating from the side of a CP Ti mesocantilever tested at a stress amplitude of 365 MPa with a fatigue life of 1.6 x 10^5 cycles and (b) Lift-out at the crack tip (location marked by a red box).*

at a triple junction before travelling along the boundary of one of the grains. Performing cross-correlation analysis on the 'bulk tip' in Figure 6.21 showed there was a high density of GNDs at the crack tip and particularly in the direction the crack travelled at the triple junction (Figure 6.22). The crack front is clearly visible in this map as it extends more than 4 µm ahead of the tip into both grains ahead of it and is ~2.5 µm wide. In addition, due to the sample prepared being

electron transparent it allowed for analysis using electron channeling contrast imaging (ECCI). These images were taken with the on-axis TKD setup and in a dark field arrangement. This allows for the observation of lattice defects such as dislocations. Figure 6.23 shows the dislocations present near the crack tip and in a separate crack in the lift-out. Both of these images support the cross-correlation analysis performed on this lift-out and the measured GND densities. As can be seen in both the GND density map and the ECCI image, there are more dislocations on the left side of the crack tip than on the right which is also the direction that the crack travels along the boundary. Lastly, what has been observed in all the samples analysed using the techniques outlined in this chapter is that the cracks always stopped at grain boundaries. Whether this be secondary cracks or primary cracks stopped mid-test, all were found to stop at grain boundaries. As has been discussed this was not effected by whether or not neighbouring grains were well oriented for the transfer of the crack between slip systems. The level of misalignment between grains along the crack path only dictated the time the crack spent at the boundary and whether the crack travelled through the grain or along the boundary thereby resulting in more slip bands forming as well as a larger amount of plastic deformation at the boundary and surrounding area (both of which were captured by GND density maps).

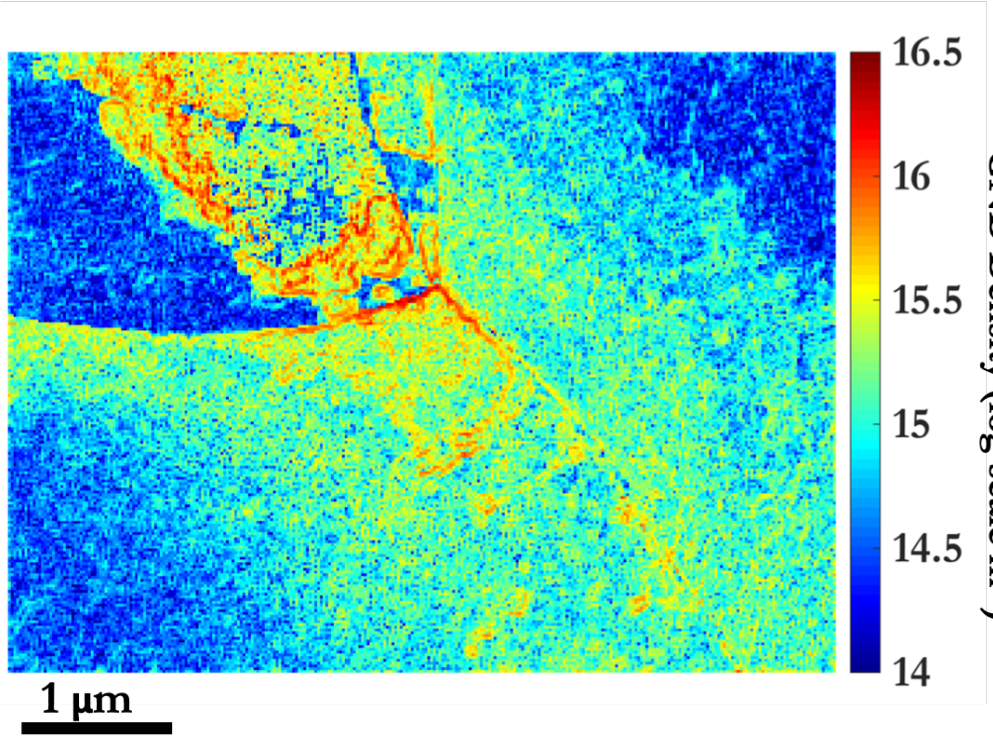
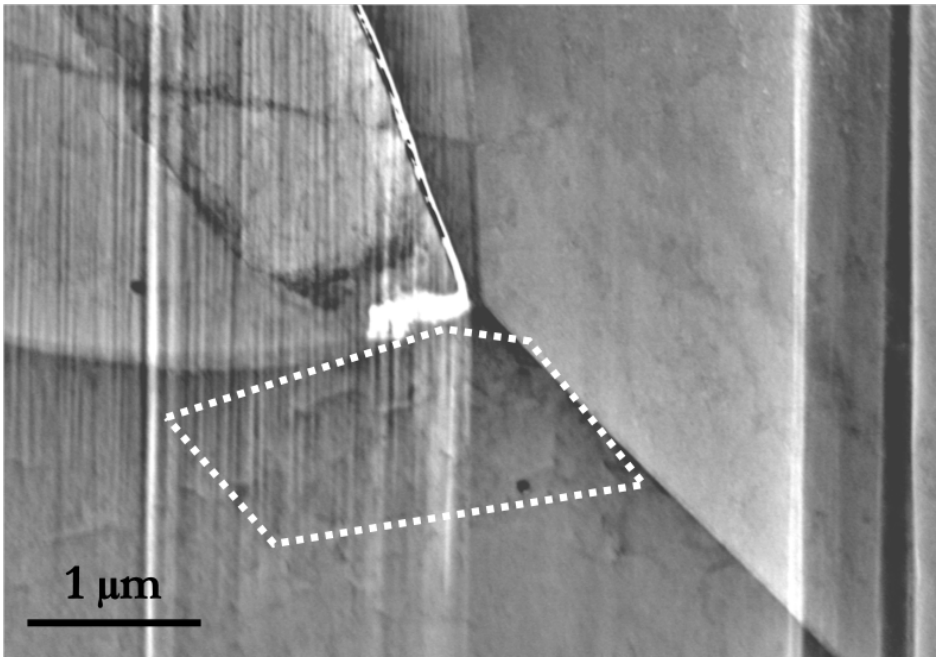


Figure 6.22: *GND Density Map of the crack area in Location 1 from the lift-out in Figure 6.21. (On-axis TKD configuration).*

(a)



(b)

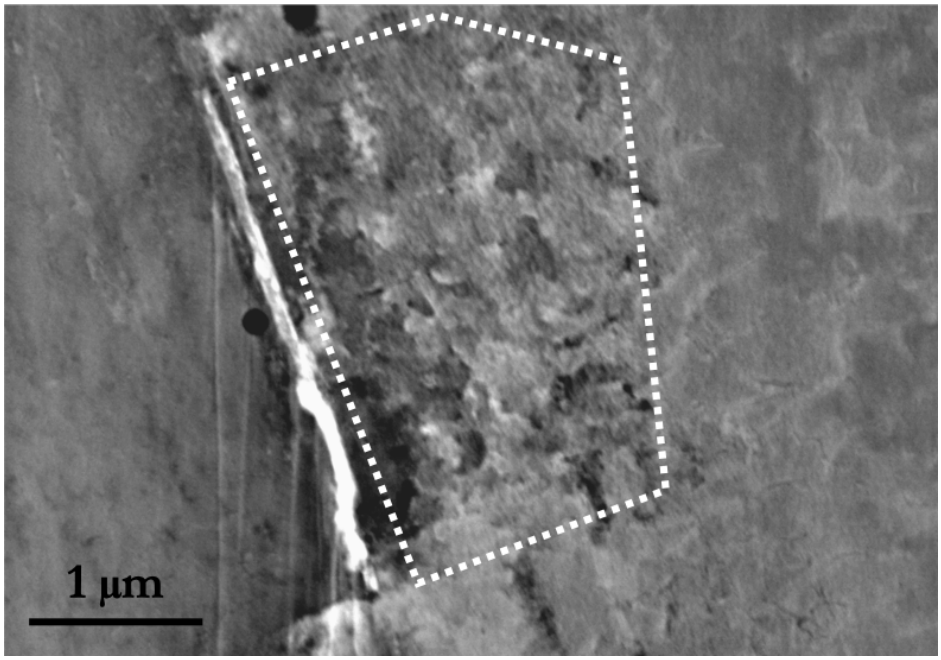


Figure 6.23: *Electron channeling contrast images (dark field) showing dislocations around (a) the crack tip shown in Location 1 in Figure 6.21 (b) secondary crack from area in Location 2 in Figure 6.21. (On-axis TKD configuration).*

6.3 Summary

In this chapter, the wealth of information that combined HR-EBSD and SEM analyses provides concerning short crack growth and fatigue crack initiation has been underscored. By using these techniques and analysis techniques together, it has been shown that primary fatigue cracks in the CP Ti mesocantilevers described will initiate within a grain rather than at a grain boundary and predominantly on the prism plane as a result of the texture of the cold-rolled material. These two observations were made by analysing EBSD maps before and after testing to determine the location of the fatigue crack initiation site as well as using polarised light images from testing to confirm that the primary crack initiated from the edge of the beam. Analysing the EBSD maps using MTEX, it was possible to calculate the most likely activated slip plane and compare it with the observed crack path. This showed that slip systems with the highest Schmid factor were predominantly prismatic. Using this information the misalignment between activated slip systems in neighbouring grains along the crack path was calculated and could be used to explain the crack's path. The crack would preferentially grow along the path of low misalignment i.e least resistance. In cases where the crack came to the boundary of a grain that had high misalignment, there would be a build up of intense slip bands before the crack progressed further. This would then typically be along the grain boundary or it would go below the surface before re-emerging at the surface in a more preferentially oriented grain. This phenomena was successfully captured by cross-correlation analysis as it would show areas of high GND density that are associated with increased plastic deformation. These GND density maps were able to show the plastic behaviour around the crack path and at the crack tip. The results presented in this chapter also showed that in all cases, the crack stopped at a grain boundary. This highlights the role grain boundaries and misalignment between grains plays in the crack growth rate. This phenomena was further confirmed in the case of the lift-out where the crack stopped at a boundary on the surface before continuing into the bulk and stopping at a triple-point. The accumulation of plasticity at this triple junction at the crack front demonstrated the size of the plastic zone ahead of a crack tip that has stopped at a boundary.

Chapter 7

Conclusions

The primary aim of this thesis was to improve the ultra high frequency fatigue testing method of miniaturised specimens and demonstrating the advanced characterisation / analysis techniques that can be combined with this technique. Secondly, it was to add to the existing database of Grade 2 CP-Ti high and ultra high cycle fatigue properties. Thirdly, to build on the understanding of the effect microstructure has on fatigue crack initiation and short crack growth in hcp metals. The primary aim can be said to have been achieved as a result of the two secondary aims. Due to its agreement with fatigue data found in literature this work has demonstrated that a significantly more reliable and improved method was developed. Likewise, this work has shown the rich data that can be achieved from using advanced techniques such as SEM, HR-EBSD and TKD. The secondary aims, and the extent to which they were met, will be explored in more detail below.

This primary aim was met by initially designing a mesocantilever that was appropriate for test conditions and that created a larger area of high stress concentration compared to preliminary cantilever geometries. In addition, by performing monotonic tests on single-crystal microscale cantilevers and bulk macroscale tensile specimens the baseline quasi-static physical properties of individual slip systems and the bulk crystal were determined. Microscale tests affirmed that the <a> prism plane is the weakest of the three slip systems investigated (Extrapolated bulk CRSS of

130 MPa). Bulk tensile tests at varying strain rates showed a trend of increasing yield points and ultimate tensile strengths. Tests on these two length scales were key in contextualising data from the mesoscale fatigue tests.

Ultrafast fatigue testing in this thesis was performed at 20 kHz with a load ratio of -1. Two testing protocols, single-step and multi-step, were employed to investigate the existence of any coaxing effect as a result of previous loading. The results presented here have shown that there is little/no coaxing effect in CP Ti as the probability of failure in the HCF regime was comparable at the same stress levels. Using a Basquin power law fit for single-step tests, the fatigue exponent (b) and fatigue coefficient (S) of single-step tests were -0.048 and 675 MPa respectively. These were comparable with values seen in literature (e.g b=-0.084, S=609.5 MPa [63]). Multi-step tests due to the uncertainty of failure stresses present during testing resulted in lower measured S and b (411 MPa and -0.0165 respectively). Single-step fatigue tests allowed for the determination of an endurance limit, a stress below which failure will not occur, of ~240 MPa for Grade 2 CP Ti. This value is in good agreement with the yield point values determined by the microscale and macroscale tests conducted. In addition, the combination of this sample design and testing method enabled for the quick measurement of fatigue performance deficit as a result of sample finish. The in-situ observation of the mesocantilevers during fatigue testing under polarised light enabled the study of the crack growth rate at specific stresses and highlighted the importance of fatigue crack initiation resistance for components designed to operate in the HCF-VHCF regime. In addition, nearly 200 individual data points were generated for Grade 2 CP-Ti fatigue performance in the high cycle and ultra high cycle regimes. This is a significant contribution to the data currently available. Therefore, it can be said that the second aim of adding to the current database of properties was also successful. However, as will be discussed in the future work section, it will be important to validate the strain rate sensitivity parameter to more accurately contextualise the results presented in this work. Likewise, it will be useful to perform addition high cycle fatigue tests at lower frequencies such as 200 - 2 kHz to evaluate the effect these lower frequency tests have on properties.

A variety of characterisation techniques, both basic and advanced, were utilised to meet the third aim of determining the effect microstructure has on FCI and growth in hcp metals. Initially, by observing the crack path in the polarised light images taken during testing that the crack arrests at boundaries before continuing. Coupling this information with that obtained by HR-EBSD analysis showed that these arrest points most likely coincide with misalignment of slip systems in neighbouring grains along the crack path. This was accompanied by higher densities of GNDs which indicated increased plastic activity at these points. Furthermore, when a crack stopped at a grain boundary it was often seen to extend into the depth of the sample before again stopping at a grain boundary. The experiments showed that in the majority of cases, crack initiation took up a large portion of a specimen's life. It was seen that, due to sample texture, fatigue crack initiation predominantly occurred on the prism plane (79% of the time) as throughout the cold-rolled CP Ti foil the prism plane had predominantly the higher Schmid factor coupled with its lower CRSS value. As was discussed in chapter 6.2, and will be explored further in the future work section, it will be important to gain a full picture of local Schmid factors to determine the effect Schmid factor has on the crack path and growth rates. In addition, this work showed that by performing fractography on a manageable surface size it allowed for the easy study of features such as striations and facets. By studying the direction of striations it was possible to ascertain the initiation point of the fatigue cracks which in the majority of cases occurred at the sample surface at the edge of the beam.

Analysing the misalignment between slip planes in neighbouring grains along the crack path provided strong evidence of the increased resistance to crack growth large misalignments provide. In the case of sufficiently large misalignments, the crack would stop at a boundary before progressing into the following grain but were the misalignment to be sufficiently large, it would preferentially grow on the grain boundary. This behaviour was always accompanied by an intense build up of slip bands, visible in SEM images, and increased GND density, as demonstrated by HR-EBSD analysis. Largely, it can therefore be said that a contribution to the effect microstructure has on FCI and short crack growth has been made by this work.

Chapter 8

Future Work

The above work has made good progress in demonstrating the viability of miniaturised ultra-fast fatigue testing as a way to measure the microstructural effects in HCF. There are, naturally, several exciting potential avenues of research that will add to the understanding of high-cycle fatigue performance and the ultrasonic testing method. This future work can be separated into three possible themes - addressing improvements in the above work, microstructural effects and advances to the testing method.

As was discussed earlier in this thesis, there were difficulties in measuring the strain rate sensitivity of the thin-foil specimens that were used to create the mesocantilevers. To overcome this, a solution would be to perform strain rate jump tests on the mesocantilevers themselves using a high-load nanoindenter. Maier et al[128] developed this new method as an alternative to conventional strain rate tests. Strain rate jump tests allow the user to apply a load to the sample at different strain rates within the same test to determine the effect these different strain rates have on the mechanical properties, thus determining the SRS. The advantages of this method are that one is able to test the same microstructure, particularly important in fine grain materials such as the one used in this thesis, to eliminate microstructural effects on the measured material strength variation. In addition, this method would be testing the mesocantilevers to be used in ultrasonic testing directly rather than testing a specimen with an entirely different geometry.

To further build on the results described in this thesis, it would be useful to model the local stresses to determine local Schmid factors and as such elucidate the role local Schmid factors play on crack growth rates and crack path. As was mentioned in section 6.2, there may be significantly different tensile stresses present in each grain due to residual stresses present in the material but also as a result of crack growth. These stresses could have a greater effect on the measured Schmid factor than the global tensile stress. Therefore, it is suggested that by using HR-EBSD techniques supported by CP-FEA modelling (as shown in work by Guo et al[129]) it will be possible to determine the local Schmid factors and then evaluate the effect it has on the crack path and growth rate.

As this work has shown that it is possible to determine the effect of microstructure in CP-Ti, an α-Ti microstructure, this can be taken further to explore other microstructures to further investigate how HCF properties are affected by microstructure. This theme of future work may continue with CP-Ti as the material of focus but focussing on, through heat treatment, changing the grain size and even shape to see how this could affect fatigue performance. Likewise, various α/β-Ti alloys can be investigated to determine the effect various microstructural features have on HCF properties. As demontstrated in the literature review (section 1.2.2) the effect of microstructure on HCF properties is pronounced. However, it would useful to determine the ability of this experimental method to reliably differentiate between the fatigue performance of various microstructures. If it can do so, then this will be a great step forward to quickly and reliably testing the properties of new alloys and will be a useful contribution towards iterative alloy development. This technique can also be leveraged for other metals and their alloys to compare their performance. The focus of this project was on as-rolled CP-Ti that had, largely, been untreated. As such, another exciting avenue would be to subject the material exposed to corrosive conditions. Aerospace components often undergo polishing steps that can result in significant amounts of hydrogen being absorbed by the material (the β-phase in titanium has a very high solubility of hydrogen [130]). Hydrogen has a strong propensity for moving to areas of high tensile stress[131] and as it is known to decrease ductility in a material [132], its presence can pose

significant problems for fatigue properties.

As was discussed in section 6.2, these tests provide a great opportunity to study crack behaviour at the grain boundary. However, more work needs to be done to generate a library of data surrounding the phenomena associated with a crack pausing at the grain boundary. This further work can start most simply from generating more data points to supplement those described in this thesis (crack path analysis of both the surface and crack-tip lift-outs). In addition, a promising direction would be to perform 3D-EBSD. This can be achieved by utilising a plasma FIB combined with EBSD techniques[133]. The process involves serial sectioning of the surface of the material followed by EBSD scans. A plasma FIB can remove material at rates 60 times greater than conventional Ga+ beam FIBs. One of the drawbacks of the lift-out technique described in this thesis and surface-only EBSD scans is that the angle of the grain boundary below the surface is not known. Likewise, the size of the grain the crack has paused in is also not known. This means that it is entirely plausible the crack has grown beyond the grain boundary below the surface and escaped the crack. By performing 3D-EBSD one would be able to get greater insight into the crack behaviour at grain boundaries and confirm the crack has indeed paused at the grain boundary. Of course, 3D-EBSD is a very time consuming process, due to the map acquisition time. An alternative method to examine the crack as it extends into the surface that is far quicker than 3D-EBSD is 3D-SEM. 3D-SEM, utilises the same principle as 3D-EBSD but instead of taking an EBSD scan it would take an SEM image. 3D-SEM would not provide information regarding the orientations of the microstructure but the information it could provide is useful nonetheless. By taking SEM images following a FIB section, one could gain great insight into the deflection / angle of the crack tip and crack path through the material surface. This increased information would be useful in understanding how the crack has interacted with grain boundaries and gain a view of the full shape of the crack tip.

Ultrasonic fatigue testing of miniaturised components is still a testing method in its infancy. As such, there are many exciting avenues that will both improve the understanding of this method and increase its applicability. Currently, work is on-going to attach a furnace to the ultrasonic

testing rig in order to test materials at various temperatures in order to investigate the effect higher temperatures have on HCF properties. Work by Kobayashi et al on 2.25Cr–1Mo steel showed that fatigue properties decrease with increasing temperature[134]. Naturally, work can be done to also investigate the effect of lower temperatures. Work has been done to investigate the effect of cryogenic temperatures on high-cycle fatigue properties and found fatigue strength to increase with decreasing temperatures[135]. These tests were performed at conventional fatigue testing strain rates rather than ultra-fast testing conditions. Due to this pronounced difference in properties as a result of temperature it would be key to determine the viability of ultra-fast testing under cryogenic conditions. Ono et al were also able to show that microstructures also play a key role in affecting fatigue properties at cryogenic temperatures (smaller grain sizes resulted in higher fatigue strengths)[136]. Being able to measure high cycle fatigue properties at cryogenic temperatures is particularly useful as these are the conditions found in the liquid hydrogen turbopumps of launch vehicles.

As was mentioned, in the body of this work, tests were frequently paused at pre-determined intervals to attempt to capture a crack as it had just initiated or at various crack path lengths. The approach to do so relied heavily on intuition and a large number of pauses during testing, and subsequent observation of the sample, to capture these moments. A significant improvement to the testing method that would improve the chances of capturing a crack at initiation or desired lengths would be to utilise higher performance measuring equipment (e.g. ultra-high-speed / higher resolution cameras). One could theoretically use the change in brightness in the image of the sample to detect a crack (as cracks often scatter and reflect more light than an uncracked surface). This would also make it significantly easier to perform pause tests where a crack has stopped at the grain boundary. Another large inefficiency of the current setup is the time taken to remove the sample from the testing rig and transferring it to the SEM to analyse the surface and to use EBSD to analyse the microstructure around the crack path. Therefore, being able to attach the ultrasonic rig to an SEM with an EBSD detector would remove this inefficiency and will allow for more accurate crack tracking and to perform EBSD more frequently as the crack progresses.

One could also use in-situ AFM for crack growth measurement. Using this technique it would be possible to scan the surface and have a sub-micron resolution of the crack tip, allowing more accurate measurement of the growth rate and crack progression.

Bibliography

[1] Tong-guang Zhai, AJ Wilkinson, and JW Martin. A crystallographic mechanism for fatigue crack propagation through grain boundaries. *Acta materialia*, 48(20):4917–4927, 2000.

[2] Gerd Lütjering and James C Williams. Titanium. 2007.

[3] EASA. Certification Specifications for Engines - Amendment 3. 2010.

[4] CH Wells and CP Sullivan. Low-Cycle Fatigue Crack Initiation In Ti–6Al–4V. 1969.

[5] Miloš Janeček, František Novỳ, Josef Stráskỳ, Petr Harcuba, and Lothar Wagner. Fatigue Endurance of Ti–6Al–4V Alloy with Electro-eroded Surface for Improved Bone In-growth. *Journal of the mechanical behavior of biomedical materials*, 4(3):417–422, 2011.

[6] RJ Morrissey, DL McDowell, and T Nicholas. Frequency and Stress Ratio Effects in High Cycle Fatigue of Ti–6Al–4V. *International Journal of Fatigue*, 21(7):679–685, 1999.

[7] D Rao. Development of an Automated High Frequency Material Test System. *Technical Report Air Force Research Laboratory, Wright-Patterson Air Force Base*, 1998.

[8] Ian Polmear. *Light alloys: from traditional alloys to nanocrystals*. Elsevier, 2005.

[9] RR Boyer. Thermec 2003. In *International Conference on Processing and Manufacturing of Advanced Materials. Trans Tech Publications, Zurich*, 2003.

[10] RR Boyer. An overview on the use of titanium in the aerospace industry. *Materials Science and Engineering: A*, 213(1-2):103–114, 1996.

[11] RR Boyer. Attributes, characteristics, and applications of titanium and its alloys. *Jom*, 62(5):21–24, 2010.

[12] Robert A Miller. Thermal barrier coatings for aircraft engines: history and directions. *Journal of thermal spray technology*, 6(1):35, 1997.

[13] Uwe Schulz, Christoph Leyens, Klaus Fritscher, Manfred Peters, Bilge Saruhan-Brings, Odile Lavigne, Jean-Marc Dorvaux, Martine Poulain, Remy Mévrel, and Michaël Caliez. Some recent trends in research and technology of advanced thermal barrier coatings. *Aerospace Science and technology*, 7(1):73–80, 2003.

[14] James M Larsen, Stephan M Russ, and JW Jones. An evaluation of fiber-reinforced titanium matrix composites for advanced high-temperature aerospace applications. *Metallurgical and Materials Transactions A*, 26(12):3211–3223, 1995.

[15] R.S.J. Corran and S.J. Williams. Lifing methods and safety criteria in aero gas turbines. *Engineering Failure Analysis*, 14:518–528, 04 2007.

[16] T Nicholas and J R. Zuiker. On the use of the goodman diagram for high cycle fatigue design. *International Journal of Fracture*, 80:219–235, 04 1989.

[17] W. A. Wood. Formation of fatigue cracks. *The Philosophical Magazine: A Journal of Theoretical Experimental and Applied Physics*, 3(31):692–699, 1958.

[18] Subra Suresh. *Fatigue of Materials*. Cambridge University Press, 1998.

[19] Y.M Hu, W Floer, Ulrich Krupp, and H.-J Christ. Microstructurally short fatigue crack initiation and growth in Ti–6.8Mo–4.5Fe–1.5Al. *Materials Science and Engineering: A*, 278:170–180, 02 2000.

[20] A. Heinz and P. Neumann. Crack initiation during high cycle fatigue of an austenitic steel. *Acta Metallurgica et Materialia*, 38(10):1933 – 1940, 1990.

[21] F. Bridier, P. Villechaise, and J. Mendez. Analysis of the different slip systems activated by tension in a α/β titanium alloy in relation with local crystallographic orientation. *Acta Materialia*, 53(3):555 – 567, 2005.

[22] F Bridier, P Villechaise, and J Mendez. Slip and fatigue crack formation processes in an α/β titanium alloy in relation to crystallographic texture on different scales. *Acta Materialia*, 56(15):3951–3962, 2008.

[23] NE Paton, RG Baggerly, and JC Williams. Deformation and solid solution strengthening of titanium-aluminum single crystals. 1976.

[24] K Le Biavant, S Pommier, and C Prioul. Local texture and fatigue crack initiation in a Ti–6Al–4V titanium alloy. *Fatigue & Fracture of Engineering Materials & Structures*, 25(6):527–545, 2002.

[25] Craig P Przybyla and David L McDowell. Simulated microstructure-sensitive extreme value probabilities for high cycle fatigue of duplex Ti–6Al–4V. *International Journal of Plasticity*, 27(12):1871–1895, 2011.

[26] David L. McDowell. Simulation-based strategies for microstructure-sensitive fatigue modeling. *Materials Science and Engineering: A*, 468-470:4 – 14, 2007. The McEvily Symposium: Fatigue and Fracture of Traditional and Advanced Materials, TMS 2006.

[27] D.L. McDowell and F.P.E. Dunne. Microstructure-sensitive computational modeling of fatigue crack formation. *International Journal of Fatigue*, 32(9):1521 – 1542, 2010. Emerging Frontiers in Fatigue.

[28] V Sinha, MJ Mills, J Cv Williams, and JE Spowart. Observations on the faceted initiation site in the dwell-fatigue tested Ti–6242 alloy: crystallographic orientation and size effects. *Metallurgical and Materials Transactions A*, 37(5):1507–1518, 2006.

[29] Ioannis Bantounas, David Dye, and Trevor C Lindley. The role of microtexture on the faceted fracture morphology in Ti–6Al–4V subjected to high-cycle fatigue. *Acta materialia*, 58(11):3908–3918, 2010.

[30] K Nakajima, K Terao, and T Miyata. The effect of microstructure on fatigue crack propagation of $\alpha+\beta$ titanium alloys: in-situ observation of short fatigue crack growth. *Materials Science and Engineering: A*, 243(1-2):176–181, 1998.

[31] Vartha Venkateswarlu, Debashish Tripathy, K Rajagopal, K Thomas Tharian, and P.V. Venkitakrishnan. Failure analysis and optimization of thermo-mechanical process parameters of titanium alloy (Ti–6Al–4V) fasteners for aerospace applications. *Case Studies in Engineering Failure Analysis*, 1:49–60, 04 2013.

[32] V. Sinha, M.J. Mills, and J.C. Williams. Crystallography of fracture facets in a near-alpha titanium alloy. *Metallurgical and Materials Transactions A: Physical Metallurgy and Materials Science*, 37(6):2015–2026, 2006. cited By 73.

[33] Ioannis Bantounas, David Dye, and Trevor C. Lindley. The effect of grain orientation on fracture morphology during high-cycle fatigue of Ti–6Al–4V. *Acta Materialia*, 57(12):3584 – 3595, 2009.

[34] MR Bache, WJ Evans, and HM Davies. Electron back scattered diffraction (ebsd) analysis of quasi-cleavage and hydrogen induced fractures under cyclic and dwell loading in titanium alloys. *Journal of Materials Science*, 32(13):3435–3442, 1997.

[35] R.J.H Wanhill, R Galatolo, and C.E.W Looije. Fractographic and microstructural analysis of fatigue crack growth in a Ti–6Al–4V fan disc forging. *International Journal of Fatigue*, 11(6):407 – 416, 1989.

[36] GR Yoder, LA Cooley, and TW Crooker. Fatigue crack propagation resistance of beta-annealed Ti-6Ai-4V alloys of differing interstitial oxygen contents. *Metallurgical Transactions A*, 9(10):1413–1420, 1978.

[37] S Suresh and RO Ritchie. A geometric model for fatigue crack closure induced by fracture surface roughness. *Metallurgical transactions A*, 13(9):1627–1631, 1982.

[38] Ervin E Underwood and Kingshuk Banerji. Fractals in fractography. *Materials Science and Engineering*, 80(1):1–14, 1986.

[39] ErvinE Underwood. Practical solutions to stereological problems. In *Practical Applications of Quantitative Metallography*. ASTM International, 1984.

[40] Bertram Hopkinson. A high-speed fatigue-tester, and the endurance of metals under alternating stresses of high frequency. *Proceedings of the Royal Society of London. Series A, Containing Papers of a Mathematical and Physical Character*, 86(584):131–149, 1912.

[41] Charles Frewen Jenkin. High-frequency fatigue tests. *Proceedings of the Royal Society of London. Series A, Containing Papers of a Mathematical and Physical Character*, 109(749):119–143, 1925.

[42] Charles Frewen Jenkin and GD Lehmann. High frequency fatigue. *Proceedings of the Royal Society of London. Series A, Containing Papers of a Mathematical and Physical Character*, 125(796):83–119, 1929.

[43] Warren P Mason and Hans Baerwald. Piezoelectric crystals and their applications to ultrasonics. *Physics Today*, 4:23, 1951.

[44] F Girard and G Vidal. Micromachine de fatigue en traction-compression à 92 000 alternances par seconde. *Revue de Métallurgie*, 56(1):25–39, 1959.

[45] M Kikukawa, Kiyotsugu Ohji, and Keiji Ogura. Push-pull fatigue strength of mild steel at very high frequencies of stress up to 100 kc/s. *Journal of Basic Engineering*, 87(4):857–864, 1965.

[46] Q. Y. Wang, J. Y. Berard, A. Dubarre, G. Baudry, S. Rathery, and C. Bathias. Gigacycle fatigue of ferrous alloys. *Fatigue & Fracture of Engineering Materials & Structures*, 22(8):667–672, 1999.

[47] Claude Bathias and Paul C. Paris. Gigacycle fatigue of metallic aircraft components. *International Journal of Fatigue*, 32(6):894 – 897, 2010. Selected Papers of the 17th European Conference of Fracture (ECF 17).

[48] I Marines, X Bin, and C Bathias. An understanding of very high cycle fatigue of metals. *International Journal of Fatigue*, 25(9):1101 – 1107, 2003. International Conference on Fatigue Damage of Structural Materials IV.

[49] August Wöhler. Bericht über die versuche, welche auf der königl. niederschlesisch-märkischen eisenbahn mit apparaten zum messen der biegung und verdrehung von eisenbahnwagen-achsen während der fahrt angestellt wurden. *Zeitschrift für Bauwesen*, 8(1858):641–652, 1858.

[50] K Asami and Y Sugiyama. Fatigue strength of various surface hardened steels. *Netsu Shori(J. Jpn. Soc. Heat Treat.)*, 25(3):147–150, 1985.

[51] Takeshi Naito, Hideo Ueda, and Masao Kikuchi. Fatigue behavior of carburized steel with internal oxides and nonmartensitic microstructure near the surface. *Metallurgical Transactions A*, 15(7):1431–1436, 1984.

[52] Y. Murakami and M. Endo. Effects of defects, inclusions and inhomogeneities on fatigue strength. *International Journal of Fatigue*, 16(3):163 – 182, 1994.

[53] Claude Bathias. Piezoelectric fatigue testing machines and devices. *International Journal of Fatigue*, 28(11):1438–1445, 2006.

[54] S. Heinz and D. Eifler. Crack initiation mechanisms of Ti–6Al–4V in the very high cycle fatigue regime. *International Journal of Fatigue*, 93:301 – 308, 2016. Gigacycle Fatigue-Theory and Applications Dedicated to the Memory of Professor Claude Bathias.

[55] R. Pollak, A. Palazotto, and T. Nicholas. A simulation-based investigation of the staircase method for fatigue strength testing. *Mechanics of Materials*, 38(12):1170 – 1181, 2006.

[56] JH Smith. Some experiments on fatigue of metals. *J. Iron Steel Inst*, 82(2):246–318, 1910.

[57] Herbert Fisher Moore, Thomas McLean Jasper, et al. An investigation of the fatigue of metals, series of 1922; a report of the investigation conducted by the engineering experiment station, university of illinois, in coöperation with the national research council, engineering foundation, the general electric company. Technical report, University of Illinois at Urbana Champaign, College of Engineering ..., 1923.

[58] Theodore Nicholas. Step loading for very high cycle fatigue. *Fatigue & Fracture of Engineering Materials & Structures*, 25(8-9):861–869, 2002.

[59] E Epremian and R Mehl. A statistical interpretation of the effect of understressing on fatigue strength. In *Symposium on Fatigue with Emphasis on Statistical Approach-II*. ASTM International, 1953.

[60] Wilfrid Joseph Dixon and Am M Mood. A method for obtaining and analyzing sensitivity data. *Journal of the American Statistical Association*, 43(241):109–126, 1948.

[61] Robert Eugene Little and Emil H Jebe. *Statistical design of fatigue experiments*. Applied Science Publishers, 1975.

[62] Equo Kobayashi, Hiroto Mochizuki, Hisashi Doi, Takayuki Yoneyama, and Takao Hanawa. Fatigue life prediction of biomedical titanium alloys under tensile/torsional stress. *Materials transactions*, 47(7):1826–1831, 2006.

[63] C Casavola, C Pappalettere, and G Pluvinage. Fatigue resistance of titanium laser and hybrid welded joints. *Materials & Design*, 32(5):3127–3135, 2011.

[64] S.V. Sajadifar, T. Wegener, G.G. Yapici, and T. Niendorf. Effect of grain size on the very high cycle fatigue behavior and notch sensitivity of titanium. *Theoretical and Applied Fracture Mechanics*, 104:102362, 2019.

[65] Jicheng Gong, T Benjamin Britton, Mitchell A Cuddihy, Fionn PE Dunne, and Angus J Wilkinson. < a> prismatic,< a> basal, and< c+ a> slip strengths of commercially pure Zr by micro-cantilever tests. *Acta Materialia*, 96:249–257, 2015.

[66] Michael D. Uchic and Dennis M. Dimiduk. A methodology to investigate size scale effects in crystalline plasticity using uniaxial compression testing. *Materials Science and Engineering: A*, 400-401:268 – 278, 2005. Dislocations 2004.

[67] S. Liu, J. M. Wheeler, P. R. Howie, X. T. Zeng, J. Michler, and W. J. Clegg. Measuring the fracture resistance of hard coatings. *Applied Physics Letters*, 102(17):171907, 2013.

[68] Nagamani Jaya B, Vikram Jayaram, and Sanjay Kumar Biswas. A new method for fracture toughness determination of graded (Pt,Ni)Al bond coats by microbeam bend tests. *Philosophical Magazine*, 92(25-27):3326–3345, 2012.

[69] Jicheng Gong and Angus J Wilkinson. Anisotropy in the plastic flow properties of single-crystal α titanium determined from micro-cantilever beams. *Acta Materialia*, 57(19):5693–5705, 2009.

[70] Rengen Ding, Jicheng Gong, Angus J Wilkinson, and Ian P Jones. < c+ a> dislocations in deformed Ti–6Al–4V micro-cantilevers. *Acta Materialia*, 76:127–134, 2014.

[71] F.P.E. Dunne, D. Rugg, and A. Walker. Lengthscale-dependent, elastically anisotropic, physically-based hcp crystal plasticity: Application to cold-dwell fatigue in Ti alloysi alloys. *International Journal of Plasticity*, 23(6):1061 – 1083, 2007.

[72] David EJ Armstrong, Angus J Wilkinson, and Steve G Roberts. Measuring anisotropy in young's modulus of copper using microcantilever testing. *Journal of materials research*, 24(11):3268–3276, 2009.

[73] Jicheng Gong and Angus Wilkinson. Investigation of elastic properties of single-crystal α-Ti using microcantilever beams. *Philosophical Magazine Letters*, 90(7):503–512, 2010.

[74] Jicheng Gong and Angus J. Wilkinson. A microcantilever investigation of size effect, solid-solution strengthening and second-phase strengthening for ⟨a⟩ prism slip in alpha–Ti. *Acta Materialia*, 59(15):5970 – 5981, 2011.

[75] J. Gong and A.J. Wilkinson. Micro-cantilever testing of a prismatic slip in commercially pure Ti. *Philosophical Magazine*, 91(7-9):1137–1149, 2011. cited By 20.

[76] Adam J Schwartz, Mukul Kumar, Brent L Adams, and David P Field. *Electron backscatter diffraction in materials science*. Springer, 2000.

[77] MN Alam, Moses Blackman, and Donald William Pashley. High-angle kikuchi patterns. *Proceedings of the Royal Society of London. Series A. Mathematical and Physical Sciences*, 221(1145):224–242, 1954.

[78] H Boersch. Über bänder bei elektronenbeugung. *Phys. Z*, 38:1000–1004, 1937.

[79] R v Meibom and E Rupp. Elektronenbeugung in weiten winkeln. *Zeitschrift für Physik*, 82(11-12):690–696, 1933.

[80] Angus J Wilkinson, David J Dingley, and Graham Meaden. Strain mapping using electron backscatter diffraction. In *Electron Backscatter Diffraction in Materials Science*, pages 231–249. Springer, 2009.

[81] PN Quested, PJ Henderson, and M McLean. Observations of deformation and fracture heterogeneities in a nickel-base superalloy using electron back scattering patterns. *Acta Metallurgica*, 36(10):2743–2752, 1988.

[82] R MacKenzie. Ph.d thesis. *University of Bristol*, 1987.

[83] Angus J Wilkinson and David J Dingley. Quantitative deformation studies using electron back scatter patterns. *Acta Metallurgica et Materialia*, 39(12):3047–3055, 1991.

[84] DJ Prior. Problems in determining the misorientation axes, for small angular misorientations, using electron backscatter diffraction in the sem. *Journal of Microscopy*, 195(3):217–225, 1999.

[85] Angus J Wilkinson. Methods for determining elastic strains from electron backscatter diffraction and electron channelling patterns. *Materials Science and Technology*, 13(1):79–84, 1997.

[86] TB Britton and AJ Wilkinson. High resolution electron backscatter diffraction measurements of elastic strain variations in the presence of larger lattice rotations. *Ultramicroscopy*, 114:82–95, 2012.

[87] Claire Maurice, Julian H Driver, and Roland Fortunier. On solving the orientation gradient dependency of high angular resolution ebsd. *Ultramicroscopy*, 113:171–181, 2012.

[88] Angus J Wilkinson, Graham Meaden, and David J Dingley. High resolution mapping of strains and rotations using electron backscatter diffraction. *Materials Science and Technology*, 22(11):1271–1278, 2006.

[89] Angus J Wilkinson, Graham Meaden, and David J Dingley. High-resolution elastic strain measurement from electron backscatter diffraction patterns: New levels of sensitivity. *Ultramicroscopy*, 106(4-5):307–313, 2006.

[90] Jun Jiang, T. Ben Britton, and Angus J. Wilkinson. The orientation and strain dependence of dislocation structure evolution in monotonically deformed polycrystalline copper. *International Journal of Plasticity*, 69:102 – 117, 2015.

[91] J Jiang, TB Britton, and AJ Wilkinson. Measurement of geometrically necessary dislocation density with high resolution electron backscatter diffraction: effects of detector binning and step size. *Ultramicroscopy*, 125:1–9, 2013.

[92] Robert R Keller and Roy H Geiss. Transmission ebsd from 10 nm domains in a scanning electron microscope. *Journal of Microscopy*, 245(3):245–251, 2012.

[93] J-J Fundenberger, E Bouzy, D Goran, J Guyon, A Morawiec, Yuan, and H. Transmission kikuchi diffraction (TKD) via a horizontally positioned detector. *Microscopy and Microanalysis*, 21(S3):1101–1102, 2015.

[94] Jean-Jacques Fundenberger, Emmanuel Bouzy, D Goran, Julien Guyon, H Yuan, and A Morawiec. Orientation mapping by transmission-sem with an on-axis detector. *Ultramicroscopy*, 161:17–22, 2016.

[95] N Brodusch, H Demers, and R Gauvin. Nanometres-resolution kikuchi patterns from materials science specimens with transmission electron forward scatter diffraction in the scanning electron microscope. *Journal of Microscopy*, 250(1):1–14, 2013.

[96] Rik van Bremen, D Ribas Gomes, LTH de Jeer, Václav Ocelík, and J Th M De Hosson. On the optimum resolution of transmission-electron backscattered diffraction (t-ebsd). *Ultramicroscopy*, 160:256–264, 2016.

[97] H Yuan, E Brodu, C Chen, E Bouzy, J-J FUNDENBERGER, and LS Toth. On-axis versus off-axis transmission kikuchi diffraction technique: application to the characterisation of severe plastic deformation-induced ultrafine-grained microstructures. *Journal of microscopy*, 267(1):70–80, 2017.

[98] Patrick W Trimby. Orientation mapping of nanostructured materials using transmission kikuchi diffraction in the scanning electron microscope. *Ultramicroscopy*, 120:16–24, 2012.

[99] Katherine P Rice, Robert R Keller, and MP Stoykovich. Specimen-thickness effects on transmission kikuchi patterns in the scanning electron microscope. *Journal of microscopy*, 254(3):129–136, 2014.

[100] DR Steinmetz and S Zaefferer. Towards ultrahigh resolution ebsd by low accelerating voltage. *Materials Science and Technology*, 26(6):640–645, 2010.

[101] Hongbing Yu, Junliang Liu, Phani Karamched, Angus J Wilkinson, and Felix Hofmann. Mapping the full lattice strain tensor of a single dislocation by high angular resolution transmission kikuchi diffraction (hr-tkd). *Scripta Materialia*, 164:36–41, 2019.

[102] J. B. Pethicai, R. Hutchings, and W. C. Oliver. Hardness Measurement at Penetration Depths as Small as 20 nm. *Philosophical Magazine A*, 48(4):593–606, 1983.

[103] Agilent Technologies. G200 Nanoindenter Application Note.

[104] F.P.E. Dunne, A.J. Wilkinson, and R. Allen. Experimental and computational studies of low cycle fatigue crack nucleation in a polycrystal. *International Journal of Plasticity*, 23(2):273 – 295, 2007.

[105] Mark Whittaker. *Titanium in the Gas Turbine Engine*. 11 2011.

[106] M. NEWMAN and I. U. OJALVO. Vibration modes of large structures by an automatic matrix-reductionmethod. *AIAA Journal*, 8(7):1234–1239, 1970.

[107] Damien Andre. https://gitlab.com/damien.andre/pydic/.

[108] J. Ahrens, Berk Geveci, and Charles Law. Paraview: An end-user tool for large data visualization. *Visualization Handbook*, 01 2005.

[109] M.A. Meyers, G. Subhash, B.K. Kad, and L. Prasad. Evolution of microstructure and shear-band formation in α-hcp titanium. *Mechanics of Materials*, 17(2):175 – 193, 1994.

[110] D.R. Chichili, K.T. Ramesh, and K.J. Hemker. The high-strain-rate response of alpha-titanium: experiments, deformation mechanisms and modeling. *Acta Materialia*, 46(3):1025 – 1043, 1998.

[111] Tea-Sung Jun, David E.J. Armstrong, and T. Benjamin Britton. A nanoindentation investigation of local strain rate sensitivity in dual-phase ti alloys. *Journal of Alloys and Compounds*, 672:282 – 291, 2016.

[112] Qinmeng Luan, T. Benjamin Britton, and Tea-Sung Jun. Strain rate sensitivity in commercial pure titanium: The competition between slip and deformation twinning. *Materials Science and Engineering: A*, 734:385 – 397, 2018.

[113] Min-Su Lee, Yong-Taek Hyun, and Tea-Sung Jun. Global and local strain rate sensitivity of commercially pure titanium. *Journal of Alloys and Compounds*, 803:711 – 720, 2019.

[114] TB Britton, FPE Dunne, and AJ Wilkinson. On the mechanistic basis of deformation at the microscale in hexagonal close-packed metals. *Proceedings of the Royal Society A: Mathematical, Physical and Engineering Sciences*, 471(2178):20140881, 2015.

[115] Parviz Soroushian and Ki-Bong Choi. Steel mechanical properties at different strain rates. *Journal of Structural Engineering*, 113(4):663–672, 1987.

[116] O Grässel, L Krüger, G Frommeyer, and L.W Meyer. High strength Fe–Mn–(Al, Si) TRIP/TWIP steels development — properties — application. *International Journal of Plasticity*, 16(10):1391 – 1409, 2000.

[117] A.E. Medvedev, H.P. Ng, R. Lapovok, Y. Estrin, T.C. Lowe, and V.N. Anumalasetty. Effect of bulk microstructure of commercially pure titanium on surface characteristics and

fatigue properties after surface modification by sand blasting and acid-etching. *Journal of the Mechanical Behavior of Biomedical Materials*, 57:55 – 68, 2016.

[118] Claude Bathias and Paul C Paris. *Gigacycle fatigue in mechanical practice*, volume 185. CRC Press, 2004.

[119] B.L. Boyce and R.O. Ritchie. Effect of load ratio and maximum stress intensity on the fatigue threshold in Ti—6Al—4V. *Engineering Fracture Mechanics*, 68(2):129 – 147, 2001.

[120] K. Hussain. Short fatigue crack behaviour and analytical models: A review. *Engineering Fracture Mechanics*, 58(4):327 – 354, 1997.

[121] A. King, W. Ludwig, M. Herbig, J.-Y. Buffière, A.A. Khan, N. Stevens, and T.J. Marrow. Three-dimensional in situ observations of short fatigue crack growth in magnesium. *Acta Materialia*, 59(17):6761 – 6771, 2011.

[122] C. W. BROWN and M. A. HICKS. A study of short fatigue crack growth behaviour in titanium alloy imi 685. *Fatigue & Fracture of Engineering Materials & Structures*, 6(1):67–76, 1983.

[123] Adam L. Pilchak. Fatigue crack growth rates in alpha titanium: Faceted vs. striation growth. *Scripta Materialia*, 68(5):277 – 280, 2013.

[124] A. Turnbull and E. R. De Los Rios. The effect of grain size on fatigue crack growth in an aluminium magnesium alloy. *Fatigue & Fracture of Engineering Materials & Structures*, 18(11):1355–1366, 1995.

[125] P Neumann. Coarse slip model of fatigue. *Acta Metallurgica*, 17(9):1219 – 1225, 1969.

[126] A. Hunsche and P. Neumann. Quantitative measurement of persistent slip band profiles and crack initiation. *Acta Metallurgica*, 34(2):207 – 217, 1986.

[127] Z.F. Zhang and Z.G. Wang. Dependence of intergranular fatigue cracking on the interactions of persistent slip bands with grain boundaries. *Acta Materialia*, 51(2):347 – 364, 2003.

[128] Verena Maier, Karsten Durst, Johannes Mueller, Björn Backes, Heinz Werner Höppel, and Mathias Göken. Nanoindentation strain-rate jump tests for determining the local strain-rate sensitivity in nanocrystalline ni and ultrafine-grained al. *Journal of materials research*, 26(11):1421–1430, 2011.

[129] Y. Guo, H. Abdolvand, T.B. Britton, and A.J. Wilkinson. Growth of 112¯2 twins in titanium: A combined experimental and modelling investigation of the local state of deformation. *Acta Materialia*, 126:221 – 235, 2017.

[130] Yanhong Chang, Andrew J. Breen, Zahra Tarzimoghadam, Philipp Kürnsteiner, Hazel Gardner, Abigail Ackerman, Anna Radecka, Paul A.J. Bagot, Wenjun Lu, Tong Li, Eric A. Jägle, Michael Herbig, Leigh T. Stephenson, Michael P. Moody, David Rugg, David Dye, Dirk Ponge, Dierk Raabe, and Baptiste Gault. Characterizing solute hydrogen and hydrides in pure and alloyed titanium at the atomic scale. *Acta Materialia*, 150:273 – 280, 2018.

[131] T. P. Chapman, D. Dye, and D. Rugg. Hydrogen in ti and zr alloys: industrial perspective, failure modes and mechanistic understanding. *Philosophical Transactions of the Royal Society A: Mathematical, Physical and Engineering Sciences*, 375(2098):20160418, 2017.

[132] M. L. Wasz, F. R. Brotzen, R. B. McLellan, and A. J. Griffin. Effect of oxygen and hydrogen on mechanical properties of commercial purity titanium. *International Materials Reviews*, 41(1):1–12, 1996.

[133] T.L. Burnett, R. Kelley, B. Winiarski, L. Contreras, M. Daly, A. Gholinia, M.G. Burke, and P.J. Withers. Large volume serial section tomography by xe plasma fib dual beam microscopy. *Ultramicroscopy*, 161:119 – 129, 2016.

[134] Hideo Kobayashi, Akira Todoroki, Toshikazu Oomura, Takeru Sano, and Tatsumi Takehana. Ultra-high-cycle fatigue properties and fracture mechanism of modified 2.25cr–1mo steel at elevated temperatures. *International Journal of Fatigue*, 28(11):1633 – 1639, 2006. Third International Conference on Very High Cycle Fatigue (VHCF-3).

[135] Yoshinori Ono, Tetsumi Yuri, Hideshi Sumiyoshi, Etsuo Takeuchi, Saburo Matsuoka, and Toshio Ogata. High-cycle fatigue properties at cryogenic temperatures in inconel 718 nickel-based superalloy. *MATERIALS TRANSACTIONS*, 45(2):342–345, 2004.

[136] Y. Ono, T. Yuri, H. Sumiyoshi, S. Matsuoka, and T. Ogata. Effect of grain size on high-cycle fatigue properties in alpha-type titanium alloy at cryogenic temperatures. *Cryogenics*, 43(8):483 – 489, 2003.